Determining S6K1 localisation and interactions with mTORC1 in live cells using fluorescence lifetime imaging microscopy

OXFORD BROOKES UNIVERSITY

A thesis submitted to and awarded by

Oxford Brookes University

in partial fulfilment of the requirements of the award of

DOCTOR OF PHILOSOPHY

Department of Biological and Medical Sciences

September 2018

Abdullah R Ahmed

Collaborating establishments: STFC, Evotec, PP-UK

In dedication to my mother Sajdah Masarrat, a single parent, without whom I would not have achieved my academic accomplishments. I express my sincere gratitude for her constant support and prayers. Her endless love and positive attitude has inspired me to reach my full potential. Without her I would not have completed my greatest achievement yet, my PhD.

Author's declaration

I hereby declare that this submission is my own work under the supervision of Professors Anthony Parker, Chris Stubbs and Chris Hawes and that, to the best of my knowledge and belief, it contains no material previously published or written by another person or material which has to a substantial extent been accepted for the award of any other degree or diploma at any university or other institute.

Name: Abdullah Ahmed

Signature: 

Date: 27/09/18

Acknowledgements

There are a number of people that without their help this thesis would not have been possible. Many thanks and gratitude to my supervisors Tony Parker (STFC), Chris Stubbs (STFC) and Chris Hawes (Oxford Brookes) for their guidance as well as support from Professor Stanley Botchway (STFC), Dr Rahul Yadav (Evotec), Dr Richard Hitchman (Evotec) and Professor Ray Owens (PP-UK). I am thankful to the BBSRC for an iCASE PhD studentship (BB/L016052/1) and thank STFC for funding access to the Central Laser Facility, Protein Production UK for access to their laboratory and expertise and Evotec for training, facility access and financial support.

My sincere gratitude to Dr Maud Dumoux for helping with the expression and purification of the SensOR protein. I would also like to thank Dr Alessia Candeo for the work done using Light sheet microscopy and Marta Szynkiewicz for her laboratory support. My heartfelt thank you to Dr John Barker (SVP, Evotec) for supporting this project, Dr Stephanie Duclos (Evotec) for supporting the construct designs, Dr Ewa Pilka (Evotec) for the large-scale purification from insect cells as well as the rest of the Evotec protein production team: Adrian Gray, Douglas Hewstone, Uzzol Miah and Berenice Rotty.

A special thank you to all my family and colleagues at the Research Complex at Harwell (RCaH), specifically Dr Sarah Needham, Dr Indran Mathavan, Sofia D'Abrantes and Dr Kay Sowoidnich for their continuous support and motivation. I would also like to extend my appreciation to Dr Konstantinos Beis and Dr Ken Raj and their groups for their discussions, help and support.

I also acknowledge Cancer Research Technology Ximbio (UK) which will provide a portal for trading the plasmids developed in this research project.

Table of Contents

Abstract

The S6K1 kinase functions downstream within the mTORC1 pathway to regulate cell proliferation, aging and adiposity. Using GFP technology and advanced imaging, localisation of S6K1 has been established (47% nucleus and 53% cytoplasm). S6K1 strongly ($\Delta\tau$=200 ps) interacts with the complex scaffold protein, raptor, and when the presence of the latter protein is increased, S6K1 translocates to the cytoplasm. S6K1 weakly interacts with mTOR ($\Delta\tau$=100 ps) and not with Rheb which is required for the inhibitor function of rapamycin (71% vs 8.9% decrease in phospho-S6K1 without Rheb). The development of a novel biosensor (SensOR) shows phosphorylation of S6K1 occurring mainly in the cytoplasm of living cells (from τ_m=2.5 to 2.3 ns).

In Chapter 4, AZD2014 and INK128, both pan-mTOR inhibitors, show fluorescent properties that can be used to investigate their cellular action. The fluorescence quantum yields for AZD2014 and INK128 are 0.47 and 0.33, respectively. Cellular uptake of the drugs is rapid with a half-life of 60 seconds and 42 seconds, respectively. Both drugs localise to mTORC1 related sub-cellular sites. Using cell spheroids to mimic a tumour environment, it was observed the outer spheroid layers take up AZD2014 5x faster than the inner layers. AZD2014 functions by interacting strongly with S6K1 (E_{FRET}=18%) and Rheb (E_{FRET}=16%) and less with mTOR and raptor (E_{FRET}=11%).

Chapter 5 investigates mass production techniques for generating sufficient quantities of S6K1 and mTORC1 proteins for future structural work. Although the baculovirus-insect cell expression system produced ~1mg of S6K1-raptor protein, impurities and degradation were present. Large quantities of the SensOR (3.7mg/ml) have been generated and purified. Solution phase studies show an open-closed SensOR conformation (from 2.7ns – 2 ns) upon the addition of ATP.

Overall the research shows how FRET-FLIM technology can be usefully employed to elucidate where active drug targets must localise with regard to targeting mTOR phosphorylation.

List of presentations and publications

Presentations

Invited speaker and tutorial speaker: Ahmed et al, 'Living Cells as Test Tubes: Directly imaging the interaction of S6K1 with the mTORC1 pathway and AZD2014 inhibitor' and 'Seeing is believing: Illuminating light onto mTORC1 signalling inside the live cell using laser microscopy' at the 10th African Laser Centre Student Workshop and Conference (Nov 2017, South Africa)

Invited Speaker: Ahmed et al, 'Behaviour of S6K1 in the mTORC1 pathway, live cell studies' at the Interdisciplinary Bioscience DTP - University of Oxford (April 2017, Oxford)

Oral presentation: Ahmed et al, 'Characteristics of mTOR signalling using advanced imaging, spectroscopy and crystal structure' at the Oxford Brookes Postgraduate Symposium (Jan 2016)

Oral presentation: Ahmed et al, 'Imaging the Localisation and Subcellular Interactions of the Pan-mTOR Inhibitor AZD2014 in the Live Cell' at the Focus on Microscopy Conference (Mar 2018, Singapore)

Poster presentation: Ahmed et al, 'S6K1 localisation, interaction and regulation by mTORC1 in live cells' at Oxford Brookes Postgraduate Symposium (Jan 2017) and at the Graduate College Annual Research Student Exhibition (May 2018)

Publications:

Ahmed et al. Imaging the recruitment and phosphorylation of S6K1 in the mTORC1 pathway in living cells. *Scientific Reports*. 2018 (manuscript in revision)

Ahmed et al. Localisation and mechanistic insight into the novel pan-mTOR inhibitors AZD2014 & INK128 inside the living cell. 2018 (manuscript in preparation)

Ahmed, Crooke & Botchway. Multicolour FRET-FLIM microscopy to analyze multiprotein interactions in live cells. Methods in Molecular Biology. *Springer Nature*. (book chapter in revision)

Awards:

Co-inventor of novel cancer activity (mTOR) reporter (SensOR) licensed to Ximbio (Cancer Research UK) 2018

2nd Place at poster competition at Oxford Brookes Graduate College Annual Research event 2017

List of Figures

List of Tables

Abbreviations

2D	Two-dimensional
2-PE	Two-photon excitation
3D	Three-dimensional
4EBP1	Eukaryotic translation initiation factor 4E-Binding Protein 1
AcMNPV	Autographa californica multiple nuclear polyhedrosis virus
ADC	Analog-Digital Converter
Anti-AP	Anti-Alkaline phosphatase
Anti-His	Anti-histidine
Anti-HRP	Anti-Horseradish peroxidase
At	Arabidopsis thaliana
ATP	Adenosine triphosphate
BCIP /NBT	5-Bromo-4-Chloro-3-Indolyl-Phosphate/ Nitro Blue Tetrazolium
BD	Bactoagar
BIIC	Baculovirus Infected Insect Cell
BLAST	Basic Local Alignment Search Tool
bp	base pair
BSA	Bovine Serum Albumin
CB	Carbenicillin
cDNA	complementary DNA
CFD	Constant Fraction Discriminator
CFP	Cyan Fluorescent Protein
chiA	chitinase
CHO	Chinese hamster ovary
CMOS	Complementary Metal-Oxide Semiconductor
CO_2	Carbon dioxide
Cryo-EM	Cryo-Electron Microscopy
Cy3/Cy5	Cyanine 3/5
DEPTOR	DEP Domain Containing mTOR-Interacting Protein
DMEM	Dulbecco's Modified Eagle Medium
DMF	Dimethylformamide

DMSO	Dimethyl sulfoxide
DNA	Deoxyribonucleic acid
DPBS	Dulbecco's phosphate-buffered saline
DTT	Dithiothreitol
E. coli	Escherichia coli
ECL	Enhanced Chemiluminescent
EDTA	Ethylenediaminetetraacetic acid
EGFP	Enhanced Green Fluorescent Protein
ER	Endoplasmic Reticulum
EV5827_EV5828	myc-mTOR + mLST8
EV5830_EV5831	FLAG-S6K1 + raptor-His
EV5831	raptor-His
EV5831_EV5832_EV5827_EV5828	raptor-His + S6K1-FLAG + myc-mTOR + mLST8
EV5832_ EV5827_ EV5828	S6K1-FLAG + myc-mTOR + mLST8
EV5832_EV5831	S6K1-FLAG + raptor-His
EV5833_EV5828	myc- truncated mTOR + mLST8
EV5834_EV5831	Truncated S6K1-FLAG + raptor-His
FBS	Foetal Bovine Serum
FIFO	First-in-first-out
FKBP12	FK506 binding protein 12
FLIM	Fluorescence Lifetime Imaging Microscopy
FP	Fluorescent Protein
FRAP1	FK506-binding protein 12-Rapamycin-Associated Protein 1
FRB	FKBP−rapamycin-binding
FRET	Förster Resonance Energy Transfer
Fwd	Forward
FWHM	Full Width at Half Maximum
GM	Göppert-Mayer
HEK293	Human embryonic kidney cells 293
HeLa	Henrietta Lacks
HEPES	4-(2-hydroxyethyl)-1-piperazineethanesulfonic acid
HUGO	Human Genome Organisation
Icorr	Index of correlation

IDT	Integrated DNA Technologies
IMAC	Immobilized metal affinity chromatography
IRF	Instrument Response Function
Kan	Kanamycin
kb	kilobase
kDA	kilodalton
KDP	Potassium dihydrogen phosphate
LB	Luria Broth
LBA	Luria Broth agar
L-glut	L-glutamine
MCF-7	Michigan Cancer Foundation-7
mDsRed	monomeric *Discosoma Sp*. Red fluorescent protein
MEM	Minimum Essential Media
mLST8	mammalian Lethal with SEC13 protein 8
MM	Michaelis–Menten
MOI	Multiplicity of infection
mTOR	mammalian Target Of Rapamycin
mTORC1	mammalian Target Of Rapamycin Complex 1
mTORC2	mammalian Target Of Rapamycin Complex 2
mTORKis	mTOR kinase inhibitors
MW	Molecular weight
Na_3VO_4	Sodium orthovanadate
NaCl	Sodium chloride
NADH	Nicotinamide adenine dinucleotide hydrogen
NaF	Sodium fluoride
NBD	Nitrobenzoxadiazole
ND	Neutral density
Ni	Nickel
NI	Non-infected
NLS	Nuclear Localisation Sequence
OD	Optical densities
OPO	Optical parametric oscillators
PBS	Phosphate-buffered saline
PBST	Phosphate buffered saline with Tween 20
PCR	Polymerase chain reaction

PDB	Protein data bank
PDT	Photodynamic therapy
PEI	Polyethylenimine
Pen-Strep	Penicillin-Streptomycin
PIKKs	Phosphatidylinositol 3-kinase-related kinases
PKB	Protein kinase B
PKC	Protein Kinase C
Protor1/2	Protein Modification Resource 1 and 2
p-S6K1	Phospho-S6K1
PVDF	Polyvinylidene Difluoride
QC	Quality control
QY	Quantum yield
R6G	Rhodamine 6G
RAFT1	Rapamycin and FKBP12 Target 1
raptor	regulatory-associated protein of mTOR
Rev	Reverse
RFP	Red Fluorescent Protein
Rheb	Ras homolog enriched in brain
Rictor	Rapamycin-insensitive companion of mTOR
RMS	Root-Mean-Squared
ROS	Reactive oxygen species
RPS6	Ribosomal Protein S6
RPS6KB1	Ribosomal Protein S6 Kinase B1
S6K1	p70-S6 Kinase 1
S6K2	S6 kinase 2
SDS-PAGE	Sodium dodecyl sulfate polyacrylamide gel electrophoresis
SEC	Size-Exclusion Chromatography
SensOR	S6K1 sensing of mammalian Target Of Rapamycin
Sf	Spodoptera frugiperda
SGK1	Serum/glucocorticoid regulated kinase 1
SIM	Structured Illumination Microscopy
Sin1	Stress-activated protein kinase-interacting protein 1
STED	Stimulated emission depletion

TAC	Time-to-Amplitude Converter
TBST	Tris buffered saline with Tween 20
TCSPC	Time-Correlated Single Photon Counting
Ti-Sapphire	Titanium- sapphire
TOR	Target of Rapamycin
TOS	TOR Signalling motif
TSC1/TSC2	Tuberous Sclerosis Complex 1/2
U2OS	Human Bone Osteosarcoma Epithelial
UV-Vis	Ultraviolet–visible
v-cath	cathepsin
WI	Water immersion
X-gal	5-bromo-4-chloro-3-indolyl-β-D-galactopyranoside
YFP	Yellow Fluorescent Protein
β-ME	β-mercaptoethanol
ΔNmTOR	N-terminal truncated mTOR

1.0 Introduction

1.1 An overview of the mTOR signalling pathway

The mechanistic or mammalian Target Of Rapamycin (mTOR) protein was identified as a consequence of the discovery of rapamycin inhibitor effects in the 1960s. Rapamycin is named after the island (Rapa Nui) where it was discovered from soil samples and exhibited anti-fungal, anti-proliferative and immunosuppressive properties (Dumont and Su, 1995). Since the first extractions of rapamycin from soil containing *Streptomyces hygroscopicus*, there have been decades of widespread research into understanding and determining its mechanism of action. In the 1990s, both Michael Hall's group and George Livi's group independently screened the yeast genome and identified two target genes: Target of Rapamycin 1 (TOR1) and Target of Rapamycin 2 (TOR2); stemming from the cytotoxic effects of rapamycin binding to the TOR specific intracellular protein, FKBP12 (Heitman, Movva and Hall, 1991; Koltin *et al.*, 1991). Soon after, Sabatini (Sabatini *et al.*, 1994), Schreiber (Brown *et al.*, 1994), Abraham (Sabers *et al.*, 1995) and Berlin (Chiu, Katz and Berlin, 1994) separately discovered the single mammalian homologue form of TOR although each group giving it different names; FK506-binding protein 12-Rapamycin-Associated Protein 1 (FRAP1), Rapamycin and FKBP12 Target 1 (RAFT1) and mechanistic Target Of Rapamycin (mTOR). The latter name was adopted by consensus and registered by the Human Genome Organisation (HUGO) gene nomenclature in 2009.

The "unearthing" of mTOR resulted in a drive to understand the involvement of this large (289 kDa) protein within the biological context of the cell. Before long, it was found that mTOR, a serine-threonine kinase, existed as part of two multi-protein complexes: mTOR Complex 1 (mTORC1) and mTOR Complex 2 (mTORC2) (Laplante *et al.*, 2009). Following these discoveries, progress was rapid as the

Rheb, raptor, mLST8, PRAS40 and DEPTOR subunit proteins were found to be associated with mTORC1 by co-immunoprecipitation assays (pull-downs) (Betz and Hall, 2013; Aylett *et al.*, 2016). Whilst two mTOR complexes were identified, rapamycin was found to be effective in inhibiting mTORC1, preventing the phosphorylation of S6K1 and 4EBP1, both downstream proteins (Dennis, Kimball and Jefferson, 2013). Studies on the upstream of TOR complexes were first performed in *Drosophila melanogaster* (Stocker *et al.*, 2003) and later in mammalian models, and identified Rheb, a small GTPase, regulated by the Tuberous Sclerosis Complex (TSC1/TSC2) to promote cellular growth through mTOR activation and subsequently S6K1 phosphorylation (Long, Lin, *et al.*, 2005; Long *et al.*, 2007).

To understand further the mTOR protein pathway, pull-down assays have also shown interactions with the rictor, Protor, mLST8, Sin1 and DEPTOR subunit proteins, to form mTORC2 which phosphorylates AKT(PKB), SGK1 and PKCα involved in insulin signalling and glucose metabolism (Laplante *et al.*, 2009; Stuttfeld *et al.*, 2018). Both mTOR complexes are now identified as being at the heart of several signalling cascades involving a multitude of upstream and downstream proteins that form the mTOR pathway (**Figure 1.1)** which includes links to other signalling pathways, fully justifying mTOR being termed as a ‘master regulator’.

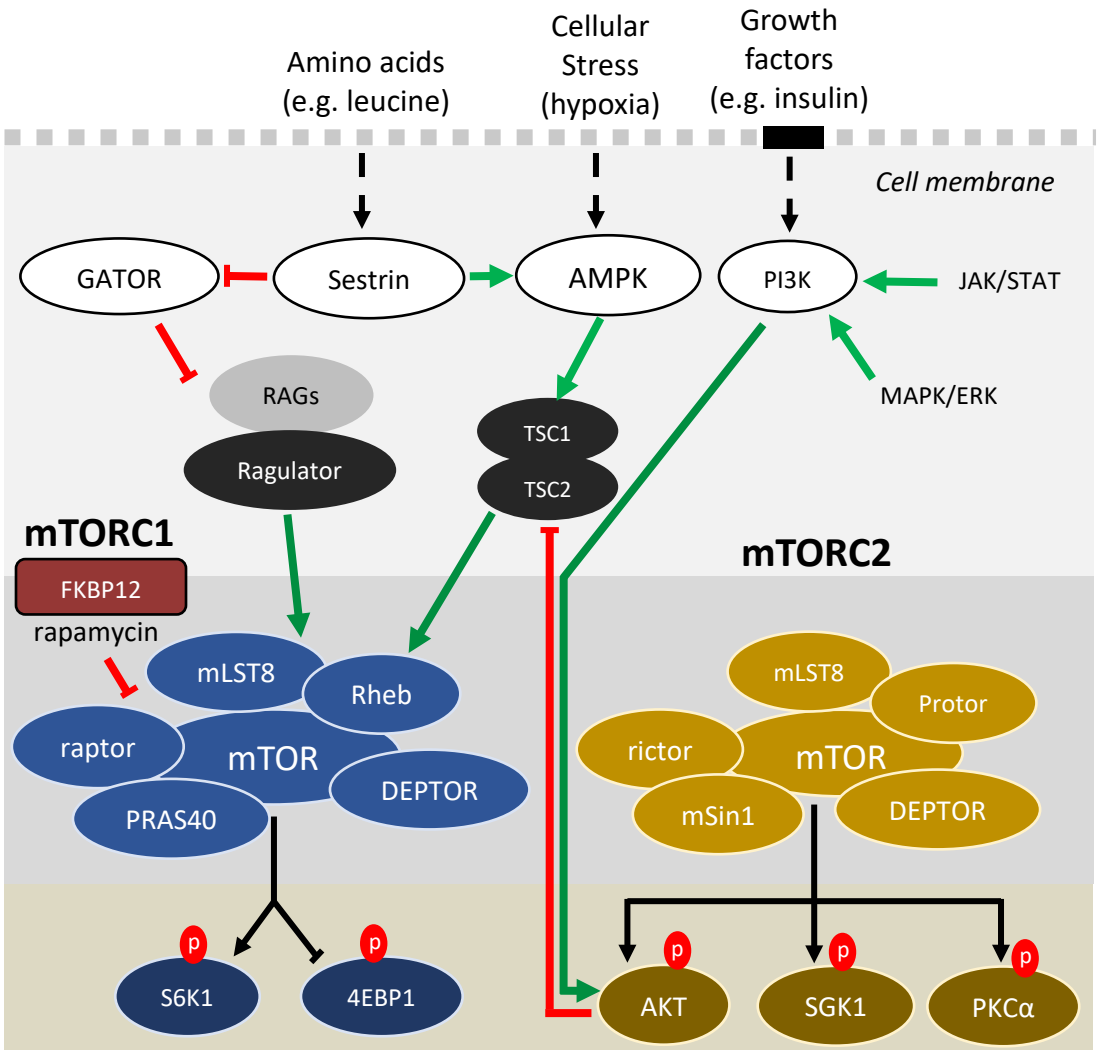

Figure 1.1: Schematic of the mTOR signalling pathway*. Upstream proteins (in white or grey filled circles) and respective upstream pathways are shown. The JAK/STAT and MAPK/ERK proteins feed into the mTOR pathway. The mTORC1 pathway is shown in blue filled circles. The mTORC2 pathway is shown in yellow filled circles. Phosphorylated substrates are depicted with phosphorylation (p) in red filled circles. Activating processes are shown with green arrows whilst inhibitory processes are shown with red arrows.*

Although each mTOR complex performs diverse functions within the cell, the mTORC1 pathway is of particular interest functioning in the co-ordination of energy (ATP), nutrients (amino acids), oxygen (hypoxia) and growth factor availability to regulate key biological processes such as cellular growth, metabolism and protein synthesis (Saxton and Sabatini, 2017). Thus, targeting mTOR1 represents a novel strategy to fight against cancer, type II diabetes, cardiovascular and neurological diseases (Laplante and Sabatini, 2012; Crino, 2016; Xie, Wang and Proud, 2016).

Hence, advancing the understanding of mTOR and its interactions with its subunit partner proteins is seen as key to the development of more effective therapies.

1.2 Lysosomal membrane a hub for mTORC1 nutrient sensing

The importance of mTOR is now recognised and emphasised by the extensive studies into both its structure and biochemistry. A recent review has described many aspects of the nutrient-sensing role of the mTORC1 pathway (González and Hall, 2017) and the notion of lysosomal membrane being a hub for mTORC1 activation has also been studied (Saxton and Sabatini, 2017). As shown in **Figure 1.2**, the mTORC1 complex is thought to translocate to the lysosomal membrane where it is tethered by both Rheb and the Ragulator–RAG GTPases (Yonehara *et al.*, 2017). Recently, other complexes associated with nutrient-sensing have been identified such as the v-ATPase (Zoncu *et al.*, 2011), KICSTOR (Wolfson *et al.*, 2017) GATOR (Parmigiani *et al.*, 2014) and CASTOR complexes (Chantranupong *et al.*, 2016). However, the S6K1 involvement within the mTOR pathway has not received much attention to date, and forms a major component of the work covered in this thesis. The role and importance of S6K1 in the mTOR pathway is therefore reviewed and discussed next.

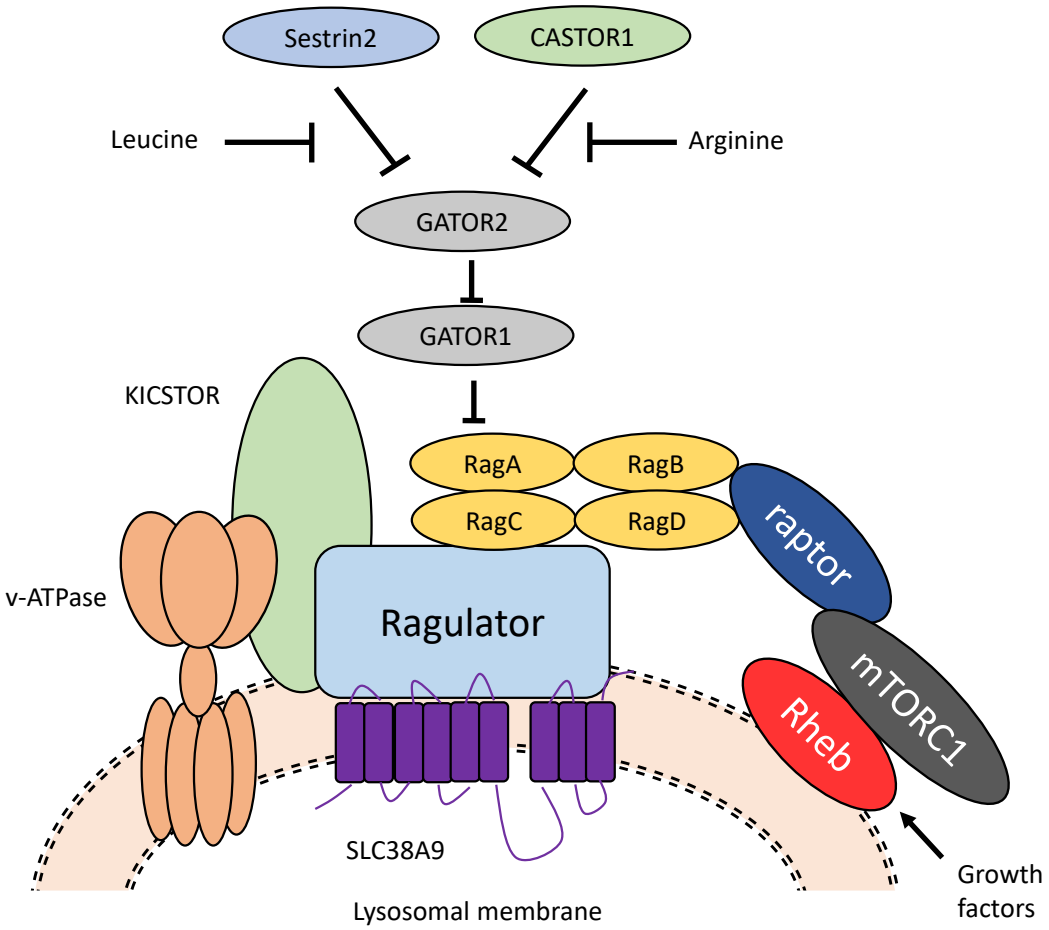

Figure 1.2: Lysosomal membrane in mTORC1 nutrient sensing. *A scaffolding complex on the lysosomal membrane is shown consisting of the v-ATPase pump, the Ragulator, SLC38A9 transporter, the Rag GTPases and KICSTOR are shown. The tethering of mTORC1 is also shown as well as regulation of the Ragulator-Rag complex by the GATOR complex and amino acid sensing proteins such as Sestrin2 and CASTOR1. Figure adapted from* (Saxton and Sabatini, 2017).

1.3 Role and function of Ribosomal Protein S6 kinase 1(S6K1)

The Ribosomal S6 Kinase (RSK) family consists of protein kinases implicated in a wide range of cellular processes (Anjum and Blenis, 2008). There are two mammalian homologues S6K1 and S6K2 of the p70 RSK subgroup. While S6K2 is known to be targeted by mTOR (Park *et al.*, 2002) and has been investigated (Pardo and Seckl, 2013), less attention has been paid to understanding S6K1. The S6K1 kinase phosphorylates various substrates that control protein synthesis, in particular Ribosomal Protein S6 (RPS6) which is part of the 40S ribosomal subunit (Roux *et*

al., 2007). S6K1 also functions in cell proliferation, apoptosis, metabolism, cell structure (Tavares *et al.*, 2015) and has been shown to regulate aging (longevity) and adiposity (Selman *et al.*, 2009; Arif *et al.*, 2017), memory (Caccamo *et al.*, 2015), immunity (Kim *et al.*, 2014), muscle hypertrophy (Marabita *et al.*, 2016) and more recently, in cell migration and tumour growth (Zhang *et al.*, 2018). A summary of some of the most important functions of S6K1 is depicted in **Figure 1.3**. Cell proliferation, size and health are major characteristics of cancer, obesity and aging and in this context the role S6K1 plays in cell proliferation and its diverse functionality in the mTOR pathway makes it a desirable target for treatments of a wide range of disease states (Dann, Selvaraj and Thomas, 2007).

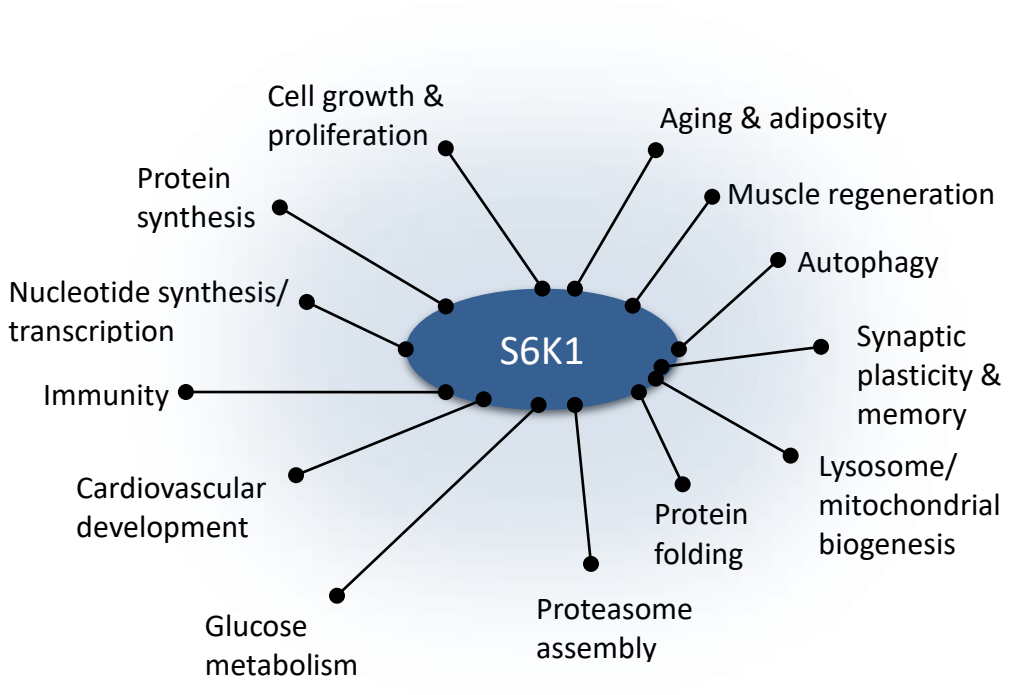

Figure 1.3: Functions of S6K1 in the mTOR pathway. *The various roles of S6K1 are shown above with black lines projecting from the S6K1 protein. The figure above is updated from* (Magnuson, Ekim and Diane C. Fingar, 2012).

S6K1 is transcribed by the RPS6KB1 gene which, due to alternative start codons, produces multiple isoforms; p85 S6K1 (85 kDa), p70 S6K1 (70 kDa) and in human breast cancer cell lines p60 S6K1 (Kim *et al.*, 2009). Humans can also produce a rare third form of S6K1 known as p31 S6K1 which is generated from the alternative

splicing of the RPS6KB1 transcript by the SF2/ASF protein (Fenton and Gout, 2011; Magnuson, Ekim and Fingar, 2012; Rosner, Schipany and Hengstschläger, 2012; Ben-Hur *et al.*, 2013; Tavares *et al.*, 2015; Amaral *et al.*, 2016). There is no evidence suggesting that mTOR phosphorylates p31 S6K1 (Rosner and Hengstschläger, 2011) and this is likely due to the latter lacking the C-terminus containing the phosphorylation site.

Both p85 S6K1 and p70 S6K1 are known as p70 S6 Kinase 1 or simply S6K1 (**Figure 1.4**) and share similarities in domain structures but the mTOR phosphorylation sites are different, occurring at threonine residue 412 and 389 respectively (Rosner and Hengstschläger, 2011). Important questions arise such as where in the cell does the phosphorylation occur and how does the phosphorylation relate to the localisation of mTORC1?

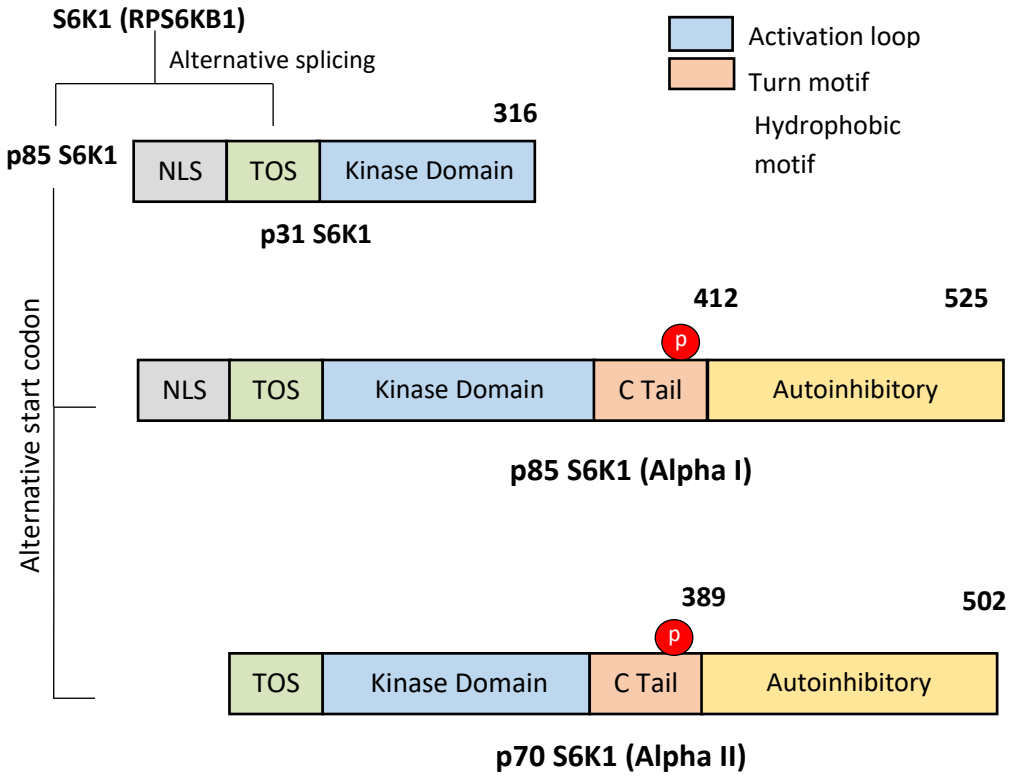

Figure 1.4: S6K1 isoform generation. *S6K1 is produced from the RPS6KB1 gene which due to alternative splicing and alternative translation start sites, generates three isoforms. The p31 isoform contains a Nuclear Localisation Sequence (NLS) and a partial kinase domain. Both p85 S6K1 (also known as Alpha 1) and p70 S6K1 (Alpha II) have a kinase domain (containing an activation loop), a C-Terminal tail (containing a turn motif and hydrophobic motif) and an autoinhibitory domain. All S6K1 isoforms have been reported to contain a TOR Signalling motif (TOS) with the amino acid sequence FDIDL. Amino acids that are phosphorylated by mTOR are indicated by their positions within the length of proteins. Figure adapted from* (Rosner and Hengstschläger, 2011).

1.4 Sub-cellular localisation of S6K1 and phosphorylated S6K1

Determining the sub-cellular localisation of S6K1 is important to help understand not only its function but also the workings of the mTOR complex within the cell. Many observations regarding the localisation of S6K1 have been made in mammalian cells; fractionation studies have indicated the presence of S6K1 both in the cytoplasm and the nucleus (Rosner and Hengstschläger, 2011; Rosner, Schipany and Hengstschläger, 2012). However, only cytoplasmic localisation was observed in fixed cells (X. K. Lun *et al.*, 2017). S6K1 has also been reported to localise in the mitochondria and stress granules (Djouder *et al.*, 2007; Sfakianos *et al.*, 2018). Immunofluorescence labelling has also been employed, where only a nuclear

localisation of S6K1 was seen (Reinhard *et al.*, 1994). The only published live cell image of S6K1 used fluorescently labelled GFP-S6K1 expressed in plant cells where both nucleus and cytoplasmic localisation were observed (Mahfouz, 2006). Thus, to date, the overall picture from all the various investigations from using different techniques and cell lines looking at S6K1 cellular distribution have reached different conclusions, and such controversy is understandably a key issue in relation to the mTOR pathway, but this is not the only issue.

The cellular localisation of the phosphorylated form of S6K1, mediated by mTOR, is also debated widely in the field. Identifying regions of the cell where S6K1 phosphorylation occurs has been, for the most part, approached using indirect and disruptive cell fractionation methods that appear to indicate that phosphorylated p70 S6K1 isoform translocates from the cytoplasm into the nucleus (Rosner and Hengstschläger, 2011). However, fractionation studies are prone to artefacts due to pooling of proteins from various organelles. With this in mind, others have resorted to the use of fixed cell immunofluorescence to detect phosphorylated S6K1 (p-S6K1). One approach has been to use amino acid regulation where phosphorylation was deregulated and phosphorylation subsequently activated, the procedure demonstrated an increase in p-S6K1 within the nucleus (Rhoads *et al.*, 2008; Kim *et al.*, 2013) following phosphorylation. Although, the immunofluorescence labelling supports the fractionation work, cell fixation is not without its limitations. It has also been reported to induce artefacts due to loss of untethered soluble proteins and poor labelling (Schnell *et al.*, 2012). A live cell FRET (Fluorescence Resonance Energy Transfer) sensor (Komatsu *et al.*, 2011), and more recently, an improved version (Komatsu *et al.*, 2018), has been developed to track S6K1 activity in real-time by measuring the phosphorylation of one of its substrates, rictor associated with mTORC2 (Treins *et al.*, 2010) in the cytoplasm. These sensors contain a hybrid form of partial rictor and S6K1 domains and can only indirectly report on mTORC1

activity in the cytoplasm and does not localise into the nucleus. A much-needed improvement to directly monitor mTOR-mediated phosphorylation of S6K1 would not only overcome the well-known problems with cell fixation but also provide a more physiologically accurate insight into live cell mTOR signalling.

1.5 S6K1 co-immunoprecipitation with raptor, mTOR and Rheb

Knowing the intra-cellular location of a protein helps us to elucidate how and with what other proteins it may interact within the same site. To date, S6K1 and raptor interactions have been studied in both mammalian and plant cells (Hara *et al.*, 2002; Nojima *et al.*, 2003; Ali and Sabatini, 2005; Mahfouz, 2006; Dennis, Kimball and Jefferson, 2013) using conventional pull-down assays but the interactions of these two proteins in living cells are unknown. The current thought in literature proposes that the raptor protein acts as a 'scaffold' owing to its ability to bind mTORC1 substrates S6K1 and 4EBP1 (Hara *et al.*, 2002; Beugnet, Wang and Proud, 2003; Choi, McMahon and Lawrence, 2003; Schalm *et al.*, 2003; Wang, Rhodes and Lawrence, 2006; Lee *et al.*, 2008), other regulatory proteins, such as the inhibitory PRAS40 (Oshiro *et al.*, 2007), TAK1 (Shin *et al.*, 2013) and activators such as the Rag GTPases mentioned in section **1.2** (Sancak *et al.*, 2008).

It is thought that all known S6K1 isoforms have a TOR Signalling (TOS) motif, on their N-terminus (Figure 1.4) (Schalm and Blenis, 2002; Kim *et al.*, 2009). The TOS motif of p85 S6K1 and p70 S6K1 mediates interaction with the N-terminus region of raptor; however, reports on the precise nature of the interaction vary. Overall pull-down assays with mutations in the S6K1 TOS sequence fail to bring down raptor (Nojima *et al.*, 2003; Ali and Sabatini, 2005). In contrast, cross-linking mass spectrometry indicates that the TOS motif does not interact with raptor (Coffman *et al.*, 2014). Other mTOR substrates such as 4EBP1 and PRAS40 also have their own unique TOS motifs, allowing them to bind to raptor (Beugnet, Wang and Proud, 2003; Schalm *et al.*, 2003; Wang, Rhodes and Lawrence, 2006; Sancak *et al.*, 2007;

Lee *et al.*, 2008). It has been proven that S6K1, 4EBP1 and PRAS40 mutually compete for the same binding site on raptor (Schalm and Blenis, 2002; Oshiro *et al.*, 2007; Wang *et al.*, 2007; Dennis, Kimball and Jefferson, 2013).

The literature reports interactions between truncated (mutated) S6K1 with mTOR (Ben-Hur *et al*., 2013) but full length S6K1 has shown no interaction (Ben-Hur *et al.*, 2013; Brown *et al.*, 2017) by pull-down with mTOR. However, pull-down of mTORC1 have found the S6K1 component bound to it, although the exact interacting components were not defined (Brown *et al.*, 1995; Ali and Sabatini, 2005).

There is no evidence that Rheb interacts with S6K1, raising the question of how mTOR phosphorylates S6K1 directly, as S6K1 phosphorylation is considerably enhanced by Rheb and increased by raptor (Garami *et al.*, 2003; Inoki *et al.*, 2003; Yonezawa *et al.*, 2004; Ali and Sabatini, 2005; Long, Ortiz-Vega, *et al.*, 2005; Wang, Rhodes and Lawrence, 2006; Ge, Yoon and Chen, 2011; Yadav *et al.*, 2013; Jain *et al.*, 2014; Martin *et al.*, 2014). However, contrary to the above, others report that raptor, as well as PRAS40, have an inhibitory effect on phosphorylation (Hara *et al.*, 2002; Kim *et al.*, 2002; Manifava *et al.*, 2016). The effect of raptor on S6K1 phosphorylation in the mTOR field remains unclear and the understanding of the interaction between raptor and S6K1 would be aided by structural studies.

1.6 Architecture of mTORC1 and structure of S6K1

The structure of a protein or a protein complex is imperative for the understanding of its activity and its mechanism within the cell and goes towards defining strategies to design and develop drug targets. Although, X-ray crystallography is considered to be the ‘gold standard’ for determining structures with atomistic levels of resolution, the technology is difficult to apply to protein complexes. The recent advances in cryo-EM technology, driven by better detectors and processing, has paved the way to studying large macromolecular protein complexes (Murata and Wolf, 2018). Cryo-

EM has been extensively applied to study mTORC1, firstly identifying the dimeric state of mTOR and secondly identifying the assembly of its interacting subunit proteins. The mTOR protein was originally thought to be monomeric (Yang *et al.*, 2013) and later found to be dimeric (as shown in **Figure 1.5A**), with a single subunit of raptor, mLST8, Rheb, PRAS40, FKBP12-rapamycin on each molecule of mTOR (Yip *et al.*, 2010; Aylett *et al.*, 2016; Yang *et al.*, 2016, 2017). It is now established that raptor is necessary for mediating mTOR (N-terminus to C-terminus) dimerisation.

Although no structural information on S6K1 complexed with raptor or mTOR is available, the latest publication of the structure of mTORC1 at 3.0 angstrom resolution shows the TOS motif of S6K1 bound to *Arabidopsis thaliana* (At) raptor (**Figure 1.5B**). The study also revealed a short region of S6K1 sequence binding to FRB domain of mTOR, indicating some form of secondary recruitment mechanism (Yang *et al.*, 2017). It was further shown that the binding of Rheb to the mTOR complex induces a global mTOR conformational change which enhances the catalytic activity of the active site (Yang *et al.*, 2017). Whilst the work provides key insights into the activation of mTORC1, the use of plant raptor protein rather than mammalian or human raptor raises some uncertainty in relation to the accuracy and relevance of these insights in regard to human mTORC1.

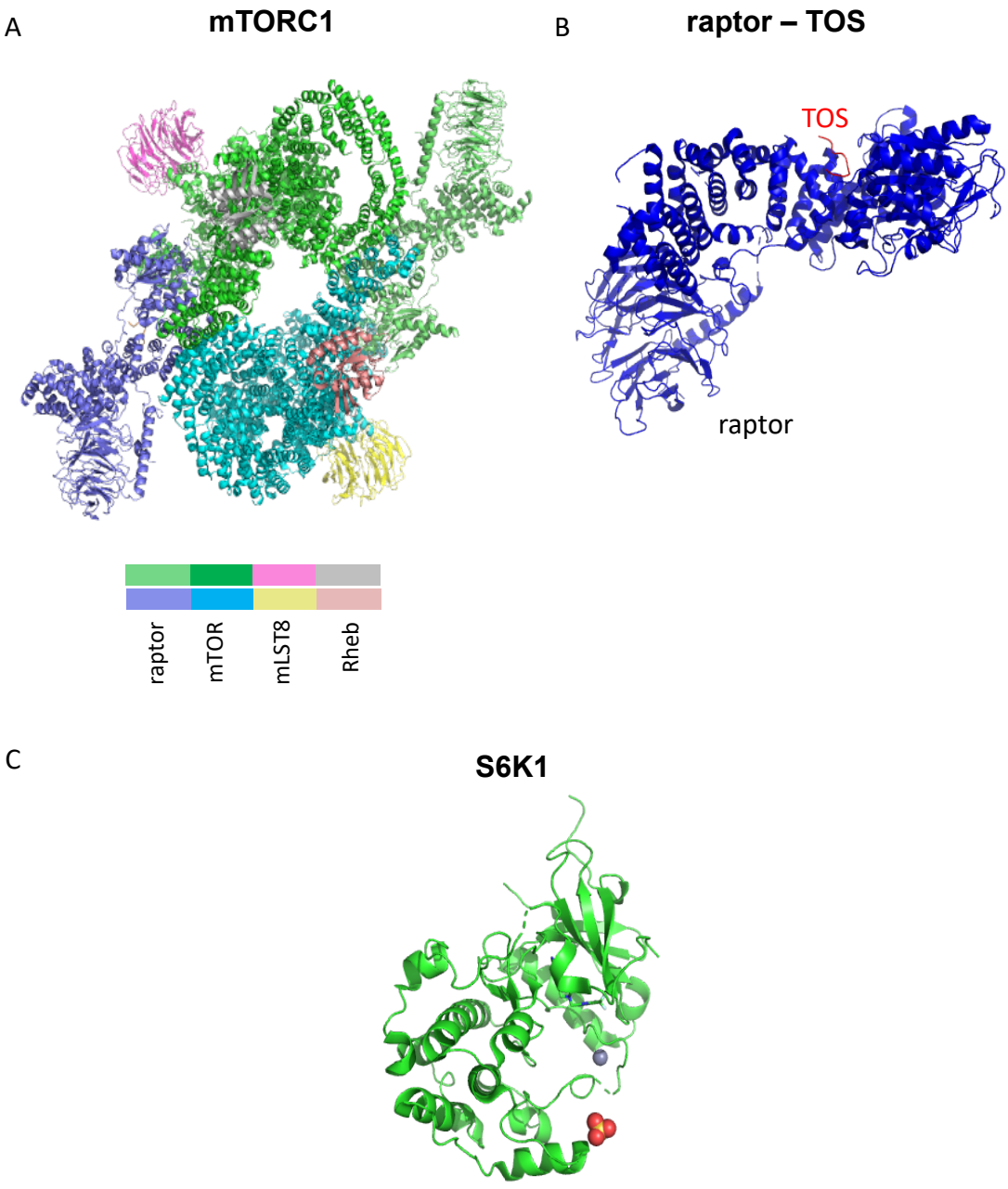

Figure 1.5: Current structures of mTORC1 and S6K1. *Three-dimensional structures obtained by cryoEM and X-ray crystallography of A) Dimeric mTORC1 where colour key shows interacting subunit proteins: raptor, mTOR, mLST8 and Rheb. B) raptor (blue) bound to the TOS motif of S6K1 (red). C) Partial length S6K1 (346 amino acids) with zinc and an S6K1 inhibitor, PF-4708671 bound in the ATP binding site. All images were generated using PyMOL (version 2.1) using PDB codes: 6BCU, 5WBK and 4L46.*

No full length structure of S6K1 has been solved to date. Identifying the conformations for phosphorylated and dephosphorylated S6K1, could be key to better understanding the action of mTOR. One of the first partial structures of S6K1 (2-3.4 angstrom resolution) was crystallised with staurosporine. Both

phosphorylated and unphosphorylated S6K1 kinase domains with staurosporine bound were structurally similar with the most notable exception that the activation loop in the phosphorylated form became ordered (Sunami *et al.*, 2010). Other published crystal structures of the S6K1 kinase domain with and without inhibitors soon followed (Wang *et al.*, 2013; Niwa *et al.*, 2014). These kinase structures were similar to that of the previous S6K1 kinase domain structure, with the subtle difference in the presence of a zinc ion in the activation loop (**Figure 1.5C**). Most importantly, it was observed that the threonine 389 residue was phosphorylated during the refinement process (Wang *et al.*, 2013) independently of other kinase proteins that have been reported to prime S6K1 for mTOR mediated phosphorylation (Keshwani *et al.*, 2011). This finding indicates the potential to monitor mTOR activity directly. Although, as of yet, there is no concrete structural evidence for differences between phosphorylated and dephosphorylated forms of S6K1, the former may be linked to a conformational change as evident by functional studies that examined N- and C-terminus truncations (Schalm, Tee and Blenis, 2005; Magnuson, Ekim and Diane C. Fingar, 2012). As the cell uses kinase proteins to activate processes, the ability to de-activate dysfunctional ones through drugs is vital for therapy.

1.7 Rapamycin and new generation mTOR inhibitors

The last two decades has seen immense research efforts in drug design and development focusing on inhibiting the mTOR kinase protein to prevent cancer growth (Sparks and Guertin, 2010; Weinberg, 2016). It is reported that mTOR is hyperactivated in almost 70% of all human cancers (Xie, Wang and Proud, 2016). Thus, the ability to manipulate the mTOR kinase through pharmaceutical intervention plays a fundamental part in the battle against cancer. Some of the types of mTOR inhibitors currently available are shown in **Figure 1.6A** and **Figure 1.7**.

The first generation inhibitors of mTOR (rapalogs) were based on the rapamycin molecule (**Figure 1.7A**), now known to target only mTORC1. There appears to be a growth of evidence for the lack of efficacy of rapalogs (dosage and duration related) as well as emerging rapalog resistance in a number of tumours (Faes, Demartines and Dormond, 2017). This 'enigma' regarding the efficacy of rapamycin (Mukhopadhyay *et al.*, 2016) may be explained by its binding mechanism. The rapamycin-FKBP12 complex, as mentioned above, binds to the FRB domain of mTOR (Banaszynski, Liu and Wandless, 2005). It was originally thought that rapamycin causes the disassembly of mTORC1 (Oshiro *et al.*, 2004; Yip *et al.*, 2010; Jain *et al.*, 2014) or may cause the degradation of raptor via caspase activity (Martin *et al.*, 2016). However, in light of recent structural studies this seems not to be the case because the binding of rapamycin-FKBP12 onto mTOR allosterically restricts the entry of mTOR substrates accessing the active site for mTOR mediated phosphorylation (Aylett *et al.*, 2016; Yang *et al.*, 2016). Rapamycin is reported to inhibit S6K1 phosphorylation completely and 4EBP1 phosphorylation incompletely on mTORC1 while its effects on mTORC2 are uncertain and effects may be cell line dependant (Choo *et al.*, 2008; Choo and Blenis, 2009). As S6K1 (70 kDa) and 4EBP1 (15 kDa) differ in size, and if raptor is indeed involved in their recruitment, it is likely that this allosteric restriction coupled with substrate competition for raptor binding would lead to reduced phosphorylation (as illustrated in **Figure 1.6B**).

Second generation mTOR kinase inhibitors (also known as mTORKis or TORKinibs) bind to the mTOR kinase domain (**Figure 1.6C**), and are mechanistically ATP-competitive inhibitors that provide broader selectivity by inhibiting both mTORC1 and mTORC2 function (Xie, Wang and Proud, 2016). These types of inhibitors have already been shown to be more effective than rapamycin and rapalogs (Zheng and Jiang, 2015). One potential candidate that is currently undergoing clinical trials is the AZD2014 molecule (**Figure 1.7B**) (Liao *et al.*, 2015). AZD2014 (3-[2,4-Bis((3S)-3-

methylmorpholin-4-yl)pyrido[5,6-e]pyrimidin-7-yl]-N-methylbenzamide) was optimised from the successful AZD8055 compound. AZD2014 is more soluble and less toxic (safer) for clinical use compared to its predecessor, AZD8055. The AZD2014 molecule has an IC_{50} value of 2.8 nM, making it one of the most effective inhibitors discovered and although it may bind to some phosphatidylinositol 3-kinase-related kinases (PIKKs) proteins, it has been shown to be unselective towards a panel of 200 other tested kinases (Pike *et al.*, 2013). AZD2014 is showing great promise as an anti-cancer reagent, particularly with combination therapies (Harada *et al.*, 2015). Preclinical (Flannery *et al.*, 2018), pharmacological characterisation (Basu *et al.*, 2015) and xenograft models (Guichard *et al.*, 2015) in mice have been performed. The exact mechanism of action of AZD2014 in a live human cancer cells is yet unclear and warrants further investigation as studies have demonstrated that AZD2014 may bind directly to the kinase domain of mTOR (Pike *et al.*, 2013) while other studies have shown mTOR complex dissociation with AZD2014 treatment (Zheng *et al.*, 2015).

INK128 is another second generation pan-mTOR inhibitor (**Figure 1.7C**) also undergoing clinical trials (Tabernero *et al.*, 2012) and has proven to be highly potent with an IC_{50} value of 1 nM (Hsieh *et al.*, 2012). Phase 1 clinical trials have evaluated the drug to be safe with minimal side effects (Burris *et al.*, 2017). This inhibitor has been used in preclinical models of breast cancer cell lines where greater inhibition to both mTOR complexes were found in comparison to rapamycin and equal effects to rapamycin in the mouse model. The work on INK128 demonstrates the drug to have great potential and we can look forward to results from future trials working against aggressive disease states such as leukaemia (Gökmen-Polar *et al.*, 2012; Guo and Kwiatkowski, 2013; Ingels *et al.*, 2013; Janes *et al.*, 2013). The clinical potential revealed by INK128 demands a complete understanding of its mechanism of action. It has been reported that INK128 induces apoptosis, mTOR complex disassembly

and inhibits cell migration (Li *et al.*, 2015; Calton and Vollrath, 2016; Zeng *et al.*, 2016).

At the leading edge of mTOR drug discovery is the recent development of third generation inhibitors, designated the name RapaLink owing to its design of combining the rapamycin molecule with a second generation inhibitor with a long linker sequence. Such new inhibitors appear to be even more potent with the novel ability to also affect tumours that have developed resistance against second generation mTOR inhibitors (Rodrik-Outmezguine *et al.*, 2016; Fan *et al.*, 2017). From a pharmaceutical perspective, although the chemical optimisation of mTOR drugs is important, it only provides a small snapshot of a drug's capabilities. The ability of a drug to localise to its target, on a subcellular level will dictate the effectiveness of the drug which ultimately must meet and bind to its target; an issue which is undervalued in the field and one with major practical challenges to observe in living cells.

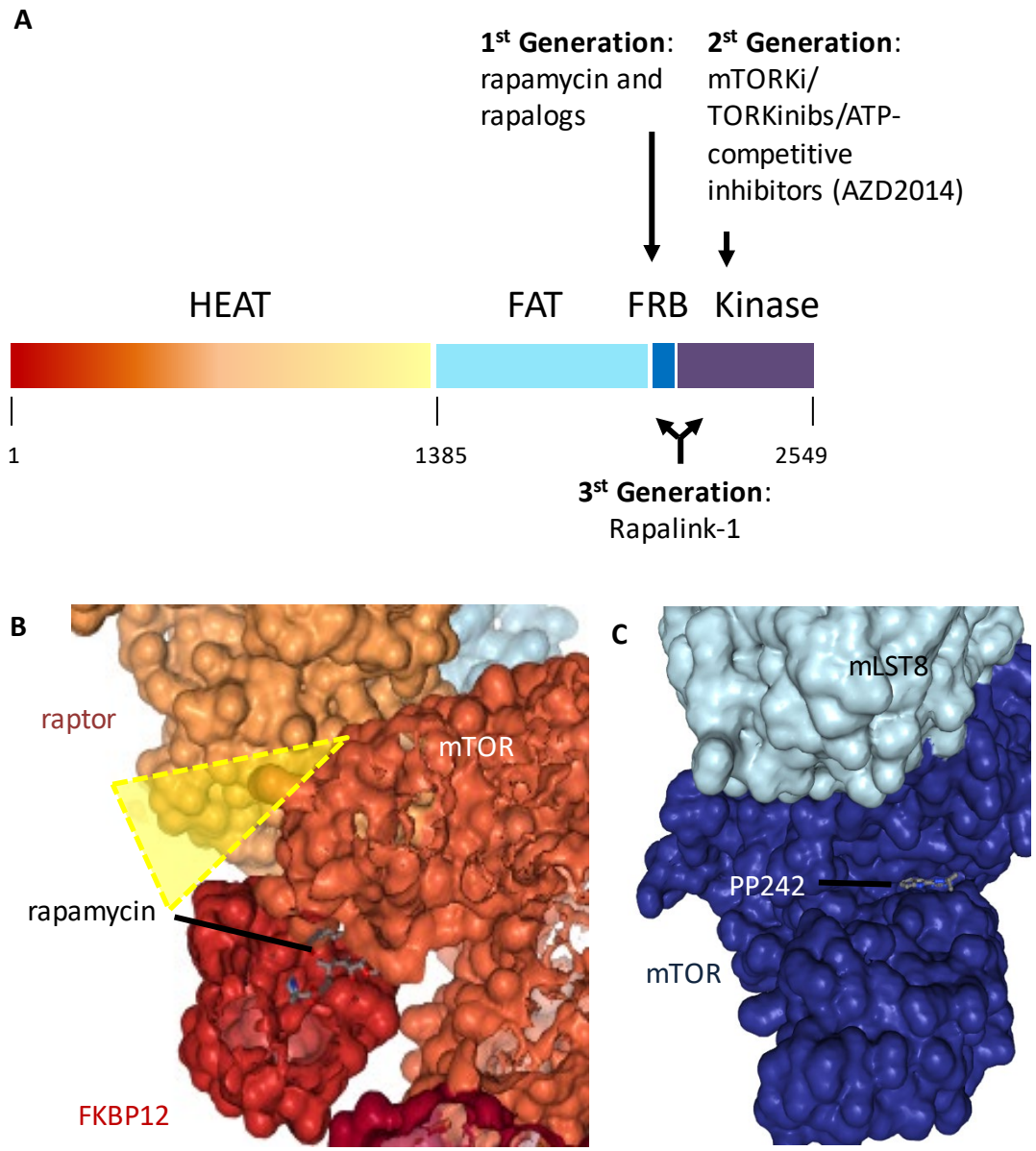

Figure 1.6: Mechanism of action of mTOR inhibitors*. A) Various mechanisms of actions of mTOR inhibitors such as rapamycin, AZD2014 and Rapalink. B) Structure of mTORC1 with bound FKBP12-rapamycin showing restriction of entry of recruited substrates to the active site with raptor. Yellow triangle area shows narrow v-shaped entry to the active site of mTOR. C) Structure of mTOR-mLST8 with an ATP-competitive inhibitor (PP242) bound to the kinase domain. Images generated in NGL* Viewer (Rose and Hildebrand, 2015) *using the PDB codes: 5FLC and 4JT5.*

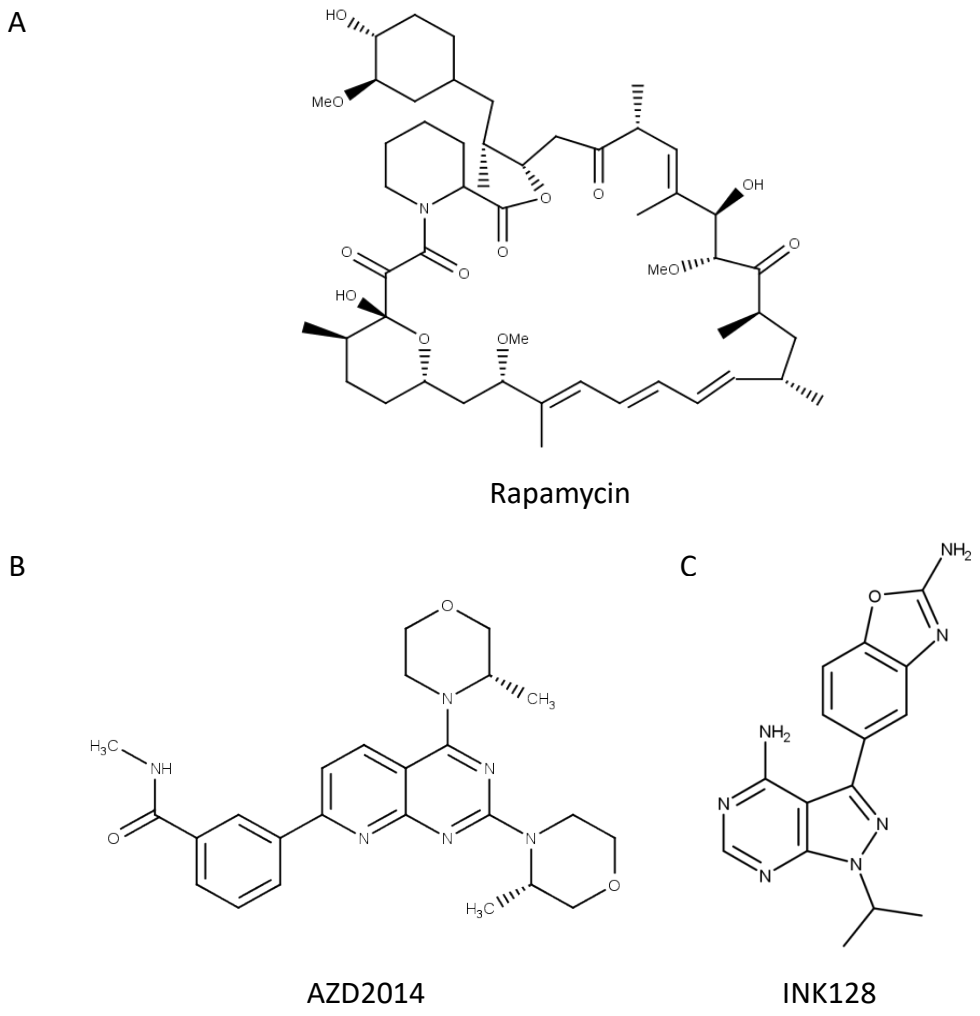

***Figure 1.7: Chemical Structures of mTOR inhibitors**. The chemical structures are shown for A) rapamycin B) AZD2014 and C) INK128. All chemical structures were generated in MarvinSketch (version 15.10.19.0)*

1.8 Mass protein expression using the Baculovirus system

The role of structural studies in providing insight into protein function as well as the means to target it through chemical inhibition has been highlighted in the previous sub-chapters. However, the greatest challenge in modern day structural biology is the generation of large amounts of pure and stable protein, particularly where multi-protein complexes are involved. One of the most advanced methods to express protein in mass quantities is the baculovirus expression system (Nettleship *et al.*, 2010; Chambers *et al.*, 2018). The baculovirus is a virus capable of infecting insect cells. The virus contains circular double-stranded DNA (80 -180 kbp) that is

packaged in a rod shaped capsid. One of the most popular choices of baculovirus for protein expression is the *Autographa californica* multiple nuclear polyhedrosis virus (AcMNPV) (Rohrmann, 2013). These viruses can be modified by replacing the polyhedrin gene with a gene(s) of interest. These viruses can then be used to infect insect cells on a large scale with the expression and production of mass quantities of recombinant protein (Hitchman *et al.*, 2011). In addition, these virus particles are released directly into the media of the insect cells allowing for further infection and details of this technique are given in **Chapter 2, Material and Methods**.

1.9 Principles of fluorescence

As micromolecular and nanomolecular entities are too small to be seen by the naked eye, making the invisible visible, like proteins, is essential in biology. The phenomenon of fluorescence was thoroughly investigated in the 1840s (Herschel, 1845) and later in 1852 by George Stokes (Stokes, 1852), building on observations from previous centuries, of 'glow' from certain types of materials and chemicals (Beecher, 2015). Stokes named this observation 'fluorescence' because the emission of this type of light had a longer wavelength to that of the absorption light. Light is considered to be a wave of energy that is composed of small packets of stored energy known as photons (E) (Planck, 1900) as shown in **Equation 1.1**:

$$E = h\nu = h\frac{c}{\lambda} \qquad \textbf{(1.1)}$$

where E is minimum energy of a photon, h is Planck's constant and ν is the frequency of light (speed of light (c)/ wavelength (λ))

When a fluorescent molecule absorbs a photon of light, it becomes instantly excited from the electronic ground state (S_o) to an electronic excited state (typically S_1), the molecule seeks to return to the ground state and this can be by emitting a fluorescent photon. Normally this photon is at a lower energy than the original

photon absorbed, termed red shift or Stokes shift. Fluorescence is a radiative process (k_r). However, excited state energy can also be dissipated as heat or lost to quenching processes (where the electronic energy is transferred to a neighbouring molecule) or vibrational states emission i.e. IR spectra, these are non-radiative processes (k_{nr}). Although not important here, the excited state of the molecule may also evolve to a triple state (t_1), a step where the spin of the excited state electron is flipped and where phosphorescence, a much longer timescale process, can occur (Lakowicz, 2006). These processes are summarised in the Jablonski diagram in **Figure 1.8**.

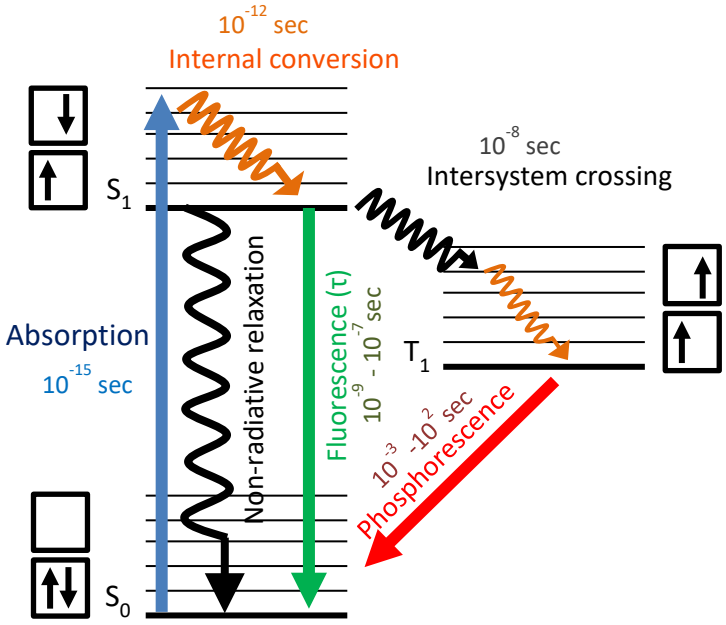

Figure 1.8: Jablonski diagram. *Horizontal lines show energy levels with thinner ones showing transitions between sub-energy levels. Ground state energy level is shown as S_0 and a higher excited state energy level as S_1. A transitional state (T_1) is also shown. Straight arrows show radiative processes and zig-zagged arrows show non-radiative processes. Electron spins (anti-parallel or parallel) are also shown next to each electronic state with time-scales for each process.*

Fluorescence is a probability and time-dependent phenomenon and its intensity change usually follows an exponential profile in function of time. Measuring this change, the fluorescence decay, we can obtain the fluorescence lifetime of the excited state molecule. The fluorescence lifetime is a statistical distribution of the

time the population of molecules spend in the excited state, following the absorption of a photon (Lakowicz, 2006). This fluorescence emission process usually occurs in the nanosecond timescale and can be defined by **Equation 1.2**:

$$\tau = \frac{1}{k_r + k_{nr}} \qquad \textbf{(1.2)}$$

where lifetime (τ) is inversely proportional to the sum of radiative (k_r) and non-radiative (k_{nr}) processes.

Thus, measuring the exponential decay of the fluorescence intensity (I_t) over time (t) following a short excitation pulse, yields parameters to extract the lifetime (τ) (Ishikawa-Ankerhold, Ankerhold and Drummen, 2012) as shown in **Equation 1.3**:

$$\tau = -\frac{t}{\ln\left({I_t}/{I_0}\right)} \qquad \textbf{(1.3)}$$

where fluorescence intensity (I_t) is proportional to the excited state population and I_0 is fluorescence intensity at time 0, t is time and τ is the fluorescence lifetime.

A fluorescent molecule may however interact with other molecules, undergo a conformational change or exhibit changes in its spectral properties depending on its environment which can affect the excited state lifetime (Bindels *et al.*, 2014; Marcu, French and Elson, 2014). Therefore, lifetime can be used as a readout to investigate protein-protein interactions and also protein activity (Schoberer and Botchway, 2014).

1.10 Green Fluorescent Protein (GFP) technology

The most commonly used fluorescent "tag" (also known as a fluorophore) in protein biology is the Green Fluorescent Protein (GFP), a 27 kDa protein composed of 238 amino acids that was isolated from the jellyfish *Aequorea Victoria* in the 1960s (Shimomura, Johnson and Saiga, 1962; Prendergast and Manni, 1978). This natural protein was found to emit green light (from its intrinsic chromophore) upon blue light

excitation and its gene was extracted for expressing fluorescent tagged protein constructs directly in living cells (Chalfie *et al.*, 1994).

Over the last few decades, the development of multi-spectral fluorescent proteins (FPs), based on mutated GFP and coral variants, have provided a toolbox for researchers that have allowed them to use the cell as a 'test tube' to observe multiple protein localisations, behaviours, interactions and activities (Shaner, Steinbach and Tsien, 2005; Dean and Palmer, 2014; Nienhaus and Nienhaus, 2014; Costantini *et al.*, 2015). Using FPs in the live cell certainly is advantageous over conventional test-tube based approaches such as immunoprecipitation and subcellular localisation fractionation which involve grinding the cell and its components together. Often, these approaches are harsh, damaging and may result in false protein interactions and localisations caused by organelle-pooling and mixing (Salomon, Janssen and Neefjes, 2010; Suzuki *et al.*, 2010).

Most commonly used FPs are those that are GFP-based such as Enhanced Green Fluorescent Protein (EGFP) (Zhang, Gurtu and Kain, 1996), the Yellow Fluorescent Protein (YFP) (Rekas *et al.*, 2002), and a Cyan Fluorescent Protein (CFP) variant, mTurqouise2 (Goedhart *et al.*, 2012) as well as Red Fluorescent Proteins (RFP) that are *Discosoma* coral derived such as the monomeric DsRed (mDsRed) (Robinson and Marchant, 2005) and the more recent, mCherry (Bevis and Glick, 2002). The structures and the spectral properties of these FPs are illustrated in **Figure 1.9**. Current reviews provide details for newer generation monomeric FPs in relation to their quantum yields and photostability, properties that are important to live cell imaging of tagged proteins (Cranfill *et al.*, 2016; Rodriguez *et al.*, 2017; Specht, Braselmann and Palmer, 2017).

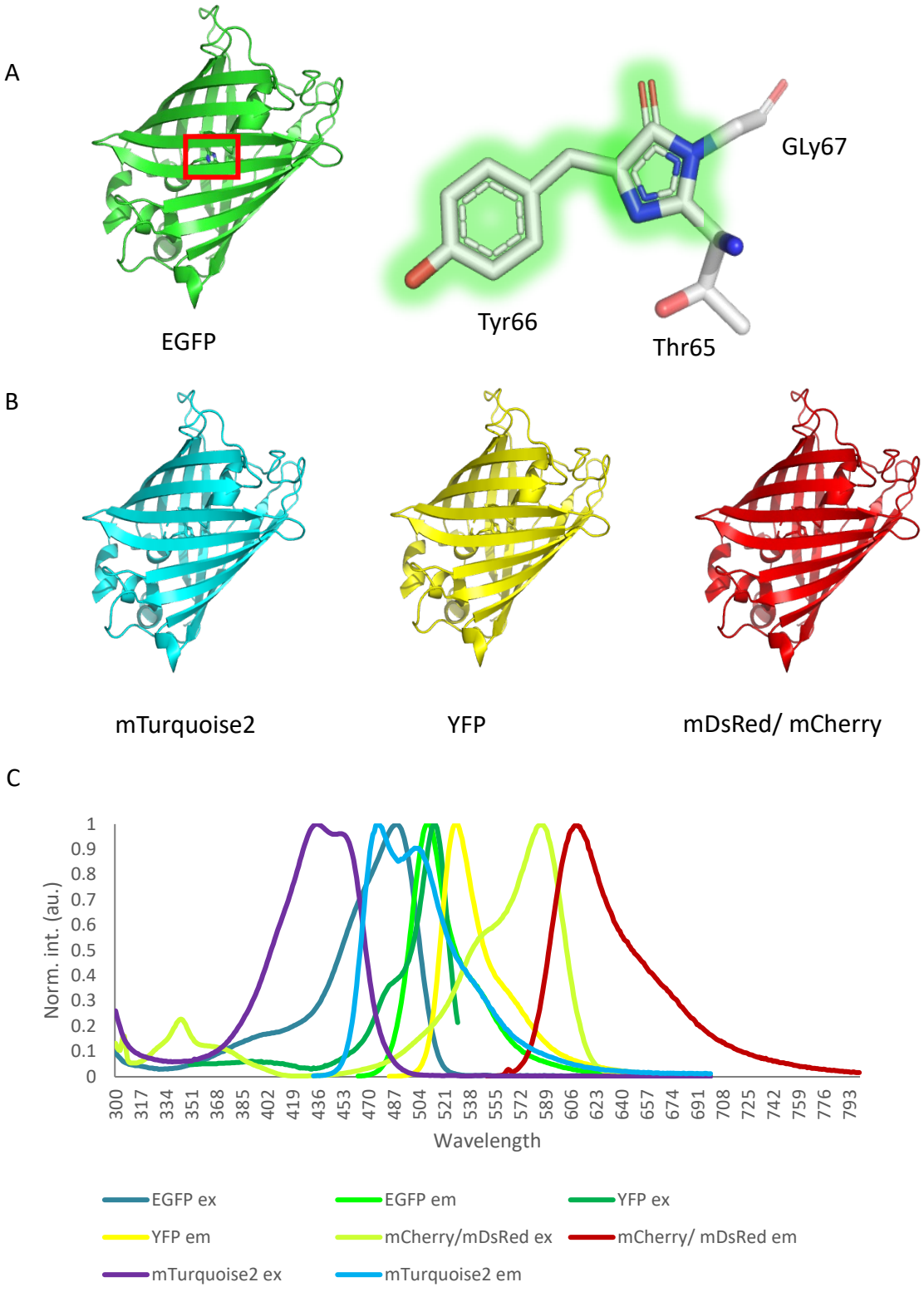

Figure 1.9: Structural and spectral properties of FPs. *A) Structure of EGFP and its chromophore tri-peptide contained within its beta barrel structure. B) Structures of cyan, yellow and red fluorescent proteins (mTurquoise2, YFP, mDsRed/ mCherry). Structures generated in Pymol using the PDB code: 2Y0G. C) Excitation and emission spectra of green, cyan, yellow and red fluorescent proteins generated using https://www.fpbase.org/spectra.*

1.11 Concepts of confocal and multiphoton microscopy

As well as the use of FPs, other forms of fluorophores can also be used such as quantum dots, nanoparticles, inorganic ions and organic dyes (particularly from the Alexa Fluor and Atto family) to label proteins, antibodies, DNA, lipids and organelles within the cell (Specht, Braselmann and Palmer, 2017). To observe these labelled components, the combination of both microscopy and laser technology created a ground-breaking era in which researchers could probe and see the “invisible”. The light microscope revolution was initiated by the construction of the first fluorescence microscope in the 1900s by Oskar Heimstädt who employed a lamp as a source of excitation, see short review (Lichtman and Conchello, 2005). This model was later improved by Philipp Ellinger and August Hirt in the late 1920s through the invention of the first *epi*-fluorescence (wide field) microscope (Ellinger and Hirt, 1929). Although the instrument was promising, the low excitation power coupled with inefficiently bright labelling techniques at the time proved to be an obstacle. This design was advanced further in the late 1960s by introducing a dichroic mirror (Ploem, 1967), a special filter placed at a 45º degree angle to the direction of excitation that allowed the reflection of the excitation light but transmission of the Stokes-shifted emitted light from the sample to the eyepiece (**Figure 1.10A**).

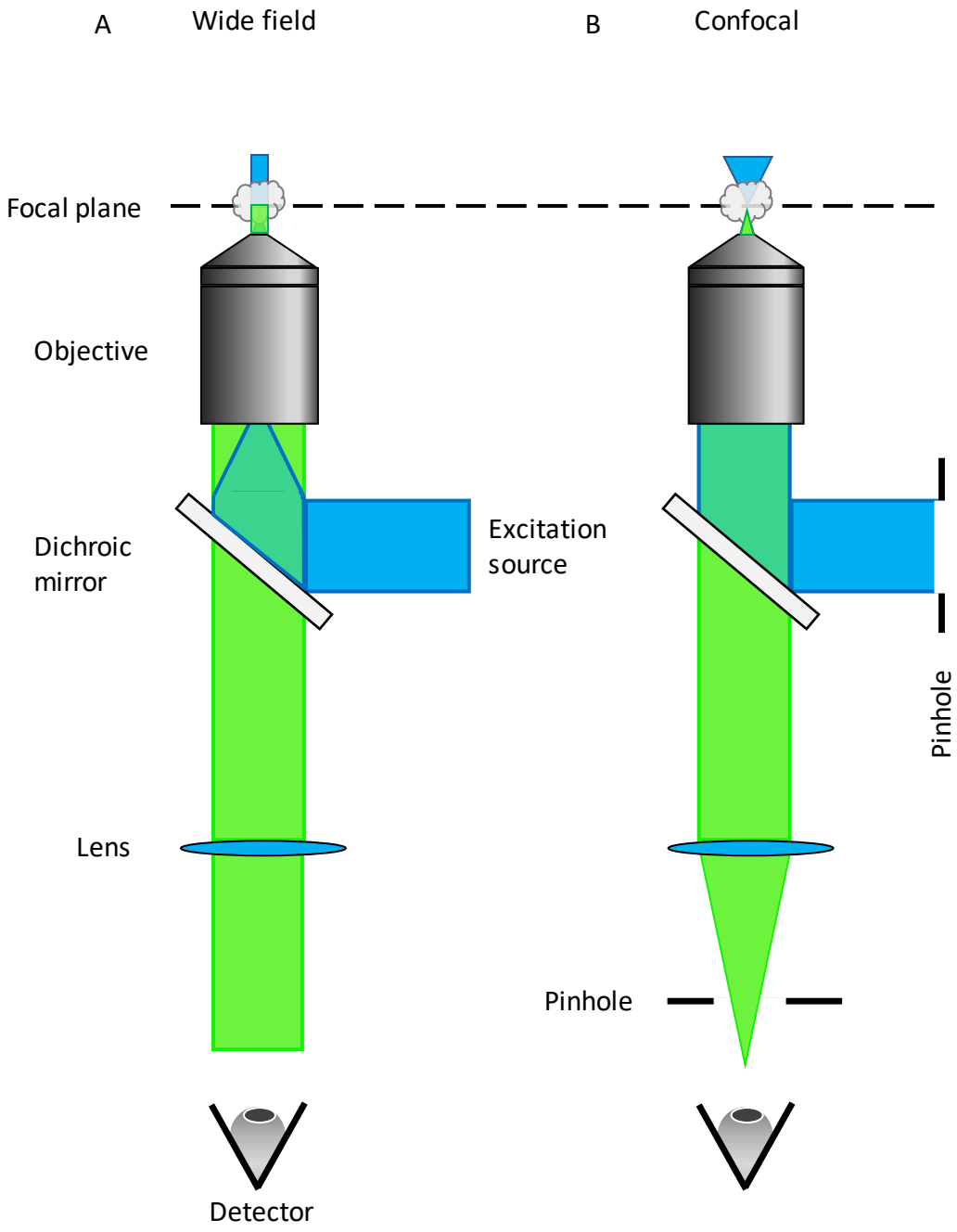

Figure 1.10: Comparison between wide field and confocal microscopy. *Excitation source light is shown in blue. Focal plane is shown by dotted black line. Sample fluorescence (in green), dichroic mirror and objective are also shown. (A) Wide field setup. (B) Confocal setup. Pinholes are shown by a slit in dark black line, lenses are shown by blue filled eclipse circles and the detector (eyepiece) is shown by a schematic of an eye.*

At the same time, the development of lasers presented a step change in the microscopy revolution (Maiman, 1960). Lasers offered high-powered monochromatic light that could be focussed by a lens to a diffraction-limited single point. In 1957, Marvin Minsky used a carbon arc lamp source, as lasers were not yet invented (Minsky, 1988) and combined it with point scanning (**Figure 1.11A**). Although this was done at the time by moving the stage, modern day microscopes can achieve this by utilising moving mirrors known as galvo mirrors (Jonkman and Brown, 2015). The implementation of a pinhole (aperture) (**Figure 1.10B**) before the detector and before the excitation source not only improves the contrast of the image by blocking out any out of focus light from above or below the focal plane of interest, but also allows the optical sectioning in the *z* plane of the sample (Sheppard and Choudhury, 1977; Wilson and Sheppard, 1984; Kimura and Wilson, 1991; Singh and Gopinathan, 1998). These 2D stacks through an object can be collated and reassembled to form a 3D image (**Figure 1.11B**). As both pinholes form conjugate planes, it is this modality that gives confocal microscopy its name. Laser (light) sources in combination with the discovery of GFP in the 1960s (Shimomura, Johnson and Saiga, 1962), developments in highly-sensitive detector systems and computer processing, have greatly improved signals from biological samples which can now be imaged with high resolution (Korobchevskaya *et al.*, 2017).

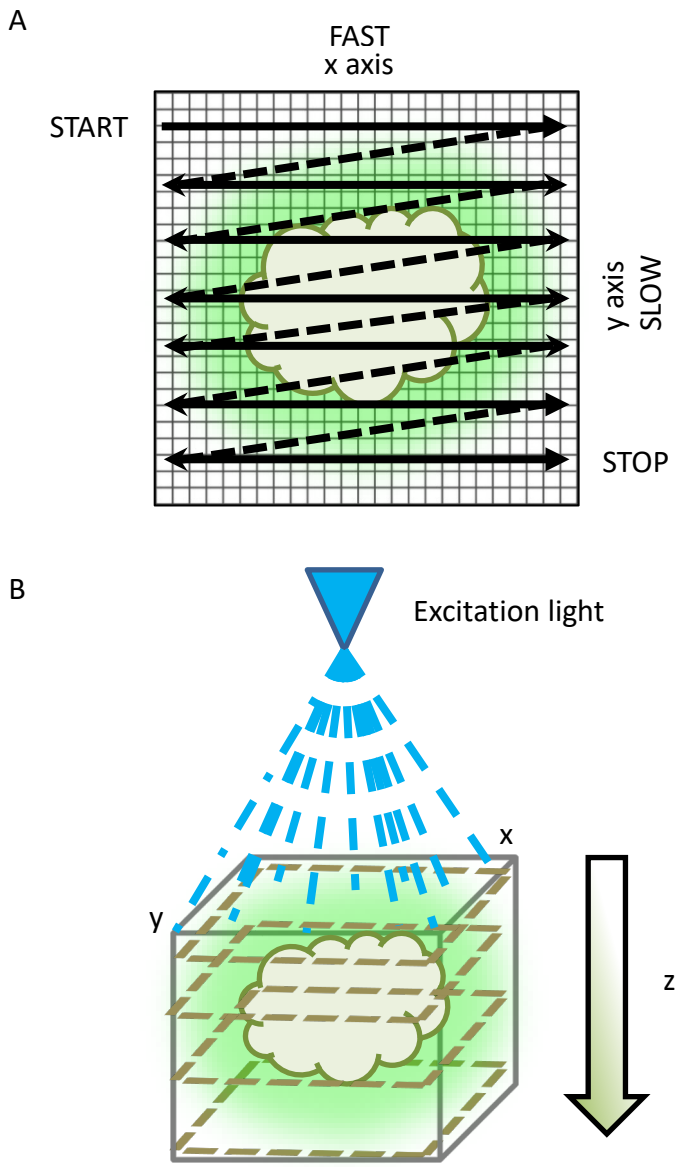

Figure 1.11: Confocal Laser Scanning Microscopy. *A) The raster scanning of a beam of light (black straight and dotted arrows) in the x-y direction (2D), point by point is shown where the gridded squares represent single pixels. A sample is shown by a glowing object. B) The light source (laser shown by a blue filled triangle) is depicted with beams of light (dotted blue lines) raster scanning through many z planes of the sample.*

A further development to the confocal laser scanning microscope was the addition of multiphoton microscopy. Although the concept of multiphoton excitation was proposed by Maria Göppert-Mayer in 1931, it was not until the development and usage of ultrafast short pulsed lasers that allowed scientists to observe and utilise this phenomenon in microscopy. Multiphoton excitation relies on the simultaneous absorption of multiple photons. In the case of two-photon excitation (2-PE), two photons each with half the energy of a single photon, are absorbed at a single point in the focal plane (Ustione and Piston, 2011) as shown in **Figure 1.12**. In relation to Planck's law seen in **Equation 1.1**, these low energy photons generally correspond to an excitation wavelength double that of a single photon wavelength. Naturally such a process is highly rare and the probability extremely low, the typical cross section (σ) (measurement for the probability of absorption) for a single photon absorption "pumping" a molecule into its electronic excited state is 10^{-18} cm^2 whilst for two photon it is of the order of 10^{-50} cm^4 s which equates to 1 Göppert-Mayer (GM) unit (Ishikawa-Ankerhold, Ankerhold and Drummen, 2012). The cross section for GFP is 10 GM. The innovation of ultrafast pulsed (picosecond-femtosecond, 10^{-12}-10^{-15} s) mode locked lasers provide high peak power to increase photon flux and density which when coupled with a high numerical aperture objective, increases the rate of 2-PE absorption as shown in **Equation 1.4** (So *et al.*, 2000):

$$N_a = \frac{p_0^2}{\tau_p}\frac{\delta}{f_p}\left(\frac{NA^2}{2hc\lambda}\right)^2 \qquad \textbf{(1.4)}$$

where N_a is the probability of photons absorbed by 2-PE per pulse of excitation. P_0 is the average laser power, δ is the two photon absorption cross section of the fluorophore, λ is the two-photon excitation wavelength, τ_p is pulsewidth of the laser, f is the repetition rate of the laser, NA is the numerical aperture of the objective, h is Planck's constant and c is the speed of light.

Most importantly, due to the non-linear characteristics of two-photon excitation (i.e. probability proportional to the square of intensity) it allows optical sectioning without

the use of a pinhole as the density of photons are only sufficient to drive the 2-photon process in the focal plane (Ustione and Piston, 2011). Advantages of using near-infrared excitation for multiphoton excitation over traditional single photon excitation include much lower total photo-bleaching, reduced sample photo-damage and cytotoxicity as well as the ability to penetrate deeper into thick biological tissues with reduced scattering and auto-fluorescence excitation, see **Figure 1.11** (Straub *et al.*, 2000; Masters and So, 2001; Tauer, 2002; Zipfel *et al.*, 2003).

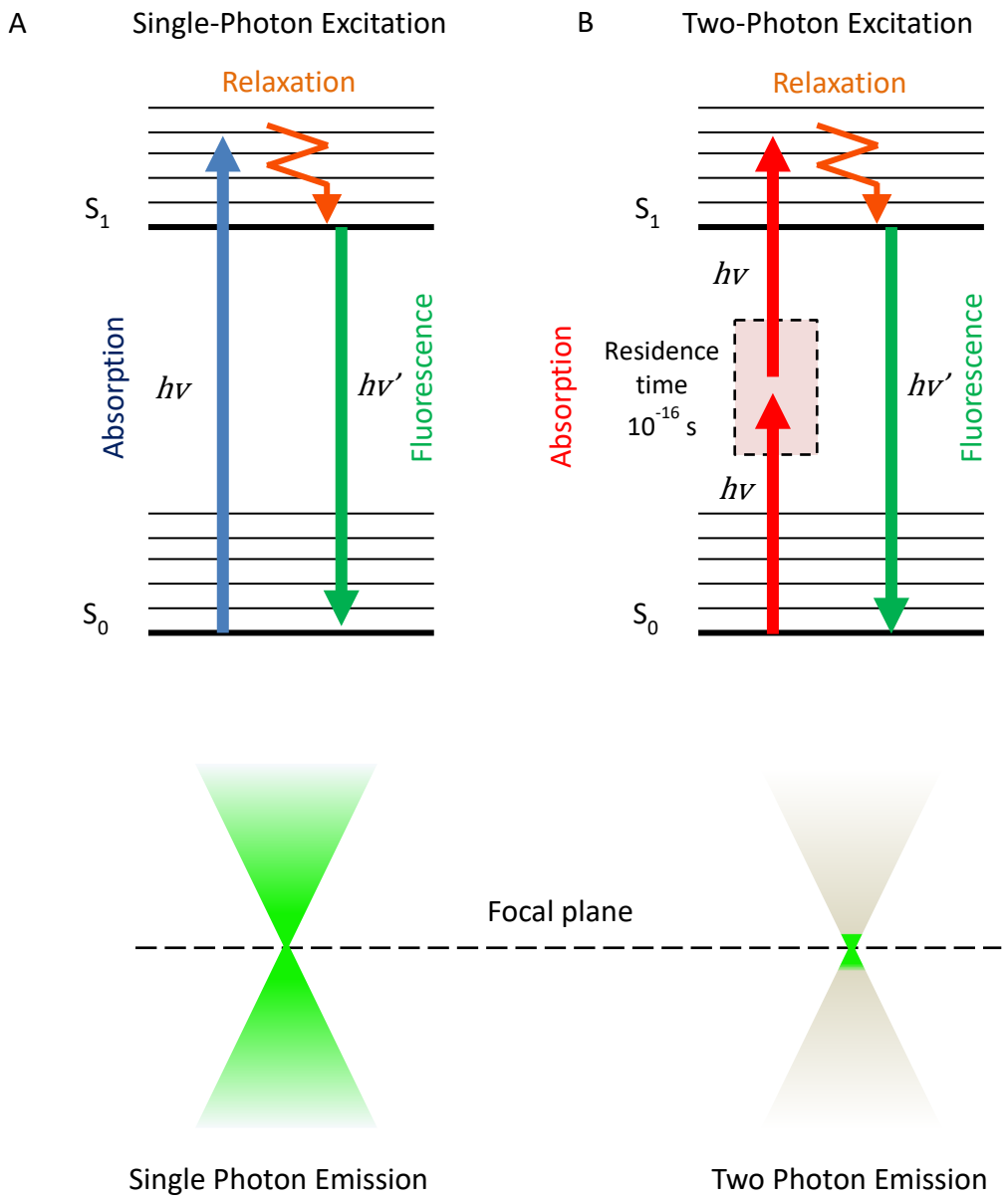

Figure 1.12: Comparison between one-photon and two-photon excitation. *A) Shows the absorption of a single (e.g. 488 nm) photon to the excited state. B) Shows the simultaneous absorption of two-photons (e.g. 976 nm, each with half the energy of a single 488 nm photon) to the excited state. Schematics of one-photon versus two-photon fluorescence emission are shown.*

1.12 Introduction to Förster resonance energy transfer (FRET) and Fluorescence-lifetime imaging microscopy (FLIM)

The birth of laser scanning microscopy and GFP technology has given rise to the growth of many quantitative techniques to study biological processes such as protein-protein interactions, protein activity as well as a whole array of other molecular interactions within living cells (Jensen, 2012). A powerful technique for monitoring molecule-molecule interactions is Förster Resonance Energy Transfer (FRET) where two molecules (*e.g.* proteins) are labelled with fluorophores. An initial excited molecule (donor) transfers its electronic energy to an adjacent second molecule (acceptor) (Selvin, 2000; Sekar and Periasamy, 2003), as shown in **Figure 1.13**. For FRET to occur, the two molecules must be within very close proximity, typically within 10 nm of each other. This non-radiative energy transfer results in the fluorescence emission of the acceptor although this is not always the case, as some "dark" acceptors do not emit fluorescence (Lakowicz, 2006; Murakoshi *et al.*, 2015). The loss of fluorescence emission from the donor by the acceptor is termed quenching. To meet the requirements of FRET, the two fluorophores must exhibit spectral overlap that is the emission spectrum of the donor must overlap significantly with the excitation spectrum of the acceptor (a condition termed resonance). As well as meeting the conditions of being within 10 nm of each other, their dipole-dipole moments must also be aligned (k^2 factor) (Marcu, French and Elson, 2014). Thus, the FRET efficiency (shown in **Equation 1.5**) relates to the distance (r) of the fluorophores and to dipole-dipole coupling; this equation demonstrates the inverse 6^{th} power law:

$$E_{FRET} = \frac{1}{1+\left(\frac{r}{R_0}\right)^6} \qquad \textbf{(1.5)}$$

where E_{FRET} is FRET efficiency, r is the distance between donor and acceptor, R_0 is the distance at which 50% FRET occurs and the inverse 6th power law takes into account the dipole-dipole coupling.

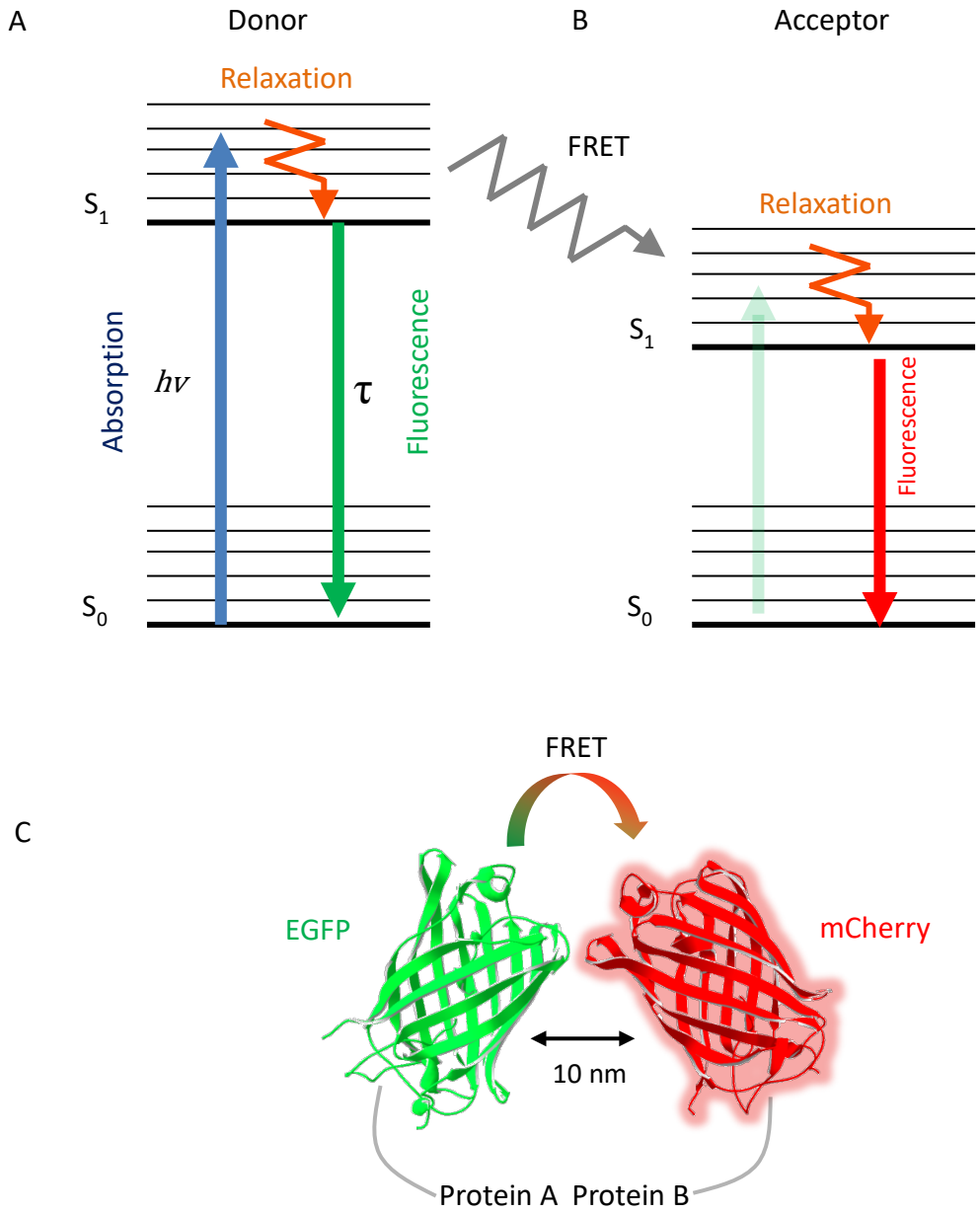

Figure 1.13: Principle of FRET. *A) and B) Energy level diagrams showing when the conditions of FRET are met for both donor and acceptor molecules. The ground state (S_0) and the first excited electronic state (S_1) are shown by horizontal black lines. The process of FRET is shown by a zig-*

zagged arrow in grey. C) Simplified cartoon schematic showing the energy transfer process between the donor (e.g. protein A labelled with EGFP) and the acceptor (e.g. protein B labelled with mCherry).

FPs are widely used as fluorophores for FRET experiments ranging from green-red FRET pairs such as the EGFP-mCherry combination to that of blue-yellow FRET-pairs as mTurquoise2-YFP which offer larger dynamic quenching due to greater spectral overlap (Bajar *et al.*, 2016; Martin *et al.*, 2018). Dyes such as those from the Alexa family can also be used as fluorophores (Berney and Danuser, 2003). However the advantage of using FPs is that molecules can be tagged, expressed and monitored in living cells. Although FRET may appear to be a simple approach, it relies on measuring accurately the intensity of the fluorescence and therefore taking measurements requires spectrally resolving the wavelengths of fluorescence of the donor (unquenched) and the acceptor, as well as other background signals and detector thresholds. Furthermore, effects from photo-bleaching whereby a fluorophore no longer fluoresces through photochemical modification over the illumination time makes interpretation of the FRET results challenging and open to misinterpretation (Piston and Kremers, 2007).

A much more robust way of performing FRET experiments is to use the time domain to measure the fluorescence intensity. Simply, this compares the natural fluorescence lifetime (τ) of the donor to the change in excited lifetime when quenched in the presence of the acceptor. Thus, FRET results in the shortening of the lifetime of the donor and hence observing molecule-molecule interactions is not purely dependent on fluorescence intensity (Sauer, Hofkens and Enderlein, 2011). The FRET efficiency is given by (**Equation 1.6)**:

$$E_{FRET} = 1 - \frac{\tau_{DA}}{\tau_D} \qquad \textbf{(1.6)}$$

where FRET efficiency (E_{FRET}) is related to the lifetimes of the donor with the acceptor (τ_{DA}) and the donor without the acceptor (τ_D).

Imaging the lifetime of a fluorophore is known as Fluorescence Lifetime Imaging Microscopy (FLIM) (Becker, A Bergmann, *et al.*, 2004; Stubbs *et al.*, 2005; Becker, 2012; Yadav *et al.*, 2013; Suhling *et al.*, 2015; Meyer-Almes, 2017). FLIM was pioneered in the late 20th century and gradually improved by others (Gerritsen *et al.*, 2002), eventually leading to the FLIM of cells, labelled organelles and proteins (Periasamy *et al.*, 1996; Peter *et al.*, 2005; Stubbs *et al.*, 2005; Llères, Swift and Lamond, 2007; Becker, 2012). Today, FLIM is a versatile tool and can be combined with multiphoton microscopy to provide a powerful instrument for live cell imaging. FLIM can be performed in two ways: time domain, and frequency domain. Briefly, the frequency domain method uses a pulsed (modulated) excitation source and using homodyne detection methods, to measure the way the phase in the fluorescence emission intensity varies in relation to the modulated excitation. This results in a frequency-domain FLIM signal from which fluorescence lifetimes can be extracted (Verveer and Hanley, 2009). Time-domain FLIM can be performed in two ways, either using time-gating where the fluorescence is measured at various times according to the excitation pulse using fast-gated image intensifiers (Scully *et al.*, 1996) or using Time-Correlated Single Photon Counting (TCSPC) (Becker, Axel Bergmann, *et al.*, 2004). The FLIM and time-resolved fluorescence data reported in this thesis has used TCSPC which delivers higher temporal resolution with photon efficient detection and minimal noise (Marcu, French and Elson, 2014) and details of this technique are given in **Chapter 2, Material and Methods**. Briefly, for TCSPC the sample is point-scanned with a high repetition rate pulsed laser. The time of single fluorescent photons reaching the detector with respect to the excitation pulse is measured using a photon-counting detector at each *X*,*Y* point producing a FLIM image where each pixel can be analysed to obtain its own fluorescence decay profile and thus its lifetime (Becker *et al.*, 2004; Stubbs *et al.*, 2005) as summarised in **Figure 1.14**.

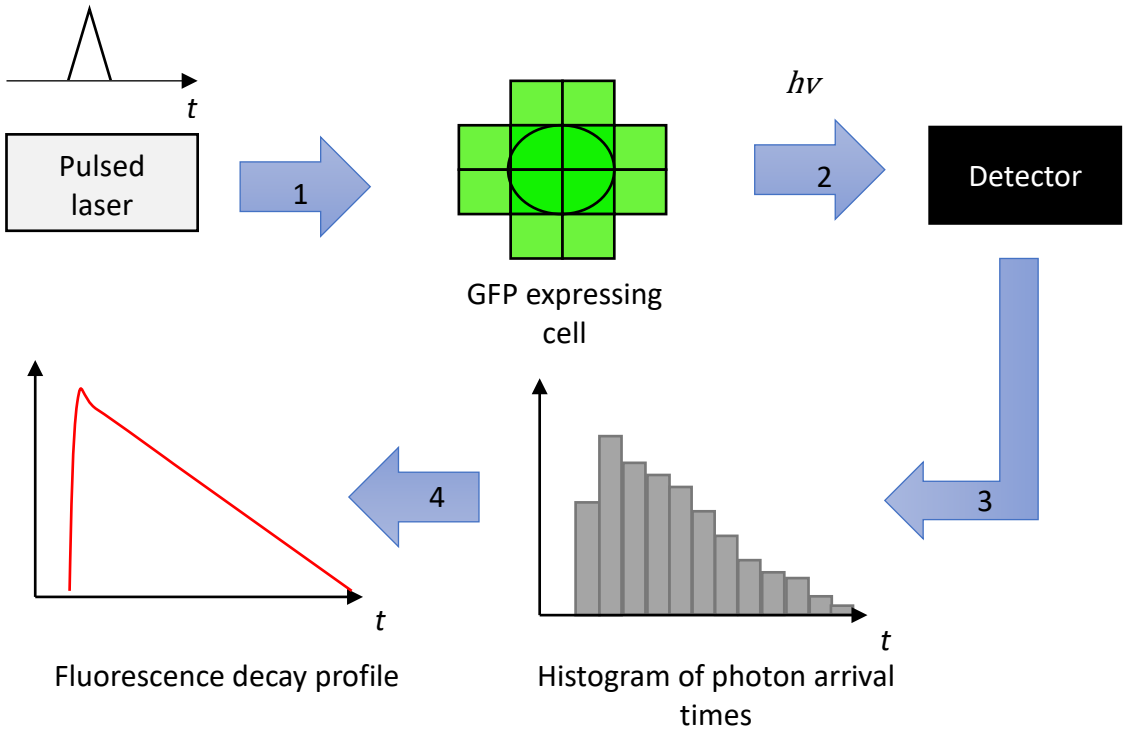

Figure 1.14: Overview of time domain FLIM using TCSPC. *1) An ultrafast pulsed laser is used to excite a cell expressing GFP (shown in green where each box represents a pixel). 2) Fluorescent photons (hv) emitted from the sample are collected at the detector and their relative arrival times with respect to the excitation pulses of the laser are measured using the TCSPC module. 3) A histogram of photon arrival times is built which is convolved with the IRF (measurement of the sensitivity of the instrument). 4) A final decay profile (shown in red) is produced for each pixel.*

Software fits the decay to a model function such as a mono-exponential one which can be used for GFP analysis. Parameters such as lifetime (τ) and the chi-square (x^2) of the fit (a determination for the 'goodness' of the fit) can be obtained for each pixel (Becker *et al.*, 2004). Ultimately, the software generates a pseudo-coloured FLIM image where the colour of each pixel represents a lifetime value (**Figure 1.15**). Thus, the combination of FLIM with FRET allows for the accurate determination of the dynamics of molecular species and mapping their sub-cellular interactions within living cells at diffraction limited resolution (Peter *et al.*, 2005; Wallrabe and Periasamy, 2005; Llères, Swift and Lamond, 2007; Laptenok *et al.*, 2010; Sun, Day and Periasamy, 2011; Schoberer and Botchway, 2014). If the donor lifetime is

quenched in the presence of an acceptor, its lifetime will shorten and this will relate to a different colour in those pixels (**Figure 1.15B**). This change in lifetime is indicative of a direct and physical interaction, making FRET-FLIM most suited for studying cancer signalling pathways such as the mTOR pathway where protein-protein interactions are a vital constituent for understanding biological functions (Yadav *et al.*, 2013).

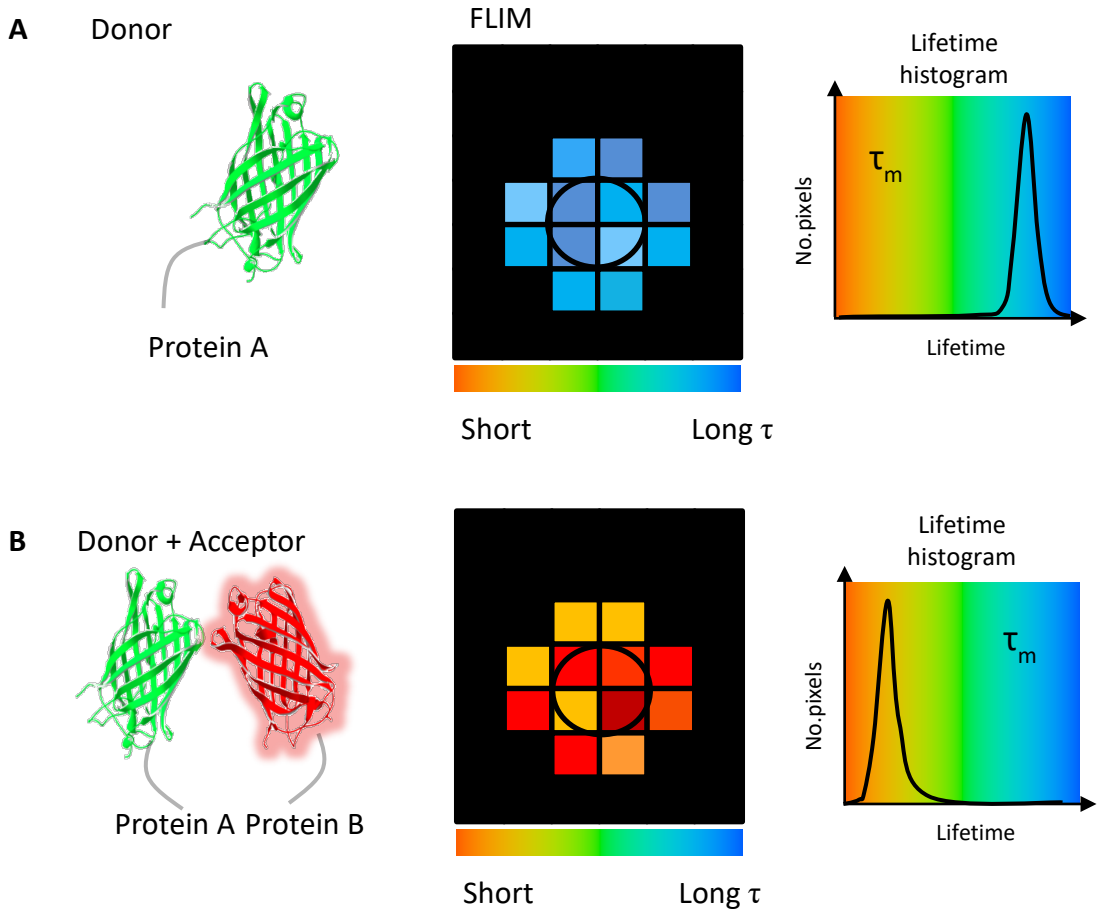

Figure 1.15: Use of FRET-FLIM to determine protein-protein interactions. *A) Protein A tagged with a donor is shown with a corresponding FLIM image where each pixel is artificially coloured with its respective lifetime value. The average lifetime distribution of all pixels is also shown in a histogram. B) Protein A tagged with a chromophore (donor) and Protein B tagged with another chromophore (acceptor) are shown when the conditions of FRET are met. A shortening of the donor lifetime is shown in the FLIM image where a change in colour of pixels indicates a different (shortened) lifetime value.*

1.13 Molecular Structure and Conformation Studies Using FRET

FRET can also be used to measure protein activity by following the way its structure changes as it performs its biological role (Hochreiter, Garcia and Schmid, 2015). FRET sensors provide the ability to study how protein conformation is related to function and quantitatively enables the determination of receptor, ion, metal, membrane and post-modification activity within living cells (Lindenburg and Merkx, 2014). Currently, bio-FRET sensors are routinely used in most laboratories and a rapidly growing area of focus is their use to determine phosphorylation (kinase activity) (Demeautis *et al.*, 2017; Komatsu *et al.*, 2018). There are various ways to construct a FRET sensor to determine phosphorylation but the two most common methods are shown in **Figure 1.16**, where partial sequences of proteins (typically a ligand domain containing a short region of the substrate phospho-domain and a sensor domain usually containing the kinase domain of the effector are linked together) are used with a FP attached to either end of the construct (Komatsu *et al.*, 2011). Alternatively, the full length protein of interest can be tagged with a FP to each end (Zhou *et al.*, 2015; Bertolin *et al.*, 2016). The structural changes of the protein upon phosphorylation brings the FRET donor and acceptor pair into or out of contact and the change in lifetime this provides can be monitored with FRET-FLIM, allowing for the direct and precise determination of when and where the phosphorylation is occurring within the live cell.

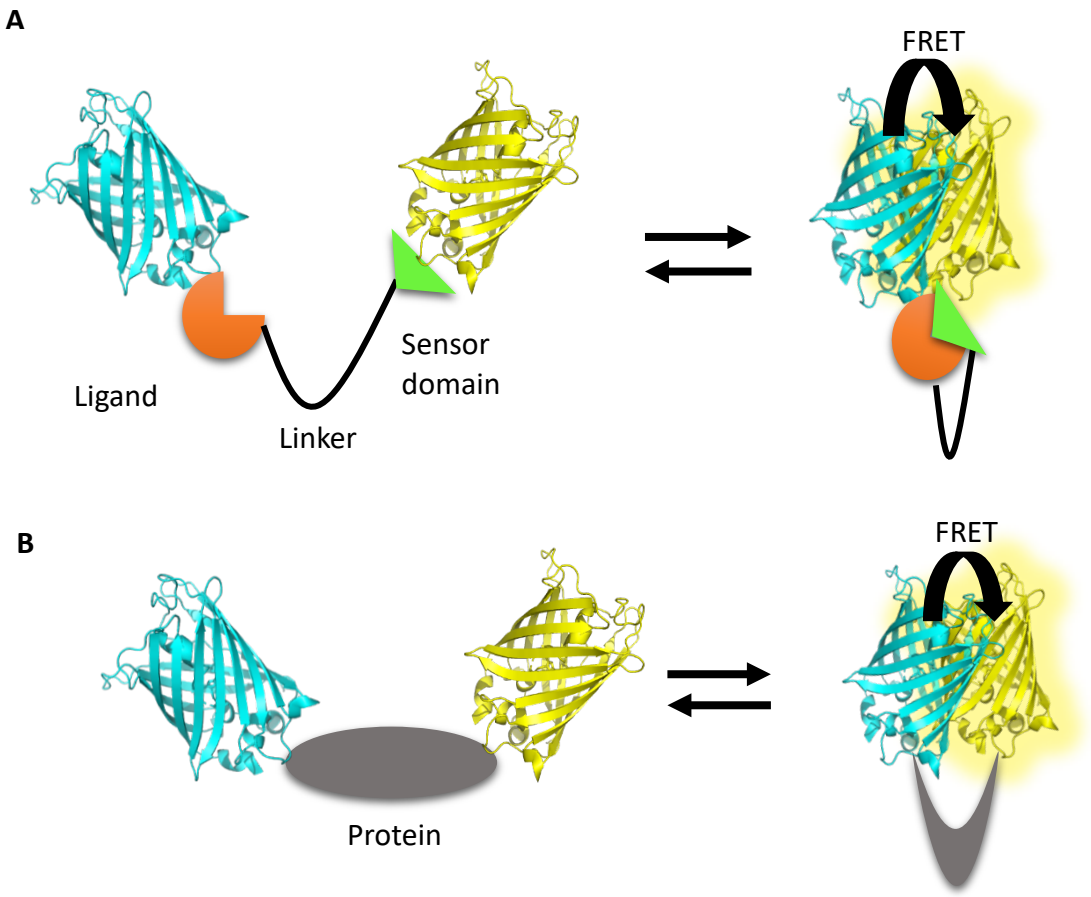

Figure 1.16: Kinase FRET sensor mechanisms. *A) A ligand domain (phospho-peptide of substrate) in orange linked by a long linker region (black line) to a sensor domain (kinase domain of kinase protein of interest) in green with a FP on either side is shown. This construct is shown in both open and closed conformations which are related to FRET efficiency. However, this form of sensor may not be reversible and therefore may only provide a single snapshot of activity. B) Kinase protein shown in grey tagging on either end of its termini with a FP is shown. Changes in conformation of the protein can be related to phosphorylation (FRET) activity.*

1.14 Review on imaging mTORC1 in live cells

Despite over 23,000 (Pubmed, 2018) published articles on mTOR to date, only a small handful of publications have investigated mTOR in living mammalian cells. Various subunit proteins of the mTORC1 have been labelled with FPs and their sub-cellular localisations studied and determined (**Table 1.1**). Taken together, a common localisation feature of all these proteins is the cytoplasm, alluding to the likelihood that the mTORC1 may assemble in the cytoplasm. The localisation of S6K1 however remains unknown.

Table 1.1: Summary of live localisations of FP labelled mTORC1 subunit proteins

Protein	*Label*	*Localisation*	*Reference*
mTOR	EGFP YFP and Venus HaloTag	Mostly cytoplasmic with some nuclear	(Liu and Zheng, 2007; Qian *et al.*, 2010; Mori *et al.*, 2013; Yadav *et al.*, 2013)
raptor	mDsRed GFP Cerulean	Cytoplasmic Lysosomes	(Qian *et al.*, 2010; Yadav *et al.*, 2013; Martin *et al.*, 2014; Manifava *et al.*, 2016)
Rheb	EGFP mDsRed mCherry CFP YFP	Cytoplasmic with strong ER, Golgi and perinuclear. Some nuclear	(Takahashi *et al.*, 2005; Buerger, DeVries and Stambolic, 2006; Li *et al.*, 2007; Zhou *et al.*, 2009; Hanker *et al.*, 2010; Ismail *et al.*, 2011; Yadav *et al.*, 2013)
4EBP1	CFF YPet- Cerulean	Equally cytoplasmic and nuclear	(Rong *et al.*, 2008; Zhou *et al.*, 2015)

It is important to stress that co-localisation of proteins does not necessarily signify a direct physical interaction, thus it is necessary to investigate mTORC1 sub-cellular interactions. FRET-FLIM, however does strongly suggest interactions. FRET has been employed to study mTORC1 interactions and activity in living cells. One of the

first studies to determine mTOR and raptor interactions used steady-state FRET (Qian *et al.*, 2010), this was later improved by using FRET-FLIM (Yadav *et al.*, 2013). The latter study was the first to determine direct interactions between Rheb and mTOR in the live cell. In particular, significant presence of both mTOR and Rheb were found in the nucleus as well as large punctate structures upon amino acid and serum starvation with EGFP-mTOR. Although the identities of these punctate structures were not defined, the importance of mTORC1 in the nucleus was highlighted because the involvement of nuclear mTOR signalling is generally overlooked. In addition, mTOR has also been investigated directly by tagging 4EBP1 with various FPs using a FRET sensor and has been found to be active in the cytoplasm, lysosome, nucleus and at the plasma membrane (Zhou *et al.*, 2015). This raises the question whether mTOR activity (i.e. 4EBP1 phosphorylation) is more active in some areas of the cell and lower in other sub-cellular structures. However, as rapamycin and rapalogues partly inhibit 4EBP1 phosphorylation, these findings on mTOR activity suggest a better downstream target of the pathway is needed for accurately monitoring mTORC1 in living cells.

Real-time imaging of endogenously labelled raptor with GFP has led to the discovery of the recruitment of mTORC1 onto lysosomes within a few minutes after amino acid starvation in living cells (Manifava *et al.*, 2016; Lawrence *et al.*, 2018). Upon replenishing the amino acids, these lysosome structures of raptor-GFP disappeared and soon returned to a homogenous expression in the cytoplasm. It was also identified through western blotting that following replenishment of the amino acids, the phospho-S6K1 expression remained elevated after mTORC1 detachment from the lysosomes. Further live-cell work has shown similar results with GFP-tagged Rags and mutant Rags to increase lysosomal recruitment and substrate phosphorylation (Lawrence *et al.*, 2018). This could provide insight into the

mechanism of Rheb (see section **1.5**) which tethers mTORC1 to the lysosomal membrane and activates the mTOR kinase protein (Hao *et al.*, 2018).

Directly observing the localisation of the remaining components of the mTORC1 pathway, namely S6K1 and PRAS40, as well as their interactions within the complex offers a new and unexplored avenue in the less studied live-cell mTOR world. Although much attention has been given to the upstream part of the complex, little is known regarding the downstream substrate interactions with the mTOR complex. Investigating the localisation, interaction and phosphorylation of the S6K1 substrate with regards to mTORC1 is therefore explored in this research and provides new advancement to the study of mTOR drug interactions using FRET-FLIM. It is hoped that these studies will provide a better understanding of the mechanism of mTOR activation in a cellular context, ultimately leading to the design and development of novel treatments against mTOR-related disease states for future clinical work.

1.15 Aim and development

This research project forms an integral part of the program aimed at studying the mechanism of mTORC1 both biochemically and structurally. The research in this work is composed of three parts. The first investigates the subcellular localisation of S6K1, its recruitment onto mTORC1 as well as its direct interactions with it and the localisation of its phosphorylated form within living cells. To date, current work has failed to provide conclusive evidence regarding such matters. The second explores the use of both single-photon and multi-photon microscopy in exciting naturally fluorescent pan-mTOR inhibitors (second generation) to observe both their sub-cellular localisation and their mechanism of action with respect to other mTORC1 subunit proteins. The final part of this project deals with the structural biology aspect, where attempts to express and purify mTORC1 proteins and a FRET bio-sensor (SensOR) in large quantities are carried out using a baculovirus expression system in insect cells. It is hoped that the latter *in vitro* work compliments the *in vivo* studies and gives further insight into the workings of the mTORC1 signalling pathway for effective strategies to prevent and treat mTOR disease states.

Firstly, it is proposed that fluorescently tagged S6K1 constructs be generated by cloning and splicing the full length cDNA S6K1 sequence into GFP vectors (mTurq2, mCherry and EGFP based) using in-fusion cloning. These constructs will be expressed in mammalian cells (HEK293, HeLa and U2OS) by means of chemical transfection and then imaged using confocal microscopy. The subcellular localisation of S6K1 in living cells is still unknown to-date. Using the results obtained from identifying the sub-cellular localisation of GFP-tagged S6K1 in living cells, the interaction of S6K1 with mTOR and other mTORC1 subunit proteins that localise within the same localisation site will be investigated using advanced FRET-FLIM imaging and pull-down assays. Although S6K1 is known to interact with raptor, its interaction with mTOR is uncertain and its interaction with Rheb is unknown. In

addition, the regulation of ectopically-expressed S6K1 with co-expressed mTORC1 subunit proteins (particularly Rheb and raptor) will be explored by Western blot analysis especially since raptor's role in regulating S6K1 appears to be an ongoing debate in the literature. Other fluorescently-labelled binding partners of raptor such as 4EBP1 and PRAS40 will also be co-expressed with S6K1 to investigate any substrate competition using three colour confocal imaging. Collectively, these findings will provide information regarding both the assembly of the S6K1 onto the mTORC1 and sub-cellular sites for expected mTOR activity. Ultimately, from this, the localisation of phosphorylated S6K1 will be examined using immunofluorescence labelling of fixed cells as well as developing a novel live cell approach using a S6K1 phosphorylation FRET-biosensor with FRET-FLIM technology.

Secondly, once the localisation of phosphorylated-S6K1, hence mTOR activity, has been identified, this information will then be used to investigate the sub-cellular target sites of second generation mTOR inhibitors, namely AZD2014 and INK128. Although the efficacy of mTOR drugs has been well-studied in the field, their localisation within the cellular system has not been explored. The absorption spectra, fluorescence emission spectra and fluorescence lifetimes of AZD2014 and INK128 in various solvents such as DMSO and PBS will be characterised and used as bench marks for predicting cellular environmental stability. These findings will be taken forward to *in vivo* work where cellular uptake and subcellular localisation of AZD2014 and INK128 using one-photon and two-photon confocal microscopy will be determined with direct excitation wavelength in various mammalian cell lines such as HEK293, CHO and MCF7. The exact mechanism of action of AZD2014 will also be explored by determining its binding with GFP-tagged mTORC1 subunit proteins using FRET-FLIM. AZD2014 has shown selectivity to other kinases during screening

and thus although not known, its interaction with the S6K1 kinase appears to be a likely candidate.

Thirdly, it is intended that new S6K1 FRET bio-sensor and mTORC1 subunit constructs suitable for insect cell expression will be made. The baculovirus expression system will be used for large-scale production and purification of these proteins for both *in vitro* studies and future cryo-EM or X-ray crystallography for identifying atomically-resolved interactions. It is expected that the data obtained from this programme will further develop mTORC1 signalling interactions and assembly, eventually leading to novel treatments where targeting these interactions provides better therapy.

2.0 Materials and methods

2.1 Materials

All chemicals and reagents in this work were purchased and used without further treatment or purification.

2.1.1 Chemicals

General laboratory reagents were purchased from Sigma-Aldrich (UK) and Millipore (UK), currently under Merck (UK) or from Fisher Scientific, Invitrogen, Gibco and Life Technologies, currently under Thermofisher Scientific (UK). Other chemical reagents and kits (all chemicals included) were obtained from Qiagen (UK), Machinery-Nagel (U.S.A.) and Agilent (UK) unless otherwise stated. Inhibitors were purchased from MedChem Express (Europe). Purified GFP was a kind gift from Dr Cameron Naylon.

2.1.2 Primers

All DNA primers were purchased from Integrated DNA Technologies (IDT) (UK) at a 25 nmole (0.27 mg) DNA oligo concentration with standard desalting to remove any impurities. All primers were designed with a T_m close to 60ºC, although this varied slightly depending on the GC content. Gene-specific primers with 15 bp extension homologous to vector ends were designed for In-Fusion™ cloning (Nettleship *et al.*, 2010) using an automated primer design tool: https://www.oppf.rc-harwell.ac.uk/Opiner/ or for fusing two inserts together using SnapGene® software (from GSL Biotech; available at snapgene.com). Primers for mutant constructs were designed using the automated primer design tool: https://www.genomics.agilent.com/primerDesignProgram. Primer stocks of 100 µM were made by re-suspending lyophilised primers with nuclease-free water (Sigma-

Aldrich). Stocks were then diluted 1:10 to make working stocks of 10 μM and stored at -20ºC.

2.1.3 DNA plasmids and vectors

S6K1-GFPSpark	HG10099-ACG, Sino Biological (China)
HA-mCherry-raptor	Plasmid #73386, Addgene
mDsRed-raptor	Yadav et al. 2013
EGFP-Rheb	Yadav et al. 2013
mDsRed-Rheb	Yadav et al. 2013
EGFP-mTOR[1]	Yadav et al. 2013
FLAG-mTOR	Plasmid #26603, Addgene
4EBP1-GFPSpark	HG10022-ACG, Sino Biological (China)
HA-YFP-PRAS40	Plasmid #73389, Addgene
mCherry-FKBP12	Plasmid #67900, Addgene
YFP-mTOR	Plasmid #73384, Addgene
YFP-Rheb	Gift from Dr. Kun-Liang Guan[2]
CFP-Rheb	Gift from Prof Won Do Heo[3]
EGFP-raptor	Gift from Prof. Jacek Jaworski[4]
pOPINE-3C-EGFP	Plasmid #41125, Addgene
pOPINE-3C-mCherry	PP-UK
pOPINE-3C-mTurquoise2	PP-UK
pOPINE-3C-YFP	PP-UK
pOPINN-EGFP	Plasmid #53541, Addgene
pOPINEneo-3C-2STREPStop	PP-UK
pBAC4x-1	Merck
AcMNPV-DsRed	Gift from Arnold Poterszman

[1] mTOR sequence contains additional glycine amino acid after methionine (ATG) start codon
[2] Zhou X et al. PNAS. 2009;106(22):8923-8
[3] Yeung T et al. Science. 2008;319(5860):210-3
[4] Urbanska M et al. J Biol Chem. 2012;287(36):30240-56

2.1.4 Cell lines

Human Embryonic Kidney Cells (HEK293) and HeLa (cervical) cells were purchased from ATCC (U.S.A), certified as mycoplasma (contamination) free. Michigan Cancer Foundation-7 (MCF-7) breast cancer and epidermoid carcinoma A431 cells were available from the Octopus (Research Complex, UK) cell line bank. Human Bone Osteosarcoma Epithelial U20S cells and a clonal isolate of *Spodoptera frugiperda* (Sf), the Sf9 insect cell line were obtained from PP-UK (Research Complex, UK). HEK293F cells and the Sf21 insect cell line were provided by Evotec (UK) Ltd. Competent *Escherichia coli* (*E. coli*) cells: XL10-Gold® ultracompetent cells were bought from Agilent (UK), One Shot™ OmniMAX™ Chemically competent were bought from Invitrogen™ (UK) and Stellar electrocompetent cells from Takara Bio (Europe).

2.1.5 Cell culture reagents

All cell culture reagents were from Thermofisher Scientific (Gibco^{TM}).

2.1.6 Antibiotics

Carbenicillin (CB)	50 mg/ml	Sigma-Aldrich (UK)
Kanamycin (Kan)	35 mg/ml	Sigma-Aldrich (UK)

2.1.7 Antibodies

Anti-Phospho-S6K1 (T389/T412)	St John's Laboratory (UK)	STJ91045
Anti-Phospho-S6K1	Cell Signalling (UK)	#9234
Anti-Phospho-S6K1	Thermofisher Scientific (UK)	PA1-526
Anti-S6K1	St John's Laboratory (UK)	STJ31332
Anti-Phospho-RPS6	Cell Signalling (UK)	#2211

(Ser235/236) (rabbit)		
Anti-Rheb antibody (goat)	Santacruz Biotechnology (UK)	sc-6341
Anti-Vinculin (mouse)	Millipore (UK)	MAB3574
Anti-His (mouse)	Qiagen (UK)	34660
Anti-FLAG (mouse)	Sigma-Aldrich (UK)	F1804
Anti-mTOR (rabbit)	Cell Signalling (UK)	#2983
Anti-myc (mouse)	Thermofisher Scientific (UK)	MA1-980
Anti-raptor (rabbit)	Cell Signalling (UK)	#2280
Anti-rabbit Alexa Fluor 405/ 488/ 555	Abcam (UK)	ab175649/ ab150073/ ab150074
Anti-mouse Cy3	Jackson Immunochemicals (Europe)	715-165-151
Ant-rabbit Cy5	Chemicon International (U.S.A.)	AP187S
Anti-rabbit HRP	Cell Signalling (UK)	#7074
Anti-mouse AP	Promega (UK)	S372B
Anti-rabbit AP	Promega (UK)	S3731
Anti-goat AP	Abcam (UK)	ab6742-1

2.2 Methods

2.2.1 Amplification of cDNA by polymerase chain reaction (PCR)

Polymerase chain reaction (PCR) reactions were setup in 0.2 ml PCR tubes or in an 8-strip PCR tube (Star Lab) on ice containing both forward (Fwd) and reverse (Rev) primers at a 10 µM working concentration, Phusion Flash High-Fidelity PCR Master Mix (Thermofisher Scientific), template plasmid DNA (100-200 ng) containing cDNA gene to be amplified and sterile water as shown in **Table 2.1**. The constituents were gently mixed by pipetting up and down.

Table 2.1: PCR reaction mixture for cDNA amplification

	Amount for one reaction
Phusion Flash Master Mix (2X)	25 µl
Forward primer (10 µM) **Reverse primer (10 µM)**	1.5 µl 1.5 µl
Template DNA plasmid	1 µl
Sterile water	21 µl
Total volume	50 µl

The PCR tubes were loaded into a Veriti^{TM} 96 well Thermal Cycler (Thermofisher Scientific) and the thermal cycles listed in **Table 2.2** were used.

Table 2.2: Parameters of thermal cycles used for PCR

Step	**Temperature**	**Time**	**Cycle**
Initial Denaturation	98ºC	10 seconds	1
Denaturation **Annealing** **Extension**	98ºC 60ºC 72ºC	1 second 5 seconds 15 sec/kbp	29
Final Extension	72ºC	2 minutes	1
Hold	4ºC	Hold	

2.2.2 Agarose gel electrophoresis of PCR products

Upon completion of the PCR reaction, 10 µl of filtered DNA loading buffer (0.25% w/v bromophenol in 30% v/v glycerol) was added to each PCR tube and mixed gently by pipetting up and down. A volume of 40 µl of the PCR-dye mix was then loaded into a pre-cast 1.0% agarose/ Tris-borate-EDTA (TBE) gel, commonly used

for DNA gel electrophoresis, containing SYBRSafe stain (Thermofisher) as listed in **Table 2.3**. Adjacent to the samples, 5 µl of Hyperladder^{TM} 1 kb (BioLine) was loaded and run in a 10 x 8 gel tank (MiniRapide) filled with TBE for 120 minutes at 70 Volts using a Power Pac 300 (Bio-Rad) power supply until the markers were separated sufficiently. After marker bands were separated, the gel was viewed with a blue light illuminator (Jencons-PLS) to both visualise and verify PCR bands at their respected correct base pair lengths.

Table 2.3: Composition of 1.0% TBE agarose gel

Composition	**Amount**
Agarose (Sigma-Aldrich)	0.5 g
TBE (1X) (Sigma-Aldrich)	50 ml
SYBRSafe (Thermofisher Scientific)	5 µl

2.2.3 DNA PCR product extraction from agarose and clean up

PCR DNA bands of correct base pair lengths were excised out of the agarose gel using a sterile surgical scalpel (Swann-Morton) whilst under blue light illumination and placed into a 1.5 ml microcentrifuge tube (Eppendorf). A microbalance (Mettler Toledo) was used to determine the weight of the excised band by blanking with an empty microcentrifuge tube. In order to purify the DNA, the agarose gel DNA extraction and PCR clean-up kit (Machinery-Nagel), contents of kit given in **Appendix A.1**, was used. For every 100 mg of agarose gel, 200 µl of NTI buffer was added to the tube and incubated at 50ºC on a heating block (Grant Instruments) for 15-20 minutes with regular mixing every 3 minutes using a vortex (Scientific Industries) until the agarose had completely dissolved. Following complete dissolution, a 700 µl aliquot was loaded into a NucleoSpin® Gel and PCR Clean-up column with a 2 ml collection tube and centrifuged for 30 seconds at 11, 000 x g in a microcentrifuge (Beckman Coulter). The flow-through was discarded from the

bottom of the collection tube. Any remaining sample was loaded and the centrifugation step was repeated. Next, 700 µl of NT3 buffer was added to the column, and the centrifugation step repeated with the removal of the flow-through after centrifugation. To completely remove any excess buffer the column was centrifuged for an additional 1 minute followed by incubation at 70ºC for 5 minutes. Finally, the column was placed into a new microcentrifuge tube and incubated with 12 µl of NE buffer (elution buffer) for 1 minute at room temperature before undergoing a final centrifugation. The eluted sample was either used immediately or stored at -20ºC until further use.

2.2.4 Cutting of pOPIN vectors using restriction digestion

Cut pOPIN vectors were generated by using appropriate restriction enzymes and buffers. The appropriate buffer (New England Biolabs) required for double digest using a combination of restriction enzymes (New England Biolabs) was selected by using the NEBcloner v1.3.4 tool (nebcloner.neb.com/#!/redigest). All pOPINE-3C-based vectors were cut using *PmeI* and *NcoI* restriction enzymes whilst the pOPINN based vector was cut using *Kpn1* and *HindIII*. The reaction components listed in **Table 2.4** were made in a 1.5 ml microcentrifuge tube.

Table 2.4: Double restriction enzyme digest of uncut vector

Components	**Amount for single reaction**
Uncut vector	10 µl
Restriction enzyme 1 **Restriction enzyme 2**	2.5 µl 2.5 µl
Enzyme buffer	1 µl
BSA	1 µl
Sterile water	83 µl
Total volume	100 µl

The mixture made from the list in **Table 2.4** was incubated for 1 hour on a heating block set at 37ºC. Following digestion, cut vector was purified using a NucleoSpin® Gel and PCR Clean-up column and the remaining PCR clean-up protocol from after sample loading in section **2.2.3** was followed**.** The cut-vector product was eluted in 50 µl of elution buffer (Qiagen) into a new clean 1.5 ml microcentrifuge tube. The eluted sample was either used immediately or stored at -20ºC for up 24 hours.

2.2.5 In-Fusion reaction with pOPIN vectors

Cloning of the PCR products with cut linearised pOPIN vectors were performed using a Quick-Fusion cloning kit (Biotool), contents of full kit given in **Appendix A.2**. For a two-way fusion cloning reaction involving one PCR DNA insert and vector, the composition in **Table 2.5** was made in PCR tubes and mixed gently by pipetting action. For a three-way fusion cloning reaction involving two PCR DNA inserts and vector, 2 µl of each insert with 2 µl of vector was added and the final volume adjusted to 10 µl with sterile water.

Table 2.5: In-Fusion reaction for a two-way fusion

Components	**Amount for one reaction**
Linearised vector (20-100 ng)	1 µl
PCR product insert (10-100 ng)	2 µl
Fusion enzyme	1 µl
5 x Fusion buffer	2 µl
Sterile water	4 µl
Total	10 µl

The in-fusion reaction was run for 30 minutes at a 37ºC step using a Veriti^{TM} 96 well Thermal Cycler. Immediately afterwards, the PCR tubes were placed on ice and the

reaction stopped with 40 µl of TE buffer (Invitrogen). Fused product was either used immediately for cell transformation or stored at -20ºC until further use.

2.2.6 Transformation using cloning-grade *Escherichia coli (E. coli)*

Pre-prepared 50 µl aliquots of competent Stellar™ (Takara) or One Shot™ OmniMAX™ (Invitogen) *E. coli* cells were thawed on ice for 15 minutes directly from -80ºC. A volume of 2-5 µl of plasmid DNA was pipetted into one aliquot tube of competent bacterial cells and mixed gently by pipetting action. Bacterial cells were left on ice for 30 minutes followed by heat-shock for 30 seconds at 42ºC by placing the tube into a tube holder in a water bath (Grant Instruments). Cells were returned to the ice and 400 µl of room-temperature S.O.C (Invitogen) medium was added per tube and mixed by pipetting action. Tubes were transferred to an incubator (Binder) set at 37ºC for 60 minutes if the antibiotic selection gene in the plasmid contained ampicillin or for 90 minutes if the plasmid contained kanamycin. Carbenicillin belongs to the penicillin family and therefore can be used as a substitute for ampicillin (Bird *et al.*, 2015). During the final 30 minutes of the incubation period, warm Luria Broth (LB) agar was supplemented with the mixture listed in **Table 2.6** into a new 50 ml falcon tube for newly in-fused plasmid inside a Class II biological safety cabinet (Nuaire) to prevent airborne contamination. For amplification of already validated plasmid, only antibiotic was added to LB agar. Details regarding making LB agar are given in the **Appendix A.3**.

Table 2.6: Making of Luria Broth (LB) Agar plates

Components	**Amount for one plate**
LB agar (warm)	25 ml
CB or Kan antibiotic	1:1000 dilution
20% X-gal in DMF (Sigma-Aldrich)	1:1000 dilution
IPTG (1 M) (Sigma-Aldrich)	1:1000 dilution

The warm LB agar mixture, prepared as **Table 2.6**, was gently mixed by inverting the closed falcon tube several times and its contents poured into a sterile 150 mm x 15 mm petri dish (Thermofisher Scientific) and left to set for 30 minutes inside the safety cabinet. After the mixture had set, coinciding with the completion of the incubation time of the transformed bacteria, 100 µl of the bacteria were plated by spreading the cells using a spreader (VWR) in a smooth continuous circular path from one concentrated starting point and allowed to dry for up to 15 minutes before turning over. Plated cells were incubated overnight at 37ºC in the incubator.

2.2.7 Colony selection and starting culture

For in-fused plasmid that has not been verified by sequencing, the formation of negative blue colonies (<10%) indicated re-circulation of linearised parental vector whilst formation of white colonies (>90%) indicated successful recombination of the DNA into the vector. Several single colonies were picked seperately using an inoculation loop and mixed directly into separate 50 ml falcon tubes containing the volume of LB listed in **Table 2.7** with a 1/1000 dilution of the appropriate antibiotic in a biological safety cabinet to reduce airborne contamination of cultures. For verified plasmid, only white colonies were formed and a single colony was picked. Tubes were left at 37ºC overnight in a shaker (Innova) set at 210-225 RPM. Details regarding making Luria Broth (LB) is described in **Appendix A.4.**

Table 2.7: Volume of LB used for each prep

Prep	**Starting culture volume per prep**
Miniprep	5-10 ml
Maxiprep	100-130 ml

2.2.8 Transformed bacterial glycerol stock preparation

Glycerol stocks of starting cultures were prepared by transferring 100 µl of culture into a microcentrifuge tube containing 100 µl of filter-sterilised LB-glycerol (30%) using a 0.2 µm pore size filter, see the **Appendix A.5**. The tubes were sealed with Parafilm M and stored at -80ºC for long term storage.

2.2.9 Miniprep of plasmid DNA

The QIAprep Spin Miniprep kit (contents given in **Appendix A.6**) was used to purify DNA from the small starting cultures. 2 ml of starting bacterial culture per purification was spun down in a 2 ml microcentrifuge tube (Eppedorf) at 6800 x g for 3 minutes at room temperature. The supernatant was discarded and the pellet was re-suspended in 250 µl of cold P1 buffer with added LyseBlue (1:1000) and RNase A solution (see **Appendix A.6**). A volume of 250 µl P2 buffer (lysis) was added and the tubes mixed several times by inversion until the solution turned blue. The bacteria were lysed for 5 minutes at room temperature and 350 µl of N3 buffer was immediately added to neutralise the lysis, followed by inversion of the tube several times until the solution turned colourless. The reacted tube was centrifuged for 10 minutes at 17,900 x g in a table-top microcentrifuge at room temperature. The supernatant (800 µl) was added to a QIAprep 2.0 spin column with a collection tube attached and centrifuged for 30 seconds. The flow-through was discarded and 500 µl of PB buffer was added to the column followed by another centrifugation and removal of the flow-through. The spin column was washed with 750 µl of PE buffer (with added ethanol) and centrifuged for 30 seconds. Following the removal of the flow-through, the column was centrifuged for a further 1 minute to remove any residual buffer. The column was placed in a new 1.5 microcentrifuge tube and incubated with 25 µl of EB buffer for 1 minute before a final minute centrifugation step to elute the DNA. The concentration of eluted DNA was determined using a NanoDrop™ 800 Spectrophotometer that provided DNA concentrations (ng/µl) as

well as purity of the DNA indicated by the 260/280 nm ratio. A ratio of 1.8 is the accepted value for a pure quality of DNA whilst lower values indicate impurities or contaminations such as remaining guanidine, phenol or other chemicals from the purification kit.

2.2.10 DNA plasmid construct verification by PCR screening

PCR reactions were setup in dedicated PCR tubes or in an 8-strip PCR tube (see section **2.2.1**) on ice with the following components where a working concentration of pOPIN forward primer or NeoRev2 reverse primer (see **Appendix A.7**) was used with the appropriate gene specific reverse primer, the in-fused DNA plasmid and Phusion Flash (**Table 2.8**). As the volume of primers required is small, a mastermix containing 10X the volume of primers and Phusion Flash was prepared and used to minimise any errors associated with pipetting smaller volumes.

Table 2.8: PCR reaction for screening in-fused clones

	For one reaction
Phusion Flash Master Mix (2X)	12.5 µl
Forward primer (10 µM) **Reverse primer (10 µM)**	0.1 µl 0.1 µl
Template DNA plasmid (100 ng)	1 µl
Sterile water	11.3 µl
Total volume	25 µl

DNA was amplified using the PCR procedure described in section **2.2.1** and the PCR products were separated using gel electrophoresis as described in section **2.2.2** with the modification of adding 5µl DNA loading dye to the sample and loading 5-30 µl of sample into agar wells. Following separation of PCR products, the agarose gels were imaged and captured using a Bio-Rad Chemidoc™MP Imaging

system (UV standard filters and 302 nm excitation) with 'auto' imaging parameters to select for the best exposure.

2.2.11 Construct verification using Sanger sequencing

The DNA inserts in plasmid clones were verified by Sanger sequencing. A volume of 5 µl at 100 ng/µl of plasmid DNA was prepared in sealed 1.5 microcentrifuge tubes and sent to Source Bioscience (UK) for sequencing. T7F primers, appropriate reverse primers at Source Bioscience (UK) or custom primers synthesised by Source Bioscience were used. Sequencing results were performed overnight and analysis was performed using SnapGene viewer 4.2.1. Sequences were manually aligned or ran through the BLAST: Basic Local Alignment Search Tool (NCBI) and matches between the insert with the original cDNA sequence was indicative of successful cloning or mismatches indicated possible mutagenesis.

2.2.12 Maxiprep of plasmid DNA

For larger yields of purified plasmid DNA (in the µg-mg range), the QIAGEN Plasmid *Plus* Maxi Kit was used (contents given in **Appendix A.8**). The starting culture was poured into a 500 ml centrifuge bottle (Corning®) and centrifuged at 6000 x g for 15 minutes at 4ºC using a centrifuge (Beckman Coulter) with a JS.5.3 rotor. The supernatant was discarded and the pellet of bacteria was re-suspended in 8 ml of P1 buffer (containing LyseBlue and RNAse A; see section **2.2.7**) by pipetting up and down with a 10 ml Stripette (Corning). An equal volume (8 ml) of P2 buffer was added and the lysate was mixed gently by inverting the tube 4-6 times until the lysate turned blue. Cells were lysed for 3 minutes and the solution was neutralised with 8 ml of S3 buffer by inverting the tube 3-4 times until the solution became colourless. The solution was then poured into a QIAfilter cartridge and incubated for 10 minutes at room temperature to allow density separation of the lysate from the cell debris. A plunger was inserted into the cartridge and pushed to filter the lysate into a new 50 ml falcon tube. BB buffer (5 ml) was added to the cleared lysate and

mixed by inverting the tube several times before loading the entire volume into a tube extender attached to a QIAGEN Plasmid *Plus* Spin column mounted onto a QIAvac 24 *Plus*, QIAvac connecting system and QIAGEN vacuum pump. Vacuum (-300 mbar) pressure was applied to draw the lysate through the column. ETR buffer (700 µl) was added and vacuum applied followed by 700 µl of PE (containing ethanol) solution. The column was placed into a 2 ml collection tube and centrifuged at 10,000 x g for 1 minute in a table-top microcentrifuge. The column was finally placed into a new 1.5 ml microcentrifuge tube and incubated with 400 µl of EB buffer (elution) for one minute before a final 1 minute centrifuge to elute the DNA. The concentration and quality of the DNA was determined as described in section **2.2.9**.

2.2.13 Generation of single amino acid mutations in plasmids

The QuikChange Lightening Site-Directed Mutagenesis Kit (Agilent), **see Appendix A.9** for contents of kit, was used to generate genetic mutations. The composition listed in **Table 2.9** was prepared in a PCR tube followed by the addition of 1 µl of QuikChange Lightning Enzyme (supplied with kit) and gentle mixing by pipetting action.

Table 2.9: QuikChange Site-Directed mutagenesis PCR reaction composition

	For one reaction
Reaction buffer (10x)	5 µl
Primers (10 µM)	1.5 µl of each (Fwd and Rev)
Template DNA plasmid (100 ng)	1 µl
dNTP mix	1 µl
QuikSolution reagent	1.5 µl
Sterile water	13.5 µl
Total volume	25 µl

The tube was then placed in a VeritiTM 96 well Thermal Cycle and the DNA amplified using the thermal cycle parameters listed in **Table 2.10**

Table 2.10: Thermal cycling parameters for QuickChange PCR reaction

Step	Temperature	Time	Cycle
Initial Denaturation	95ºC	2 minutes	1
Denaturation **Annealing** **Extension**	95ºC 60ºC 68ºC	20 second 10 seconds 30 sec/kbp	18
Final Extension	68ºC	5 minutes	1
Hold	4ºC	Hold	

Upon completion of the PCR reaction, *Dpn* I restriction enzyme (1 µl) was added directly into the PCR tube and incubated at 37°C for 5 minutes to digest any parental DNA. An aliquot (45 µl) of pre-prepared XL10-Gold ultracompetent cells (Agilent) in a microcentrifuge tube was thawed on ice straight from the -80°C freezer. Whilst still on ice, 2 µl of β-mercaptoethanol (β-ME) was added to increase transformation efficiency. The tube was mixed gently by tapping the tube and left to incubate on ice for 2 minutes. The DNA treated with *Dpn* I was then transformed into the XL10-Gold-β-ME treated cells and plated as described in section **2.2.6**. Single colonies were picked (section **2.2.7**) and mini-prep DNA purification performed (section **2.2.9**). Constructs were validated by Sanger sequencing (section **2.2.11**).

2.2.14 Cloning of EGFP-S6K1

The EGFP-S6K1 construct was made by in-fusing the full length S6K1 PCR product from the S6K1-GFPSpark plasmid into a cut pOPINN-EGFP vector (see full uncut vector map in **Appendix A.10.1**) using the primers in **Table 2.11**.

Table 2.11: Primers for EGFP-S6K1. Read from 5' → 3'

EGFP-S6K1 Fwd	AAGTTCTGTTTCAGGGCCCGAGGCGACGAAGGAGGCGGG
EGFP-S6K1 Rev	ATGGTCTAGAAAGCTTTA TAGATTCATACGCAGGTGCTCTG

The final in-fused construct is shown below in **Figure 2.1**.

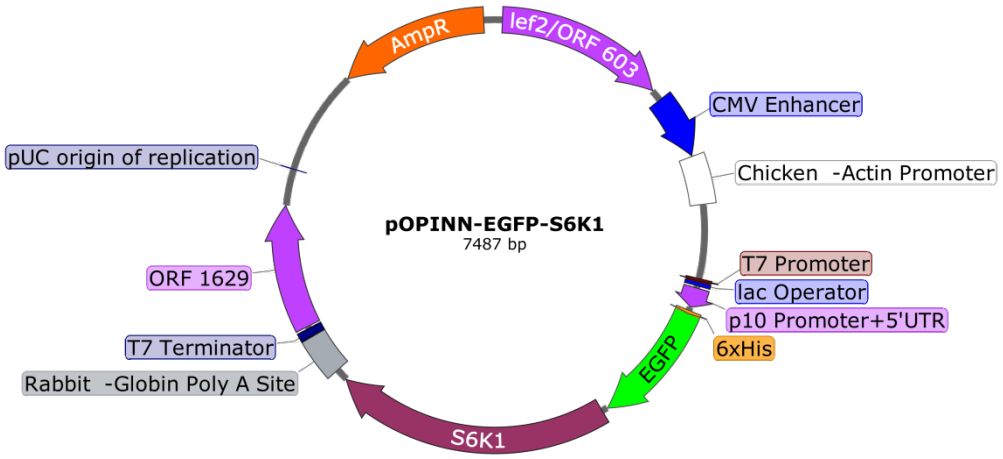

Figure 2.1: Plasmid map of EGFP-S6K1. Full vector map of S6K1 cloned into the pOPINN-EGFP vector. Map generated in SnapGene® (Version 3.2.1) software.

2.2.15 Cloning of S6K1-mCherry and S6K1-mTurquoise2

Both S6K1-mCherry and S6K1-mTurquoise2 constructs were made by in-fusing the full length S6K1 PCR product from the S6K1-GFPSpark plasmid into cut pOPINE-3C-mCherry or pOPINE-3C-mTurquoise2 vectors (see full uncut vector maps in **Appendix A.10.2 and A.10.3**) using the primers in **Table 2.12**. The vectors for both pOPINE-3C-mCherry and pOPINE-3C-mTurquoise2 originated from the pOPINE-3C-EGFP vector (Bird *et al.*, 2015), see **Appendix A.10.4** and thus contained same primer overhangs for cloning.

Table 2.12: PCR primers for S6K1-mCherry and S6K1-mTurq2. Read from 5' → 3'

S6K1-mCherry/ mTurq2 Fwd	AGGAGATATACCATGAGGCGACGAAGGAGGCGG
S6K1-mCherry/ mTurq2 Rev	CAGAACTTCCAGTTTTAGATTCATACGCAGGTGCTCTG

Final in-fused constructs are shown below in **Figure 2.2**.

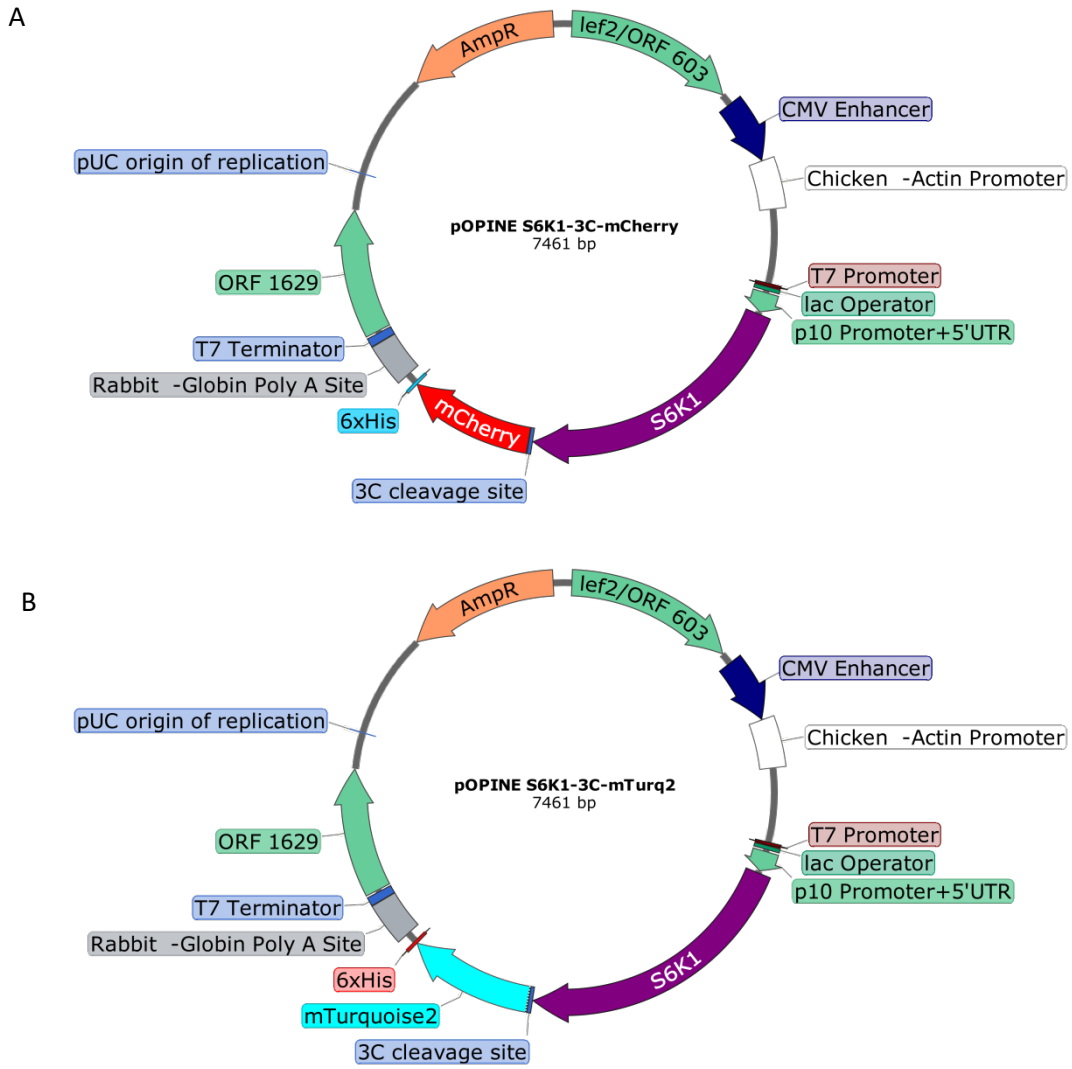

Figure 2.2: Plasmid maps of S6K1-mCherry and S6K1-mTurq2. A) Full vector map of S6K1 cloned into the pOPINE-3C-mCherry vector. B) Full vector map of S6K1 cloned into the pOPINE-3C-mTurq2 vector. Map generated in SnapGene® (Version 3.2.1) software.

2.2.16 Cloning of raptor-YFP

The raptor-YFP construct was made by in-fusing full length raptor PCR product from the mDsRed-raptor plasmid into cut pOPINE-3C-YFP vector (see full uncut vector maps in **Appendix A.10.5**) which also originated from the pOPINE-3C-EGFP vector using the primers in **Table 2.13**.

Table 2.13: PCR primers for raptor-YFP. Read from 5' → 3'

raptor-YFP Fwd	AGGAGATATACCATGGAGTCCGAAATGCTGCAATCG
raptor-YFP Rev	CAGAACTTCCAGTTTTCTGACACGCTTCTCCACCG

The final in-fused construct is shown below in **Figure 2.3**.

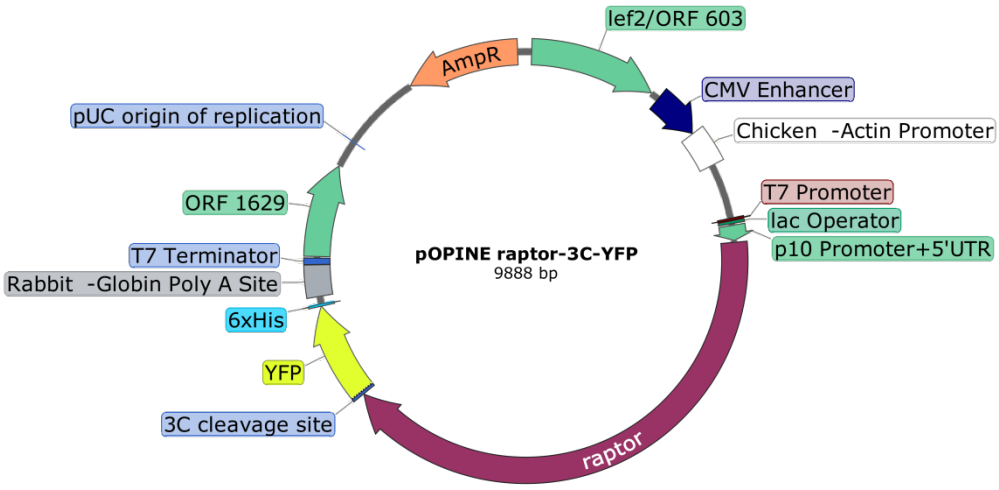

Figure 2.3: Plasmid map of raptor-YFP. Full vector map of raptor cloned into the pOPINE-3C-YFP vector. Map generated in SnapGene® (Version 3.2.1) software.

2.2.17 Cloning of mutant (ΔN) mTOR-mCherry

The truncated mTOR-mCherry construct was originally made by in-fusing the full length mTOR PCR product from the EGFP-mTOR plasmid into cut pOPINE-3C-mCherry vector using the primers in **Table 2.14.** Sequencing revealed that the full length mTOR sequence was not present but instead a truncated sequence of mTOR

was cloned into the vector. This could be most likely due to internal repeats or sequence similarity with primers from the mTOR sequence.

Table 2.14: PCR primers for truncated mTOR-mCherry. Read from 5' → 3'

ΔmTOR-mCherry Fwd	AGGAGATATACCATGCTTGGAACCGGACCTGCC
ΔmTOR -mCherry Rev	CAGAACTTCCAGTTTCCAGAAAGGGCACCAGCC

The final in-fused construct is shown below in **Figure 2.4**.

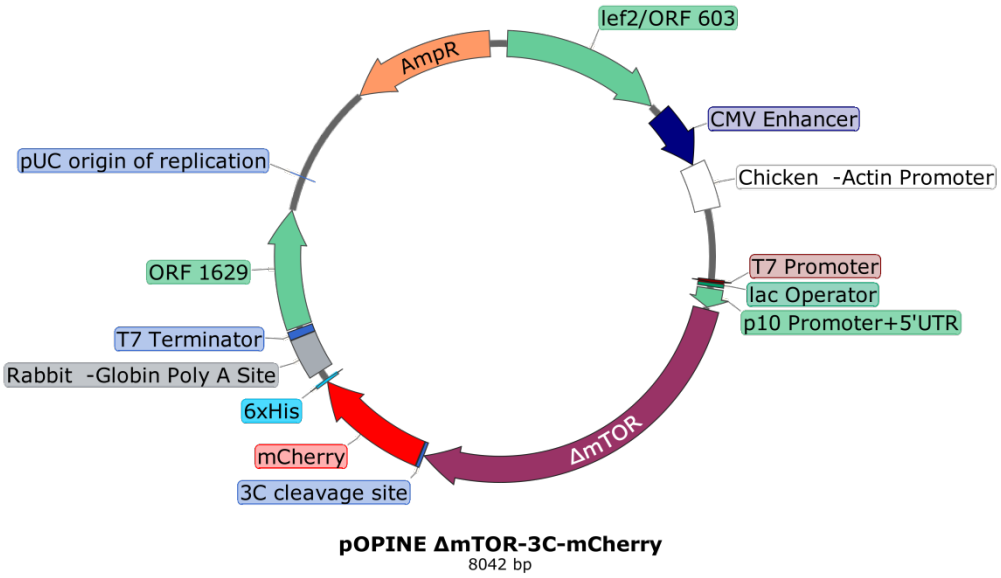

Figure 2.4: Plasmid map of ΔmTOR-mCherry. Full vector map of truncated mTOR cloned into the pOPINE-3C-mCherry vector. Map generated in SnapGene® (Version 3.2.1) software.

2.2.18 Cloning of mCherry-S6K1-EGFP (SensOR)

The mCherry-S6K1-EGFP FRET sensor construct was made by in-fusing the full length S6K1 PCR product from S6K1-GFPSpark and the mCherry PCR product from ΔmTOR-mCherry into cut pOPINE-3C-EGFP vector using the primers in **Table 2.15.**

Table 2.15: PCR primers for mCherry-S6K1-EGFP. Read from 5' → 3'

mCherry-S6K1 Fwd	GACGAGCTGTACAAGATGAGGCGACGAAGGAGGCG
mCherry-S6K1 Rev	CCTTCGTCGCCTCATCTTGTACAGCTCGTCCATGC
mCherry-S6K1-EGFP Fwd	AGGAGATATACCATGGCCATCATCAAGGAGTTCATG
mCherry-S6K1-EGFP Rev	CAGAACTTCCAGTTTTAGATTCATACGCAGGTGCTC

The final in-fused construct is shown below in **Figure 2.5**.

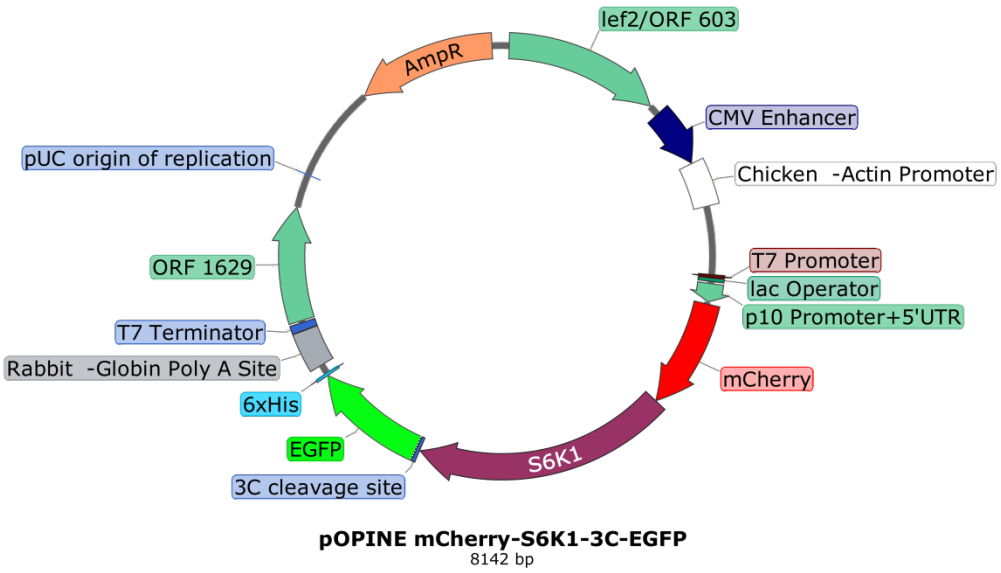

Figure 2.5: Plasmid map of mCherry-S6K1-EGFP. Full vector map of mCherry-S6K1 cloned into the pOPINE-3C-EGFP vector. Map generated in SnapGene® (Version 3.2.1) software.

2.2.19 Cloning of mCherry-S6K1-EGFP-2STREP

The mCherry-S6K1-EGFP FRET sensor construct with a STREP tag for purification was made by in-fusing the mCherry-S6K1 PCR product from mCherry-S6K1-EGFP and EGFP from EGFP-S6K1 into cut pOPINEneo-3C-2STREPStop vector (see full uncut vector maps in **Appendix A.10.6**) using the primers in **Table 2.16.**

Table 2.16: PCR primers for mCherry-S6K1-EGFP-2STREP. Read from 5' → 3'

mCherry-S6K1 Fwd	AGGAGATATACCATGGCCATCATCAAGGAGTTCATG
mCherry-S6K1 Rev	CACTAGATTCATACGCAGGTGCTCTGGCCGTTTGGAG
mCherry-S6K1-GFP Fwd	CGTATGAATCTAGTGAGCAAGGGCGAGGAGCTGTTCACCGGG
mCherry-S6K1-GFP Rev	CAGAACTTCCAGTTTCTTGTACAGCTCGTCCATGCCGA

The final in-fused construct is shown below in **Figure 2.6**.

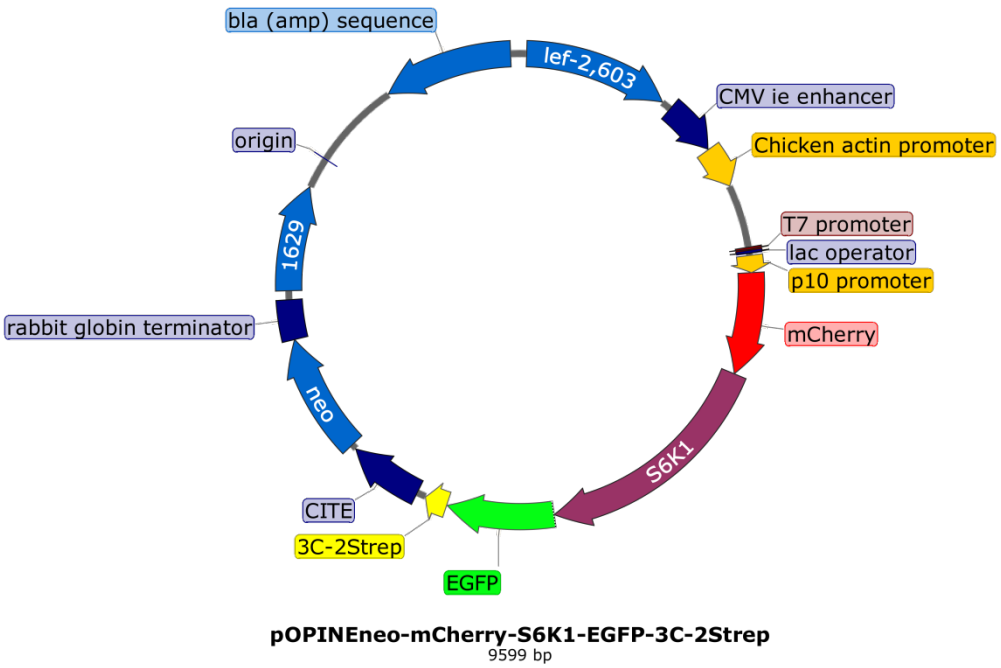

Figure 2.6: Plasmid map of mCherry-S6K1-EGFP-2Strep. Full plasmid map of mCherry-S6K1 and EGFP cloned into the pOPINEneo-3C-2STREPStop vector. Map generated in SnapGene® (Version 3.2.1) software.

2.2.20 Generation of EGFP-F29A S6K1 mutant

The TOS motif of S6K1 was mutated by altering the phenylalanine position at 29 to alanine in the EGFP-S6K1 construct using the primers in **Table 2.17**.

Table 2.17: PCR primers for EGFP-F29A S6K1. Read from 5' → 3'

EGFP-F28A-S6K1 Fwd	AGGACATGGCAGGAGTGGCTGACATAGACCTGGACC
EGFP-F28A-S6K1 Rev	GGTCCAGGTCTATGTCAGCCACTCCTGCCATGTCCT

2.2.21 Generation of EGFP- S6K1 T389A mutant

The phosphorylated motif of S6K1 was mutated by altering the threonine position at 389 to alanine in the EGFP-S6K1 construct using the primers in **Table 2.18**.

Table 2.18: PCR primers for EGFP-F29A S6K1. Read from 5' → 3'

EGFP-S6K1 T389A Fwd	CAGGTCTTTCTGGGTTTTGCATATGTGGCTCCATCTG
EGFP-S6K1 T389A Rev	CAGATGGAGCCACATATGCAAAACCCAGAAAGACCTG

2.2.22 Cloning of raptor-His (EV5831)

All constructs were designed, codon optimised for insect expression, cloned and sequence-verified by GenScript. The raptor cDNA was cloned into the pBAC4x-1 vector (**Appendix A.10.7**) from the mCherry-raptor plasmid. The addition of the His epitope tag was added to the C-terminus of raptor to prevent any protein-protein disruption or tag interference during pull-down. The final vector map of the construct is shown in **Figure 2.7.**

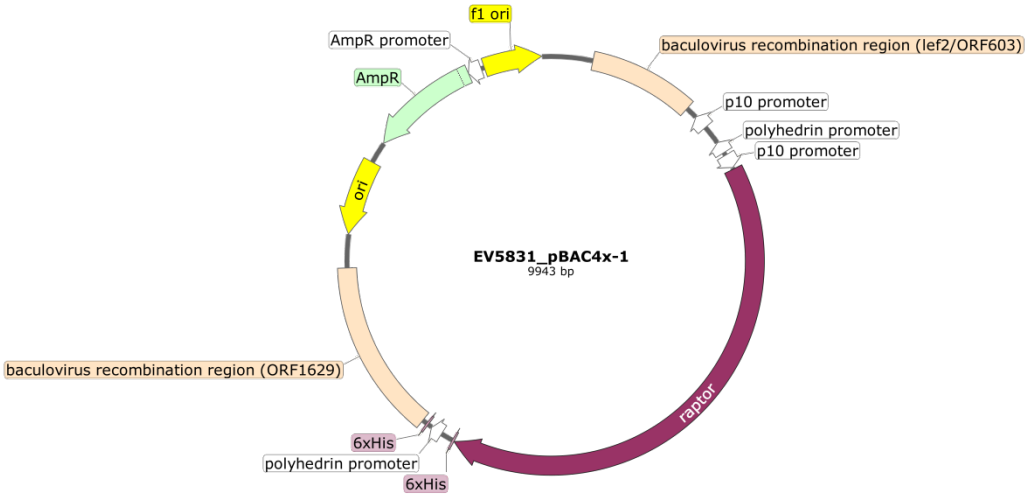

Figure 2.7: Plasmid map of raptor-His (EV5831). Full vector map of raptor-His cloned into the pBAC4x-1 vector. Map generated in SnapGene® (Version 3.2.1) software.

2.2.23 Cloning of S6K1-FLAG and raptor-His (EV5832_EV5831)

The raptor-His from section **2.2.22** was cloned with full length S6K1 from S6K1-GFPSpark with the addition of a FLAG epitope tag to S6K1 into the pBAC4x-1 vector. The final vector map of the construct is shown in **Figure 2.8**.

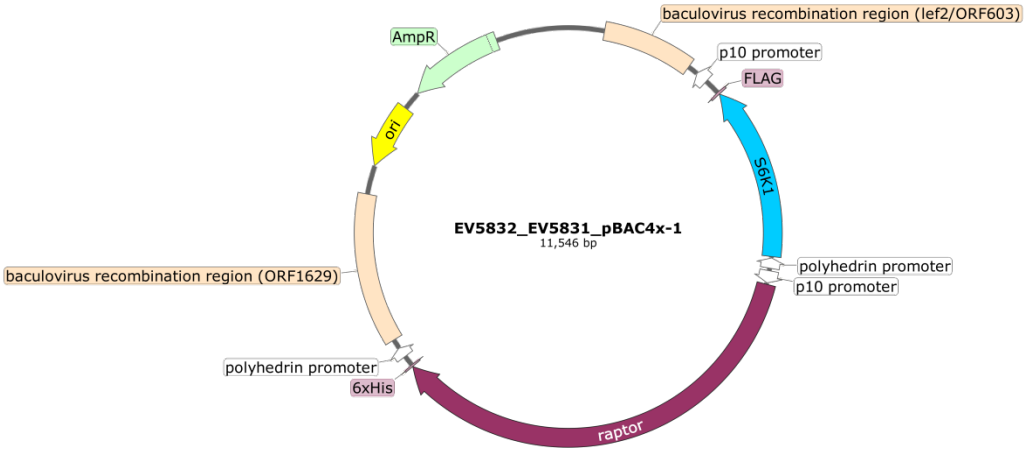

Figure 2.8: Plasmid map of S6K1-FLAG (EV5832) and raptor-His (EV5831). *Full vector map of S6K1-FLAG and raptor-His cloned into the pBAC4x-1 vector. Map generated in SnapGene® (Version 3.2.1) software.*

2.2.24 Cloning of FLAG-S6K1 and raptor-His (EV5830_EV5831)

A variant construct of S6K1-FLAG and raptor-His (EV5832_EV5831) (section **2.2.23**) was made by tagging the N-terminus gene of S6K1 with the FLAG epitope.

This was designed in mind for testing the best purification conditions. The final vector map of the construct is shown in **Figure 2.9.**

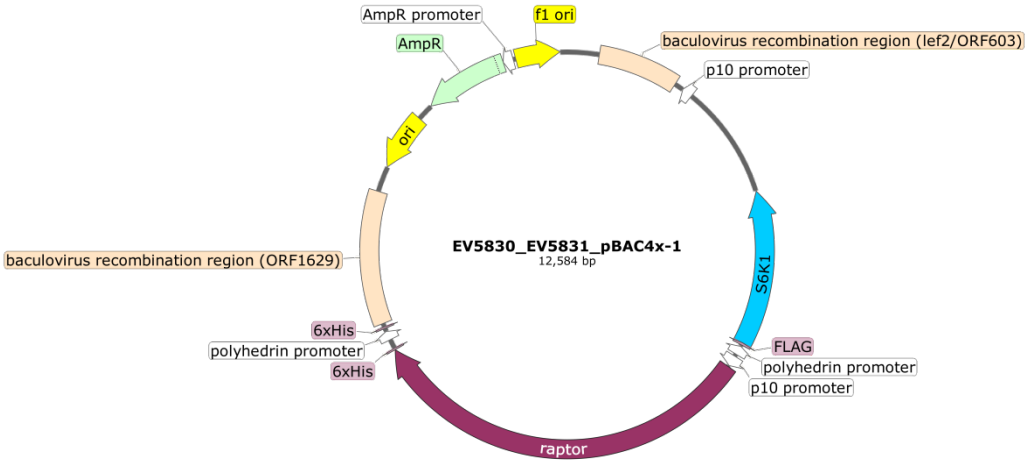

Figure 2.9: Plasmid map of FLAG-S6K1 (EV5830) and raptor-His (EV5831). Full plasmid map of FLAG-S6K1 and raptor-His cloned into the pBAC4x-1 vector. Map generated in SnapGene® (Version 3.2.1) software.

2.2.25 Cloning of TOS-ΔS6K1-FLAG and raptor-His (EV5834_EV5831)

A truncated form of S6K1 (Wang *et al.*, 2013) with the addition of a FLAG motif to the C-terminus was cloned into a pBAC4x-1 vector with raptor-His. A TOS motif was purposely engineered onto the N-terminus of the truncated S6K1 to allow binding onto mTORC1 through raptor binding. The final vector map of the construct is shown in **Figure 2.10**.

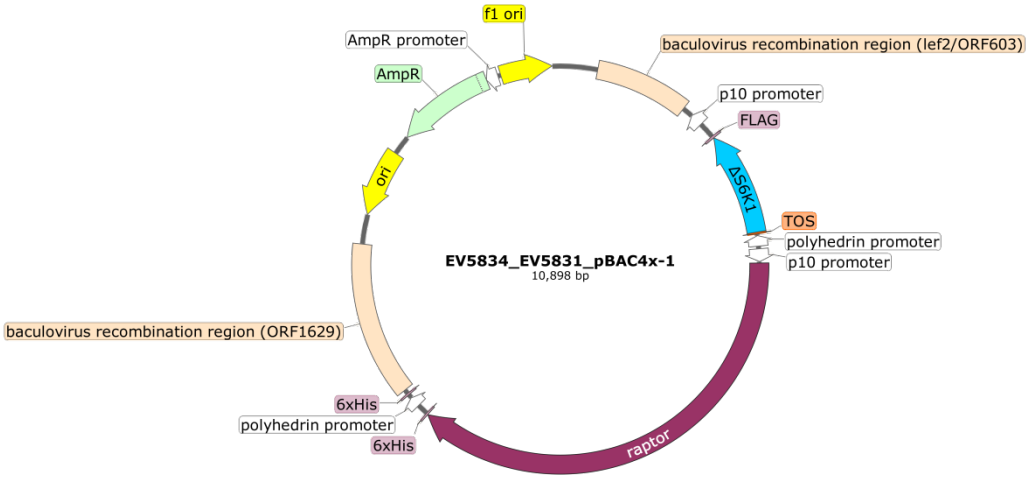

Figure 2.10: Plasmid map of TOS-ΔS6K1-FLAG (EV5834) and raptor-His (EV5831). Full vector map of TOS-ΔS6K1-FLAG and raptor-His cloned into the pBAC4x-1 vector. Map generated in SnapGene® (Version 3.2.1) software.

2.2.26 Cloning of mTOR-myc and mLST8 (EV5827_EV5828)

Full length mTOR was cloned into the pBAC4x-1 vector from FLAG-mTOR(wt) with a myc purification tag. The mLST8 gene (see **Appendix A11**) was optimised and cloned into the vector for maintaining the stability of the complex (Yang *et al.*, 2013) without a purification tag. The final vector map of the construct is shown in **Figure 2.11**.

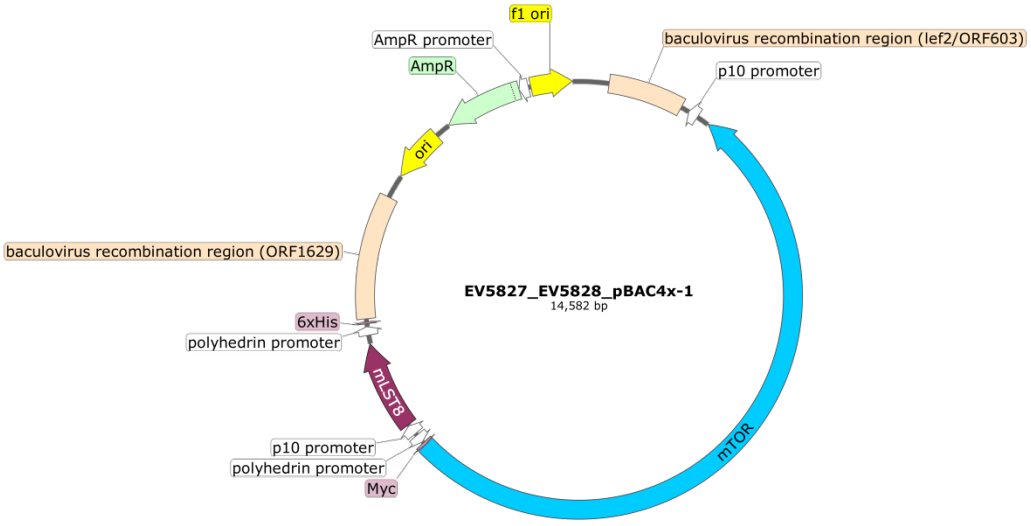

Figure 2.11: Plasmid map of mTOR (EV5827) and mLST8 (EV5828). *Full vector map of myc-mTOR and untagged mLST8 were cloned into the pBAC4x-1 vector. Map generated in SnapGene® (Version 3.2.1) software.*

2.2.27 Cloning of N-truncated mTOR-myc and mLST8 (EV5833_EV5828)

A variant construct of that prepared in section **2.2.26,** known to express and purify more efficiently than the full length mTOR construct, was made with a truncated N-terminus of mTOR (Yang *et al.*, 2013) tagged with a myc tag. The final vector map of the construct is shown in **Figure 2.12**.

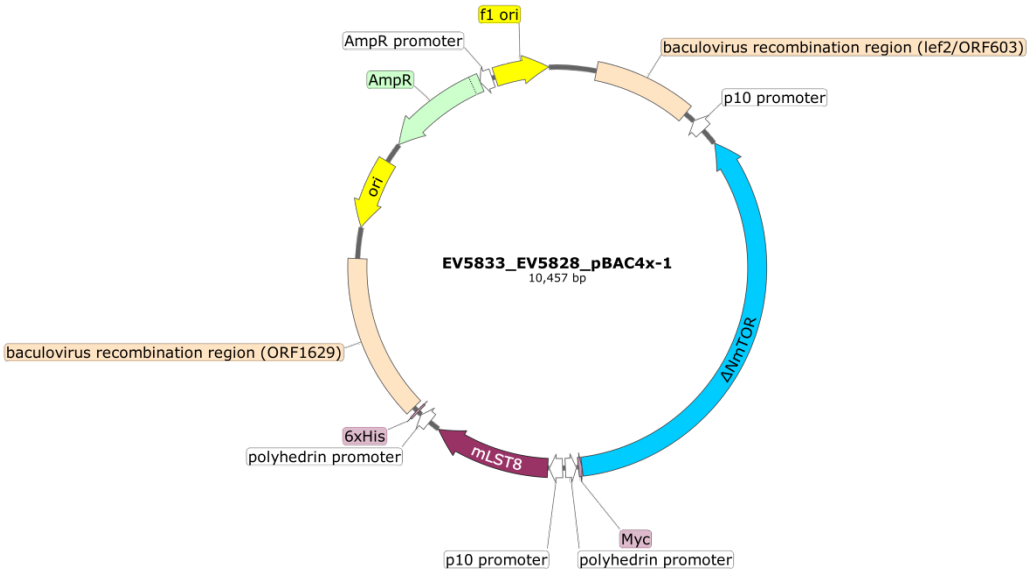

Figure 2.12: Plasmid map of N-terminus truncated mTOR (EV5833) and mLST8 (EV5828). *Full vector map of myc-ΔNmTOR and untagged mLST8 cloned into the pBAC4x-1 vector. Map generated in SnapGene® (Version 3.2.1) software.*

2.2.28 Cloning of mTOR-myc, S6K1-FLAG and mLST8 (EV5827_ EV5832_EV5828)

Another variant construct of mTOR-myc and mLST8 (EV5827_EV5828) (section **2.2.26**) was made with the addition of S6K1 with its FLAG tag from section **2.2.23**. The final vector map of the construct is shown in **Figure 2.13**.

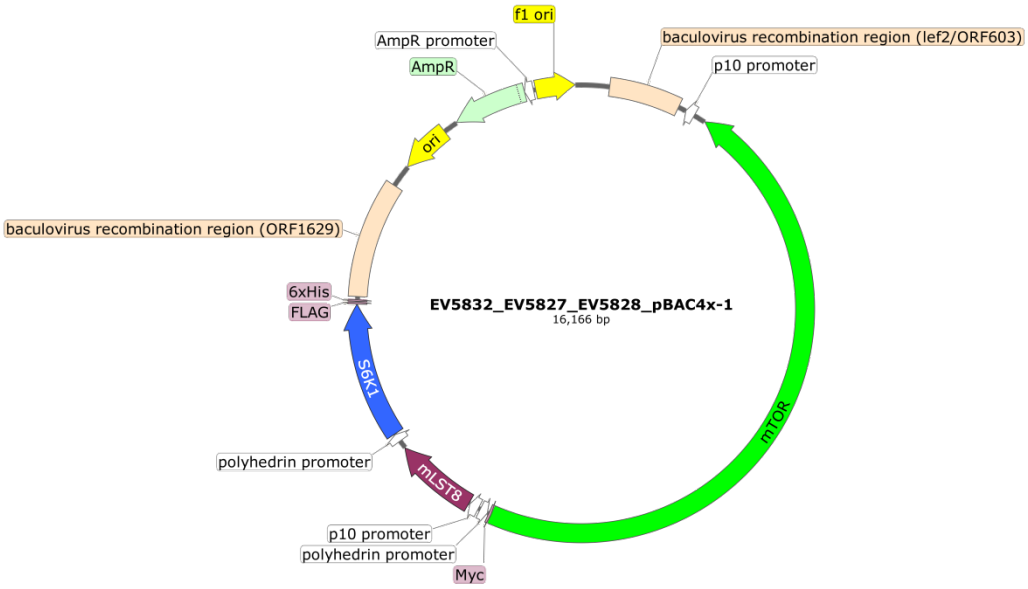

Figure 2.13: Plasmid map of S6K1 (EV5832), mTOR (EV5827) mLST8 (EV5828). *Full vector map of S6K1-FLAG, myc-mTOR and untagged mLST8 into the pBAC4x-1 vector. Map generated in SnapGene® (Version 3.2.1) software.*

2.2.29 Cloning of mTOR-myc, S6K1-FLAG, raptor-His and mLST8 (EV5827_ EV5832_EV5831_EV5828)

A final variant combining the genes from the plasmids constructed in sections **2.2.26** and **2.2.23** together was also made. This “mega-construct” was designed in order to help purify an intact mTOR complex with all the proteins of interest complexed together from one expression and one-step purification. The final vector map of the construct is shown in **Figure 2.14**.

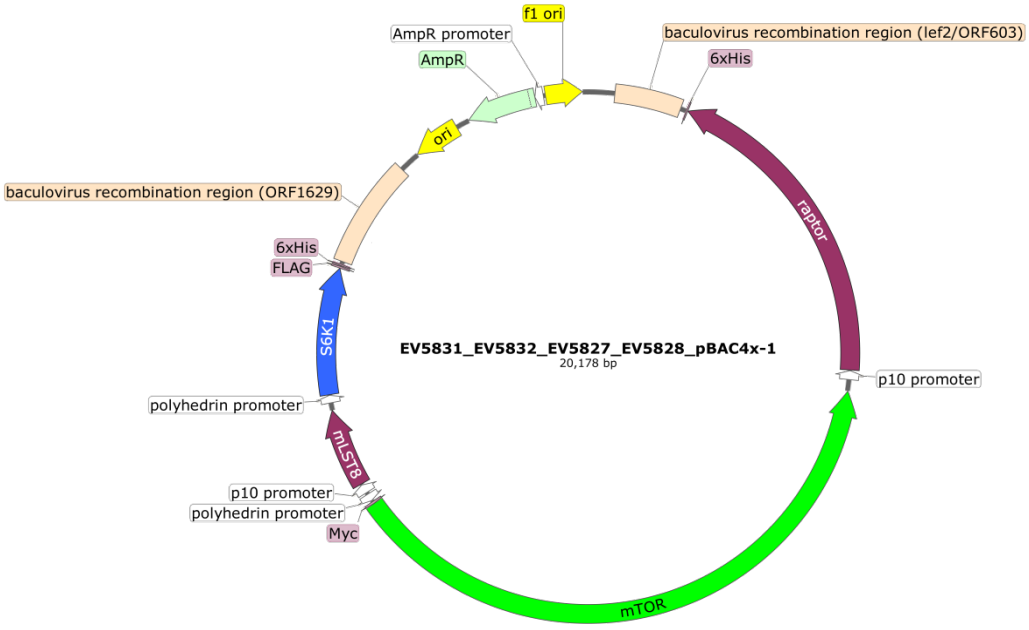

Figure 2.14: Plasmid map of raptor (EV5831), S6K1 (EV5832), mTOR (EV5827) mLST8 (EV5828). *Full plasmid map of raptor-His, S6K1-FLAG, myc-mTOR and untagged mLST8 cloned into the pBAC4x-1 vector. Map generated in SnapGene® (Version 3.2.1) software.*

2.2.30 Mammalian cell culture

HEK293 and HeLa cells were cultured in Minimum Essential Media (MEM) supplemented with 10% Foetal Bovine Serum (FBS), 2 mM L-glutamine (L-glut) and 1% Penicillin-Streptomycin (Pen-Strep) for HEK293. FreeStyle 293 (HEK293F) cells were grown in serum-free media (Gibco/Life Technologies, UK). MCF-7, A431 and U2OS cells were cultured in DMEM supplemented with 10% FBS, L-glut and Pen-Strep. Cells were incubated at 37°C with 5% CO_2 humidified air in T25 or T75 culture flasks (ThermoFisher Scientific) or in 50 mL tubes (Corning®).

Cells were passaged three times a week once confluency had reached ~80% exponential growth. Adherent cells were washed once with 10 ml of PBS (1X) after the removal of media using sterile Stripettes (Corning®). The PBS wash was removed and 2 ml of trypsin-EDTA (1X) added to cover the entire monolayer. Cells were placed inside an incubator at 37°C for 3-5 minutes to allow the cells to detach. Following the incubation period, 8 ml of pre-warmed growth medium was added to minimise the trypsin effect and cells were re-suspended several times by pipette

action. Cells were counted directly from the flask by taking a 10 µl sample of cell suspension and diluting it with an equal volume of trypan blue (Bio-Rad). A final volume of 10 µl of the mixture was then loaded into a chamber of a counting slide (Bio-Rad) and cells were counted using a TC20 automated cell counter (Cell counter) for seeding or the stock suspension was diluted 1:20 with the remaining volume made up with pre-warmed growth medium in a new sterile flask. The flask was swirled gently from side to side and incubated at 37°C with 5% CO_2 humidified air.

For suspension cells, flasks were swirled gently to re-suspend any settled cells from keeping the flasks stationary. Cells were directly split (1:20) and seeded after counting as described above using a Countess Automated Cell Counter (Thermofisher Scientific) into a new sterile tube with pre-warmed growth medium. Tubes containing cell and growth medium were incubated at 37°C with 5% CO_2 humidified air at 110 RPM on an orbital shaker placed inside the incubator.

2.2.31 Long-term mammalian cell storage

All cell lines were passaged as described in section **2.2.30** following centrifugation in a 50 ml falcon tube at 1200 RPM. The supernatant was removed and the cell pellet re-suspended in 10 ml freezing media (complete growth media containing 10% dimethyl sulfoxide (DMSO). Aliquots (1 ml) of cells diluted to (1 x 10^6 cell/ml in the freezing media) were pipetted into sterile cryotubes (VWR). Tubes were placed in a CoolCell (BioCision) cooling container and placed at -80°C overnight before transfer into liquid nitrogen for long-term storage.

2.2.32 Trypan blue exclusion test of cell viability

To accurately determine the cell viability of mammalian cells during passaging or insect cells during infection (see section **2.2.31** onwards) or the effect of varying concentrations of AZD2014 on trypsinised HEK293 cells, 10 µl of cells were mixed

with 10 µl of trypan blue (Bio-Rad). A final 10 µl of the mixture was then loaded into counting slide chamber and number of live cells determined by a TC20 (Bio-Rad) or Countess II (Thermofisher Scientific) automated cell counter.

2.2.33 Insect cell culture

Sf9 cells were cultured in Sf 900 III media supplemented with 1% Pen-Strep. Sf21 cells were cultured in Sf 900 II or III media supplemented with gentamicin (5 µg/ mL). Cells were incubated in Erlenmeyer shake flasks (Corning®) or 24-deep well blocks (Qiagen) at 27°C.

Stock Sf9/Sf21 cells were counted as described in section **2.2.30** using a Countess Automated Cell Counter (Thermofisher Scientific) and cell viability determined (see section **2.2.32**). Cells were sub-cultured into Erlenmeyer shake flasks with pre-warmed growth media or seeded in 6-well plates (Thermofisher Scientific). Cells were often sub-cultured at 5 or 6 x 10^5 cells/ml every 2-3 days and incubated at 27°C with shaking at 120 RPM.

2.2.34 Long-term storage of insect and baculovirus infected insect cells (BIICs)

Insect cells were centrifuged in 50 ml falcon tubes at 12,000 x g for 12 minutes and the supernatant removed. Cells were counted as described in sections **2.2.30** and **2.2.32**. They were then re-suspended to a density of 2 x 10^7 cells/mL in freezing mix (Sf900-II SFM containing 5 µg/mL gentamicin + 10% heat inactivated FBS + 10% DMSO) and aliquoted in 1 mL volumes into cryovials (Nalgene # 5001-0020). The vials were then frozen at -80°C (Mr Frosty) or frozen slowly from 4°C to -20°C before being placed at -80°C for 24 hours and transferred to liquid nitrogen. P1 and P2 liquid virus was stored in the dark at 4°C.

Baculovirus infected insect cells (BIICs) were made as described above with a 2 x 10^7 cells/ml concentration. Volume of freezing media required was calculated by **Equation 2.1**:

$$V_1 = \frac{C_1 \times V_2}{20} \qquad (2.1)$$

where the volume (V_1) of freezing medium (ml) used is related to the concentration (C_1) of the cells (cells/ml), final volume of culture (V_2) and a correction factor of 20, to factor in a final titre concentration of the virus as 2 x 10^9 cells/ml.

2.2.35 Thawing mammalian and insect cell /BIICs

Cryovials containing mammalian cells were returned from low temperature storage in liquid nitrogen and placed into a CoolCell. Cryovials were then placed into a vial holder in a 37°C water bath (Ultrawave) for 1-2 minutes before being cultured inside a flask with pre-warmed growth medium.

Cryovials containing insect cells and frozen BIICs were placed in a Mr. Frosty container and thawed in a plastic vessel containing warm (27°C) water for 2-3 minutes with gently swirling of the tube before use for culture or infection.

2.2.36 Growing mammalian spheroids

HEK293 cells were passaged and seeded as described in section **2.2.30** into a 96-U-well bottom plate at a cell density of 10,000 cells per well with a final volume of 100 µl in complete growth media. Each well was pre-cast with 100 µl of autoclaved 1.5% low melting point agarose (Sigma-Aldrich) in water prior to seeding. 200 µl of PBS (1X) was added to the outer wells of the 96-well plate to maintain humidity due to evaporation losses from inner wells. The plate was incubated at 37°C with 5% CO_2 humidified air for 3-4 days until spheroids were formed in suspension above the agar layer.

2.2.37 Mammalian cell transfection using plasmid DNA

HEK293 cells were transfected after 24 hours following cell seeding at a density of 1 x 10^5 or 1.5 x 10^5 cells/ml on uncoated 35 mm number 1.5 glass bottom dishes (MatTek, U.S.A.) or seeded and transfected straightway in shake flasks. For adherent HEK293 cells transfected with FuGENE HD (Promega, UK), the composition in **Table 2.19** was prepared in a sterile 1.5 ml microcentrifuge tube. For co-transfections, the amount of FuGENE and the final volume remained the same but two quantities of DNA were added, one for each plasmid.

Table 2.19: Composition of DNA-FuGENE transfection complex

Components	**Amount per transfection**
DNA plasmid	500 ng
FuGENE HD	6 µl
Opti-MEM	Final volume made to 100µl

20 ml of HEK293F cells in 50 ml falcon tubes were transfected with polyethylenimine (PEI) Max (Polysciences). The DNA: PEI MAX ratio of 1:3 was used where 1 µg of sterile DNA plasmid and 3 µg of PEI Max (1 mg/ml) were used per ml of suspension cells. DNA was mixed with 300 µl of Opti-PRO (serum free medium) by pipette action in a sterile 1.5 ml microcentrifuge tube. The mixture of PEI MAX and 300 µl of Opti-PRO was also prepared in an additional tube. The contents of one tube was pipetted into the other, mixed by gentle re-pipetting, and incubated at room temperature for 15 minutes. Following the incubation period, the DNA-transfection mixture was added to cells drop-wise. Sodium butyrate (10 mM) added 24 hrs later.

2.2.38 Insect cell baculovirus-plasmid preparation infection

The baculovirus system was used to infect insect cells using the flashBAC GOLD bacmid (Oxford Expression Technologies) or using a combined bacmid consisting of

the *Autographa californica* nucleopolyhedrovirus (AcMNPV) genome with deletions of the ORF 1629, baculovirus chitinase (chiA) protease, cathepsin (v-cath) protease genes and insertion of the DsRed marker for verifying protein expression (Berrow *et al.*, 2007; Osz-Papai *et al.*, 2015). 1 ml of antibiotic-free insect cell medium was aliquoted into a sterile 7 ml bijou tube (Medfor) and 100 ng per reaction of linearised flashBAC GOLD bacmid (stock 20 ng/ µl) or AcMNPV-DsRed bacmid was added to the medium with gentle mixing by pipette action. 500 ng of sterile plasmid DNA with 10 µl of Cellfectin II Reagent or FuGENE HD (Promega) with the bacmid was added. The transfection mixture was left to incubate at room temperature for 30-35 minutes. Media from insect cells following 24 hours of seeding in 6-well plates was removed and recombinant baculovirus mixture added drop-wise to generate recombinant baculovirus P0 stock. Plates were incubated for 6-7 days at 27°C with the addition of 1ml of antibiotic-free insect cell medium after the first 24 hours of incubation. Control (GFP plasmid) was also used for expression to determine the success of the transfection process.

The P0 stock was amplified to make P1 stock by pipetting 300 µl of the supernatant media containing the recombinant baculovirus from a 6-well plate into a 125 ml shaker flask (Thermofisher Scientific) containing a 30 ml volume of cells at 1.3 x 10^6 and medium supplemented with antibiotic. Flasks were incubated at 27°C on a shaker (Infors HT) for 72 hours. Expression was determined by fluorescence or by cell size where successful infection resulted in an increase in cell size (typically by 3 or more microns). P1 stock was harvested and frozen as described in section **2.2.34**.

P2 BIICs were amplified from P1 BIICs. 250 ml shaker flasks containing a final volume of 100 ml of Sf21 cells at ~1.3 x 10^6 cell density were infected at MOI 0.1 in antibiotic-medium using **Equation 2.2**. The infected shake cultures were incubated for 72 hours at 27°C on an orbital shaker at 110 rpm and cells were then observed

under an inverted microscope and compared to a non-infected control culture using a Cell Countess to confirm infection. P2-BIICs were harvested and frozen as described in section **2.2.34**. The volume of BIICs depended on the multiplicity of infection (MOI), the average number of virus particles that can infect an individual insect cell. The MOI used for P2 was 0.2.

$$V_1 = \frac{C_1 \times V_2 \times M}{T_1} \qquad \textbf{(2.2)}$$

where the volume (V_1) of BIICs (ml) used is related to the concentration (C_1) of the cells (cells/ml), final volume (V_2), MOI (M) and the titre concentration (T_1) of frozen BIICs

P2 BIICs (calculated from **Equation 2.2**) were used for "scouting" best protein expression conditions in Sf21 cells by pipetting BIICs into 3 ml wells of a 24-deep well block at 0.2, 1 and 5 MOI test conditions. The block was centrifuged at 2000 RPM for 10 minutes, the supernatant decanted and the pellets stored at -20°C. Insect cells (passage 5-30) were prepared from cultures in logarithmic phase growth and >98% viable. Cells were seeded into 2.5 L of SF900II medium (containing 5µg/ml Gentimicin) in 5L Thomson flasks at 0.65 x 10^6 cells/mL and allowed to grow overnight on orbital shaker (110 RPM, 27°C). The overnight cultures were counted and then infected at MOI-5 with P2 BIICs. Following 53 hours of expression (Sf21) or 73 hours of expression (Sf9), cell suspension was divided into 500 ml tubes (Corning) and centrifuged at 6,000 g for 15 minutes at 4°C. The supernatant was removed and the pellets were pooled into a single tube by swirling one pellet with 100 ml of supernatant and transferring it into the next pellet with further swirling until all the pellets were collected for Sf21 cells. The combined pellet was transferred into a 500 ml tube and centrifuged again at 6,000 g for 15 minutes 4°C. The supernatant was discarded and the final pellet was stored at -80°C.

2.2.39 SensOR purification from insect cells

Expression test and protein production in insect (Sf9) for large scale production was performed as described in (Nettleship *et al.*, 2010). Following 72 hours of infection to obtain 90% infection rate, 2.5 litres of Sf9 cells were aliquoted into 6 x 500 ml centrifuge tubes and harvested by centrifugation for 15 minutes at 6000 x g and 4°C. Cell pellets were frozen at -80°C prior to cell lysis. Pellet were lysed in 50 ml of lysis buffer (containing 50 mM HEPES, 150 mM NaCl, 3 mM DTT, 0.1% (w/v) CHAPS, protease inhibitors cocktail and 25 U/ml benzonase) either by passing the lysate through a syringe needle or by sonication, followed by centrifugation (13,000 g, 30 minutes, 4°C). The supernatant was filtered using a Nalgene® vacuum filtration system capacity 500 mL, with a pore size of 0.2 µm prior to affinity purification using a StrepTrap column (GE Healthcare). Protein was eluted in 2.5 mM desthiobiotin (Sigma-Aldrich) followed immediately by gel filtration using a Superdex 200 10/300 (GE Healthcare) on the ÄKTA Express system using manufacturer standard protocols (GE Healthcare). Purified protein stability was tested after 48 hrs and 72 hours for degradation. The protein was aliquoted, flash-freezed in liquid nitrogen and stored at -80°C. Purified protein was loaded into gels for western blotting as described in section **2.2.43** or for in-gel fluorescence by not boiling the samples and imaged directly using the ChemiDoc imager with epi-illumination, 530/28 (green) and 605/50 (red) filters.

2.2.40 mTORC1 purification from insect cells

Following 72 hours or 53 hours infection of SF21 cells, cell pellets were harvested as described in section **2.2.38** from 3 ml, 45 ml or a 5 litre expression. Cell pellets were lysed in 1ml (small scale or ‘scouting’) or 300 ml (large scale) of filtered lysis buffer (50 mM HEPES (pH 7.4), 150 mM NaCl, 3 mM DTT, protease inhibitor, 10 U/ml benzonase). Lysates were either sonicated as described later in section **2.2.43** or were passed through a microfluidizer twice and the lysate was then poured into

50 ml centrifuge tubes and spun at 45,000 x g for 45 minutes at 4°C (Beckman ultracentrifuge). Supernatant was loaded and protein purified using a HisTrap (1 ml) HP column (GE Healthcare) overnight and eluted in 25 ml of elution buffer (50 mM HEPES (pH 7.4), 150 mM NaCl, 3 mM DTT, 500 mM imidazole) with gradient elution collected in 1.5 ml fractions in a 96-well plate. Elution fractions (positions C9-D10 of plate) were concentrated in a 50 K concentrator (Millipore) to a final volume of 5 ml by centrifugation at 4°C and 4000 RPM for 15-20 minutes. Sample was injected using a syringe into a Size-Exclusion Chromatography (SEC) Superdex 200 pg column (GE Healthcare) performed on the ÄKTA Purifier system overnight using standard manufacture protocol. The column was equilibrated with SEC buffer (25 mM HEPES (pH 7.5), 200 mM NaCl, 1 mM TCEP, 10% glycerol) and fractions were collected in a 96-well plate. Eluted samples from SEC were then concentrated on nickel resin tips using the Phynexus (see section **2.2.44**) and eluted 3 x 150 µl. Wash and elution buffer used were the same as that used in the HisTrap purification above. All samples were run on gels for western blotting or comassie staining.

2.2.41 Cell fixation

Following 48 hours transfection and mock transfection, growth medium from HEK293 cells was removed and either 1 ml of 4% paraformaldehyde (Electron Microscopy Sciences) was added and placed on a rocker (Stuart) for 15 minutes, or 1 ml of glyoxal mixture (Richter *et al.*, 2017) (see **Table 2.20**) was added for 15 minutes, or 1 ml of ice-cold methanol (Sigma-Aldrich) was added with a 20 minute incubation at -20°C. Dishes were washed three times for 5 minutes in cold PBS (1X) by placing on a rocker with removal of PBS after each wash.

Table 2.20: Glyoxal fixative composition

Components	Amount for 4 ml solution
Ethanol (Sigma-Aldrich)	0.789 ml
Glyoxal 40% (Sigma-Aldrich)	0.313 ml
Acetic acid (Sigma-Aldrich	0.03 ml
Sterile water	2.835 ml

2.2.42 Immunofluorescence labelling of fixed cells

Following fixation, cells were permeabilised with 0.3% Triton X-100/PBS/0.1% Bovine Serum Albumin (BSA) solution (Sigma-Aldrich) and washed three times with 1 ml PBS (1X), each wash lasting 5 minutes with removal of PBS after each wash. The fixed cells were blocked with 1 ml of 5% BSA in PBS for 30 minutes to reduce non-specific binding. The blocking buffer was removed and cells were incubated for 1 hour with primary antibody. The primary antibody was diluted 1:200 with 5% BSA/PBS in a final volume of 500 µl, with gently vortex mixing before addition. After incubation, fixed cells were washed three times as previously and incubated with a 1:500 dilution of conjugated-fluorescently labelled secondary antibody, made in blocking buffer, for 1 hour in the dark (dishes were wrapped with aluminium foil) to avoid any photo-bleaching of the conjugated-fluorescently labelled secondary antibody. Cells were washed twice and maintained in 1 ml of PBS before imaging. Dishes were imaged immediately or stored at 4°C.

2.2.43 Western blot analysis for phospho-S6K1 and mTORC1 proteins

Following 48 hours or 72 hours transfection, adherent HEK293 cells were washed once with PBS (1X) and detached using 500 µl of trypsin (1X) as described in section **2.2.30**. Trypsinised cells were transferred into 1.5 ml microcentrifuge tubes and cell pellets were obtained by centrifugation using a table-top microcentrifuge at

13,000 x g for 3 minutes whilst 5 or 10 ml of 1 x 10^6 cells/ml of HEK293F (suspension cells) treated with and without 200 nM rapamycin for 2 hours (Sigma-Aldrich) in 50 ml mini bioreactor tubes were spun down at 1200 RPM for 5 minutes at 4°C. Pellets were re-suspended in 125 µl of Cellytic M lysis buffer (Sigma-Aldrich) or in 1 ml of lysis buffer (50 mM HEPES (Teknova) pH 7.4, 150 mM NaCl, 3 mM dithiothreitol (DTT) and 0.4% CHAPS (all from Sigma-Aldrich)) containing 1:1000 dilution of protease inhibitor cocktail (Thermo Fisher Scientific) with added 1:1000 sodium fluoride (NaF) and 1:5 sodium orthovanadate (Na_3VO_4) (Sigma-Aldrich). HEK293F pellets were re-suspended in lysis buffer and suspension transferred into a cold 2 ml microcentrifuge tube. Samples were vortexed for 2 minutes and then incubated on ice for 20 minutes or lysed by ultrasonication (30 sec on/off cycle) (Sonic Vibra Cell) for 4 minutes on ice. Total protein was quantified by Bradford reagent (Sigma-Aldrich) with known BSA standards (Sigma-Aldrich) using a microplate (Thermofisher Scientific) and SpectraMax plate-reader (Molecular Devices). Samples were diluted to 50 µg with cold lysis buffer and 50 µl of sample was pipetted into cold microcentrifuge tubes. Equal volumes of 2X Laemmli buffer containing β-ME (Bio-Rad) or 2X LDS sample buffer (Thermofisher Scientific) was added and boiled for 5 minutes in a heating block. 10 µl of sample was loaded into each well of a NuPAGE Novex Bis-Tris protein gel (Thermofisher Scientific) with a Novex Sharp pre-stained protein standard marker (Thermofisher Scientific) and run with MES (1X) buffer (Thermofisher Scientific) for 35 minutes at 200 V (voltage) using a XCell SureLock™ mini-cell tank (Thermofisher Scientific) or run in Mini-PROTEAN® TGX precast gels (Bio-Rad) with a PageRuler prestained protein ladder (Thermofisher Scientific) in a Mini-PROTEAN tank (Bio-Rad) filled with 1X tris/glycine buffer (Bio-Rad). Gels were transferred to Polyvinylidene Difluoride (PVDF) membranes using the iBlot I or II Gel transfer device (Thermofisher Scientific) or with a Trans-Blot® Turbo™ Transfer System (Bio-Rad) with appropriate transfer stacks (Bio-Rad/ Thermofisher Scientific). The membranes

were placed into sealed plastic pouches or containers and incubated with 10 ml of blocking buffer (5% milk powder (Sigma-Aldrich) in tris buffered saline with Tween 20 (TBST) (see **Appendix A.12**)) or Blocker™ Casein in water (Thermofisher) for 1 hour. Following blocking, the pouches were opened using a sterile scalpel and re-sealed in new plastic pouches or kept in a container with 10 ml blocking buffer with a 1/1000 dilution of primary antibodies pipetted and mixed into it. The sealed pouches were gently shaken by hand and incubated at 4°C overnight on a rocker (VWR). The membrane was removed out of the pouch and washed three times with 10 ml TBST (1X) or phosphate buffered saline with Tween 20 (PBST) (1X), each wash lasting for 5 minutes. The blots were re-sealed in plastic pouches and incubated with a 1:3000 dilution of HRP-linked or AP-linked secondary antibody in blocking buffer for 1 hour at room temperature. The blots were washed three times with TBST or PBST and a final wash in deionised water was performed. The blot was removed from the pouch or from the container and placed into a dark container. Blots were developed in a final volume of 5-10 ml of Pierce™ ECL Western blotting substrate (Thermo Fisher Scientific) for 5 minutes prior to chemiluminescent imaging or with 5 ml of 5-Bromo-4-Chloro-3-Indolyl-Phosphate with Nitro Blue Tetrazolium (BCIP /NBT) substrate solution (Thermofisher) for 5 minutes before washing the blot twice in water and imaging. ECL developed blots were “stripped” using Restore Western Blot Stripping Buffer (Thermo Fisher Scientific) for 15 minutes at 37°C and re-blotted using other antibodies such as S6K1 and vinculin to determine loading of protein for normalisation. All gels were imaged using the Bio-Rad Chemidoc™MP Imaging system. Standard factory settings for Western blot image acquisition were used and set to ‘auto-detection’ in order to obtain best contrast and gain. Bands in captured images of the blots were quantified using densitometry in Image J (version 1.48) and the levels of normalised phospho-S6K1 levels from each sample was determined using **Equation 2.3:**

$$\% \boldsymbol{P} = \left(\frac{\boldsymbol{I_p}}{\boldsymbol{I_t}}\right) \times \mathbf{100} \qquad \textbf{(2.3)}$$

Where the percentage of phosphorylation (%P) is equal to the intensity of the band for phosphorylated protein (I_p) divided by the intensity of the total protein (I_t).

2.2.44 Pull-down assays of S6K1-mTORC1 interactions

Following 72 hours of transfection, 5 or 10 ml of 1 x 10^6 cells/ml were centrifuged and lysed as stated in section **2.2.43**. Following lysis on ice, tubes containing lysates were spun-down by centrifugation for 45 minutes at 20,000 x g and 4°C. 50 µl samples of total and soluble fractions were collected. 1 ml of the supernatant (soluble fraction) was loaded onto a 10 µl Ni-NTA resin PhyTip using a robot (PhyNexus) at 4°C, washed (wash buffer: lysis buffer + 20 mM imidazole) and eluted (elution buffer: lysis buffer + 500 mM imidazole) in a 40 µl final volume. The robot was programmed using the PhyNexus operating software and standard manufacture protocol was used. Eluted proteins and complexes were separated using midi-gels (Bio-Rad, UK) for western blotting as described in section **2.2.43** or for coomassie staining by transferring the gel onto pads soaked in equal volumes (~10 ml) of stain and de-stain solutions (Thermofisher Scientific) and stained using the Power Blotter (Thermofisher Scientific). Stained gels were kept in deionised water and left on the rocker for at least an hour to remove any excess stain before imaging.

2.2.45 Cell starvation, amino acid activation and inhibition studies

Following 48 hours transfection, HEK293 cells were washed once with 1 ml of pre-warmed PBS (1X) and then incubated in 1 ml of pre-warmed serum-free medium overnight for serum starvation. Afterwards, cells were amino acid starved for 1-2 hour prior to imaging by washing the cells once with 1 ml of pre-warmed Dulbecco's

phosphate-buffered saline (DPBS) containing magnesium and calcium and incubated in 1 ml DPBS prior to imaging. DPBS was used as it prevents cells from detaching over long period incubations compared to PBS. Leucine (1 mM) and serine (500 mM) (Sigma-Aldrich) were made in full serum media and added dropwise directly onto cells already in 1 ml media using a pipette to initiate activation. Rapamycin (200 nM or 250 nM) (Sigma-Aldrich) and AZD2014 (200 nM or 7 μM) (MedChem Express) were also made in full serum media and added in a dropwise manner to initiate inhibition.

2.2.46 Confocal imaging of live and fixed cells

Confocal images were acquired using either an inverted Nikon TE2000-U or Ti-E microscope with a Nikon C1 or C2 confocal scanning unit with a GFP (488 nm excitation) or mDsRed/mCherry/Alexa Fluor 555 (543 or 561 nm excitation) and mTurquoise2/Alexa Fluor 405 (405 nm excitation) filter set, or by using a Leica TCS SP8X confocal microscope using internal GFP, mCherry software settings and filters, or using a Zeiss LSM 880 microscope with Airyscan with a 405 nm excitation laser and internal Alexa405 Fluor filter.

2.2.47 Quantifying percentage of cytoplasmic or nuclear fluorescence in cells

Levels of GFP/RFP in live cells or fluorescence intensity from conjugated-fluorescent secondary antibodies in fixed cells were determined in the nucleus and the cytoplasm per cell by masking sub-cellular regions in ImageJ (version 1.48) and incorporating extracted mean intensity values to **Equation 2.4** or **Equation 2.5**:

$$\% \boldsymbol{C} = \left(\frac{\boldsymbol{I_c}}{\boldsymbol{I_t}}\right) \times \mathbf{100} \qquad \textbf{(2.4)}$$

$$\% \boldsymbol{N} = \left(\frac{\boldsymbol{I_N}}{\boldsymbol{I_t}}\right) \times \mathbf{100} \qquad \textbf{(2.5)}$$

where percentage in the cytoplasm is $\% C$, percentage in the nucleus is $\% N$, mean intensity in the cytoplasm is I_C, mean intensity in the nucleus is I_N and mean total intensity in both the cytoplasm and nucleus is I_t.

2.2.48 UV-Vis and fluorimeter studies

Inhibitor concentrations of rapamycin (10 μM), AZD2014 (7 μM or 11 μM) and INK128 (7 μM or 16 μM) were prepared in 2 ml of DMSO (Thermofisher Scientific) or in other solutions such as 0.5-1 mM BSA, water or PBS. Purified GFP was prepared in water. The solutions were vortexed mixed and the tubes wrapped in aluminium foil to protect the drugs from photo-bleaching or photo-damage by ambient light. Using a UV quartz glass cuvette (Hellma) measurements were taken using a UV-Vis spectrometer (Shimadzu) or fluorescence spectrometer (Agilent Technologies).

2.2.49 Determining quantum yields of AZD2014 in solution

The quantum yields of AZD2014 in DMSO and PBS were calculated using standards, Coumarin-1 (Exciton, UK) in ethanol (Sigma-Aldrich), Quinine (Sigma-Aldrich) in 0.5 M sulphuric acid and Rhodamine 6G (Exciton, UK) in ethanol with known quantum yields of 0.73, 0.55 and 0.94 in ethanol, respectively. Quantum yields were determined by measuring the absorbance of AZD2014 and standard solutions at concentrations with similar ODs below 0.1 (absorbance) using a UV-Vis spectrometer and then converting these to fraction of light absorbed ($1\text{-}10^{-OD}$). Relative fluorescence intensities see section **2.2.48,** at a single excitation (393 nm) under the same detection settings were also measured. The relative and comparative methods were used to extract the quantum yield using **Equation 2.6**.

$$Q = Q_R \frac{I}{I_R} \frac{A_R}{A} \frac{n^2}{n_R^2} \quad \textbf{(2.6)}$$

where Q is the unknown quantum yield of the sample, Q_R is the quantum yield of the standard, I is the integrated fluorescence intensity of the sample, I_R is the integrated fluorescence intensity of the reference standard, A_R is the absorbance of the standard, A is the absorbance of the sample (scatter considered), n_2 is the refractive index of the sample and n^2_R is the refractive index of the standard.

The comparative method was used to determine quantum yields by plotting the absorbance and integrated fluorescence intensities of three different dilutions of the sample and standards. The slope of the line obtained could be substituted for both $[I / I_R]$ *and* $[OD_R / OD]$ in the equation above.

2.2.50 Two-photon FRET-FLIM setup for interaction and spectroscopy studies

Principles of FRET and FLIM are briefly covered in **Chapter 1: Introduction**. For multiphoton FLIM acquisition, the settings and instrument setup used has been described previously (Yadav *et al.*, 2013). Briefly, multiphoton excitation using 910 ± 5 nm or 600 ± 5 nm from a tuneable mode-locked titanium sapphire (Ti:Sapphire) laser (Mira 900, Coherent Lasers, UK) that generated 180 fs pulses at 76 MHz pumped by a 532 nm solid-state Neodymium Vanadate laser source (Verdi, Coherent Lasers) was used. Alternatively, the wavelength range of the MIRA-900 was extended using Optical Parametric Oscillators (Mira-OPO, Coherent Lasers, UK). FLIM images of 256 x 256 pixels were acquired. Collected fluorescence emission was passed through a BG39 bandpass filter (Comar) for laser excitation rejection and GFP collection or through 460/60 nm (Semrock) for selective AZD2014 collection before reaching a high speed hybrid detector (HPM-100) for Time-Correlated Single Photon Counting TCSPC (Becker-Hickl, GmbH). The laser power

was controlled using a circular Neutral Density (ND) filter and the setup is depicted in **Figure 2.15**.

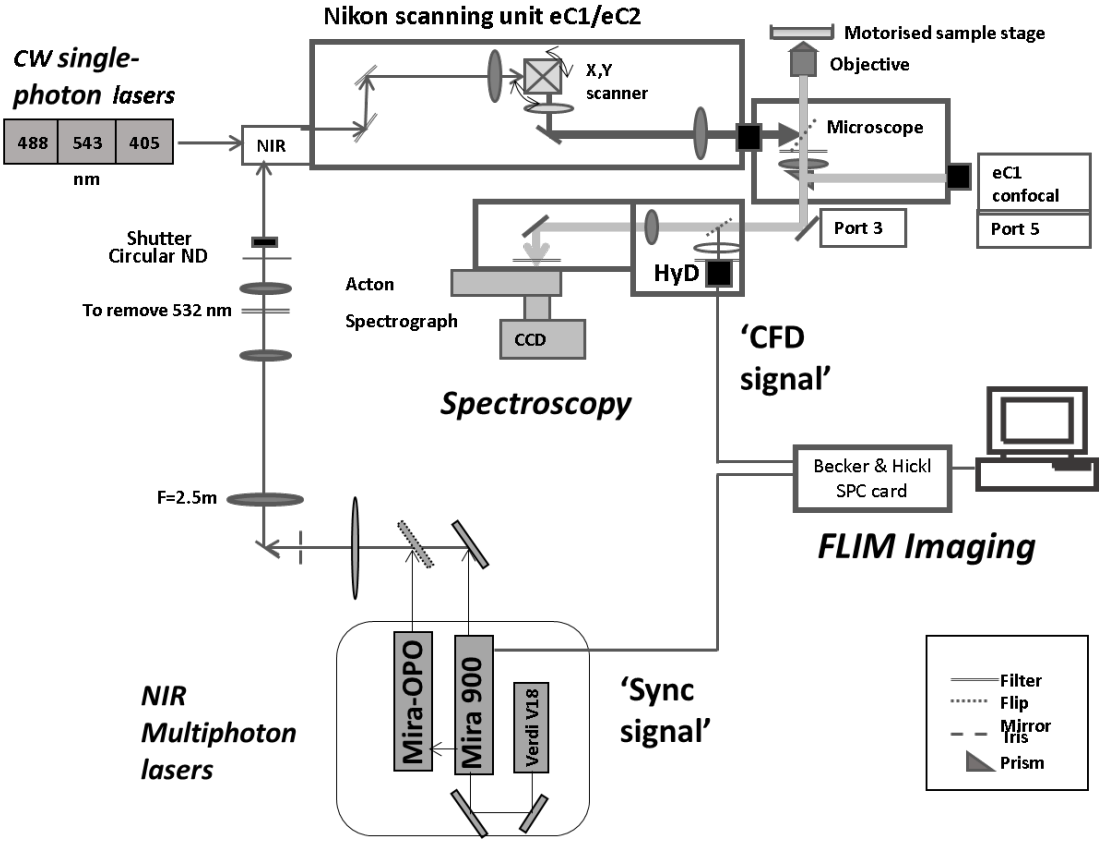

Figure 2.15: Schematic of multiphoton FRET-FLIM system. *The above figure was adapted from* (Schoberer and Botchway, 2014)

The high repetition femtosecond pulsed excitation beam from the Ti:Sapphire was focussed onto the sample on the microscope stage by using a high numerical aperture (1.2) x60 water immersion (WI) objective (Nikon). The TCSPC PC module SPC830 (Becker-Hickl) was synchronised to the Nikon scanning unit (x,y and pixel clock signals). The synchronisation or 'sync' signal was derived from the pulses of the Ti:Sapphire laser in order to have a reference for the timing of the fluorescent photons arrival after the excitation pulses. This allowed for the detection and measurement time of single fluorescent photon arrival time from the sample relative to the excitation pulse enabling the build-up of a histogram of photons emitted over

time in picoseconds. This information was built up in the TCSPC PC card or in the computer memory to store fluorescent photon distributions both temporally (t) and spatially, pixel by pixel (x,y). A Constant Fraction Discriminator (CFD) following the detector signal was used as a stop signal in a forward ready mode. A Time-to-Amplitude Converter (TAC) was used to record the time of a detected photon with respect to the 'sync' and CFD by generating an output voltage that ended with the start of the next detected photon. An Analog-Digital Converter (ADC) was used to convert the electrical TAC signal into a digital signal to be stored on the memory of the TCSPC unit.

As the Instrument Response Function (IRF) of the detector was 31 picoseconds (ps) (measured using KDP crystals) and the electrical response was 6.8 ps with an electrical timing jitter of 3 ps RMS, very accurate and short lifetimes could be measured with high precision using this setup. For protein-protein interaction studies, cells equally expressing EGFP and mCherry tagged proteins were selected and imaged in First-In-First-Out (FIFO) Imaging mode where the photon data was sent directly onto the memory of the computer rather than the TCSPC card. FLIM images were acquired using 0.25-6 mW of laser power for the sample excitation depending on the intensity of the fluorescence. The acquisition times were 60-120 seconds or until the final counts collected were at least 100 counts per pixel in the first peak channel from the rise time. The files were imported into the SPC Image (version 6.0) software and fitted to mono-exponential decay models convoluted with the IRF by an algorithm to extract model parameters such as lifetime, amplitude and chi-square (goodness of the fit). The fluorescence lifetime (τ) of a molecule is the average time it spends in the excited state following excitation and emission of a fluorescence photon. The weighted average (τ_m) of the different lifetime components in each pixel of a multi-exponential decay profiles can be extracted from **Equation 2.7**:

$$\tau_m = \frac{\sum_{i=1}^{N} a_i \tau_i^2}{\sum_{i=1}^{N} a_i \tau_i} \qquad \textbf{(2.7)}$$

where the mean lifetime (τ_m) corresponds to the total number of fluorophores (N), a_i and τ_i are respectively amplitude and lifetime respectively for the (i) fluorophore.

The goodness of the fit was evaluated through the reduced chi-square (χ^2) value, defined in **Equation 2.8:**

$$x^2 = \frac{1}{N-p} \sum_{i=1}^{N} \frac{(d_i - f_i)^2}{d_i} \qquad \textbf{(2.8)}$$

where d_i represents real data points and f_i the corresponding points from the fit-model. N represents the total number of time sample points and p is the number of fitting parameters. The reduced chi-square can be calculated from the fitted lifetime, 1 being indicative of a "perfect fit", a value >1 or <1 indicates that the model is over-fitting or under-fitting the data.

Where the counts were insufficient to give a good chi-square, pixels were binned to a factor of 2 where surrounding pixels were summed to give a better statistics per pixel. A final FLIM image matrix is obtained where each pixel is colour-coded accordingly to its lifetime and chi-square value, and a histogram showing the lifetime distribution (number of pixels vs lifetime values) of the complete imaged area is produced. To statistically determine differences between lifetime distributions of donor alone and donor with acceptor, distributions were fitted to a Gaussian model and Full Width at Half Maximum (FWHM) was obtained. As well as cell based imaging studies, TCSPC measurements (O'Connor and Phillips, 1984) were also performed for in-solution studies where drops of samples (e.g. inhibitors) in solution or purified protein solutions were placed on open coverslips (VWR) to determine fluorescence lifetime changes. Purified GFP and AZD2014 were prepared in ethyl

glycol (Sigma-Aldrich) with water and mixed 1:1 to make solutions for in solution FRET.

2.2.51 One-photon FRET-FLIM setup for interaction and spectroscopy studies

A similar system to the one described above, where one-photon pulsed excitation sources, namely a 405 nm pulsed laser (405BDL, Becker-Hickl) or a pulsed NKT supercontinuum laser set to 488 nm laser was used to perform one-photon FRET-FLIM. The laser pulses were synchronised with the TCSPC PC module SPC150 (Becker-Hickl). The fluorescence emission was passed through a 515/30 (Thorlabs) filter or through a 460/60 nm (Semrock) before reaching the hybrid detector.

2.2.52 Lightsheet setup for monitoring AZD2014 uptake in spheroids

A commercial light sheet fluorescence microscope, the Leica TCS SP8 DLS (Digital Light-Sheet), was used to acquire 3D time-lapse images of spheroids after administration of AZD2014. The basic principle of this technique is that the detection of the sample is acquired perpendicularly to the illumination axis. The illumination consists of a beam of light, shaped into the so-called “sheet”, exciting in one shot only the fluorescence of the sample at the focal plane of the detection objective. This technique produces fast imaging of wide fields of view with subcellular detail in a less phototoxic way compared to confocal and multiphoton microscopy, allowing for long-term time-lapse imaging. The use of a CMOS camera for the detection enables the fast volumetric imaging, allowing collection of quasi-real time data for longer periods of time.

With the commercial Leica TCS SP8 DLS, stacks of images were acquired using a 10X/0.3 NA detection objective, with a field of view of 735 µm x 735 µm. For the light sheet generation, a laser emitting at 405 nm wavelength was used, focused with a 2.5X/0.07 NA objective and scanned by galvanometric mirrors, digitally creating a light sheet with a thickness of 3.7 µm and a Rayleigh length of 240 µm. Two

counter-propagating light sheets were also used in order to reduce blur, reduce striping effect and improve the image quality of the acquired sample, and were automatically merged into a single image.

HEK293 cell spheroids, following 72 hours of seeding in agarose-coated 96 U-well plates, were pipetted into a custom 3D printed agarose holder (capable of hosting up to 5 spheroids) that was placed inside a 35 mm glass bottom dish and filled with 7 ml of complete growth media. The samples were placed inside the Leica TCS SP8 DLS box, with the temperature set at 37°C and CO_2 set to 5%. The compound AZD2014 was administrated in the media, and uptake into spheroids was monitored for 2 hours by recording stacks of 780 µm x 780 µm x 300 µm volume composed of 44 planes taken every 15 seconds.

2.2.53 Quantifying uptake of AZD2014 in cellular models

The fluorescence intensities of AZD2014 or INK128 in either monolayer HEK293 or multi-cellular spheroids over time from point of administration were extracted using ImageJ and then modelled using Michaelis–Menten type kinetics where K constant, K_{uptake} in this case, can be used to determine rate of uptake as given in **Equation 2.9**:

$$F_I = \frac{F_{max} \times t}{K_{uptake} + t} \qquad \textbf{(2.9)}$$

where F_I is fluorescence intensity, F_{max} is the maximum fluorescence intensity, t is time and K_{uptake} is the time at half maximum fluorescence intensity saturation.

2.2.54 Lambda scan for multiphoton excitation of AZD2014

Series of confocal images were taken using the Leica TCS SP8 in xyλ acquisition mode, steps of 5 nm using a defined wavelength range (from 680-1300 nm) with an

InSight® DS ultrafast (120 fs pulse width) laser system (Spectra-Physics, UK) for multiphoton imaging. This laser system is more advantageous than Ti:Sapphire ultrafast lasers as it offers double the tuning range and gap free tuning.

3.0 S6K1 interaction and phosphorylation with mTORC1 in living cells

3.1 Brief introduction

The interactions of the S6K1 kinase protein with mTOR and its subunit binding proteins has been implicated using fixed cells and pulled down techniques. Despite current knowledge on S6K1 function as a major effector in regulating protein synthesis and cellular growth, live cell studies are lacking. This chapter seeks to develop the understandings of S6K1 localisation, interaction, regulation and phosphorylation in relation to the mTORC1 pathway in live cells. In particular, this programme of work aims to develop experimental methods to identify the direct sub-cellular location and regions of mTOR activity. Ultimately, it is hoped this work will aid the development of novel treatments against mTOR disease states including cancer where targeting S6K1 interaction with mTORC1 may result in more selective and potent therapy.

The working hypothesis of this chapter is that:

- The S6K1 (mTOR substrate) is recruited onto mTORC1 via the TOS motif of S6K1. Physical interaction between S6K1 and the raptor in the cytoplasm is aided by mTOR initially in the nucleus. The combination of these steps leads to the phosphorylation of S6K1 by mTOR which is assisted by S6K1 conformational changes.

3.2 Results

3.2.1 PCR screening of EGFP-S6K1, S6K1-mCherry and S6K1-mTurq2 constructs

In order to observe the live cell localisation of S6K1, fluorescently tagged S6K1 constructs were made by in-fusion cloning as described in **Chapter 2: materials and methods**. Full length S6K1 cDNA was cloned into the pOPINN-EGFP, pOPINE-3C-mCherry and pOPINE-3C-mTurquoise2 backbone vectors to produce constructs with S6K1 tagged on either the N- or C- terminus. A PCR screen using a pOPIN T7 forward primer and reverse S6K1 primer was performed to assess the success of the cloning prior to sequencing. PCR bands of the insert product corresponding to correct base pair lengths (~2522 and ~1741 bp) were observed corresponding to EGFP-S6K1 and S6K1 only respectively from EGFP-S6K1 and S6K1-mCherry/S6K1-mTurq2 plasmids shown in the gel of **Figure 3.1**. Constructs were Sanger sequenced and results showed a positive match to the original S6K1 sequence, indicating that S6K1 was successfully cloned into the pOPINN-EGFP and pOPINE-3C-mCherry/ pOPINE-3C-mTurquoise2 vectors.

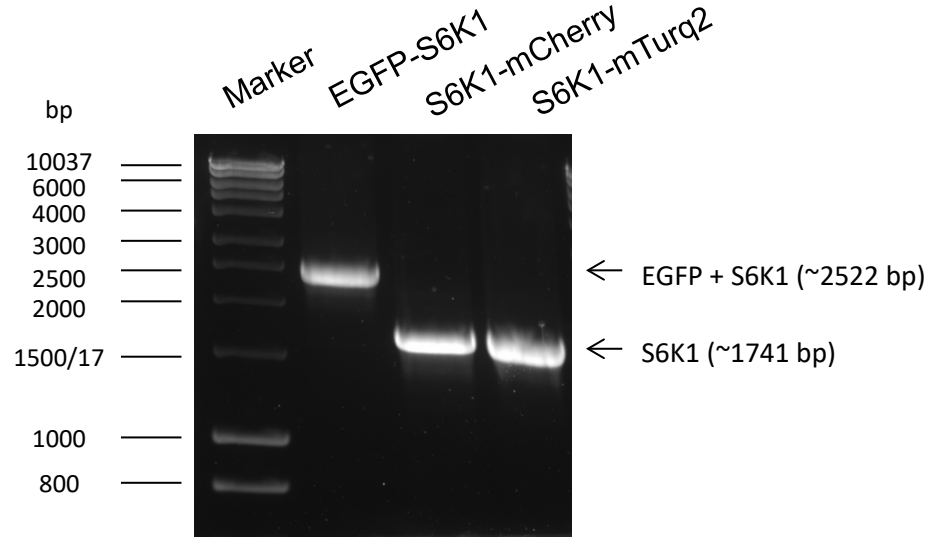

Figure 3.1: Reverse PCR screen of S6K1 constructs. *Analysis of PCR products ran using agarose gel electrophoresis. Marker is shown on the left (bp) with insert products on the right with bands corresponding to EGFP with S6K1 in the pOPINN-EGFP vector and S6K1 only in both the pOPINE-3C-mCherry/ mTurquoise2 (mTurq2) vectors.*

3.2.2 Expression and imaging of tagged S6K1 in live mammalian cells

Upon the verification of the fluorescently tagged S6K1 constructs, HEK293 cells were transfected as described in **Chapter 2: materials and methods,** and the subcellular localisation of overexpressed S6K1 was imaged using single-photon confocal microscopy after 24 or 48 hours of transfection as shown in **Figure 3.2**. Overall, EGFP-S6K1, S6K1-mCherry, S6K1-mTurq2 and commercially available S6K1-GFPSpark constructs all localised in near equal amounts in both the cytoplasm and the nucleus. Fluorescence intensity ratios of 48 ± 2% in the nucleus and 52 ± 2% in the cytoplasm for EGFP-S6K1 and S6K1-mTurq2, 47 ± 2% in the nucleus and 53 ± 2% in the cytoplasm for S6K1-GFPSpark and 43 ± 2% in the nucleus and 57 ± 2% in the cytoplasm for S6K1-mCherry were determined. The tagging of S6K1 with the fluorescent protein mTurquoise2 did not disrupt nor interfere with S6K1 localisation. However, the use of the mCherry tag resulted in a more cytoplasmic localisation evident by an increase in the intensity ratio of 9.3%. This may be due to mislocalisation issues related to the leaking of mCherry tagged proteins into other cellular compartments (Ghodke *et al.*, 2016).

Different cell lines were also tested with EGFP-S6K1 transfected in HeLa or U2OS cells and similar nucleocytoplasmic localisations was observed by confocal microscopy after 24 or 48 hours of transfection, results are shown in **Figure 3.3**.

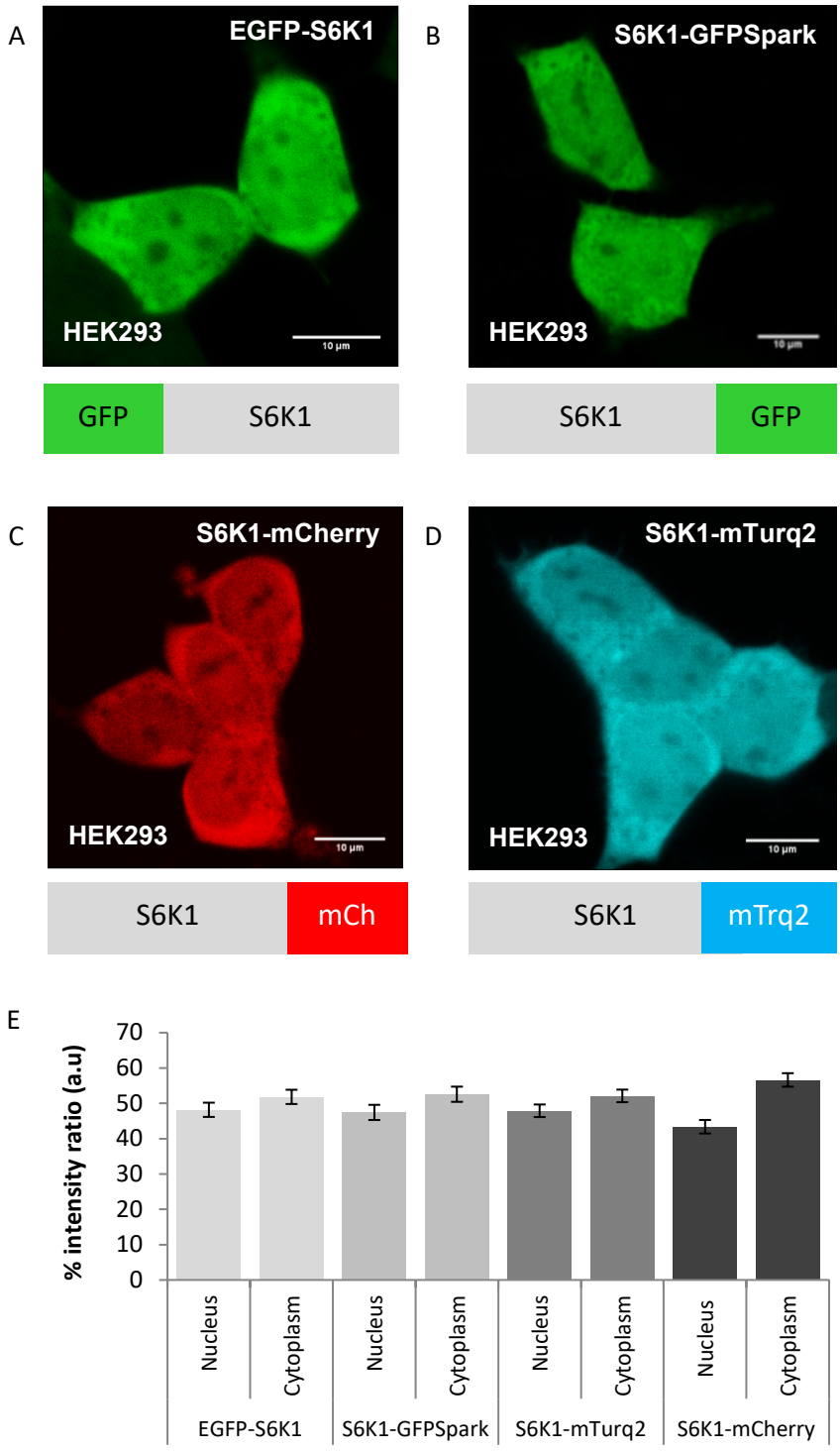

Figure 3.2: Live cell localisation of both N and C-terminally tagged S6K1 in HEK293 cells. *Confocal images of A) EGFP-S6K1, B) S6K1-GFPSpark, C) S6K1-mCherry), D) S6K1-mTurq2 and E) graph showing % of nuclear and cytoplasmic intensities in HEK293 cells expressing EGFP-S6K1, S6K1-GFPSpark, S6K1-mTurq2 and S6K1-mCherry (n=10 in each construct) from three independent experiments. Relative intensities quantified in ImageJ 1.48V. Error bars show the standard deviation. Scale bar = 10 µm in all images.*

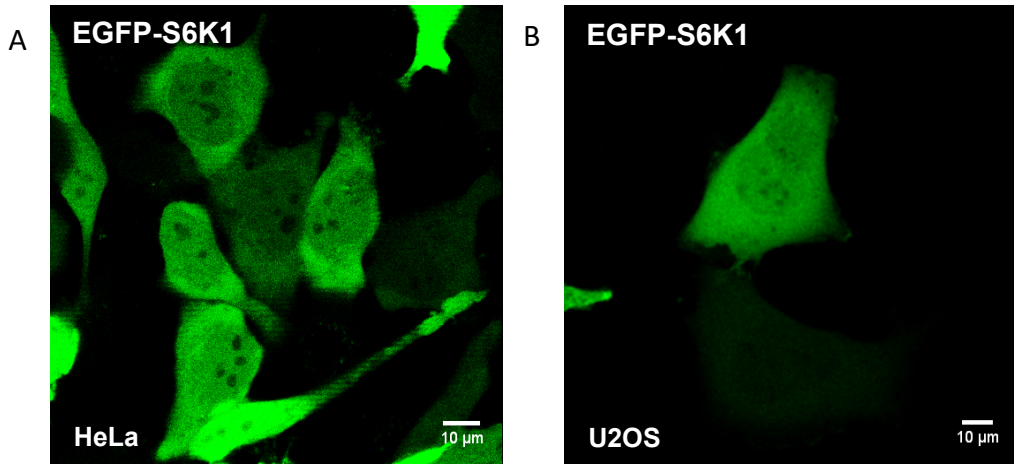

Figure 3.3: Nucleocytoplasmic localisation of EGFP-S6K1 in other mammalian cell lines. *Confocal images of EGFP-S6K1 expressed in A) HeLa and B) U2OS cells. Scale bar = 10 µm in all images. Imaging was representative of three independent experiments.*

3.2.3 Western blot validation of tagged S6K1 constructs

After confirming the expression of EGFP-S6K1, S6K1-mTurq2 and S6K1-mCherry presented in **Figure 3.2** and **3.3**, these constructs were validated by Western blotting and probed for mTOR activity using antibodies. As described in **Chapter 2: materials and methods**, following 48 hours of transfection of EGFP-S6K1, S6K1-mTurq2 and S6K1-mCherry in HEK293 cells, lysates were subjected to Western blot analysis and probed for mTOR mediated phosphorylation using anti-phospho-S6K1 (T412/T389) primary antibodies and for S6K1 activity by using anti-phospho-RPS6 (Ser235/236) antibodies. As shown in **Figure 3.4**, bands at 110 kDa (combined molecular weight of S6K1 and GFP) for phosphorylated S6K1 were observed in overexpressed samples compared to non-transfected control samples. Endogenous phospho-S6K1 bands were not detected in HEK293; see **Appendix B.1**. Western blot analysis of S6K1-mTurq2 functionality is shown in section **3.2.14**. However, basal levels of phospho-RPS6 were detected, with a 6-fold increase when EGFP-S6K1 was overexpressed. In summary, the combination of the Western blots confirms fully functioning S6K1 (i.e. capable of being phosphorylated by mTORC1) and validates the expression observed in sub-chapter **3.2.2**.

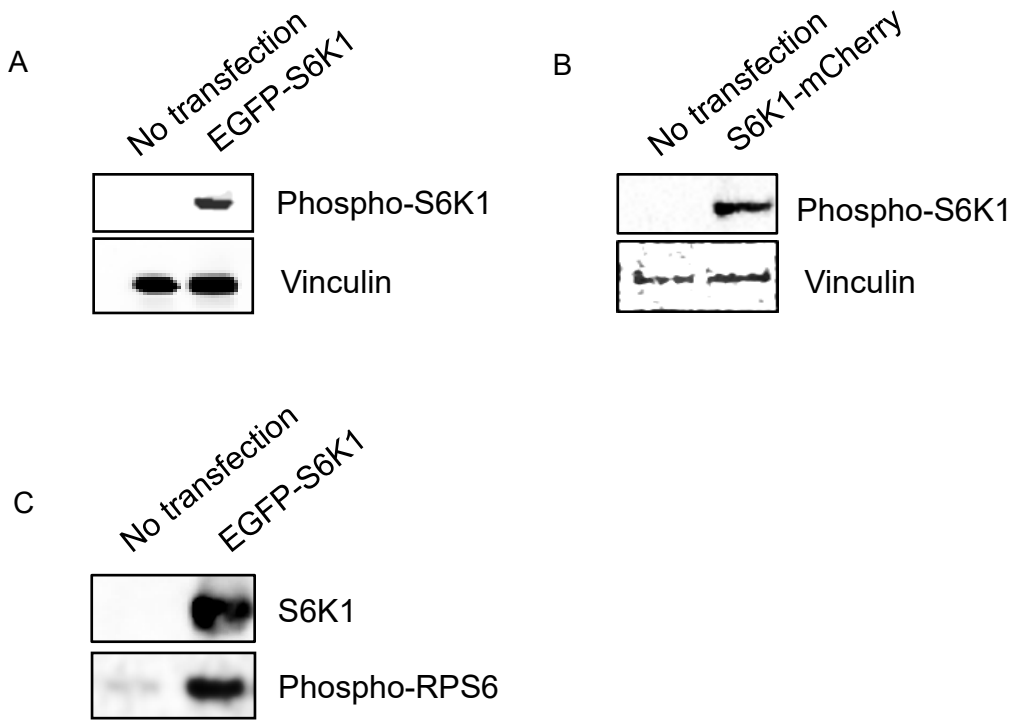

Figure 3.4: Validation of fluorescently tagged S6K1 using Western blot analysis. *Western blots of A) transfected (EGFP-S6K1) and non-transfected HEK293 cells labelled with anti-phospho-S6K1 (Thr389/412), as well as anti-vinculin (loading control) antibodies. B) Transfected (S6K1-mCherry) and non-transfected HEK293 cells labelled with anti-phospho-S6K1 and anti-vinculin antibodies. C) Transfected (EGFP-S6K1) and non-transfected HEK293 cells labelled with phospho-RPS6 (Ser235/236) and anti-S6K1 antibodies.*

3.2.4 Live cell translocation of fluorescently tagged S6K1 from the nucleus to the cytoplasm

EGFP-S6K1 was co-transfected with fluorescently tagged raptor to investigate the co-localisation and interaction between S6K1 and raptor in live HEK293 cells. Confocal imaging was used to determine the relationship between the two proteins. A novel change to a predominately cytoplasmic localisation, similar to that of raptor alone, of EGFP-S6K1 was observed upon mCherry-raptor co-expression with the movement of S6K1 out of the nucleus (**Figure 3.5**). Furthermore, it was found that this movement, termed ‘translocation’ throughout this thesis, correlated with increased intensity (levels) of mCherry-raptor co-expression as shown in **Figure 3.5C**.

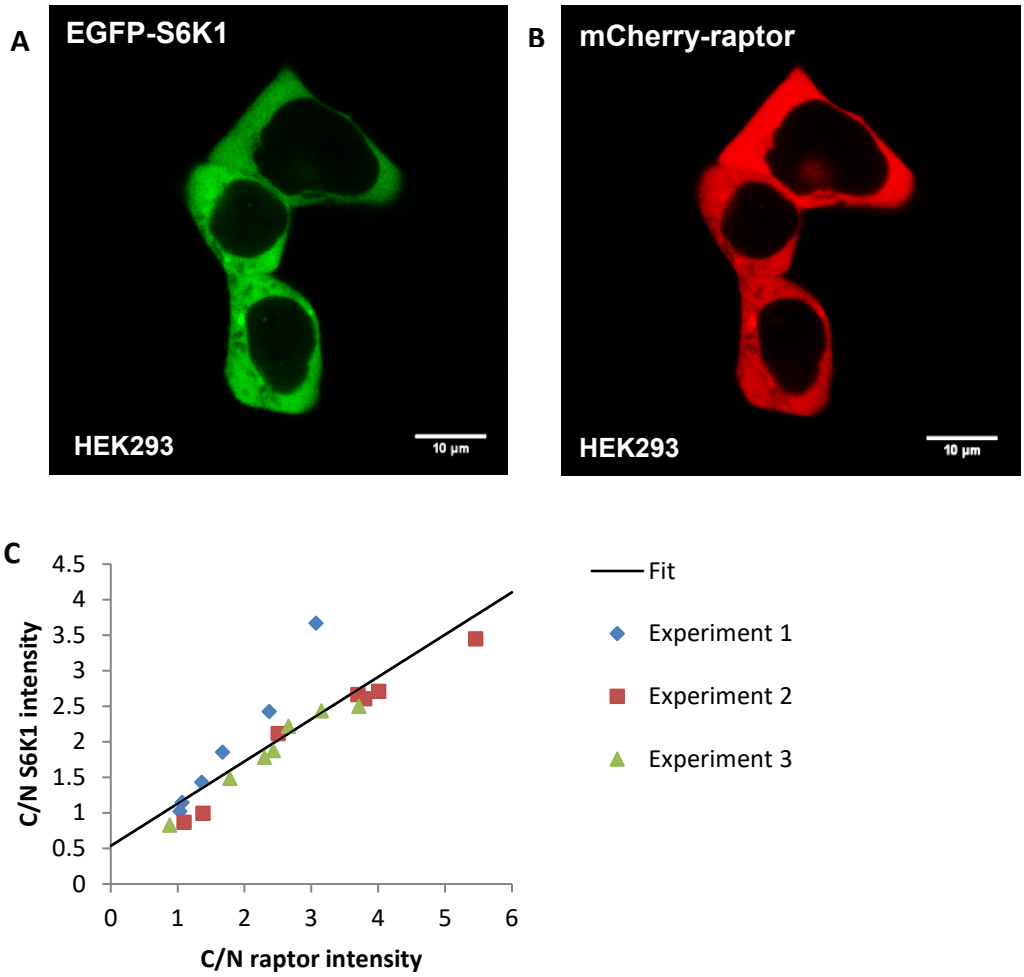

Figure 3.5: Translocation of S6K1 out of the nucleus to the cytoplasm with raptor co-expression. *Confocal images of A) EGFP-S6K1 with co-expression of B) mCherry-raptor. C) Graph of fraction of mean cytoplasmic/nuclear (C/N) S6K1 intensities against fraction of mean C/N raptor intensities. Data has been taken from three independent experiments. Intensities quantified in ImageJ 1.48V. Scale bar = 10 µm in all images.*

This observed translocation of S6K1 was further validated by co-transfecting HEK293 cells with different fluorescently tagged S6K1 and raptor constructs. As shown in **Figure 3.6**, the movement of mTurq2 or mCherry labelled S6K1 out of the nucleus to the cytoplasm with msDsRed or YFP tagged raptor was similar to that observed above with the EGFP and mCherry combination of the proteins; although for reasons unknown, the combination with YFP tagged raptor showed less efficient translocation in some cells. This inefficiency may be due to steric hindrance or

distortion from the bulkiness of the YFP tag (Pedersen, Carmosino and Forbush, 2008) and thus may block the translocation event.

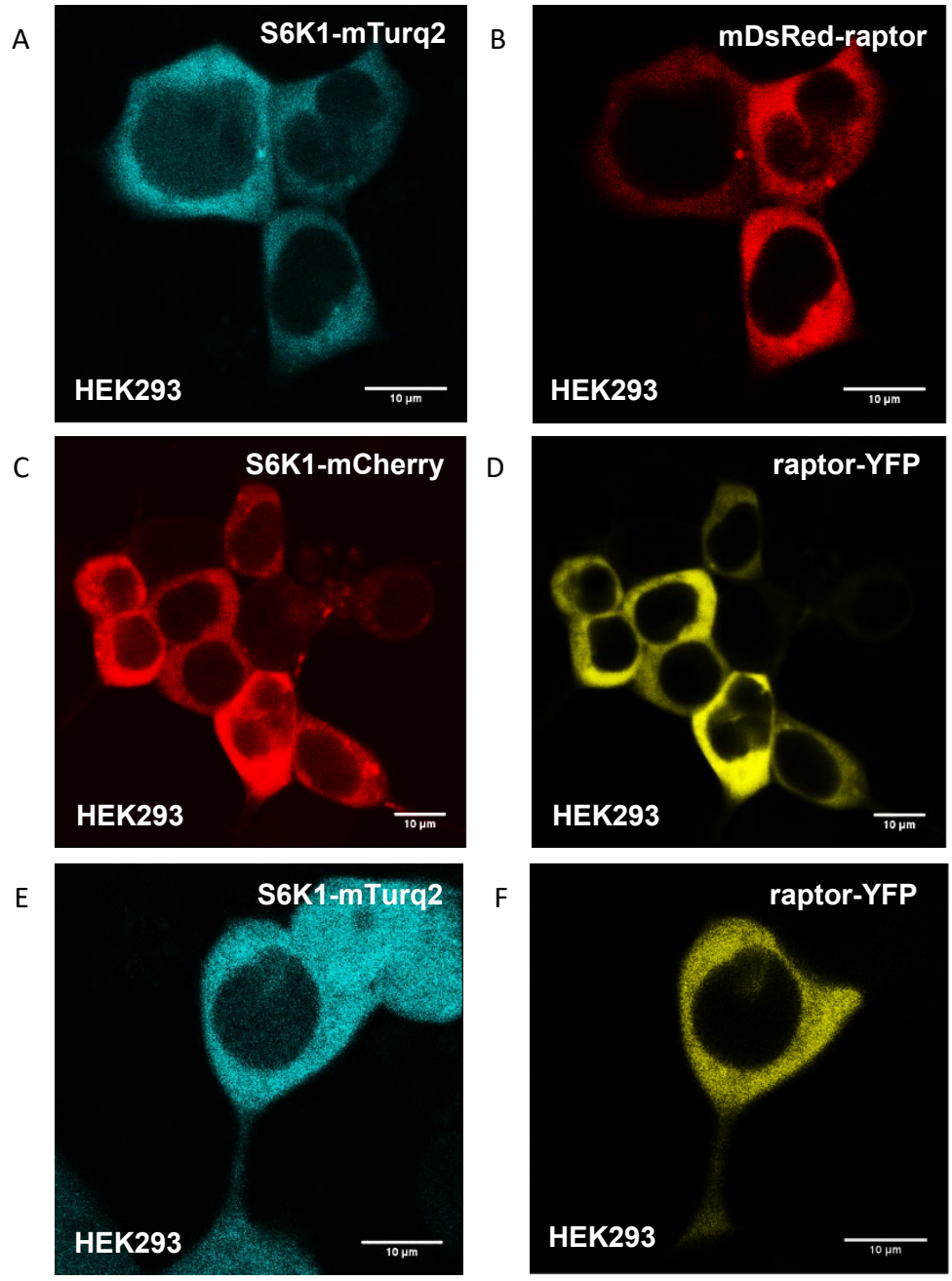

Figure 3.6: Translocation of S6K1 out of the nucleus with other fluorescently tagged raptor proteins. *Confocal images of A) S6K1- mTurquoise2 with B) mDsRed-raptor co-expression. C) S6K1-mCherry with D) raptor-YFP co-expression and E) S6K1-mTurquoise2 with F) raptor-YFP co-expression in HEK293 cells. Representative data from three independent experiments are shown. Scale bar = 10 µm in all images.*

To verify that the translocation was representative amongst other mammalian cell lines, EGFP-S6K1 and mCherry-raptor was co-transfected in the HeLa cell line and

imaged using confocal microscopy. Similar results as seen in HEK293 cells were observed in HeLa cells, see **Figure 3.7,** where S6K1 translocated with raptor co-expression evident by a lack of GFP intensity in the nucleus. It is worth noting that the translocation was less efficient compared to that in HEK293 cells and this may be due to differences in transfection efficiency (~60%) and expression levels.

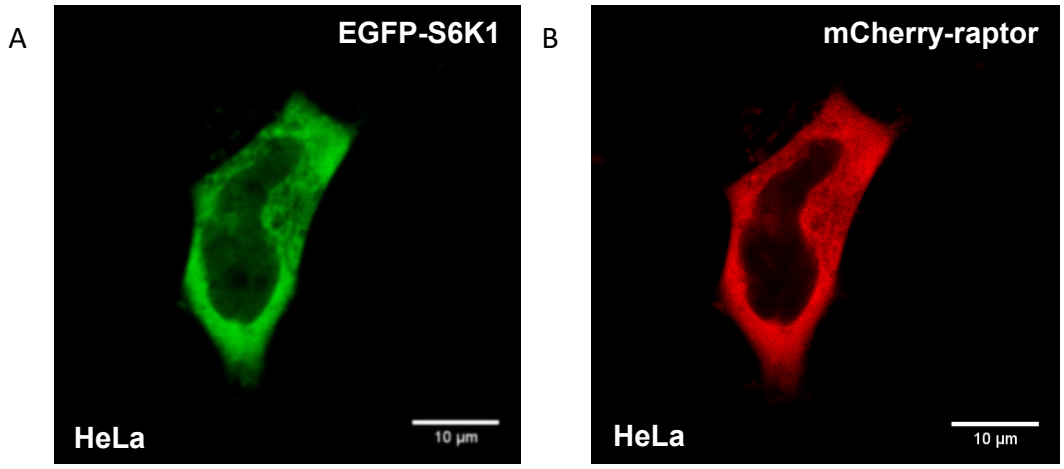

Figure 3.7: Translocation of S6K1 in HeLa cells. *Confocal images of A) EGFP-S6K1 and B) mCherry-raptor co-expressed in HeLa cells. Scale bar = 10 µm in all images. Representative data from three independent experiments are shown.*

3.2.5 S6K1 translocation with serum/AA starvation or inhibitor treatment

Having identified the subcellular localisation of S6K1 with respect to the raptor scaffold protein, the significance of the S6K1 translocation process was next turned to. As nutrient regulation of cells is linked to mTOR mediated phosphorylation of S6K1, see **Chapter 1**, depriving HEK293 cells of nutrients was investigated to test if the translocation of S6K1 was associated with mTOR mediated phosphorylation. The combination of overnight serum and 1 hour of amino acid starvation of HEK293 cells transiently co-expressing both EGFP-S6K1 and mCherry-raptor did not disrupt the translocation of S6K1 as shown by the confocal images in **Figure 3.8** where EGFP-S6K1 remained predominately localised in the cytoplasm. Furthermore, the treatment of live HEK293 cells co-expressing both EGFP-S6K1 and mCherry-raptor with mTOR inhibitors such as rapamycin and AZD2014 for up to 17 hours also did not disrupt or revert the translocation of S6K1 (**Figure 3.8**), as mentioned above,

further demonstrating that the translocation may be independent of mTOR mediated phosphorylation.

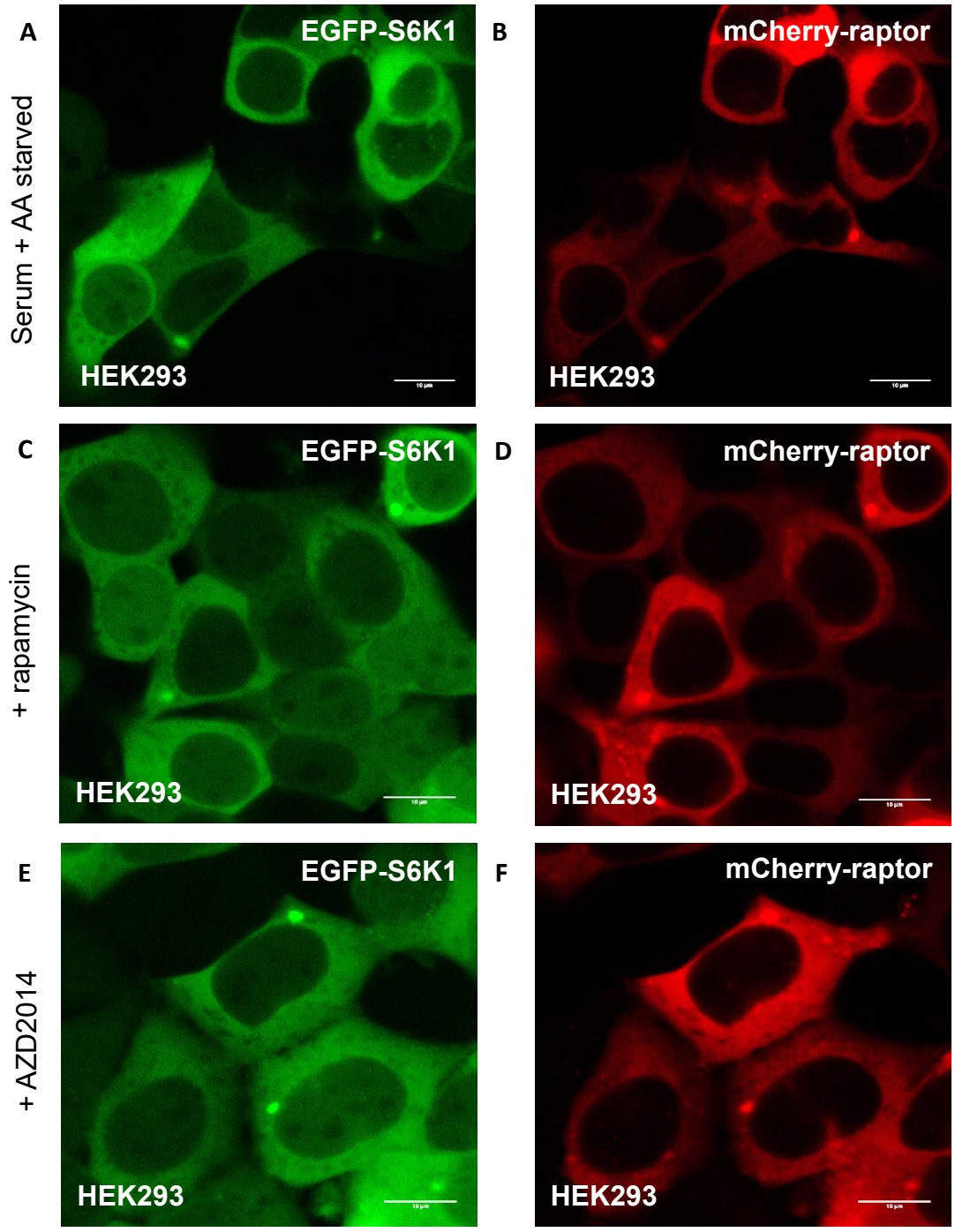

Figure 3.8: Effect of serum and amino acid starvation on translocated S6K1. *Confocal images of live HEK293 cells co-expressing both A) EGFP-S6K1 and B) mCherry-raptor with 17 hours of serum and 1 hour of amino acid starvation. C) EGFP-S6K1 and D) mCherry-raptor with 17 hours of 200 nM rapamycin treatment. E) EGFP-S6K1 and F) mCherry-raptor with 17 hours of 200 nM AZD2014 treatment. Representative data from three independent*

experiments are shown. Scale bar = 10 μm in all images. Any visual differences in translocation efficiency compared to previous figures are due to different contrast settings.

3.2.6 S6K1 translocation with S6K1 TOS and phospho-domain mutations

Having found that the S6K1 translocation process may not be dependent on mTOR phosphorylation, the S6K1 sequence was mutated to test if the S6K1 translocation was directly related to raptor binding. An S6K1 mutant construct (EGFP-F28A-S6K1) was generated where phenylalanine at amino acid position 28 of the TOS motif known to mediate interaction with raptor was mutated to an alanine from the EGFP-S6K1 construct (see **Chapter 2: materials and methods**) and expressed either alone or co-expressed with mCherry-raptor in live HEK293 cells. **Figure 3.9** shows that the translocation of S6K1 out of the nucleus was inhibited in all cells with EGFP-F28A-S6K1 and mCherry-raptor co-expression as GFP intensity levels remained equally distributed in both the nucleus and cytoplasm, indicating that the translocation of S6K1 may be linked to raptor binding. Furthermore, the phosphorylation site on S6K1 in the EGFP-S6K1 construct was mutated to generate another mutant construct (EGFP-S6K1-T389A), where threonine at amino acid position 389, the target for mTOR phosphorylation, was mutated to an alanine. Confocal imaging results showed that when EGFP-S6K1-T389A was co-expressed with mCherry-raptor in HEK293 cells, no effect on S6K1 translocation was observed as well as no change in cytoplasmic S6K1 GFP distribution (**Figure 3.9)**. From the experiments with the two mutant S6K1 forms it is concluded that the translocation of S6K1 event is independent of mTOR phosphorylation and rather may be related to an initial raptor interaction.

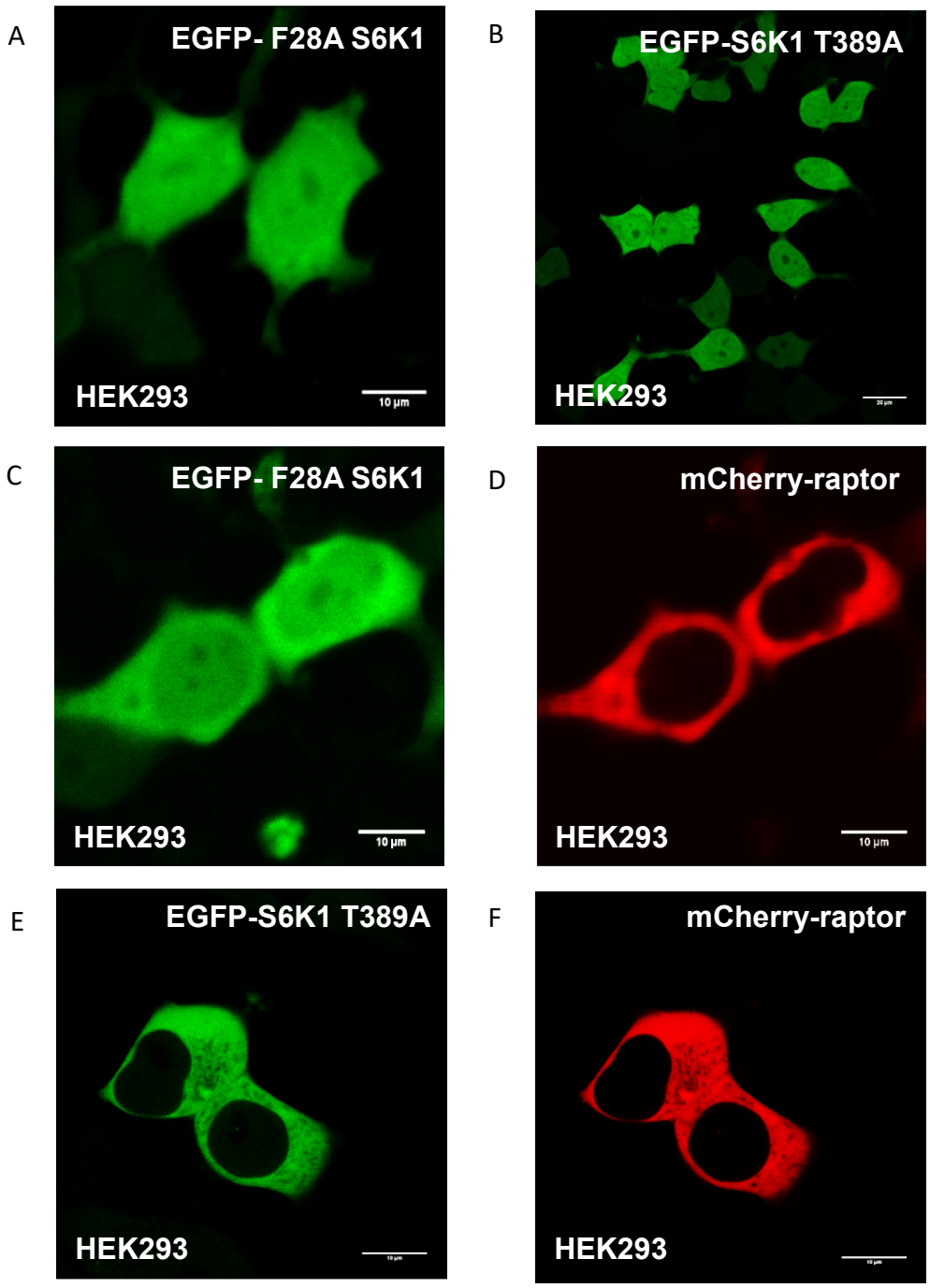

Figure 3.9: Effects of S6K1 mutations on S6K1 translocation with raptor. *Confocal images of A) EGFP-F28A S6K1 (TOS motif mutant), B) EGFP-S6K1 T389A (phosphorylation mutant), C) EGFP-F28A S6K1 with D) mCherry-raptor co-expression, E) EGFP-S6K1 T389A with F) mCherry-raptor co-expression. Representative data from three independent experiments are shown. Scale bar = 10 µm in all images.*

3.2.7 mDsRed acceptor unsuitability for multiphoton FRET-FLIM

Since the mutagenesis studies indicated a role of a functioning TOS motif in mediating the S6K1 translocation, it was hypothesised that the translocation of S6K1

out of the nucleus with raptor co-expression may be related to S6K1 directly binding to raptor in the cytoplasm. To investigate whether S6K1 and raptor underwent a direct physical interaction, FRET-FLIM were performed on HEK293 cells co-expressing EGFP-S6K1 (donor) and mDsRed-raptor (acceptor). Cells expressing equal intensities of both fluorescently tagged molecules were selected and imaged as described in **Chapter 2: materials and methods**. **Figure 3.10** gives the results for the fluorescence lifetime measurements of EGFP-S6K1 in the presence of mDsRed-raptor. Whilst the value of 2.40 ± 0.03 ns is lower than the natural lifetime of EGFP-S6K1 (2.60 ± 0.01 ns), suggests an interaction between the two proteins, this however requires further analysis and is discussed below. In order to establish the assembly of S6K1 onto the complex, HEK293 cells were co-transfected to express both EGFP-S6K1 and mDsRed-Rheb. FRET-FLIM imaging showed quenching of the lifetime of EGFP-S6K1 (stated above) to 2.40 ± 0.05 ns (**Figure 3.10**). Whilst a reduction of 200 ps normally indicates a direct interaction, before any conclusions may be drawn from FRET-FLIM measurements, it is necessary to perform a few validation checks.

HEK293 cells expressing mDsRed alone were excited at 910 nm, the same wavelength used to excite the GFP donor. An emission of mDsRed using filters to collect GFP emission was found indicating an evoked green emission upon multiphoton excitation. The decay of this emission was short with a lifetime of 435 ± 11 ps. However, the decay fitted best to a multi-exponential in comparison to the mono-exponential decay of EGFP (**Figure 3.11**). The importance of this result means a skewed lifetime measurement towards shorter values. This is discussed at the end of the chapter in **3.3 Discussion**. In comparison, another acceptor fluorescent protein, mCherry was imaged at the same settings and no photon count was collected, evident by no image in the FLIM (**Figure 3.11**). This showed that

mCherry is a more suitable acceptor for multiphoton FRET-FLIM and does not give any green emission upon multiphoton excitation.

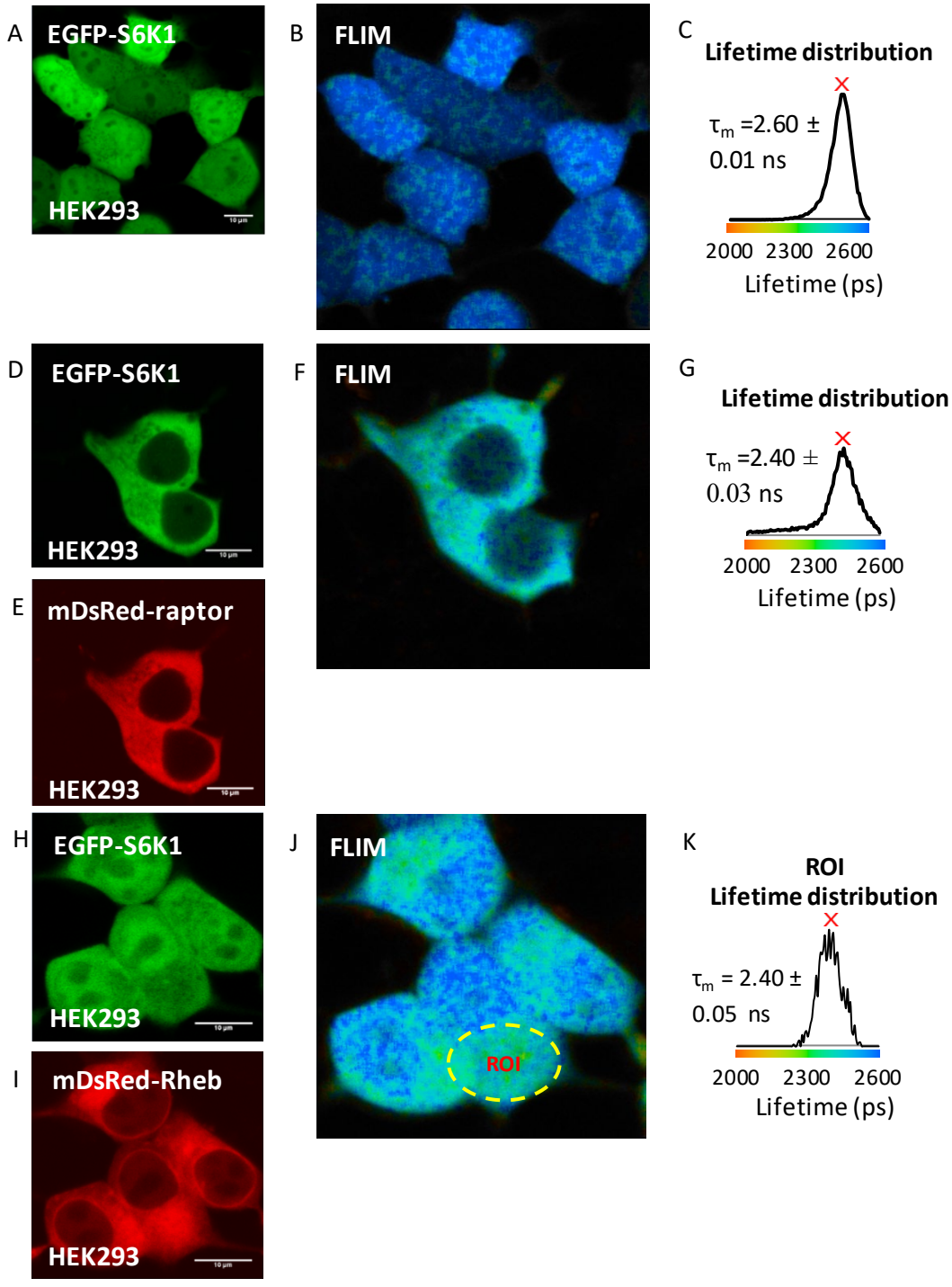

Figure 3.10: Live cell S6K1 interaction with mDsRed-mTORC1 acceptor proteins. *A) Confocal image of EGFP-S6K1 in HEK293 cells. B) FLIM image of the fluorescent lifetimes of EGFP-S6K1. C) Corresponding lifetime distribution map of each pixel lifetime value with a lifetime mean (τ_m). D) Confocal images of EGFP-S6K1 with E) mDsRed-raptor co-expression. F) FLIM image of the fluorescent lifetimes of EGFP-S6K1 with G) Corresponding*

lifetime distribution map. H) Confocal images of EGFP-S6K1 with I) mDsRed-Rheb co-expression. J) FLIM image of the fluorescent lifetimes of EGFP-S6K1 with K) Corresponding lifetime distribution map. All FLIM images generated by the FLIM analysis software and distributions exported (B&H SPCImage version 6.0). Representative data from three independent experiments are shown. Error bars show the standard deviation. Scale bar = 10 µm in all images.

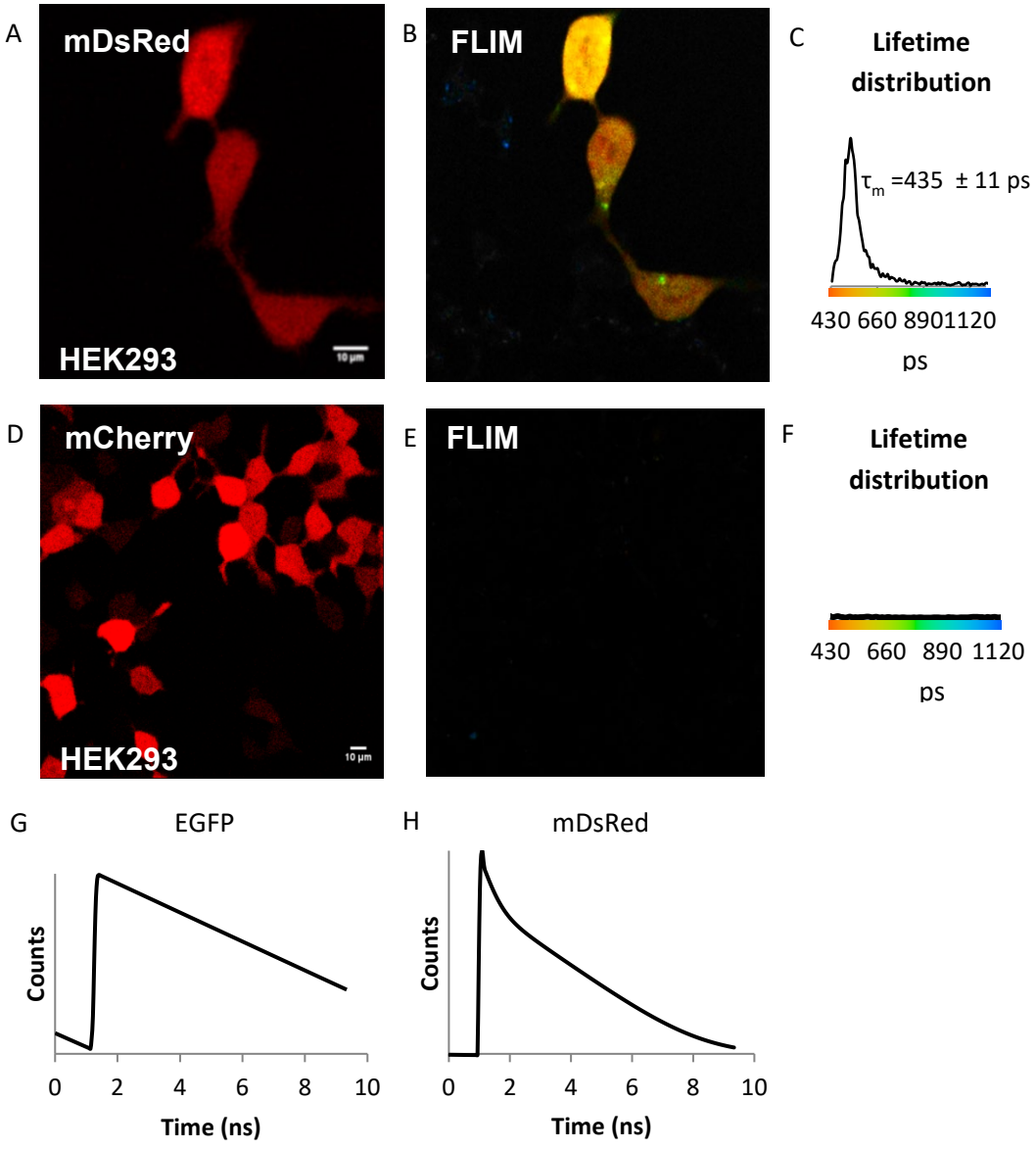

Figure 3.11: mDsRed unsuitable for multiphoton GFP-RFP (protein-protein) FRET-FLIM studies. *A) Confocal image of mDsRed only in HEK293 cells. B) FLIM image of the fluorescent lifetimes of mDsRed at 910 nm excitation. C) Corresponding lifetime distribution map of each pixel lifetime value with a lifetime mean (τ_m). D) Confocal image of mCherry only in HEK293 cells. E) FLIM image of the fluorescent lifetimes of mCherry at 910 nm excitation. F) Corresponding lifetime distribution map of each pixel lifetime value. All FLIM images generated by the FLIM analysis software and distributions exported (B&H SPCImage*

version 6.0). G) Fitted mono-exponential decay of EGFP on a y-axis log scale. H) Fitted multi-exponential decay of mDsRed on a y-axis log scale. Scale bar = 10 µm in all images.

3.2.8 S6K1 interaction with raptor in live cells using FRET-FLIM

Having confirmed the suitability of mCherry as an acceptor for multiphoton FRET-FLIM with GFP tagged proteins, FRET-FLIM was then performed on live HEK293 cells co-expressing EGFP-S6K1 and mCherry-raptor. As shown in **Figure 3.12**, the lifetime of EGFP-S6K1 (2.6 ± 0.01 ns) was quenched to 2.4 ± 0.05 ns when co-expressed with mCherry-raptor. The quenching of the EGFP-S6K1 lifetime appeared to be stronger in the cytoplasm with a lifetime of 2.3 ± 0.03 ns where raptor is predominately localised, compared to the lifetime (2.4 ± 0.05 ns) of whole cells (**Figure 3.12H**). This indicates direct physical interaction between S6K1 and raptor in living cells. The change in donor lifetime was statistically determined by fitting to a gaussian function as shown in **Figure 3.12J**, and a difference of 200 ps in the peak profile identified, a value considered to be significant as discussed in sub-chapter **3.3: Discussion**. These interaction studies provide strong evidence to support the notion that the translocation of S6K1 to the cytoplasm with raptor co-expression is related to its interaction.

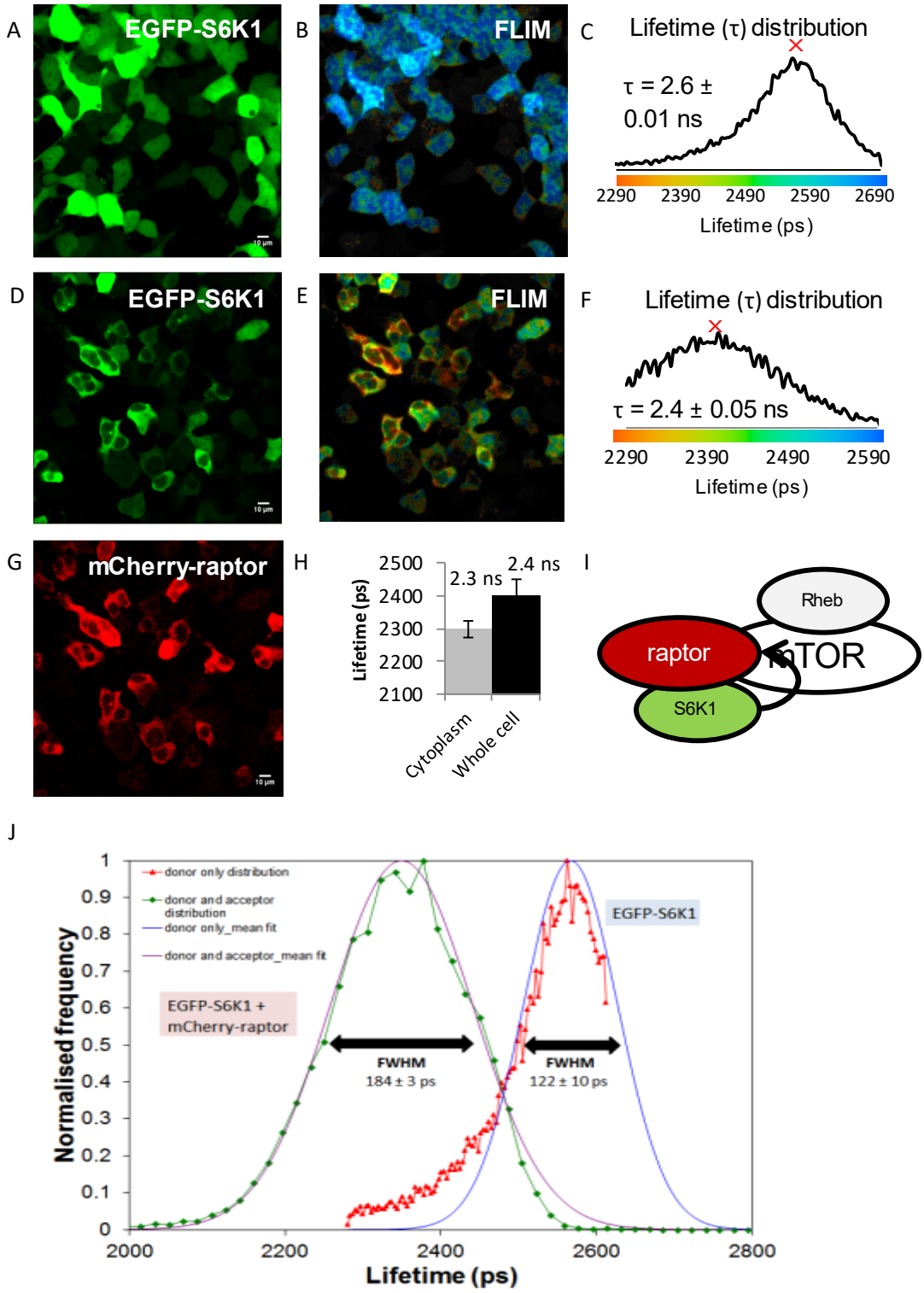

Figure 3.12: Direct interactions between S6K1 and raptor in living cells. *Confocal image of A) EGFP-S6K1 expressed in HEK293 cells. B) FLIM image of the fluorescent lifetimes of EGFP-S6K1. C) Corresponding lifetime distribution map of each pixel lifetime value with a lifetime mean (τ_m). Confocal images of D) EGFP-S6K1 with G) mCherry-raptor co-expression. E) FLIM image of EGFP-S6K1. F) Corresponding lifetime distribution map of each pixel lifetime value. H) Graph of FRET changes between cytoplasm and whole cell lifetimes. I) Schematic of proposed interaction. J) Graph showing lifetime separation of*

*EGFP-S6K1 (donor) with EGFP-S6K1 and mCherry-raptor (acceptor) fitted in MATLAB V.R2013A in conjunction with ezyfit software (V.2.42) to a Gaussian distribution 'a*exp(-((x-x_0)^2)/(2*sigma^2))' where x_0 = mean and 2*sigma is Full Width at Half Maximum (FWHM). All FLIM images generated by the FLIM analysis software and distributions exported (B&H SPCImage version 6.0). Experiments performed minimum of three independent times. Error representative of standard deviation. Scale bar = 10 μm in all images.*

3.2.9 S6K1 interaction with mTOR in live cells using FRET-FLIM

The interaction between S6K1 and the rest of the subunit proteins, including mTOR, was also investigated to obtain a spatial understanding of S6K1 binding onto the complex. **Figure 3.13** gives the donor lifetime of EGFP-mTOR alone (2.60 ± 0.01 ns) in HEK293 cells and the lifetime of EGFP-mTOR co-expressed with S6K1-mCherry (2.50 ± 0.04 ns). This lower lifetime change, 100 ps, in comparison to the 200 ps interaction (found between S6K1 and raptor) suggests a weaker interaction between mTOR and S6K1 and this is discussed further in section **3.3: Discussion**.

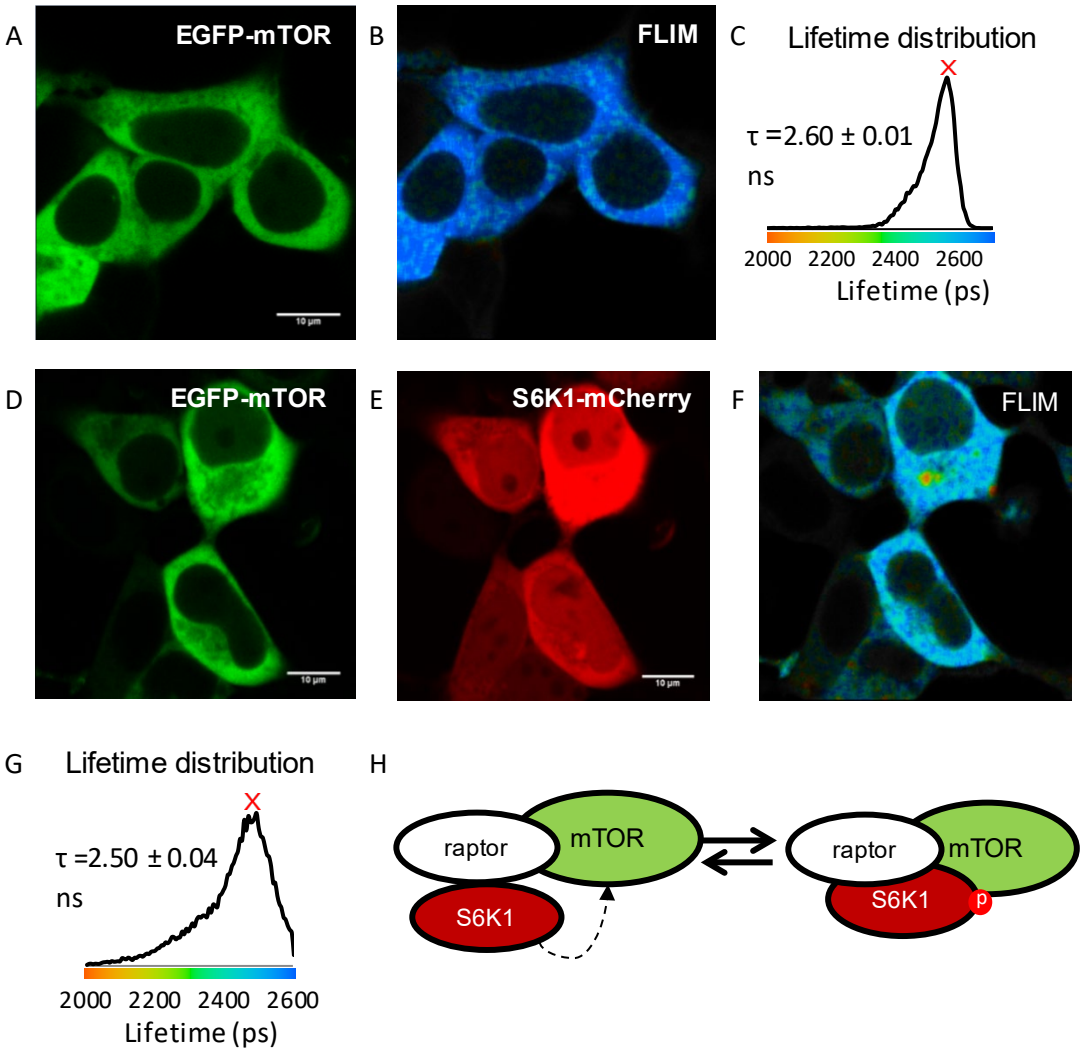

Figure 3.13: Interactions between S6K1 and mTOR in living cells. *Confocal image of A) EGFP-mTOR expressed in HEK293 cells. B) FLIM image of the fluorescent lifetimes of EGFP-mTOR. C) Corresponding lifetime distribution map of each pixel lifetime value with a lifetime mean (τ_m). Confocal images of D) EGFP-mTOR with E) S6K1-mCherry co-expression. F) FLIM image of EGFP-mTOR. G) Corresponding lifetime distribution map of each pixel lifetime value. H) Schematic of possible dynamic or long distance interaction that could be masked in lifetime collection. Black dashed arrow shows possible dynamic movement/conformational change. Experiments performed a minimum of three independent times. Error representative of standard deviation. Scale bar = 10 µm in all images.*

3.2.10 Lack of S6K1 interaction with Rheb in live cells using FRET-FLIM

FRET-FLIM experiments were also performed between EGFP-Rheb and S6K1-mCherry, co-expressed in living HEK293 cells. As shown in **Figure 3.14**, no interaction between S6K1 and Rheb was observed as evident by lack of change in the natural lifetime of EGFP-Rheb (2.5 ± 0.01 ns). In addition, the lack of

interactions between Rheb and S6K1 were supported by co-localisation studies using high resolution imaging. The results obtained showed poor co-localisation of S6K1 and Rheb when EGFP-S6K1 was co-expressed with mDsRed-Rheb in live HEK293 cells. An absence of S6K1 fluorescence in the ER/Golgi/peri-nuclear regions was observed whilst Rheb fluorescence was higher in these sub-cellular regions (**Appendix B.2**).

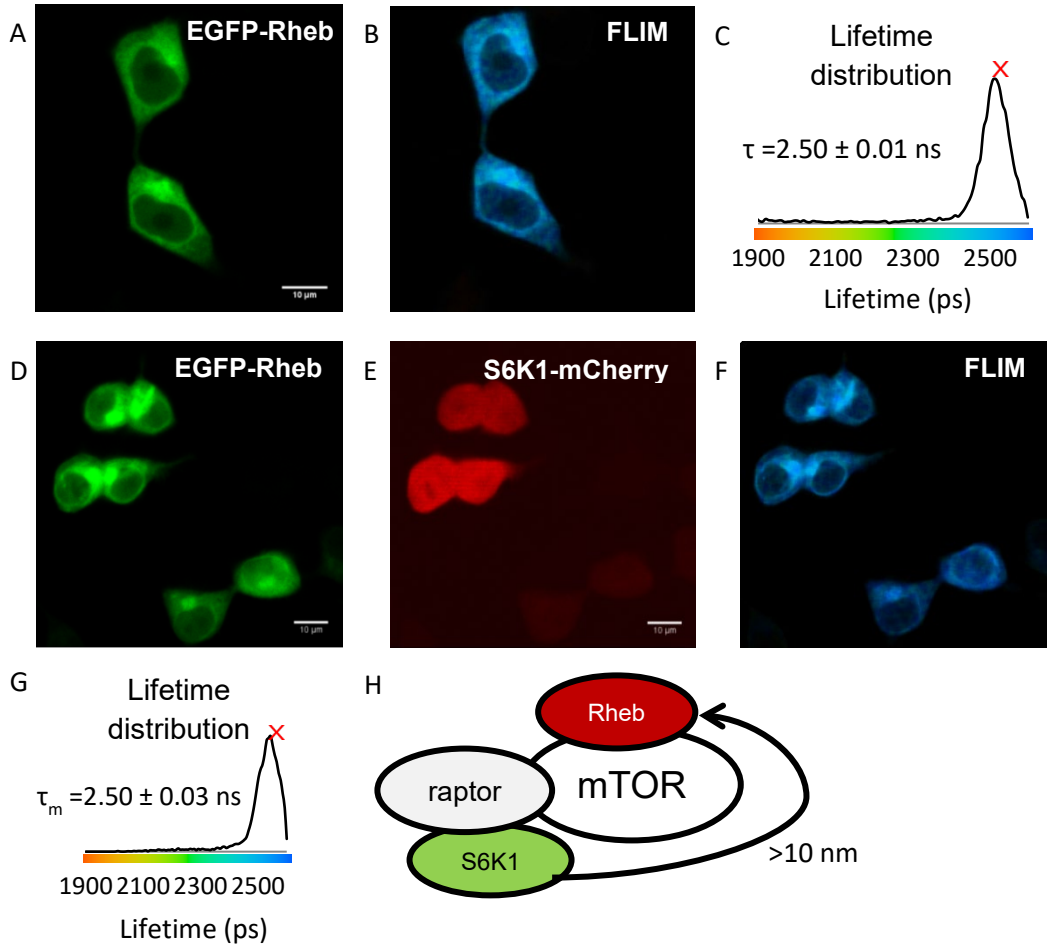

Figure 3.14: Interactions between S6K1 and Rheb in living cells. *Confocal image of A) EGFP-Rheb expressed in HEK293 cells. B) FLIM image of the fluorescent lifetimes of EGFP-Rheb. C) Corresponding lifetime distribution map of each pixel lifetime value with a lifetime mean (τ_m). Confocal images of D) EGFP-Rheb with E) S6K1-mCherry co-expression. F) FLIM image of EGFP-Rheb. G) Corresponding lifetime distribution map of each pixel lifetime value. H) Schematic of proposed long distance interaction. Representative data from three independent experiments are shown. Error representative of standard deviation. Scale bar = 10 μm in all images.*

3.2.11 S6K1 pull-down with raptor, mTOR and Rheb

To further validate the FRET-FLIM findings, pull-down (co-immunoprecipitation) assays were performed in HEK293F cells expressing the following constructs alone or in combination: EGFP-S6K1, mCherry-raptor, FLAG-mTOR and mDsRed-Rheb. Experimental detail of this technique is given in **Chapter 2: materials and methods**. Complexes were bound to nickel resins and eluted. As summarised in **Figure 3.15** from the compilation of Western blots and coomassie gels; pulled-down results were in line with the FRET-FLIM data where strong interaction between S6K1 and raptor was observed while a weak interaction between S6K1 and mTOR and no interaction with Rheb were detected. Furthermore, S6K1 with both mTOR and raptor were all pulled-down together indicating S6K1 is bound onto the complex.

3.2.12 S6K1 interaction with FKBP12 in live cells using FRET-FLIM

Having placed S6K1 onto mTORC1, the assembly and relative orientation of S6K1 binding onto the complex as a whole was investigated by determining the interaction between S6K1 and the FKBP12-rapamycin complex, known to bind to mTOR (Sabers *et al.*, 1995). HEK293 cells co-expressing both mCherry-FKBP12 and EGFP-S6K1 were treated with rapamycin for 30 minutes and then imaged using FRET-FLIM. The natural lifetime of EGFP-S6K1 (2.6 ± 0.01 ns, as stated in **3.2.8)** was quenched to 2.50 ± 0.02 ns in the presence of mCherry-FKBP12-rapamycin, shown in **Figure 3.16**. This 100 ps change in lifetime was similar to that observed between mTOR and S6K1 (see **3.2.9**) and falls outside the 200 ps confidence for a direct interaction, suggestive of long distance interactions with S6K1 binding equidistantly to both FKBP12-rapamycin and mTOR.

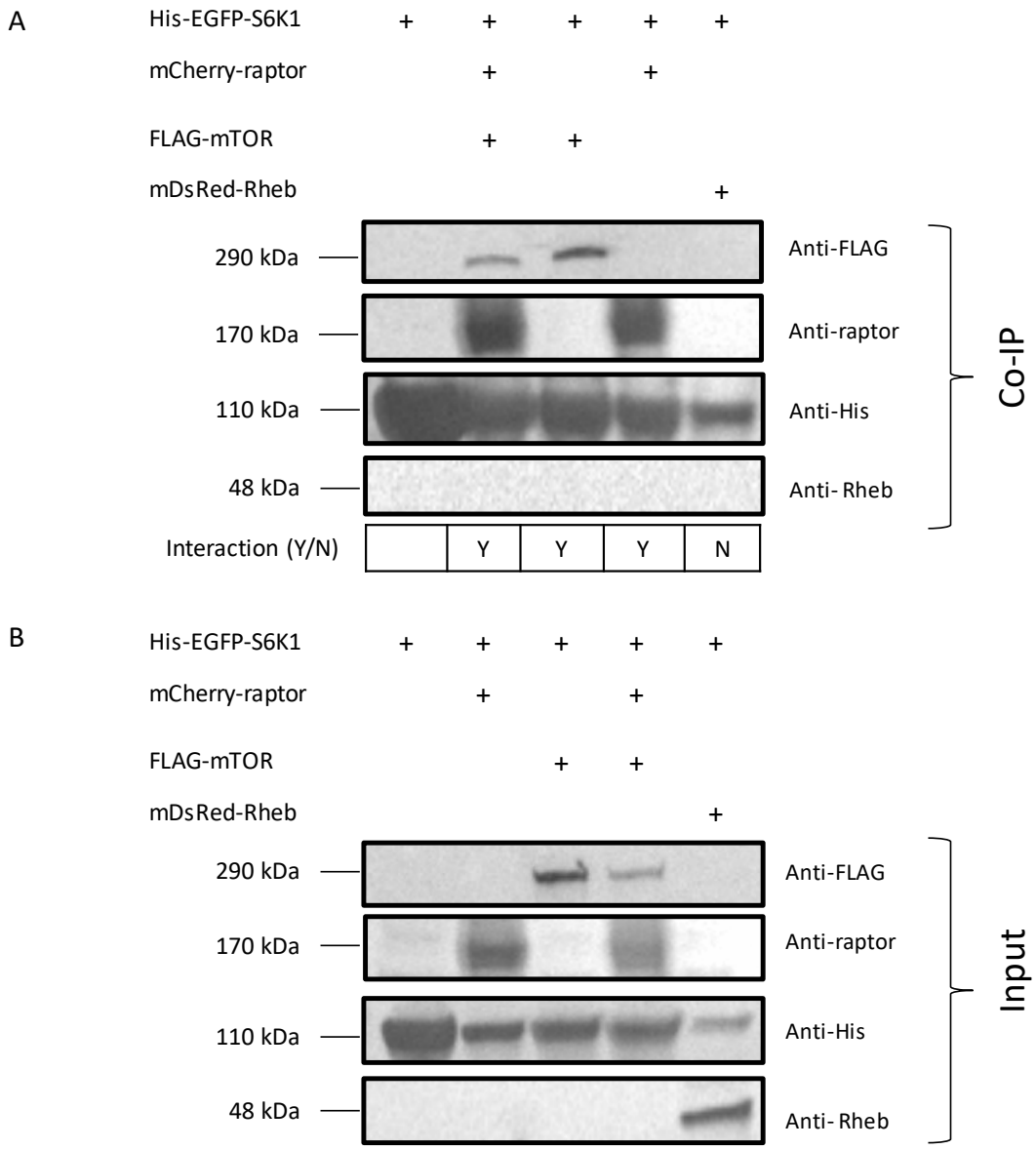

Figure 3.15: Pull-down interactions between S6K1 and mTORC1 in mammalian cells. *A) Western blots of denatured (by SDS) eluted complexes (from 40 µL of eluted sample) of S6K1 + raptor, S6K1 + mTOR, S6K1 + raptor + mTOR and S6K1 + Rheb are shown from HEK293F cells. Presence of all expected interacting proteins + His-EGFP-S6K1 ("bait" protein) shows interaction in the co-IP blots whilst absence of expected binding protein + presence of His-EGFP-S6K1 ("bait" protein) indicates no interaction. Summary of interactions are shown and assigned (yes/no) Y/N. B) Lysates are shown (input) of lysed soluble sample before pull-down (from 1 mL of sample). HA-mCherry-raptor was blotted for using anti-raptor antibodies, His-EGFP-S6K1 was blotted for using anti-His antibodies, mDsRed-Rheb was blotted using anti-Rheb antibodies and FLAG-mTOR was blotted for using anti-FLAG antibodies. Full-length gels and blots are presented in* ***Appendix B3****.*

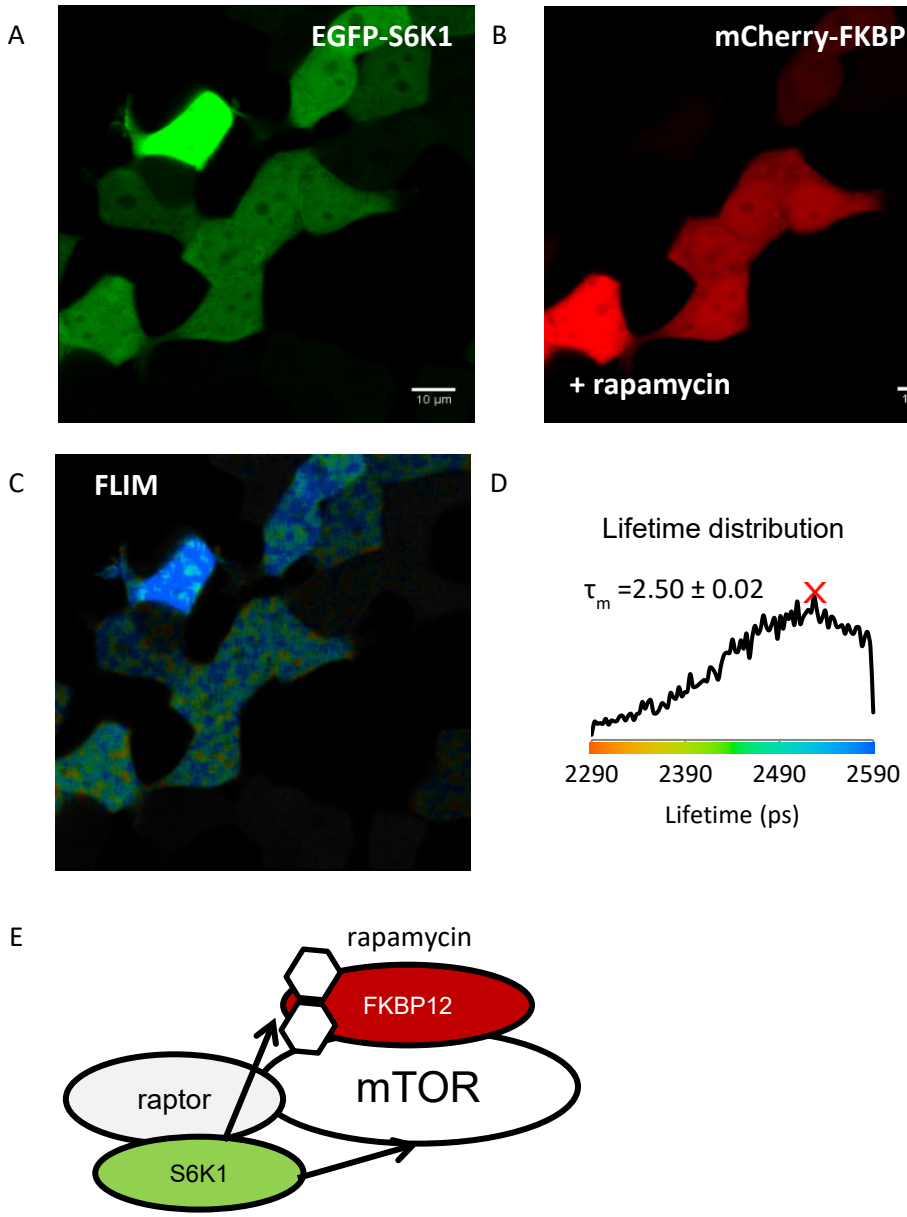

Figure 3.16 Interactions between S6K1 and FKBP12-rapamycin in living cells. *Confocal images of A) EGFP-S6K1 with B) mCherry-FKBP12 co-expressed and treated with rapamycin (1 µM) for 30 minutes in HEK293 cells. C) FLIM image of the fluorescent lifetimes of EGFP-S6K1. (D) Corresponding lifetime distribution map of each pixel lifetime value with a lifetime mean (τ_m). E) Predicted schematic of S6K1 interaction with mTOR and the FKBP12-rapamyin complex. Representative data from three independent experiments are shown. Error representative of standard deviation. Scale bar = 10 µm in all images.*

3.2.13 PCR screen of ΔmTOR-mCherry and sequencing of raptor-YFP

Multi-colour tagging of mTORC1 sub-unit proteins for studying the mTOR complex, its assembly and dynamics in living cells was addressed in light of the findings above where the expression of the raptor component was seen to be critical in the

recruitment of S6K1 onto the mTOR complex. To this end, other fluorescently tagged mTORC1 constructs were made. Full length mTOR cloned with a mCherry tag was attempted using in-fusion cloning (see **Chapter 2: materials and methods**). A PCR screen using a pOPIN T7 forward primer and reverse mTOR primer was carried out to verify the plasmid. However, unexpectedly as shown in **Figure 3.17A**, a PCR band of the insert product corresponding to a truncation (~2323 bp) was seen. This was further validated by sequencing. In addition, full length raptor was cloned with a YFP tag. Due to the large nature of the insert product (~4000 bp), a PCR screen was simulated using the pOPIN T7 forward primer and the reverse raptor primer using software (**Figure 3.17B**). After successfully simulating the PCR screen, the final construct was sent for sequencing and positively matched with the original raptor sequence as shown in **Figure 3.17C**.

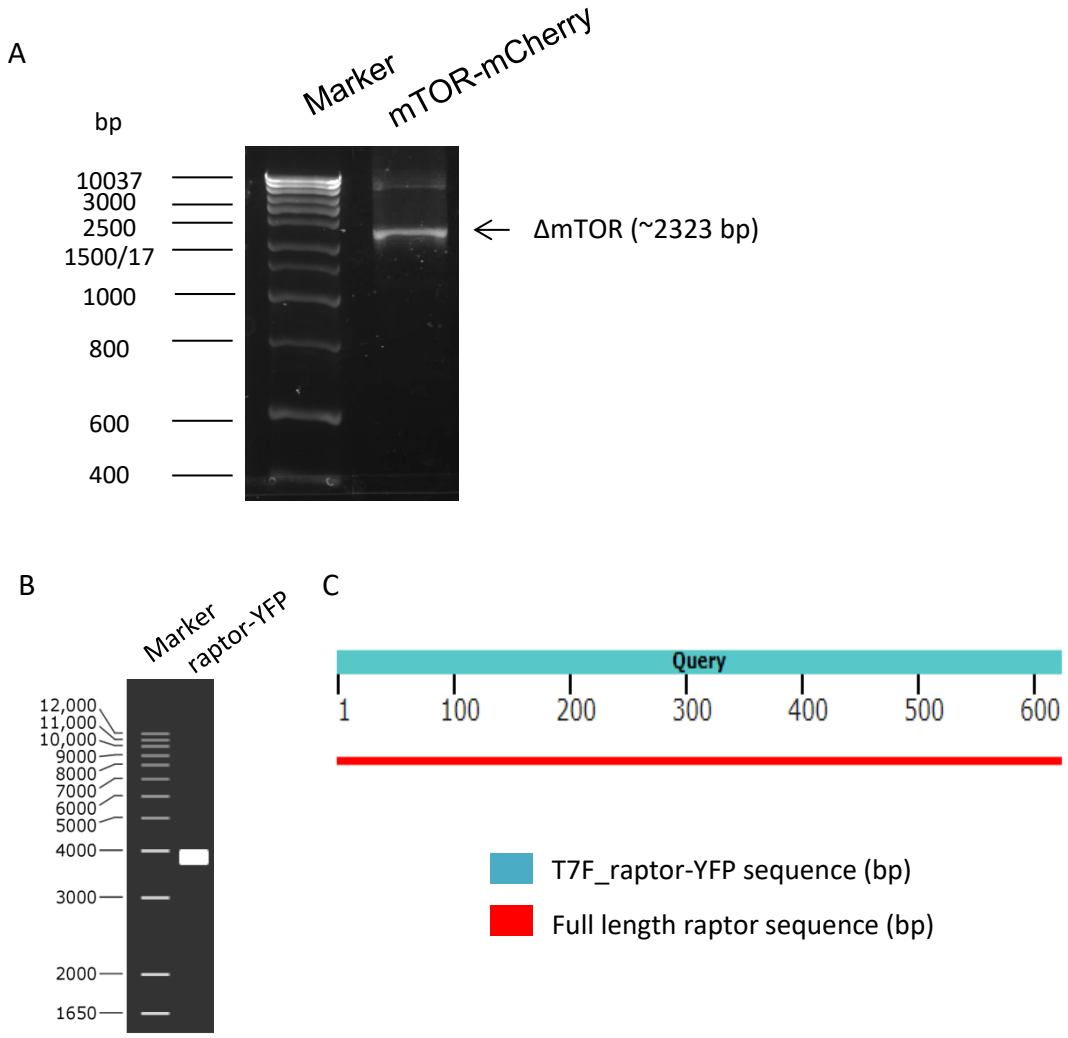

Figure 3.17: PCR screen for ΔNmTOR-mCherry and sequencing of raptor-YFP. *A) Analysis of PCR products ran by agarose gel electrophoresis with marker shown on the left (bp) and insert product on the right indicating a band corresponding to truncated mTOR in the pOPINE-3C-mCherry vector. B) Simulated analysis of PCR products by agarose gel electrophoresis using the SnapGene software. A band corresponding to full length raptor was predicted. C) Sequence alignment of sequencing results with original raptor sequence using Basic Local Alignment Search Tool (NCBI) (date generated 30_07_18).*

3.2.14 Imaging S6K1 translocation with mutated (ΔN) mTOR

Having confirmed that the translocation of S6K1 in the living cell is a process driven by raptor binding and thus recruitment onto mTORC1, the mechanism of this event in relation to mTOR was investigated with the non-functional mTOR mutant generated in **3.2.13**. Imaging multiple fluorescently tagged mTORC1 subunit proteins with the newly made N-terminus truncated mTOR construct (ΔNmTOR-

mCherry) in HEK293 cells by confocal microscopy showed that although S6K1 translocation was present in wildtype (YFP-mTOR) triple-expression, S6K1 translocation with the mutant was repressed (**Figure 3.18**). In addition, the expression of raptor yielded an increase in S6K1 phosphorylation determined by Western blot analysis while expression of the mutant mTOR resulted in an inhibition in phosphorylation, indicating that mTOR, particularly the N-terminus (**Figure 3.18**), may have an involvement in a secondary recruitment mechanism which may be required to stabilise S6K1 onto the complex.

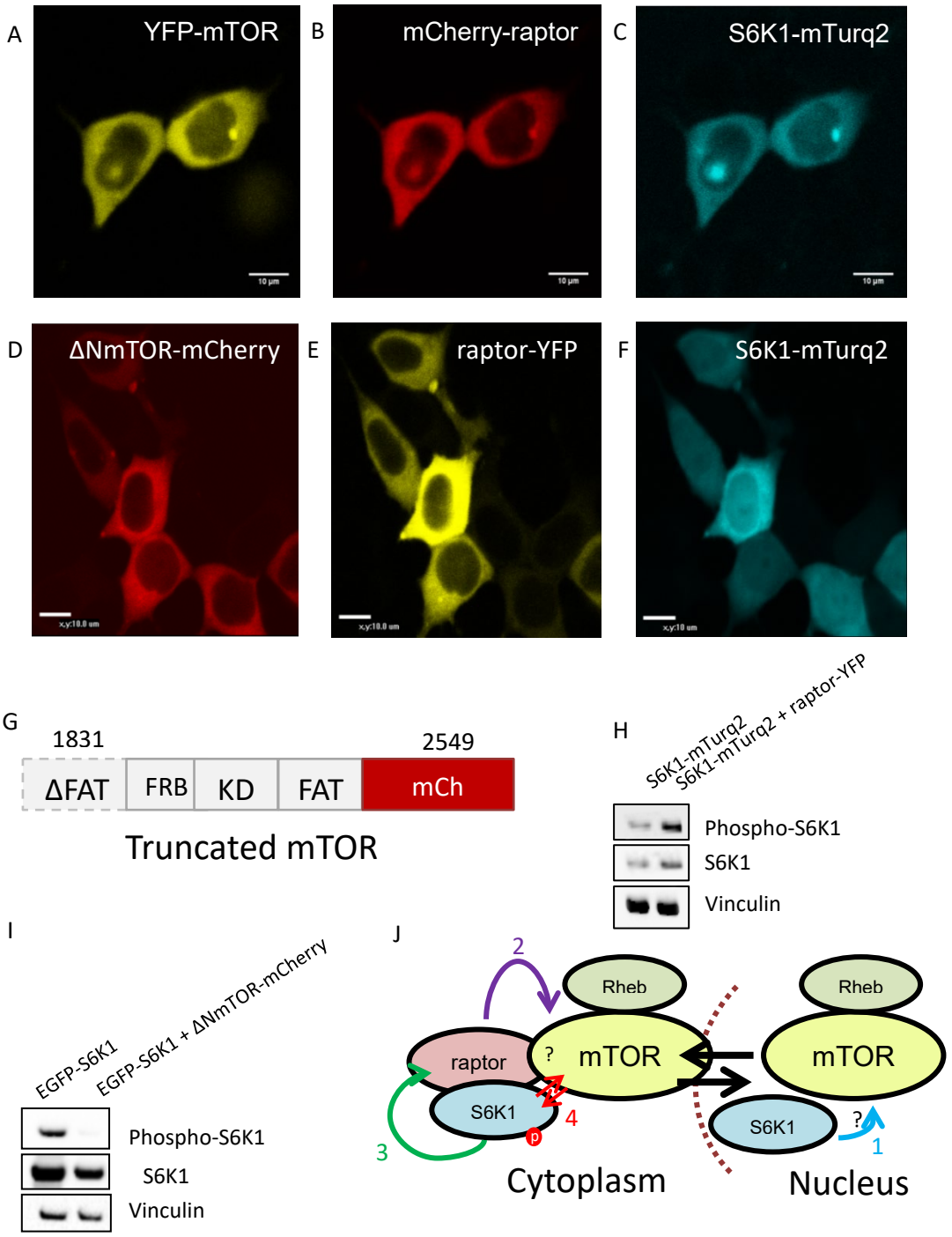

Figure 3.18: Secondary recruitment mechanism involving functioning mTORC1. *Confocal images of triple expression of A) YFP-mTOR, B) mCherry-raptor and C) S6K1-mTurquoise2. Confocal images of D) N-terminal truncated mTOR-mCherry, E) raptor-YFP and F) S6K1-mTurquoise2. G) Structure of N-terminal truncated mTOR-mCherry construct showing domains and numbered amino acid sequence. H) and I) Western blots for phospho-S6K1 with either raptor or ΔNmTOR-mCherry co-expression with S6K1. J) Schematic of proposed sequence of recruitment and interaction of S6K1 onto mTORC1. Representative data from three independent experiments are shown. Scale bar = 10 μm in all images.*

3.2.15 Imaging S6K1 translocation with PRAS40 and 4EBP1

Next, the relationship between other mTORC1 substrates such as PRAS40 and 4EBP1 with S6K1 was investigated. Live HEK293 cells co-expressing fluorescently tagged 4EBP1 (4EBP1-GFPspark) with mCherry-raptor also showed a translocation effect with 4EBP1 moving out of the nucleus, giving a cytoplasmic localisation as shown in **Figure 3.19**. These results suggest that 4EBP1 could compete with S6K1 for binding onto mTORC1 and this is presented below. The PRAS40 protein, known to bind to both raptor and mTOR was expressed with a fluorescent tag (YFP-PRAS40). YFP-PRAS40 localisation alone was cytoplasmic. When S6K1-mTurq2 was expressed with mCherry-raptor and either 4EBP1-GFPSpark or YFP-PRAS40, a 2-times decrease in S6K1 translocation to the cytoplasm was observed as interpreted by the presence of mTurq2 intensity in the nucleus (**Figure 3.19**) indicating that the translocation/binding to raptor can be dynamically manipulated in living cells with other mTORC1 binding substrates.

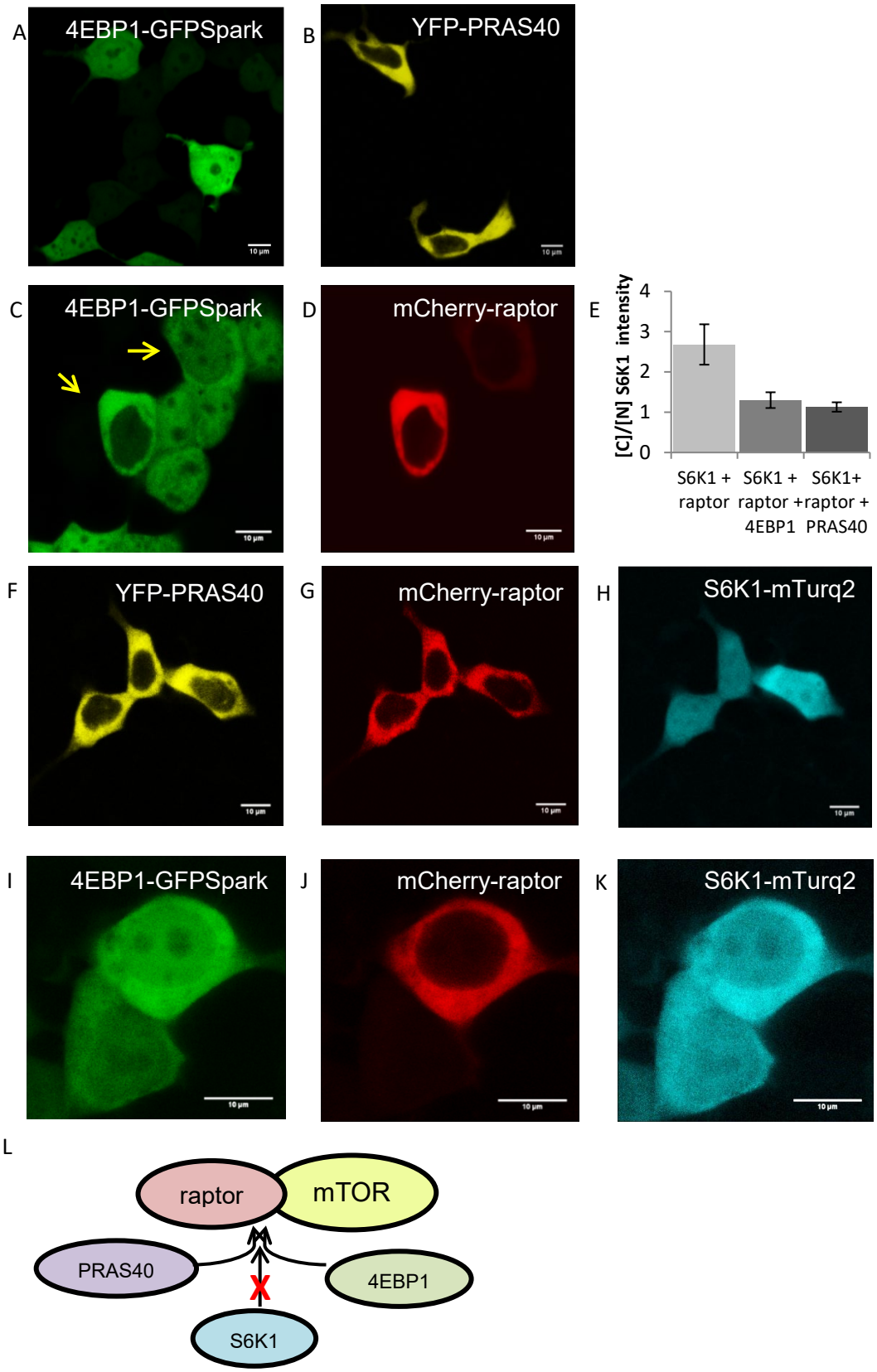

Figure 3.19: Inhibition of S6K1 translocation with PRAS40 and 4EBP1 competitive binding. *Confocal images of A) 4EBP1-GFPSpark only, B) YFP-PRAS40 only, C) 4EBP1-GFPSpark with D) mCherry-raptor co-expression, E) graph showing cytoplasmic/nuclear intensity of S6K1 with raptor +/- 4EBP1 or PRAS40 expression (n=10) taken from three*

independent experiments where the error represents the standard deviation. Confocal images of triple expression of F) YFP-PRAS40 with G) mCherry-raptor and H) S6K1-mTurquoise2. Confocal images of triple expression of I) 4EBP1-GFPSpark with J) mCherry-raptor and K) S6K1-mTurquoise2. L) Schematic of proposed dynamic interactions of other mTORC1 substrates. Yellow arrows show translocation of 4EBP1. Experiments performed a minimum of three independent times. Scale bar = 10 μm in all images.

3.2.16 4EBP1 interaction with raptor using FRET-FLIM

The interaction between 4EBP1 observed with mCherry-raptor was investigated using FRET-FLIM to support the hypothesis that just like with S6K1, the translocation event is related to direct physical interaction with the raptor scaffold protein. **Figure 3.20** gives the natural lifetime of 4EBP1-GFPSpark in living HEK293 cells as 2.40 ± 0.05 ns. Upon co-expressing with mCherry-raptor in HEK293 cells, the donor lifetime was quenched to 2.20 ±0.06 ns. These results show that 4EBP1 directly interacts with raptor and may also be recruited onto mTORC1 in live cells.

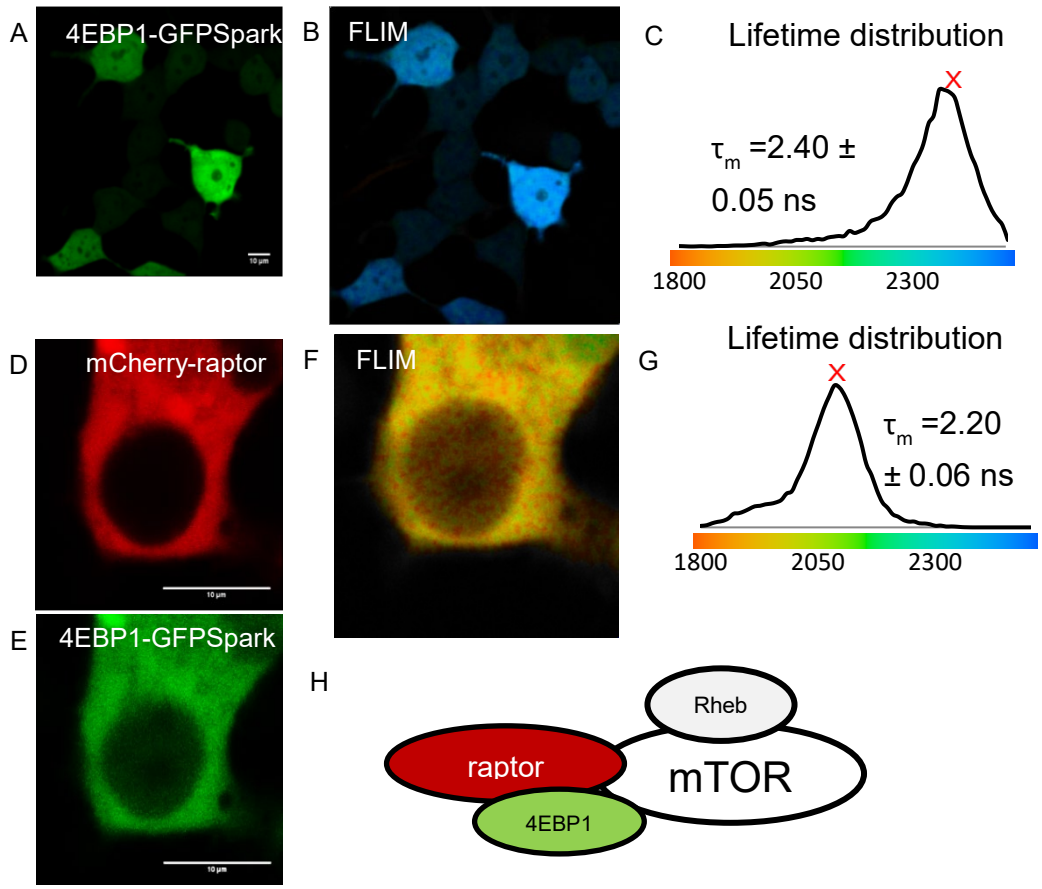

Figure 3.20: Interactions between 4EBP1 and raptor in living cells. *Confocal image of A) 4EBP1-GFPSpark. B) FLIM image of the fluorescent lifetimes of 4EBP1-GFPSpark. C)*

Corresponding lifetime distribution map of each pixel lifetime value with a lifetime mean (τ_m). D) Confocal image of mCherry-raptor co-expressed with E) 4EBP1-GFPSpark. F) FLIM image of the fluorescent lifetimes of 4EBP1-GFPSpark. G) Corresponding lifetime distribution map of each pixel lifetime value with a lifetime mean (τ_m). H) Proposed schematic of 4EBP1 interaction with mTORC1. Experiments performed a minimum of three independent times. Scale bar = 10 μm in all images.

3.2.17 Phospho-S6K1 inhibition with rapamycin and Rheb

As Rheb is known to activate mTORC1 (see **Chapter 1**), the regulation of S6K1 and the effect by Rheb was next examined. The overexpression of EGFP-S6K1 with mDsRed-Rheb in HEK293 cells resulted in a 128% induction in S6K1 phosphorylation quantified by Western blot analysis as shown in **Figure 3.21**. Inhibition of S6K1 phosphorylation with rapamycin treatment was only observed when both EGFP-S6K1 and mDsRed-Rheb were co-expressed together (71% decrease in phosphorylation). This highlights Rheb to be sensitive to rapamycin treatment and may function in a role beyond upstream mTOR activation.

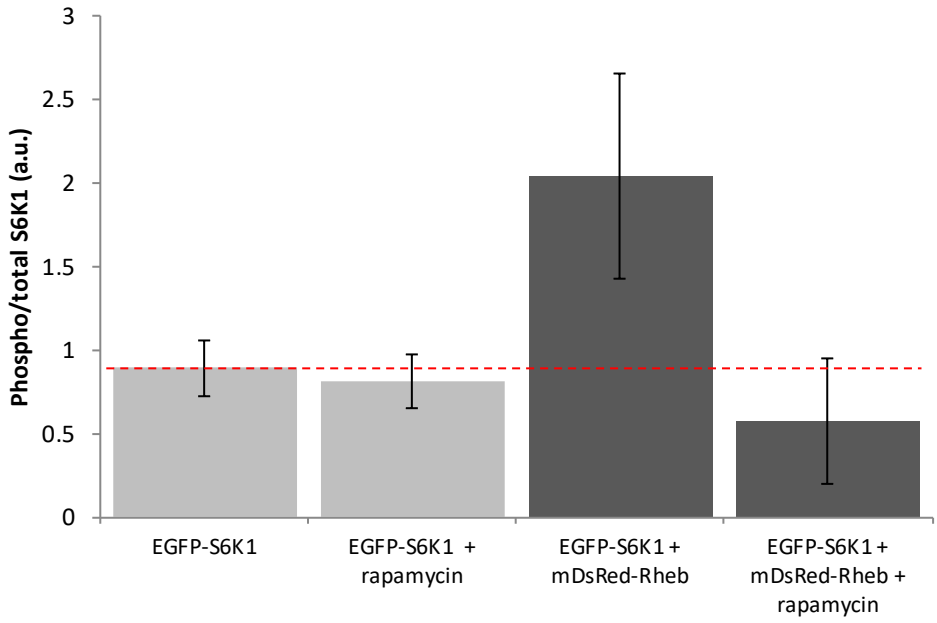

Figure 3.21: S6K1 phosphorylation with Rheb expression and rapamycin treatment. *Quantified western blot data showing % phospho-S6K1 of EGFP-S6K1 (phosphorylated S6K1/ total S6K1 x 100) with and without rapamycin (200 nM for 2 hour treatment) as well as with Rheb co-expression, with and without rapamycin treatment. Data representative of three independent experiments where error shows standard deviation. Red dotted line = baseline.*

3.2.18 Imaging S6K1 translocation with both Rheb and rapamycin

Using the information from section **3.2.17**, studies were performed in HEK293 cells transfected with YFP-Rheb, S6K1-mTurqouise2 and mCherry-raptor and treated with and without rapamycin (1 μM) treatment (**Figure 3.22**). No effect was observed on the translocation of S6K1 as shown by no change in S6K1 nuclear fluorescence localisation, cementing the idea that the translocation of S6K1 is not triggered by mTOR mediated phosphorylation. The translocation of S6K1 to the cytoplasm may however be required for mTOR to function efficiently for S6K1 phosphorylation and this will be presented next.

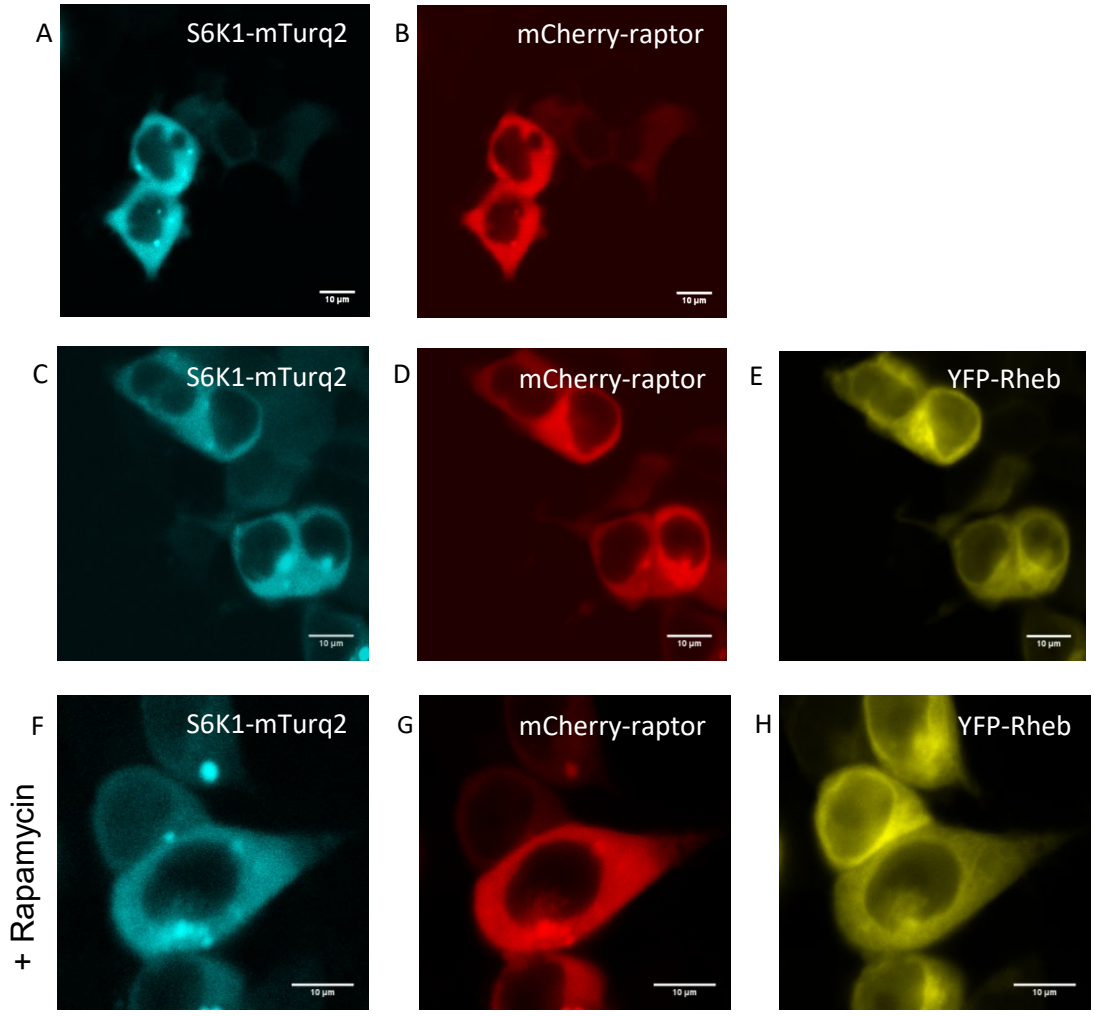

Figure 3.22: Effect of rapamycin on translocated S6K1 with Rheb expression. *Confocal images of A) S6K1-mTurq2 co-expressed with B) mCherry-raptor. C) S6K1-mTurq2 triple expression with D) mCherry raptor and E) YFP-Rheb. F) S6K -mTurq2 triple expression with*

G) mCherry raptor and H) YFP-Rheb with 2 hour rapamycin (1 μM) treatment. Experiments performed a minimum of three independent times. Scale bar = 10 μm in all images.

3.2.19 Immunofluorescence labelling of p-S6K1 in fixed cells

The localisation of mTOR mediated phosphorylation of S6K1 was then investigated as follow-on from the interaction studies to study the mechanism of mTOR phosphorylation in the cell. The use of cell fixation with immunofluorescence labelling (see **Chapter 2: materials and methods** for details) was first turned to as a means to investigate the localisation of phospho-S6K1. Cells expressing EGFP tagged S6K1 were fixed with paraformaldehyde (formaldehyde), methanol (alcohol) or glyoxal (dialdehyde) fixatives. After permeabilisation, primary anti-phospho-S6K1 and secondary fluorescently-conjugated antibodies were introduced and imaged as shown in **Figure 3.23**. Paraformaldehyde (PFA) fixation caused loss of soluble EGFP-S6K1 from the cytoplasm and this was evident by a loss of 37.3% GFP distribution in the cytoplasm. It was also observed that EGFP-S6K1 leaked into the nucleolus of the cells and that cells generally had more GFP in the nucleus which was not seen prior to PFA fixation. EGFP intensities were quantified to be 67.5 ± 4% in the nucleus and 32.5 ± 4% in the cytoplasm (**Figure 3.24A**). Imaging phospho-S6K1 labelling in PFA fixed cells showed a similar localisation with 60 ± 2% in the nucleus and 40 ± 2% in the cytoplasm (**Figure 3.24B**).

On the other hand, methanol fixation caused loss of EGFP-S6K1 mostly from the nucleus, as evident by the lack of green fluorescence with cytosolic membrane like the peri-nuclear region exhibiting high EGFP-S6K1 intensity. EGFP intensities were quantified to be 39.8 ± 4% in the nucleus and 60.8 ± 4% in the cytoplasm (**Figure 3.24A**). Imaging phospho-S6K1 labelling in methanol fixed cells showed a similar localisation with 41 ± 8% in the nucleus and 59 ± 8% in the cytoplasm (**Figure 3.24B**).

Interestingly, imaging glyoxal fixed EGFP-S6K1 cells provided the best localisation results close to live cell imaging as GFP distributions in both the nucleus and cytoplasm were maintained in almost equal amounts. EGFP intensities were quantified to be 49.5 ± 6% in the nucleus and 50.5 ± 6% in the cytoplasm (**Figure 3.24A**). Imaging phospho-S6K1 in glyoxal fixed cells showed 40 ± 3% staining in the nucleus and 60 ± 3% staining in the cytoplasm (**Figure 3.24B**). The relative higher amounts of phospho-fluorescence in the cytoplasm show that mTOR mediated phosphorylation may be occuring in the cytoplasm. The studies performed with glyoxal fixation were not pursued further as the potential for the reagent as a fixative was not known at the start of the research project and only discovered towards the end.

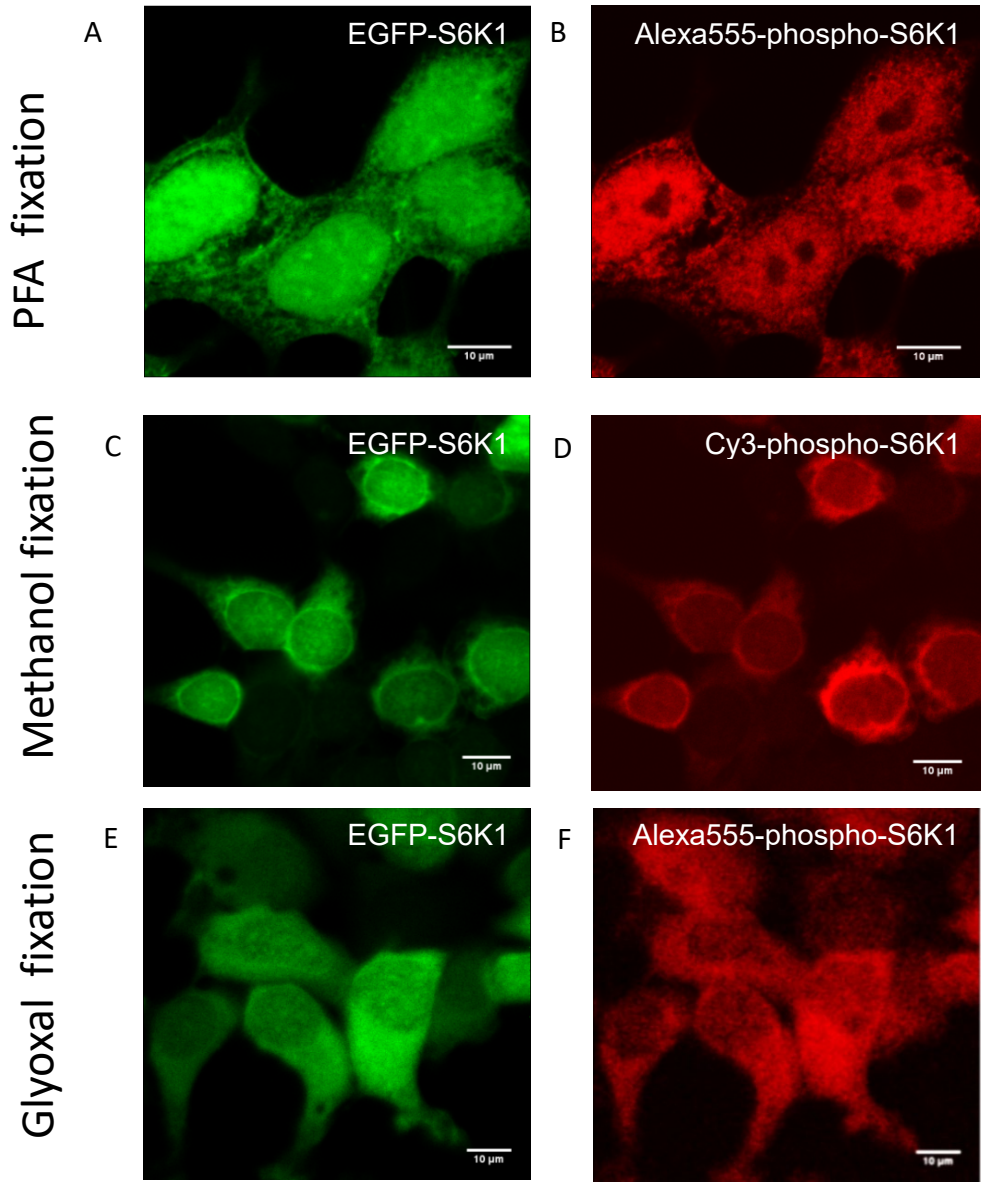

Figure 3.23: Imaging the localisation of phospho-S6K1 in fixed EGFP-S6K1 expressing cells. *Confocal images of paraformaldehyde fixed HEK293 cells expressing (A) EGFP-S6K1 labelled with (B) anti-phospho-S6K1 and Alexa555 antibodies. Methanol fixed HEK293 cells expressing (C) EGFP-S6K1 labelled with (D) anti-phospho-S6K1 and Cy3 antibodies. Glyoxal fixed HEK293 cells expressing (E) EGFP-S6K1 and labelled with (F) anti-phospho-S6K1 and Alexa555 antibodies. Experiments performed a minimum of three independent times. Scale bar = 10 µm in all images*

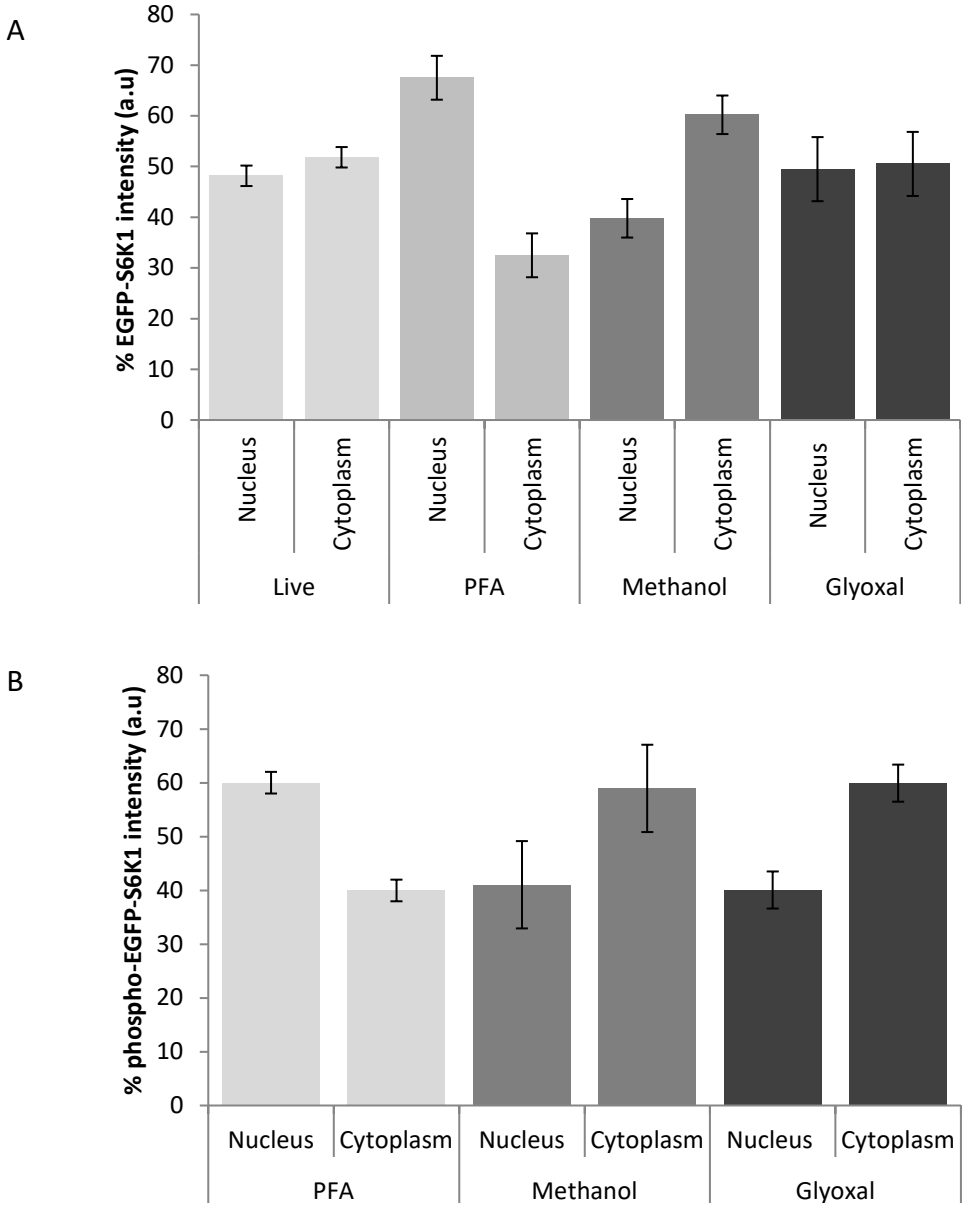

Figure 3.24: Nuclear and cytoplasmic distributions of S6K1 and phospho-S6K1 in various fixatives*. A) Bar graph of nuclear and cytoplasmic distributions of EGFP-S6K1 in live, paraformaldehyde, methanol and glyoxal fixed cells. B) Bar graph of nuclear and cytoplasmic distributions of phospho-EGFP-S6K1 (Cy3/ Alexa555) in paraformaldehyde, methanol and glyoxal fixed cells (number of cells = 10 for each sample) with error bars showing standard deviation. Representative data from three independent experiments are shown.*

3.2.20 S6K1 and p-S6K1 artefacts from immunofluorescence labelling

In addition to the results found above, it was also observed that the PFA fixation process caused extraction of EGFP-S6K1 from the cytoplasm as evident by leaving areas or holes where protein was absent (**Figure 3.25B**). Furthermore, inefficient

labelling was observed at times in some cells where antibodies were unable to reach the nucleus of the cell, leaving a gradient effect staining appearance only in the cytoplasm (**Figure 3.25**). The differences in distribution of EGFP-S6K1 observed for the different fixation methods could hinder and compromise any conclusions regarding phospho-S6K1 localisation. It is also worth noting that PFA fixation of HEK293 cells caused a change in its natural lifetime of EGFP; see **Appendix B.4**, thus demonstrating the need for live cell FRET-FLIM imaging.

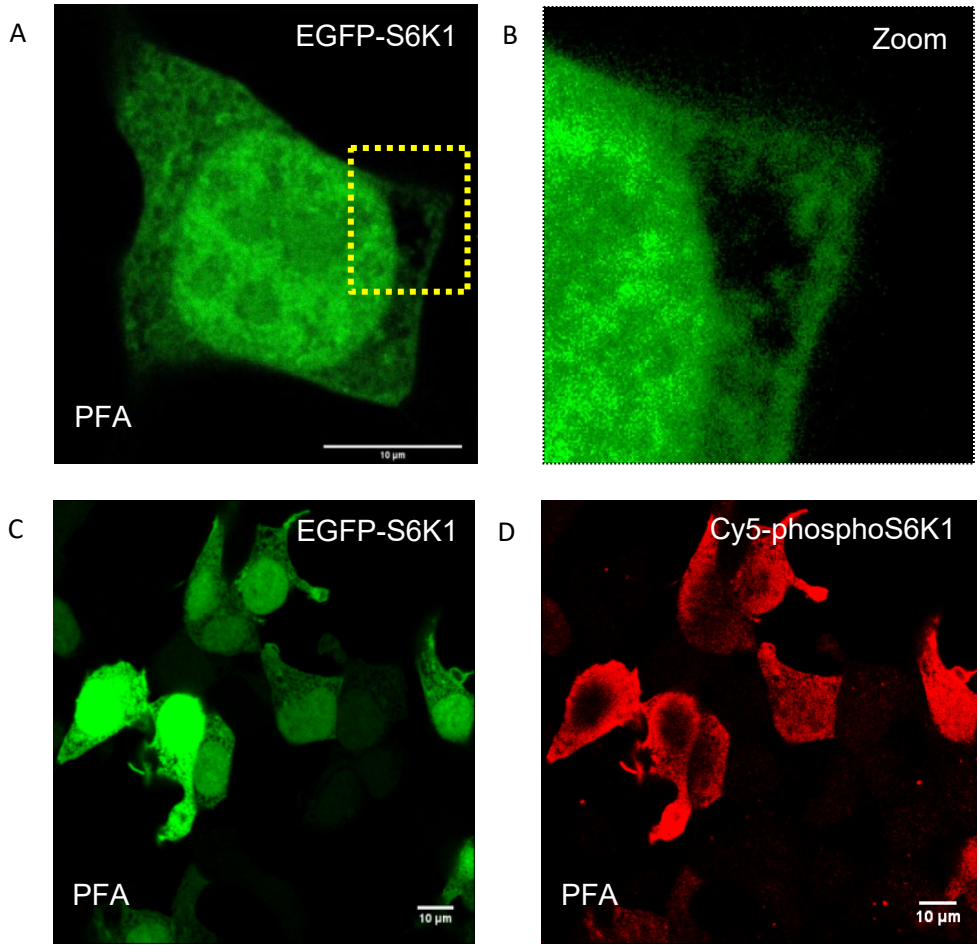

Figure 3.25: Artefact generation from PFA fixation. *Confocal images of HEK293 cells expressing A) EGFP-S6K1 with B) zoom-in area of yellow box. C) EGFP-S6K1 labelled with D) anti-phospho-S6K1 and Cy5 secondary antibody labelling. Experiments performed a minimum of three independent times. Scale bar = 10 µm in all images.*

3.2.21 p-S6K1 immunofluorescence labelling of translocated S6K1

The localisation of phosphorylated S6K1 upon translocation of S6K1 was investigated using immunofluorescence staining. HEK293 cells expressing both

EGFP-S6K1 and mDsRed-raptor were fixed in PFA and labelled for anti-phospho S6K1. The translocated EGFP-S6K1 and labelled phospho-EGFP-S6K1 with Alexa405 showed similar levels of fluorescence in the cytoplasm, **Figure 3.26**, indicating that phosphorylation follows after the translocation of S6K1 and occurs in the cytoplasm. Although some soluble EGFP-S6K1 extraction from the cytoplasm may still have occurred as found in the previous subchapters, the more diffused localisation of S6K1 with raptor in the cytoplasm suggests that S6K1 may be tethered to sub-cellular structures preventing it from being extracted.

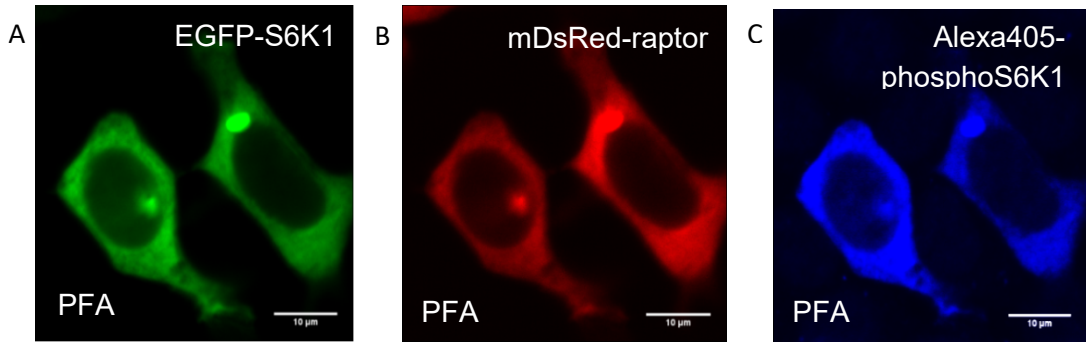

Figure 3.26: Phospho-S6K1 labelling of translocated S6K1. *Confocal images of A) EGFP-S6K1 with B) mDsRed-raptor co-expression with C) anti-phospho-S6K1 and Alexa405 secondary antibody labelling. All cells fixed in PFA. Experiments performed a minimum of three independent times. Scale bar = 10 µm in all images.*

3.2.22 Quantification of overexpressed p-S6K1 with Rheb in fixed cells

As overexpression of Rheb induces a dramatic increase in S6K1 phosphorylation, found earlier in section **3.2.17**, it was hypothesised that higher expression of Rheb would lead to higher phospho-S6K1 staining levels in fixed cells co-expressing fluorescently tagged S6K1. Using transient overexpression as a useful tool to observe differing expression levels of Rheb, cells were fixed in PFA. Given in **Appendix B.5**, no clear correlation between highly expressing Rheb cells and phospho-S6K1 levels was observed, most likely owing to the fixation method. This was apparent by the findings that brighter Rheb cells did not show brighter phospho-S6K1 fluorescence. However, the levels of phospho-S6K1 did appear to correlate to

the levels of S6K1 overexpressed (i.e. brighter GFP S6K1 cells showed brighter phospho-S6K1 fluorescence) and thus no conclusions could be made.

3.2.23 Variation in endogenous p-S6K1 with antibody labelling

A recognised hurdle to overcome in immunofluorescence staining is the lack of specificity and sensitivity of commercially available antibodies which are required to bind to the target of interest. This means non-specific antibody binding may lead to discrepancies in the localisation of phospho-S6K1 indicating that different antibodies to the same target could produce artefacts other than that induced by cell fixation shown in section **3.2.19**. Although Western blot analysis, was unable to detect endogenous phospho-S6K1 levels (section **2.2.3**), immunofluorescence labelling for determining the localisation of endogenous phospho-S6K1 was relied on using several commercial primary antibodies. When using the Cell Signalling antibody (#9234) homogenous levels of endogenous phospho-S6K1 fluorescence in the cytoplasm and nucleus were stained in both PFA fixed HEK293 and HeLa cells, whilst the Millipore (MABS82) antibody stain appeared more cytoplasmic in PFA fixed HEK293 cells, and to some degree in PFA fixed HeLa cells **(Appendix B.6**). A phospho-S6K1 antibody from Thermofisher Scientific (PA1-526) was also trialled in PFA fixed A431 and MCF-7 cells known to have inherit constitutive mTOR activity and thus higher phospho-S6K1 levels in those cell lines are expected, and the labelling stained the cytoplasm with higher fluorescence between cell junctions (**Appendix B.6**). Labelling with only secondary antibodies did not provide any labelling (controls) and these results are shown in **Appendix B7**.

3.2.24 Localisation of endogenous p-S6K1 with Rheb in fixed cells

After further trialling and validation, antibodies from St John's Laboratory were used to label phospho-S6K1 and total S6K1 in PFA fixed HEK293 cells. Confocal imaging provided endogenous phospho-S6K1 and S6K1 localisation labelling results more in line with the current literature compared to that presented before. Endogenous anti-

S6K1 labelling provided similar localisation staining to that observed with GFP tagged S6K1 overexpression by showing fluorescence staining in both the nucleus and cytoplasm in equal amounts. These results may be due to more specific labelling of this antibody compared to previously trialled antibodies for phospho-S6K1. Interestingly, fluorescent punctate structures were observed with endogenous phospho-S6K1 staining and overall the majority of the fluorescence was localised in the nucleus of HEK293 cells (**Appendix B.8**). In order to investigate the translocation of phospho-S6K1 in fixed cells following the stimulation of S6K1 phosphorylation, HEK293 cells with fluorescently labelled Rheb or raptor co-expression were stained for phospho-S6K1. No change in endogenous phospho-S6K1 localisation was observed as seen by a lack of change in fluorescence staining of sub-cellular distributions between transfected and non-transfected cells (**Appendix B.8**) demonstrating that phospho-S6K1 localisation may not be regulated by phosphorylation.

3.2.25 Quantification of endogenous p-S6K1 with Rheb in fixed cells

In order to obtain more insight into Rheb's mechanism of activation in cells, the quantification of Rheb intensity against endogenous phospho-S6K1 levels in HEK293 cells fixed in PFA were carried out similar to that performed with overexpressed S6K1 in section **3.2.22**. As seen with overexpressed S6K1, high Rheb levels (red fluorescence) did not correlate with higher phospho-S6K1 levels (green fluorescence) by cell-cell analysis as shown in **Appendix B.9**. These results suggest that poor fixation may affect S6K1 as a whole and that extraction of soluble proteins may also extend to endogenous proteins.

3.2.26 PCR screen of mCherry-S6K1-EGFP

Having faced issues with fixed cell imaging of S6K1 phosphorylation, attempts were made to determine S6K1 phosphorylation in living cells. Two fluorescent labels were tagged to either end of the S6K1 protein to make a donor-acceptor pair bio-sensor

that would undergo a FRET process following an induced conformational change post mTOR mediated phosphorylation (Komatsu *et al.*, 2011; Zhou *et al.*, 2015), see **Figure 3.28A**. The biosensor should ideally function in living cells and with this in mind was achieved by cloning mCherry and S6K1 together into the pOPINE-3C-EGFP vector (see **Chapter 2: materials and methods**). A PCR screen was performed using the pOPIN T7 forward primer with a reverse S6K1 primer to confirm successful incorporation of insert product. **Figure 3.27** shows a band at around 2256 bp which equates to a mCherry combined with S6K1 PCR insert. Sequencing of both the join ends of the two insert products and vector ends further showed successful cloning. The construct was named S6K1 sensing of mammalian Target Of Rapamycin (SensOR).

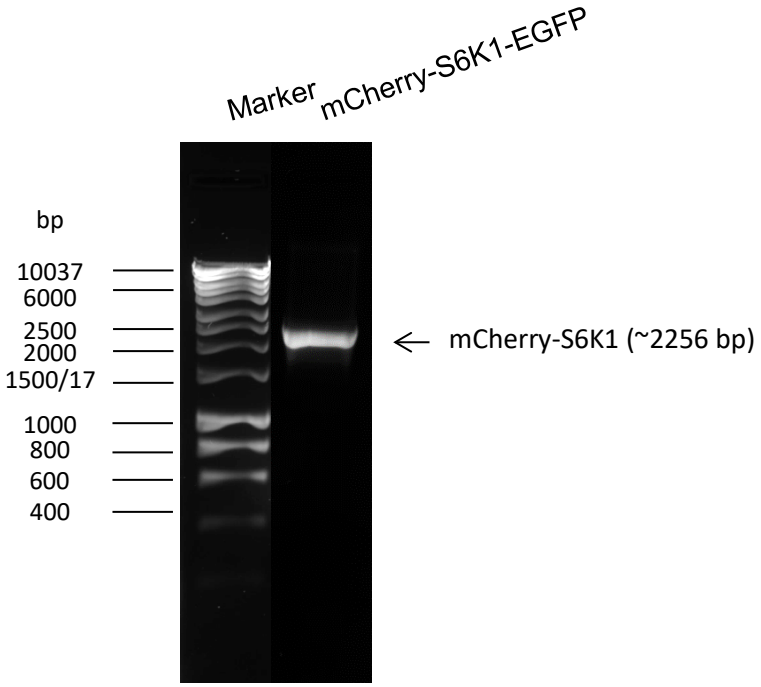

Figure 3.27: Reverse PCR screen of mCherry-S6K1-EGFP. *Analysis of PCR product ran by agarose gel electrophoresis. Marker is shown on the left (bp) with insert product on the right with a band corresponding to mCherry combined with S6K1 in the pOPINE-3C-EGFP vector.*

3.2.27 S6K1 live cell FRET bio-sensor western blot validation

A key goal of this thesis is to show that mCherry-S6K1-EGFP (SensOR) does undergo conformational changes upon phosphorylation and such changes can be

monitored using FRET-FLIM in living cells. An initial validation step for SensOR functionality was to perform Western blot studies on HEK293 cells expressing the construct and probing for mTOR mediated phosphorylation. A band at 130 kDA (MW of mCherry, S6K1 and EGFP combined) was detected by chemiluminescence using anti-S6K1 antibodies as well as a corresponding band using anti-phospho-S6K1 antibodies at the same molecular weight, suggesting that the construct was functional (i.e. could be phosphorylated in the mTORC1 pathway), see **Figure 3.28**.

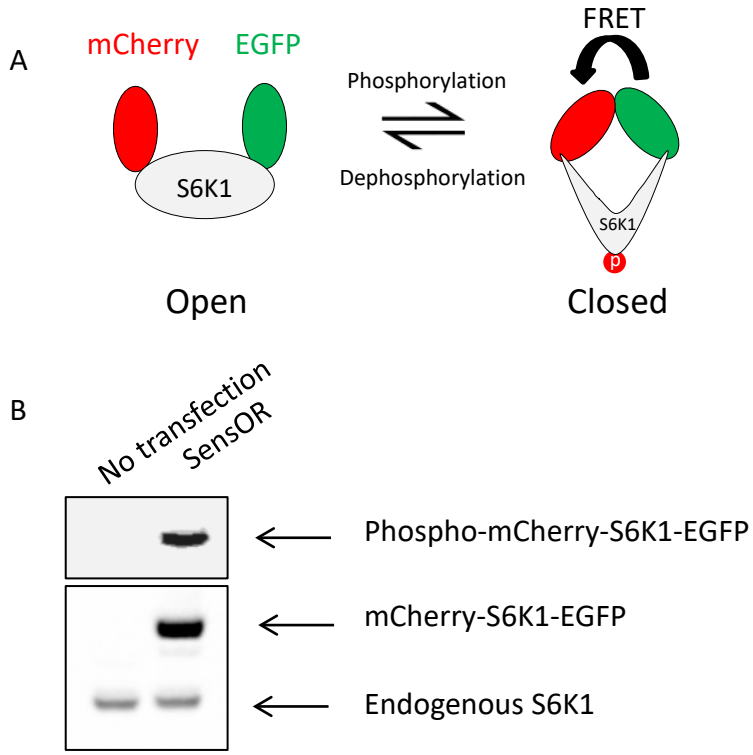

Figure 3.28: Western blot validation of SensOR. *A) Schematic diagram showing mechanism of biosensor. B) Western blots showing S6K1 and phospho-S6K1 labelling in mCherry-S6K1-EGFP (SensOR) transfected and non-transfected HEK293 cells.*

3.2.28 Phospho-S6K1 localisation in living cells using SensOR

When SensOR was expressed in HEK293 cells and imaged, it was noticed that in highly expressing cells, the localisation of the SensOR appeared to be more cytoplasmic. Using FRET-FLIM, the fluorescence lifetime was measured of the bio-sensor and a shorter lifetime (2.1 ± 0.06 ns) in the cytoplasm compared to the nucleus (2.3 ± 0.01 ns) was found (**Figure 3.29**). This difference in lifetime was less

pronounced in low to moderate expressing cells, HEK293 cells expressing the SensOR, but still observable (**Figure 3.30**). These lifetime changes mentioned above between the nucleus and cytoplasm were not observed with the singly tagged S6K1 construct (EGFP-S6K1) which showed a lifetime of 2.6 ns in both cellular compartments, indicating that the shorter lifetime in the cytoplasm may be linked to the phosphorylated state of S6K1; highlighting the importance of targeting S6K1 to the cytoplasm.

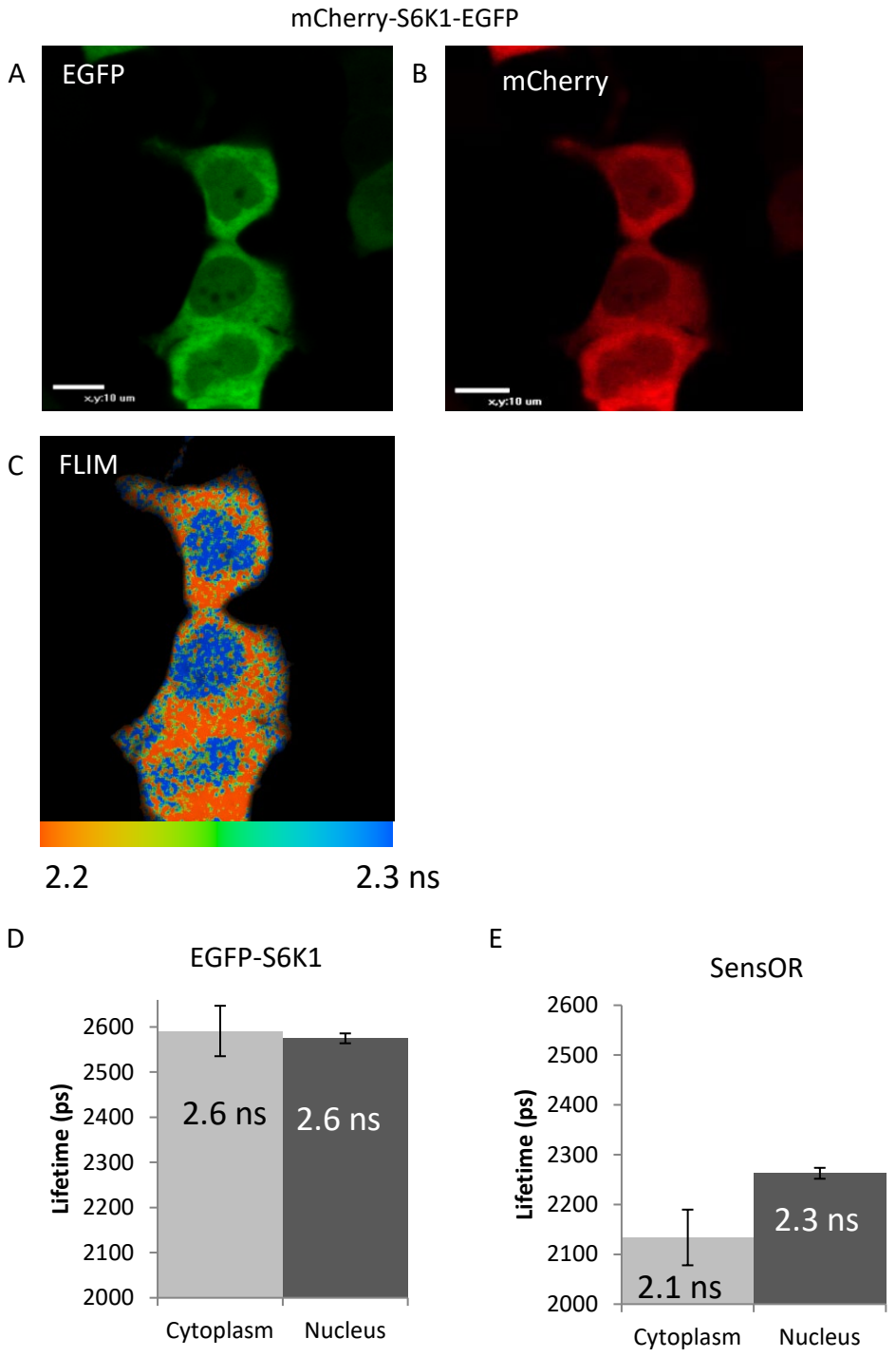

Figure 3.29: Localisation of phospho-S6K1 in living cells using SensOR. *A) and B) Confocal images of biosensor alone in HEK293 cells. C) FLIM of SensOR with lifetime scale bar below in nanoseconds (ns). D) Cytoplasmic versus nuclear lifetime distributions of EGFP-S6K1. E) Graph showing cytoplasmic against nuclear lifetime distributions of SensOR, selected by masking and obtaining the mode lifetime in SPCImage V6.0 software. Data representative of three independent experiments. Scale bar = 10 µm in all images. Error represents standard deviation.*

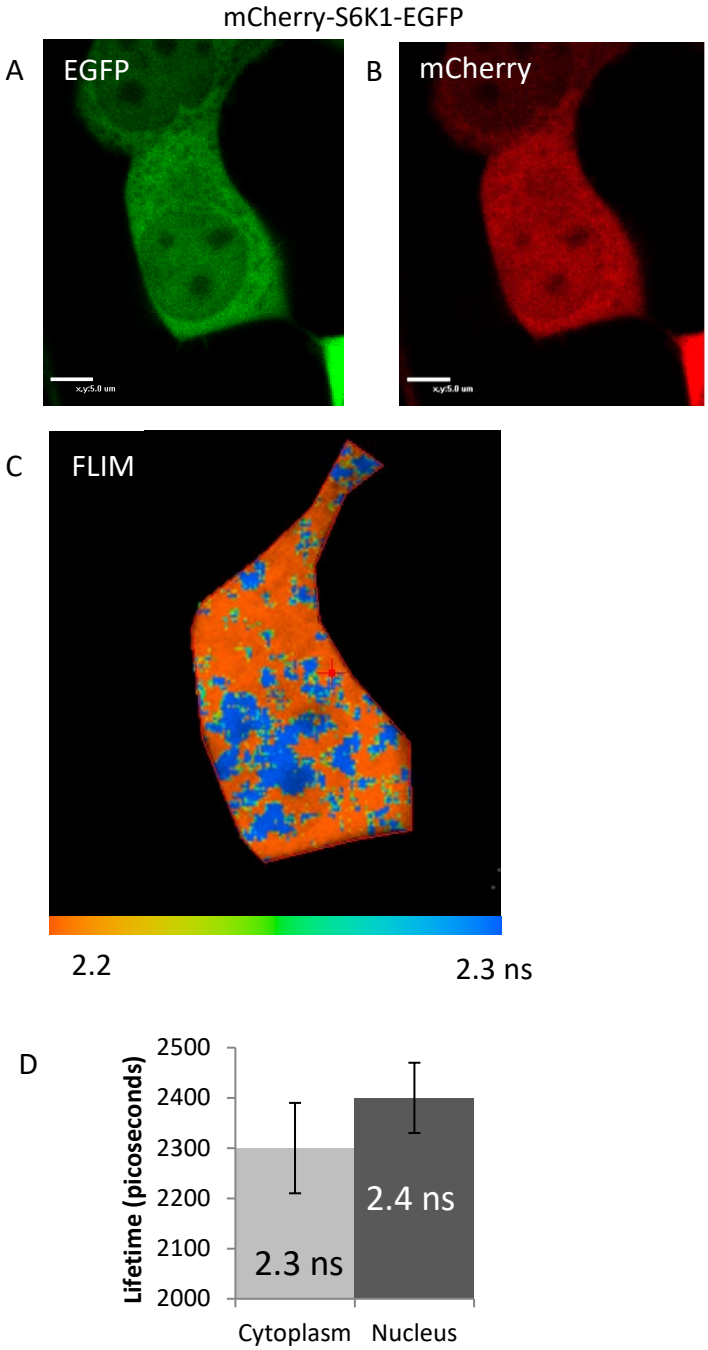

Figure 3.30: Localisation and cellular lifetimes of SensOR. *A) and B) Confocal images showing S6K1-FRET construct. C) FLIM image of SensOR with lifetime scale. D) Graph comparing lifetime of SensOR between cytoplasm and nucleus in low to moderate SensOR expressing HEK293 cells. Data representative of three independent experiments. Scale bar = 5 µm in all images. Error represents standard deviation.*

3.2.29 Imaging p-S6K1 with activation and inhibition in living cells

To investigate the sub-cellular localisation of mTOR activity, the SensOR construct was tested by serum (overnight) and then amino acid (1-2 hours) starving expressing HEK293 cells to de-activate the mTOR pathway. The lifetime of the bio-sensor was measured under these conditions and found to be 2.5 ± 0.03 ns (**Figure 3.31**). This increase in lifetime, from 2.3 ns in SensOR expressed in cells with complete growth medium, is indicative of a subtle environment and/or conformational change of SensOR in living cells showing that the biosensor may not be in a phosphorylated form. Amino acids including leucine and arginine were then subsequently added to re-activate the mTOR pathway and the fluorescence immediately monitored. Within a few minutes lower lifetimes of 2.3 ± 0.02 ns were observed in the cytoplasm. These lifetimes were similar to those observed with untreated cells and indicative of phosphorylation. When these cells were then treated with rapamycin, lifetimes returned to 2.5 ± 0.04 ns (dephosphorylation), it was noted that the FLIM images showed such changes within the cytoplasm (**Figure 3.31**). Taking all these findings together it was concluded that the cytoplasmic region is important for phosphorylation of S6K1.

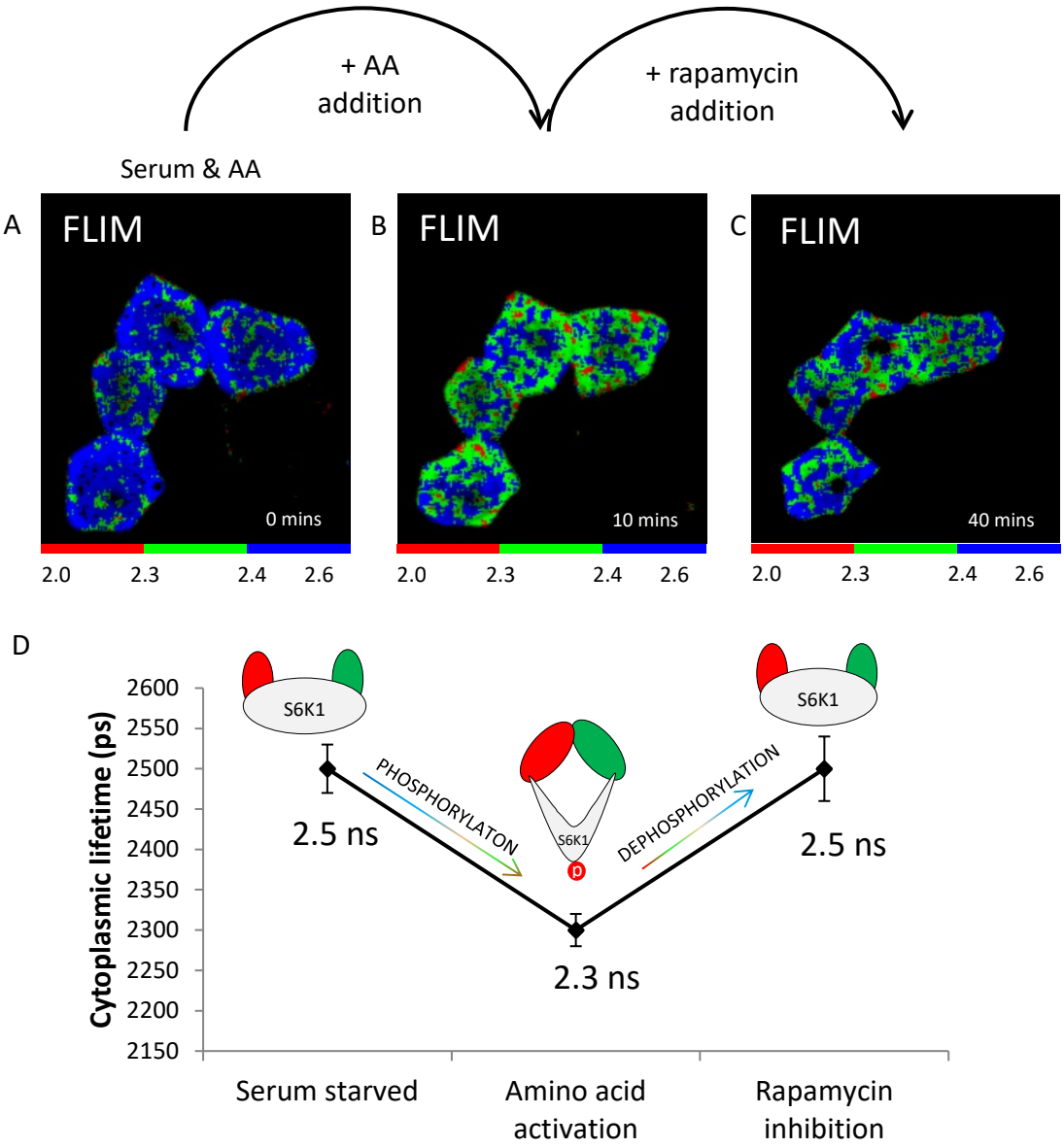

Figure 3.31: mTORC1 activation and inhibition using SensOR. *A) FLIM of serum and amino acid starved HEK293 cells expressing SensOR. B) FLIM at 10 minutes following serine and leucine activation. C) FLIM at 40 minutes after subsequent rapamycin treatment of AA activated cells for 30 minutes. D) Summary of lifetime changes of SensOR with serum starvation, amino acid addition and rapamycin treatment from mean lifetimes and also pixel by pixel analysis of image (n=10). Opening and closing of sensor also shown via schematics. Data representative of three independent experiments where two experiments were treated with leucine and the third treated with the combination of leucine and serine. Error represents standard deviation.*

3.2.30 *In vitro* and *in vivo* temperature studies of purified SensOR

Temperature dependence of the protein folding kinetics has been studied using FRET to show conformational changes within a kinase structure with temperature (Guo, Xu and Gruebele, 2012). Therefore, SensOR in live HEK293 cells was investigated in order to correlate lifetime values observed with phosphorylation *in vivo* with the opening and closing of the SensOR *in vitro* with temperature changes. To do this, mCherry-S6K1-EGFP was re-cloned with a STREP tag and expressed in insect cells and purified, see **Chapter 5** for details regarding cloning, expression and purification. TCSPC measurements were performed on drops of purified SensOR, as described in **Chapter 2: materials and methods**. Preliminary data showed that the lifetime of the SensOR decreased (closing of sensor) with increasing temperature as shown in **Figure 3.32**. When compared to FLIM of *in vivo work* expressing the construct in live HEK293 cells, similar results were observed with lower lifetimes related to hotter temperature (**Figure 3.32**).

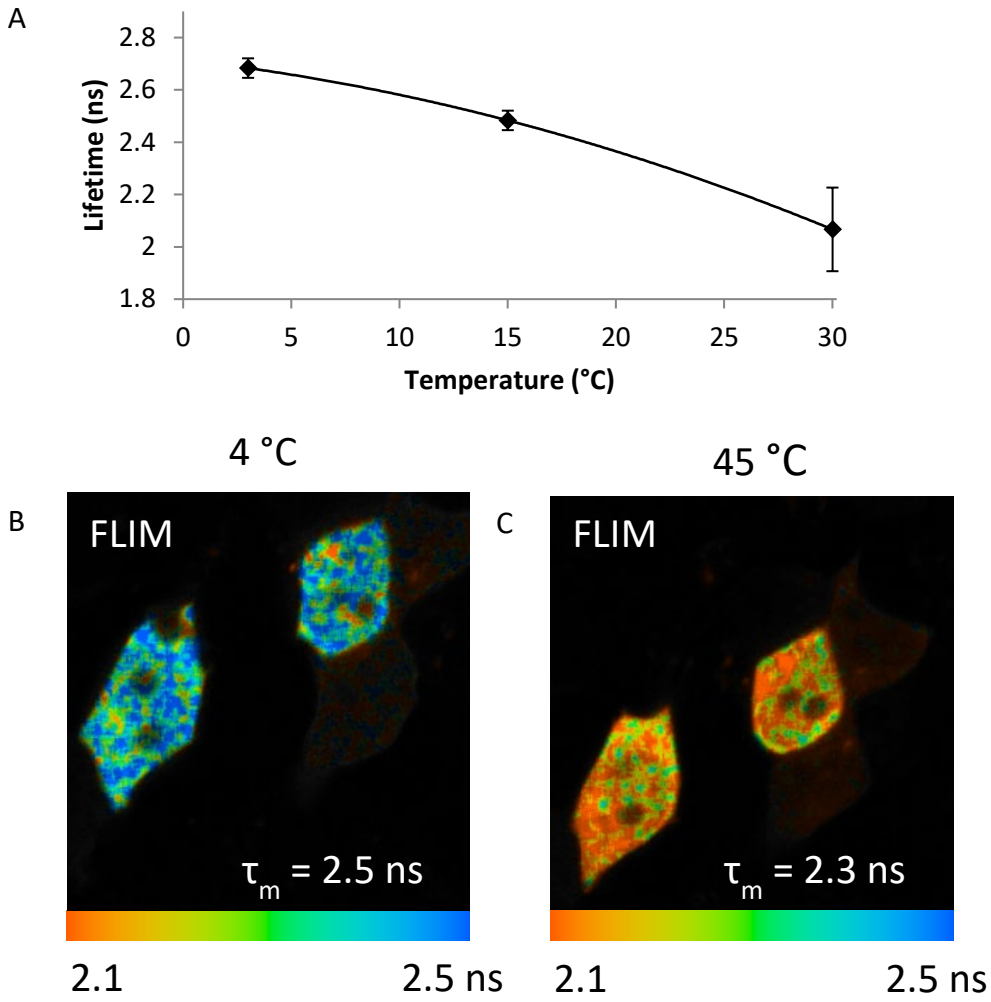

Figure 3.32: Temperature dependence study on SensOR folding. *A) Graph showing lifetime of purified SensOR (60 µg) with temperature (°C) in vitro, fitted to polynomial order 2. Measurements taken from 6 repeats. B) FLIM of HEK293 cells expressing SensOR at 4°C. C) FLIM of HEK293 cells expressing SensOR at 45°C. Mean lifetime (τ_m) is shown with lifetime scale bar in nanoseconds (ns). Error represents standard deviation.*

3.2.31 *In vitro* activation of SensOR with ATP

Using the temperature dependence study of SensOR as a calibration for the opening and closing of the biosensor with respect to lifetime, purified SensOR was incubated on ice to force the biosensor into the open confirmation. TCSPC measurements were performed at room temperature and a lifetime of 2.7 ± 0.01 ns was observed. An equal volume of ATP solution was mixed with the purified SensOR and a quenched lifetime of 2.0 ± 0.01 ns was determined as shown in

Figure 3.33. These results show that the phosphorylated state of S6K1 is linked to the closed form, i.e. such as the lower lifetime values (2.1-2.3 ns) observed in the cytoplasm by FRET-FLIM throughout these set of studies. These findings do not rule out the nucleus as a home for the phosphorylated state of S6K1 as fully unfolded SensOR is expected to show much longer lifetimes, thus indicating a form of phosphorylated S6K1 could reside in the nucleus.

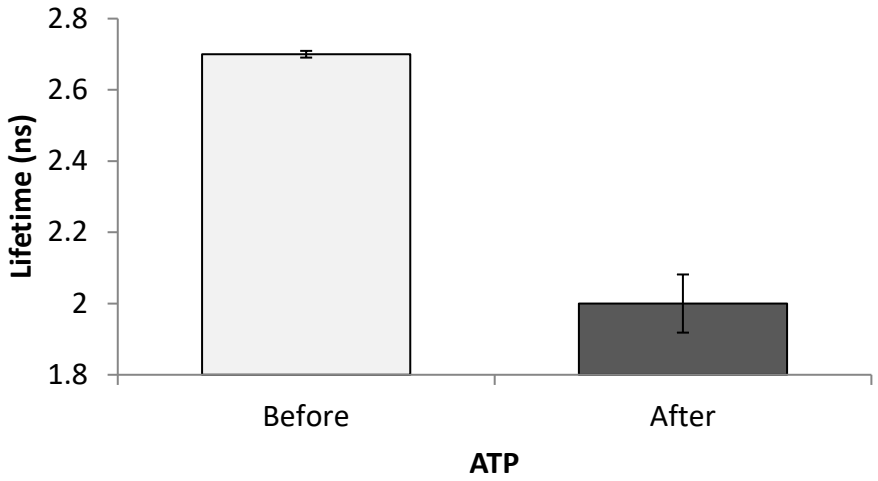

Figure 3.33: ATP activation of SensOR. *Graph showing lifetime of purified (60 µg) before addition and after addition of ATP containing Mg^{2+} (2.4 mM). Data taken from 3 repeats. Error represents standard deviation.*

3.3 Discussion

The transient overexpression of EGFP, mCherry and mTurquoise2 (mTurq2) tagged S6K1 showed localisation of S6K1 in near equal amounts in both the nucleus and the cytoplasm of living mammalian cells using confocal microscopy. These findings support both cell fractionation studies (Coffer and Woodgett, 1994; Rosner and Hengstschläger, 2011) that detected S6K1 in both cytoplasmic and nuclear fractions as well as immunofluorescence work where anti-S6K1 antibodies stained both cellular compartments in fixed HEK293 cells (Skorokhod, Khoruzhenko and Filonenko, 2013). Interestingly, fluorescence imaging of GFP-S6K1 expressing live plant cells also shows an equal nucleocytoplasmic localisation of S6K1 (Mahfouz,

2006), in agreement with the live mammalian cell localisation of fluorescently tagged S6K1 determined in this thesis. Whilst recognising these agreements, the results do however differ with previous studies where cell fractionation of HEK293 cells (Zhang *et al.*, 2002) showed detection of S6K1 predominately in the cytoplasm and imaging of fixed HEK293T cells expressing GFP tagged S6K1 (Lun *et al.*, 2017) has shown a predominately cytoplasmic localisation of GFP-S6K1. The live cell work in this thesis provides an improved method for better understanding of S6K1 function in living cells through imaging its real time cellular dynamics. The live cell application applied here to the imaging of tagged proteins is more advantageous compared to conventional methodologies such as those mentioned above, namely cell fractionation and cell fixation due to lesser susceptibility to experimental artefact generation stemming from maintaining cellular integrity (Huber, Pfaller and Vietor, 2003; Say and Hooper, 2007; Schnell *et al.*, 2012). In context with the present-day literature, the use of S6K1 live cell imaging validates the functions of S6K1 in relation to its sub-cellular localisation as S6K1 in the nucleus is involved in histone phosphorylation (Lee *et al.*, 2016; Yi, Han and Han, 2016) whilst in the cytoplasm, S6K1 is associated with cell growth and survival that involves S6K1 in the mitochondria (Djouder *et al.*, 2007).

Although the overexpression of a gene within a cell provides a useful tool for determining pathway components that could stay undetected using traditional detection methods used for ectopic expression, it must not be forgotten that overexpression could lead to artefacts as such high levels of one protein may lead to cells promoting abnormal behaviour (Prelich, 2012). Protein production in mass quantities within the cell could be toxic to the cell leading to the leakage of protein into other cellular compartments (Lowder *et al.*, 2000). In addition, inaccurate findings may be deduced where the overexpression system forces non-interacting proteins together (Taipale, 2018). Equally, it must be noted that both the choice of

fluorescent protein used to tag a protein of interest as well as the terminus to which it is added to, is important and could lead to differences in localisation in living cells (Fritz *et al.*, 2008). In the case of S6K1 neither the EGFP, mCherry nor mTurquoise2 tags or addition of them on either terminus end of S6K1 significantly disrupted localisation although S6K1-mCherry appeared slightly more cytoplasmic. Problems with using mCherry as fluorophore for protein tagging have been reported before (Shemiakina *et al.*, 2012; Huang *et al.*, 2014; Costantini *et al.*, 2015). Unlike EGFP and mTurqouise2, mCherry is a coral derived FP and although this effect may also appear to affect the FRET biosensor, SensOR (mCherry-S6K1-EGFP), this is not the case as a later developed version of SensOR (mTurq2-S6K1-EGFP) localised similarly to its predecessor.

A unique translocation of S6K1 was identified when co-expressed with raptor using several fluorescent constructs (YFP, mCherry, mTuq2 and mDsRed) in living mammalian cells, and the results support the current thinking that raptor acts as a scaffold protein in recruiting downstream mTOR substrates (Schalm and Blenis, 2002; Nojima *et al.*, 2003; Schalm *et al.*, 2003; Yonezawa *et al.*, 2004; Oshiro *et al.*, 2007). The translocation of S6K1 to the cytoplasm may embody the first steps in S6K1 recruitment onto the mTORC1 complex as live cell imaging of fluorescently labelled mTORC1 subunit proteins such as raptor, mTOR and Rheb are predominately cytoplasmic in live cells (Qian *et al.*, 2010; Yadav *et al.*, 2013; Manifava *et al.*, 2016). Since raptor does not localise in the nucleus (Yadav *et al.*, 2013), a novel sensing mechanism could be involved. The notion that raptor is directly involved with substrate recruitment is further supported by the observation that S6K1 phosphorylation was increased with raptor co-expression and adds strength to similar findings from others (Yadav *et al.*, 2013; Jain *et al.*, 2014; Martin *et al.*, 2014).

Whether S6K1 phosphorylation is an effect of its translocation is still unresolved. The work reported has also identified that the S6K1 translocation was not triggered by mTOR mediated phosphorylation, firstly by serum and amino acid starvation of wildtype EGFP-S6K1 and secondly by the generation of a non-phosphorylated EGFP-S6K1 (T389A) construct, in line with fractionation work (Kim *et al.*, 2009). Interestingly, no large punctate structures were formed of EGFP-S6K1 upon nutrient starvation compared to previous live HEK293 cell imaging studies where punctates of EGFP-mTOR were observed under starvation conditions (Yadav *et al.*, 2013). Also no punctate structures were observed with mCherry-raptor under nutrient starvation similar to previous findings (Yadav *et al.*, 2013). However, smaller punctate structures have been identified with nutrient starved HEK293 and HAP-1 cells expressing raptor-GFP (Manifava *et al.*, 2016). The discrepancy between these results could be explained by the fact that the latter work knocked-in GFP to endogenous raptor protein whilst the work reported in this thesis used overexpression. Thus, combining gene editing tools such as CRISPR-Cas9 technology (Lackner *et al.*, 2015) with microscopy may overcome some of the disadvantages of using overexpression where the balance of components within a signalling pathway may be better controlled.

The translocation of S6K1 has been recognised to be dependent on S6K1 binding to raptor as the expression of a mutated TOS S6K1 construct (EGFP-F28A S6K1) with mCherry-raptor, resulted in a lack of translocation. This finding supports previous pulled-down studies where TOS motif mutated S6K1 was unable to co-immunoprecipitate with raptor (Nojima *et al.*, 2003; Ali and Sabatini, 2005). S6K1 TOS mutants have also shown diminished phosphorylation by pull-down assays (Schalm and Blenis, 2002; Nojima *et al.*, 2003) indicating that S6K1 and raptor binding is essential to the mTOR mediated phosphorylation of S6K1. The lack of evidence for raptor localisation in the nucleus begs the question as to whether raptor

actively recruits and binds S6K1 onto mTORC1 complex and if so what is the recruitment mechanism? This is discussed next.

A secondary mechanism for S6K1 translocation has been identified in results section **3.2.14** involving a fully functioning mTOR protein. Shuttling of mTOR to the nucleus has been reported for maximal S6K1 phosphorylation (Kim and Chen, 2000; Bachmann *et al.*, 2006), both hypothesised that mTOR may be involved in recruitment and this was made apparent in the results of this chapter when the translocation of S6K1-mTurq2 with raptor was inhibited with an N-terminal truncated mTOR construct (ΔN-mTOR-mCherry). These results lead to the deduction that mTOR itself may be involved in a primary or secondary recruitment mechanism involving the N-terminus (presumably the HEAT repeat domains) other than the reported FRB domain of mTOR in mediating recruitment (Yang *et al.*, 2017). If mTOR dimerisation plays an active role in secondary recruitment of S6K1, an obvious experiment is to test whether a mutated mTOR construct engineered to prevent formation of the mTOR (N-to C-terminus) dimer (Jain *et al.*, 2014) would inhibit translocation, assuming formation of the mTORC1 dimer is required for S6K1 translocation and subsequent phosphorylation.

The belief that S6K1 is recruited onto the complex is supported by the direct interactions found between EGFP-S6K1 and mCherry-raptor in live HEK293 cells in this chapter, as evident by a ~200 picosecond change in the fluorescence lifetime of the EGFP-S6K1 donor and also with previous live cell EGFP-mTOR and mDsRed-raptor interaction studies (Yadav *et al.*, 2013). The ~200 picosecond change in lifetime has been previously shown to be statistically significant for protein-protein interaction studies based on comparisons with protein-protein mass spectrometry (Stubbs *et al.*, 2005; Kriechbaumer *et al.*, 2015; Kriechbaumer, Botchway and Hawes, 2016). The FRET-FLIM results from this chapter confirms several studies that have pulled-down S6K1 and raptor together using cell disruptive pulled-down

assays (Schalm and Blenis, 2002; Nojima *et al.*, 2003; Yonezawa *et al.*, 2004; Schalm, Tee and Blenis, 2005). The requirement of S6K1 to dock onto the complex through raptor recruitment leading to mTOR mediated phosphorylation is made more apparent through the evidence presented by previous raptor-knockout studies that observed abolishment in S6K1 phosphorylation (Ali and Sabatini, 2005). The disassembly of S6K1 on the complex by either targeting the recruitment mechanism or raptor binding has potential as a novel method to inhibit mTOR activity by pharmaceutical involvement.

It was previously found that Rheb and raptor both directly interact with mTOR in live HEK293 cells whilst no interaction between Rheb and raptor was determined (Yadav *et al.*, 2013). In this thesis, only a ~100 ps change in the natural EGFP-mTOR lifetime was observed with S6K1-mCherry. This change in lifetime is smaller than expected compared to the 200 picosecond change mentioned above for an interaction. As mTOR has been reported to phosphorylate S6K1 (Brown *et al.*, 1995), one would expect a direct and physical interaction between the two proteins. However, this smaller magnitude of FRET may reflect a weak long distance interaction (>10 nm) between S6K1 and mTOR, owing to the large geometry of the complex. Also, the interaction observed could be one of a fast and dynamic nature which due to averaging events over several tens of seconds during FLIM acquisition may provide a bias lifetime favouring the dominate lifetime. Alternatively, a lack of interaction observed may be masked due to the lack of the raptor component, in excess of endogenous levels, needed to dock S6K1 onto the complex. The SPC instrument response of the FLIM detection is 31 picoseconds and thus any changes in lifetime beyond this value can be accurately measured and can be considered significant with good time resolution. Taken together, these FRET-FLIM data would support pulled-down studies that have failed to pull-down full length S6K1 and mTOR together (Ben-Hur *et al.*, 2013; Brown *et al.*, 2017). In the cases where S6K1

has been pulled down with mTOR (Brown *et al.*, 1995; Ali and Sabatini, 2005), the finding from this thesis that showed EGFP-S6K1 pulled down with both mCherry-raptor and FLAG-mTOR together from HEK293F cells provides plausible evidence for endogenous raptor acting as a tertiary component to bridge subunits together on the complex in other works.

Similarly, only a 100 ps change in EGFP-S6K1 lifetime was observed with mCherry-FKBP12 in cells supplemented with rapamycin. The FKBP12-rapamycin complex has been shown to bind to the FRB domain of mTOR (Choi *et al.*, 1996) and a peptide sequence of S6K1 has been shown to bind with the same mTOR domain (Yang *et al.*, 2017), thus an interaction within near proximity between S6K1 and FKBP12 is plausible. The FRET-FLIM result presented in this chapter does support such an interaction as the mTOR protein would be sandwiched between S6K1 and the FKBP12–rapamycin complex resulting in less FRET efficiency. However, whilst this is an attractive interpretation, the 100 ps lower lifetime could also be due to the binding of S6K1 on the complex at an interface opposite to where Rheb and FKBP12-rapmaycin bind, such positioning would lead to a long distance interaction and a falloff in quenching efficiency.

Interestingly, no change in the unquenched lifetime of EGFP-Rheb was observed with S6K1-mCherry co-expression, indicating a lack of direct interaction despite a 129% induction in S6K1 phosphorylation with Rheb overexpression. Although no change in donor EGFP-Rheb lifetime was observed, the probability that the fluorophores could be in an unfavourable orientation or beyond the 10 nm distance for FRET should be considered. The interaction between S6K1 and Rheb has not to date been investigated. The newly resolved structure of mTORC1 with Rheb determined using cryoEM indicates that Rheb and raptor do not interact (Yang *et al.*, 2017) and thus if mTOR substrates are recruited by raptor interaction, they are expected not to interact with Rheb. In addition, if the TOS motif of S6K1 is involved

in mediating the interaction with raptor, a belief heavily supported by previous structural studies that have shown the N-terminus of raptor is within close proximity to mTOR (Aylett *et al.*, 2016; Yang *et al.*, 2016), then S6K1 is expected to be within close proximity to the active site of mTOR. In summary, combining the FRET-FLIM data and the pull-down work with the previously reported mTOR interactions (Yadav *et al.*, 2013), provides an assembly of S6K1 that can be modelled in 3D and is shown in **Figure 3.34** with the summary of the main lifetime interactions from this chapter.

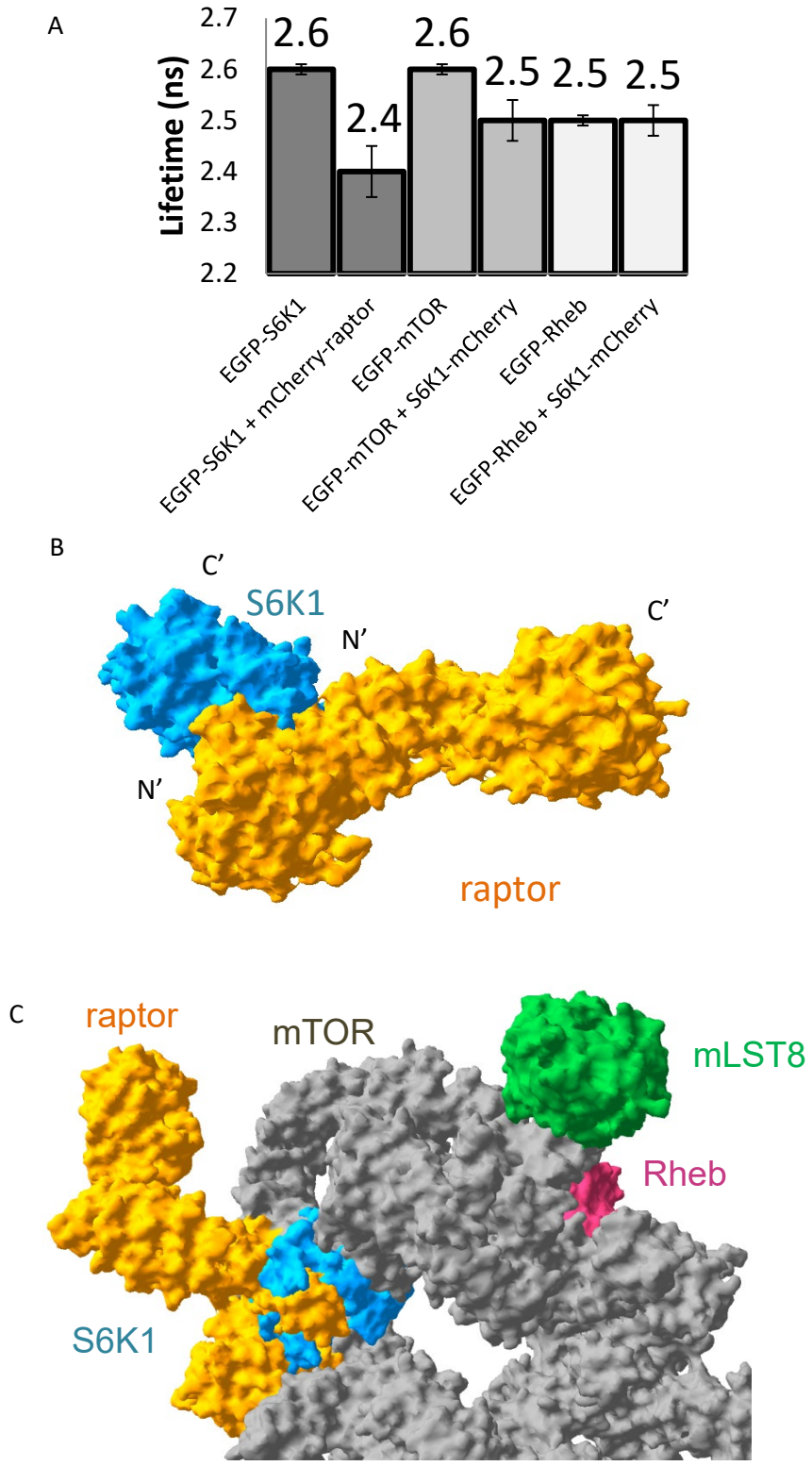

Figure 3.34: **Summary of mTORC1-S6K1 interactions.** A) Graph summarising FRET-FLIM interactions. B) 3D model of S6K1 and raptor interaction. C) 3D model of S6K1 docked onto mTORC1. Made in Swiss PDB Viewer V4.10 software using PDB files: 3a62, 1xts, 5h64

The choice of fluorescent acceptor for FRET-FLIM studies has also been shown to be important in this results chapter. The green emission observed from the mDsRed acceptor evoked by multiphoton excitation has been reported previously and has been termed the 'greening' effect stemming from emission between 510–550 nm (Marchant *et al.*, 2001; Nifosı and Yi, 2007; Kremers *et al.*, 2009; Subach and Verkhusha, 2012). It has been proposed that this phenomenon is due to photo-conversion where an immature 'green' intermediate of the chromophore is formed. Although DsRed has been used in FRET studies (Erickson, Moon and Yue, 2003) and FRET-FLIM studies (Peter *et al.*, 2005; Stubbs *et al.*, 2005; Yadav *et al.*, 2013) to determine protein-protein interactions, the collection of the 'green' component of the mDsRed acceptor with the EGFP donor can lead to a shorter average lifetime as reported here resulting in false conclusions regarding interactions. It has been reported that mCherry on the other hand does not have any multiphoton evoked green emission (Kim *et al.*, 2012). With this in mind, experiments between mTOR with raptor were re-performed using EGFP-mTOR and mCherry-raptor (see **Appendix B.10**) and direct interactions were observed with a similar change in lifetime of 200 picoseconds as reported previously (Yadav *et al.*, 2013).

Another important finding in this chapter has been identifying the involvement of Rheb in both phosphorylation and dephosphorylation (Inoki *et al.*, 2003; Yonezawa *et al.*, 2004; Long *et al.*, 2007). A ~72% decrease in S6K1 phosphorylation was only observed with the combination of both Rheb and S6K1 overexpression with rapamycin treatment whilst no effect was observed with S6K1 overexpression alone. Although there is no direct explanation for this difference, possible explanations are that the role of Rheb may go beyond what was originally thought of as a GTPase activator of mTOR or that the endogenous levels of FKBP12 may be too low to compensate for the overexpressed S6K1.

The mechanism of Rheb in activating the mTOR kinase protein and drastically inducing S6K1 phosphorylation without directly interacting with S6K1 raises the questions of how mTOR induces hyperphosphorylation and how the combined effect of rapamycin and Rheb leads to a reduction in S6K1 phosphorylation. Advanced confocal imaging using deconvolution to go beyond the diffraction limit showed poor co-localisation between EGFP-S6K1 and mDsRed-Rheb suggesting that the two proteins are not within the same localisation site. The recent cryoEM structure of mTORC1 with Rheb has shed light on its mechanism of activation by proposing that the binding of Rheb to the mTORC1 complex results in a conformation change in mTOR that primes its active site for substrate phosphorylation (Yang *et al.*, 2017). Other than structural studies, computational modelling has been used to simulate the dynamics of the complex, in particular to predict Rheb's mechanism of action. It has been suggested that Rheb may function to increase mTORC1 substrate phosphorylation by increasing mTORC1 substrate binding to raptor (Rahman and Haugh, 2017; Sulaimanov *et al.*, 2017). Although this model is supported by previous experimental data where Rheb overexpression increased 4EBP1 binding to raptor (Sato *et al.*, 2009) by pulled-down assay, no translocation of S6K1 was observed with both Rheb and raptor expression in this results chapter.

It has also been shown from other work that S6K1 phosphorylation levels remain heightened after nutrient activation, evaluated by Western blot analysis, after mTORC1 has detached from lysosomes into the cytoplasm and thus provides a spatial understanding for activation as Rheb has been reported to tether the complex to the lysosomal membrane (Yao, Jones and Inoki, 2017). This raise questions as to whether the entire mTOR1 complex is assembled on the lysosomal membrane and then finally rests in the cytoplasm and/or upon mTOR activation is Rheb still bound onto the complex? Taken together, this chapter proposes that the mechanism of Rheb in S6K1 phosphorylation may be strongly related to dynamic

conformational changes within the complex that enhances the dynamic interaction between mTOR and S6K1 inevitably leading to the localisation of the complete complex in the cytoplasm as a final resting point. It has been suggested that S6K1 detaches from the complex after phosphorylation (Holz *et al.*, 2005), however this does not hold true with our findings as the translocated S6K1 in the cytoplasm is shown to be in the phosphorylated form, as evident by both the lower lifetimes observed in the cytoplasm with the live cell S6K1 phosphorylation FRET sensor (SensOR) as well as Alexa405 labelling for phospho-S6K1 in fixed cells. However, the results obtained from cell fixation must not be ignored as the detrimental effects of the fixation process causes artefacts.

The dynamics of S6K1 binding onto mTORC1 have been shown in relation to other raptor binding proteins such as PRAS40 and 4EBP1, also known to contain their own TOS motif sequences (Schalm and Blenis, 2002; Beugnet, Wang and Proud, 2003; Choi, McMahon and Lawrence, 2003; Wang, Rhodes and Lawrence, 2006; Oshiro *et al.*, 2007; Lee *et al.*, 2008). Both the confocal and FRET-FLIM microscopy results supports the previously stated literature as shown by the translocation and interaction of 4EBP1-GFPSpark with mCherry-raptor. This indicates that 4EBP1, similar to S6K1, may also be recruited onto the complex. Fluorescently labelled PRAS40 did not translocate with raptor co-expression and localised to the cytoplasm, in line with the findings that PRAS40 is jointly bound onto the complex by mTOR and PRAS40 (Oshiro *et al.*, 2007; Sancak *et al.*, 2007; Wang *et al.*, 2007). The results from three colour live cell imaging with expression of 4EBP1-GFPSpark or YFP-PRAS40 and fluorescently tagged S6K1 together with raptor indicated the S6K1 translocation was inhibited, by up 2-times, a result in agreement with the notion that mTOR substrates competitively compete for raptor binding on the same site (Hara *et al.*, 2002; Wang *et al.*, 2007; Dennis, Kimball and Jefferson, 2013). In the triple colour imaging studies, although not always the case as 4EBP1 did appear

slightly translocated in some cells, both S6K1 and 4EBP1 translocation was inhibited. This ‘cancelling-out’ effect suggests that raptor does not have specificity towards either mTOR substrate. However, the fluorescence levels of a FP is not a robust tool for measuring the concentration of tagged proteins as differences in quantum yields and extinction coefficients of the FPs may affect quantification. However, it has been suggested through the use of *in vitro* studies, that raptor has a higher affinity for 4EBP1 than S6K1 for binding (Schalm *et al.*, 2003), therefore 4EBP1 may still be expected to possess some translocation.

The localisation and distribution of the phosphorylated form of EGFP-S6K1 was investigated by paraformaldehyde, methanol and glyoxal cell fixation methods, as no readily available live cell phosphorylation labelling methods were available at the start of this work. It was found that paraformaldehyde caused the extraction and loss of soluble EGFP-S6K1 from the cytoplasm, movement of EGFP-S6K1 into the nucleoli and masking of the epitopes of S6K1 for sufficient antibody labelling. These observations have been previously investigated using GFP expressed protein or quantum dots (Williams *et al.*, 2008; Schnell *et al.*, 2012). Methanol fixation also resulted in mis-localisation of EGFP-S6K1 with higher fluorescence intensities found in the peri-nuclear region (Williams *et al.*, 2008). However, glyoxal fixation provided the least amount of mis-localisation, indicating its superior suitability for fixed cell immunofluorescence labelling (Richter *et al.*, 2017). Taken together, these findings show that cell fixation induces artefacts which are likely to influence the localisation of a phosphorylated protein. Such detrimental effects of fixation have been reported previously for mTORC1 studies (Sancak *et al.*, 2008; Yadav *et al.*, 2013). Variable results were also obtained using different phospho-S6K1 antibodies from various commercial companies. Thus, the choice of the fixative and antibody used will significantly influence the localisation of phosphorylated S6K1.

In agreement with previous studies that have shown a dose-dependent effect of Rheb (Garami *et al.*, 2003; Inoki *et al.*, 2003; Stocker *et al.*, 2003; Long, Ortiz-Vega, *et al.*, 2005; Long *et al.*, 2007; Yadav *et al.*, 2013; Gonzalez *et al.*, 2014; Martin *et al.*, 2014), the co-expression of S6K1 with Rheb induced an increase (129%) in S6K1 phosphorylation and this was quantified by Western blot analysis in this chapter. However, when HEK293 cells were fixed in paraformaldehyde and immunofluorescence was used to label both overexpressed and endogenous phospho-S6K1, no correlation between high Rheb and high phospho-S6K1 intensities were observed from single cell-to-cell analysis. The discrepancy between these two techniques could be explained by the fact that Western blotting involves pooling all the proteins from all the cells together and thus an accumulated increase in S6K1 phosphorylation is detected whereas on a cell to cell basis, levels of phosphorylation may vary and may be much lower when combined with insensitive antibody labelling and poor detection. Furthermore, having covered the obstacles faced with cell fixation in the discussion above, it is equally plausible that soluble phospho-S6K1 may be lost from the cytoplasm and thus renders the findings from the immunofluorescence work inconclusive. Based on the evidence presented in this chapter translocation of labelled phosphorylated S6K1 from the cytoplasm into the nucleus upon activation is not observed which is contrary to that previously reported (Kim and Kahn, 1997; Rhoads *et al.*, 2008; Rosner, Schipany and Hengstschläger, 2012; Kim *et al.*, 2013). Instead, using the novel real-time live cell S6K1 phosphorylation FRET bio-sensor (SensOR) activation of S6K1 in the cytoplasm was observed, as evident by the mCherry-S6K1-EGFP protein having a significant lifetime change (~200 picosecond) mainly in the cytoplasm following a cycle of nutrient starvation, nutrient replenishment and rapamycin treatment. It is concluded from the SensOR study that S6K1 activity is under mTORC1 regulation. The observed reduction in lifetime of SensOR is similar to the ~200 picosecond change observed in a study using a similar FRET sensor design to monitor the activity of the

aurora kinase protein (Bertolin *et al.*, 2016). Although it has been found that a two-step amino acid mechanism activates mTOR where a priming amino acid as well as an activating amino acid is required (Dyachok *et al.*, 2016), the work in this chapter found FRET changes with both the activating amino acid (leucine) alone or with both the activating and priming (arginine) amino acid.

The lifetime changes observed with the phosphorylation events above relate to structural changes in the protein which can also be manipulated with temperature (i.e. opening and closing) the sensor. The combined dynamics of purified SensOR with *in vitro* temperature kinetic and ATP activation studies validates the use of the construct for monitoring mTOR activity. The mechanism of the bio-sensor is summarised in the schematic in **Figure 3.35**. The changes in lifetime observed with the FRET bio-sensor support the idea that phosphorylation of S6K1 is linked to a conformational change (Magnuson, Ekim and Fingar, 2012) and agree with findings of other FRET sensors where S6K1 or mTOR activity has been observed in the cytoplasm of living cells (Komatsu *et al.*, 2011, 2018; Zhou *et al.*, 2015). The novel FRET sensor developed in this work surpasses previous FRET sensors cited above as SensOR directly reports on mTOR activity whilst the Eevee-S6K sensor gives a read-out for S6K1 activity and does not locate into the nucleus due to truncated rictor and S6K1 sequences (Komatsu *et al.*, 2011). SensOR monitors complete rapamycin sensitivity whilst the TORCAR sensor for observing 4EBP1 activity is insensitive to rapamycin (Zhou *et al.*, 2015). Furthermore, the steady state FRET used in the previous studies by others is unable to determine very small structural changes which can be better resolved using time-resolved FRET-FLIM.

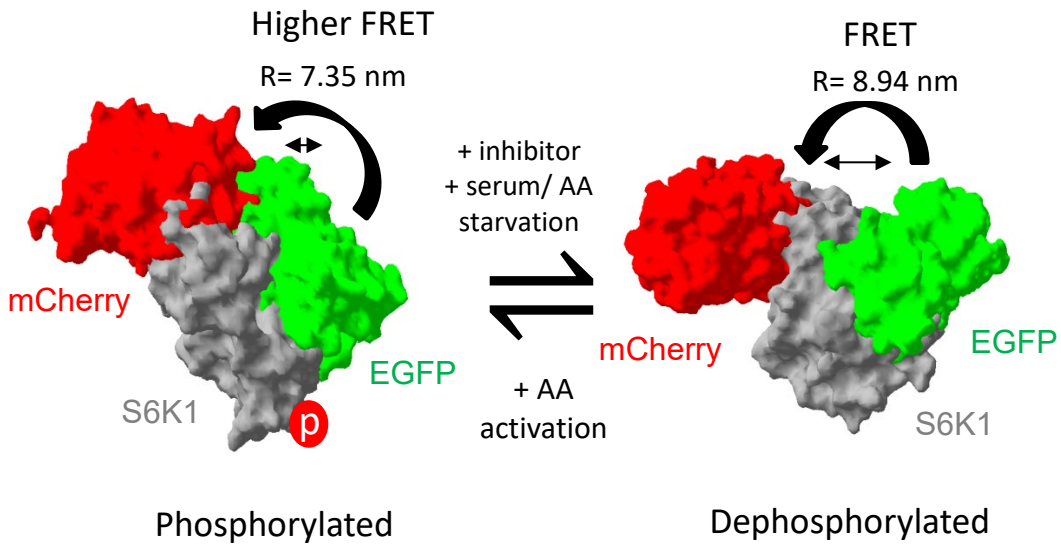

Figure 3.35: Schematic showing mechanism of SensOR. *3D models of SensOR opening and closing are shown. Conditions at which conformational change occurs is also shown. Made in Swiss PDB Viewer V4.10 software. PDB codes used: 2Y0G and 4L46. The donor-to-acceptor separation distance (r) has been calculated from* $R=R_0(\sqrt[3]{1/E} -1)$ *where the Förster distance* (R_0) *is 52.88 Å and the FRET efficiency (E) was determined from the lifetime values.*

The fact that highly expressing cells showed translocation of SensOR without any co-expression is interesting. Since the amount of endogenous raptor is unknown, the translocation of the FRET sensor may be due to enhanced phospho-S6K1 shuttling based on observations that the FRET was heterogeneous amongst cells, which is expected when there are variations in levels of activity. Furthermore, it is also possible that the addition of two fluorescent proteins may have caused mis-localisation as the addition of both GFP and mCherry to the Aurura Kinase FRET sensor also showed a translocated localisation although not explicitly reported (Bertolin *et al.*, 2016). However, as Western blot analysis of SensOR has shown functionality, it is more likely that the translocation of the SensOR is biologically related. Nevertheless, the SensOR studies has shown distinct FRET variations in the cytoplasm which may be related to sub-cellular regional mTOR activity that cannot be resolved using standard diffraction limited confocal based FRET-FLIM microscopy. Also, although the nuclear localisation of the SensOR, collected with a

high count for accurate model fitting, shows longer lifetimes than its cytoplasmic localisation, this doesn't necessary mean phosphorylation is not occurring in the nucleus. Although, the majority of the S6K1 phosphorylation is identified to be in the cytoplasm it is plausible that a much lower level of phosphorylation in the nucleus may not have been detected if the S6K1 conformational change is inefficient in the nucleus or if this closed-state population is too small and masked by surrounding pixels that contain the open-state S6K1 during FLIM analysis.

In summary, the data from this chapter can be combined to produce an updated scheme of the mTORC1 pathway showing the recruitment and dynamics of S6K1 assembly and phosphorylation in living cells, see **Figure 3.36**.

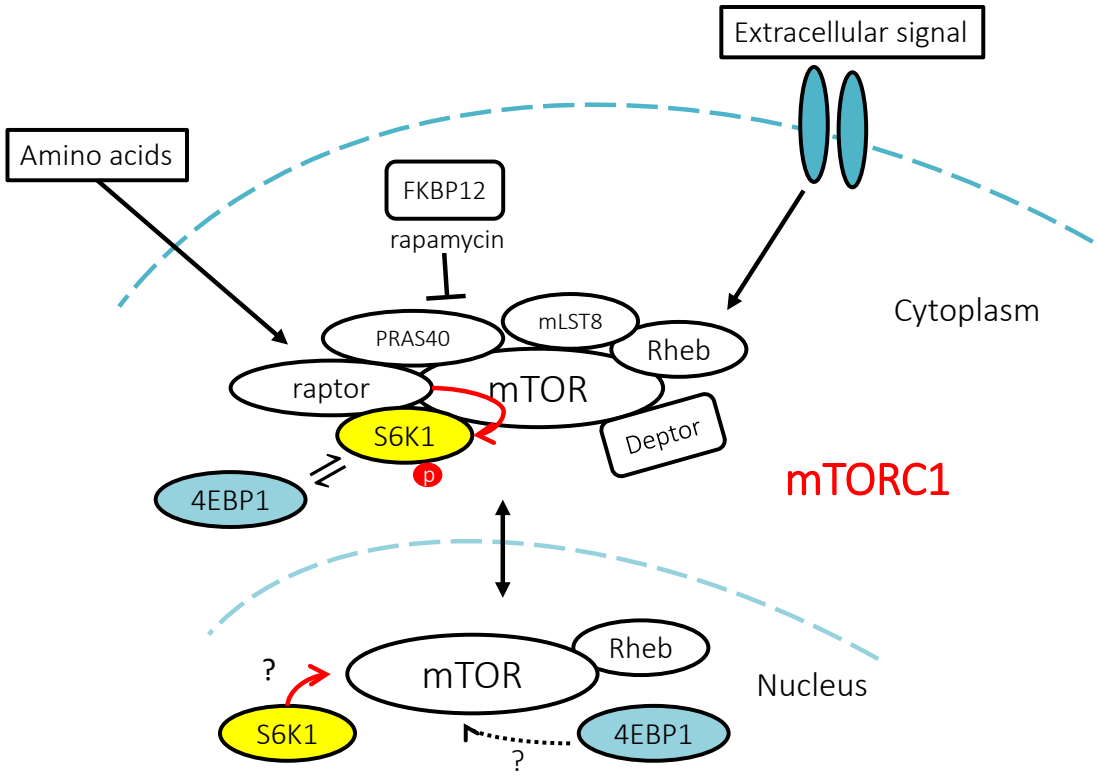

Figure 3.36: Schematic of updated mTORC1 pathway. *Modified and updated schematic taken from* (Yadav *et al.*, 2013)*. Red arrows show recruitment. Black dotted arrow shows unknown recruitment. Resonance arrows show dynamic exchange.*

3.4 Conclusions

S6K1 localises to both the nucleus and cytoplasm in live mammalian cells using GFP tagged S6K1. S6K1 is recruited primarily by raptor via a functional S6K1 TOS motif resulting in the movement of S6K1 from the nucleus to the cytoplasm. This movement (translocation) is not triggered by mTOR mediated phosphorylation. A secondary recruitment mechanism involving the N-terminus of mTOR may be also involved. S6K1 directly interacts with raptor to allow mTOR substrate docking onto mTORC1. Although there is a lack of interaction between S6K1 and Rheb, there is an enhancement in S6K1 phosphorylation only with Rheb co-expression. Rapamycin appears to only function in the presence of Rheb. Once S6K1 is docked onto the complex, phosphorylation occurs and this predominately takes place in the cytoplasm as evident by phosphorylation triggered S6K1 conformational changes both *in vivo* and *in vitro* utilising SensOR.

4.0 Directly imaging AZD2014 and INK128 pan-mTOR inhibitors in living cells

4.1 Brief introduction

AZD2014 and INK128 are currently referred to as second generation mTOR inhibitors that are undergoing pre-clinical and clinical trials (Li *et al.*, 2015; Powles *et al.*, 2016). These inhibitors are also known as pan-mTOR inhibitors as they are designed to bind to the mTOR kinase domain, competing with ATP binding, and thus are suggested to be more selective than rapamycin or rapalogue derivatives. AZD2014 and INK128 target mTORC1 and mTORC2 similarly. However, the exact localisation and mechanism of these drugs has not been well-studied despite advancements in the clinical context (Li *et al.*, 2018).

This chapter reports the use of advanced microscopies that utilise the natural fluorescence from AZD2014 and INK128 without the need for additional fluorescent tags (Miller, Fricker and Drewe, 1997; Kozany *et al.*, 2009). In this chapter, their fluorescence properties have been characterised as well as their real-time uptake in living mammalian cells. Particular focus has been paid to AZD2014 with respect to both its localisation and interaction with mTORC1. In general, where and how mTOR inhibitors localise is imperative and crucial in drug design and development.

The hypothesis of this chapter is:

- The regulation of the mTORC1 pathway by pan-mTOR inhibitors may function by targeting mTOR, the complex, or downstream substrates directly

4.2 Results

4.2.1 UV-Vis spectroscopy analysis of rapamycin, AZD2014 and INK128

In order to obtain information regarding possible luminescent properties of the mTOR inhibitors required for imaging in cell studies, the absorption properties in the ultraviolet-visible (UV-VIS) spectral region of AZD2014, INK128 and rapamycin were investigated. These drugs were dissolved in DMSO as the solvent, per manufacturer's recommendation and absorbance measured using a UV-vis spectrophotometer. The experimental UV-VIS absorption spectra were deconvolved by subtracting the solvent absorbance and are presented in **Figure 4.1**. AZD2014 showed two absorbance peaks at 283 nm and 393 nm, respectively. INK128 gave absorbance below 330 nm with a peak at 293 nm whilst rapamycin absorbed below 280 nm. The DMSO solvent alone also showed strong absorbance below 290 nm and this is given in **Appendix C.1**.

The absorbance information was used to determine their molar extinction coefficients, a measure of how strongly a compound is likely to absorb light at a specific wavelength. The molar extinction coefficient (ε) of AZD2014 at the 393 nm wavelength was determined as 1,166 M^{-1} cm^{-1} whilst at 283 nm, it was found to be 36,790 M^{-1} cm^{-1} using Beer-Lambert law. The extinction coefficients of INK128 and rapamycin were calculated as 16,215 M^{-1} cm^{-1} at 293 nm and 41,425 M^{-1} cm^{-1} at 279 nm respectively (**Appendix C.2**). In comparison, EGFP has a value of 55,000 M^{-1} cm^{-1} at 488 nm. The high ε values for AZD2014 and INK128 at around 300 nm indicate that these inhibitors are good at absorbing this wavelength of light.

A

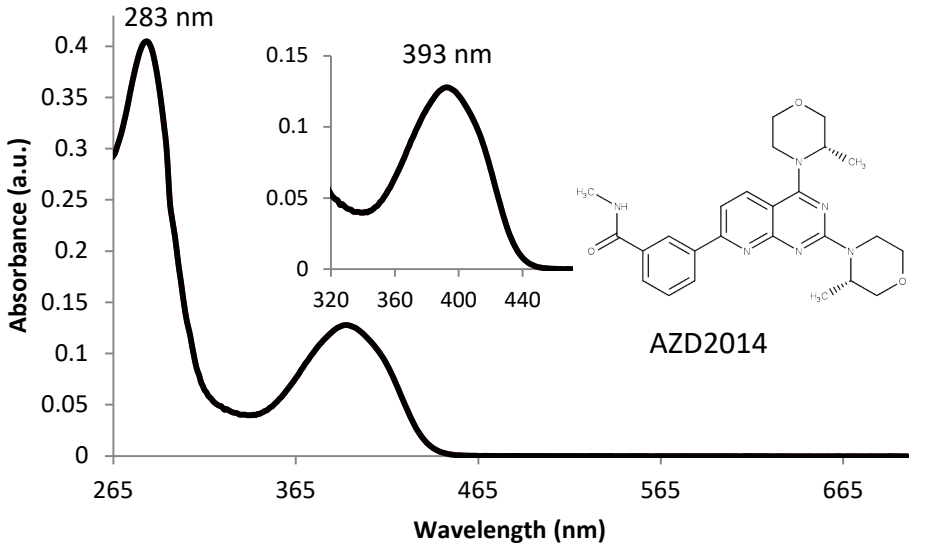
283 nm
393 nm
Absorbance (a.u.)
Wavelength (nm)
AZD2014

B

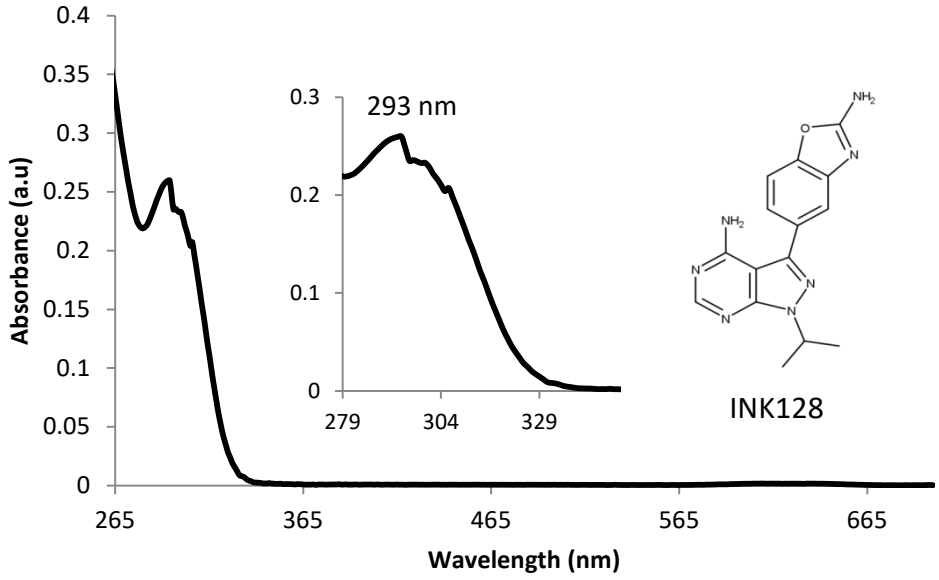
293 nm
Absorbance (a.u)
Wavelength (nm)
INK128

C

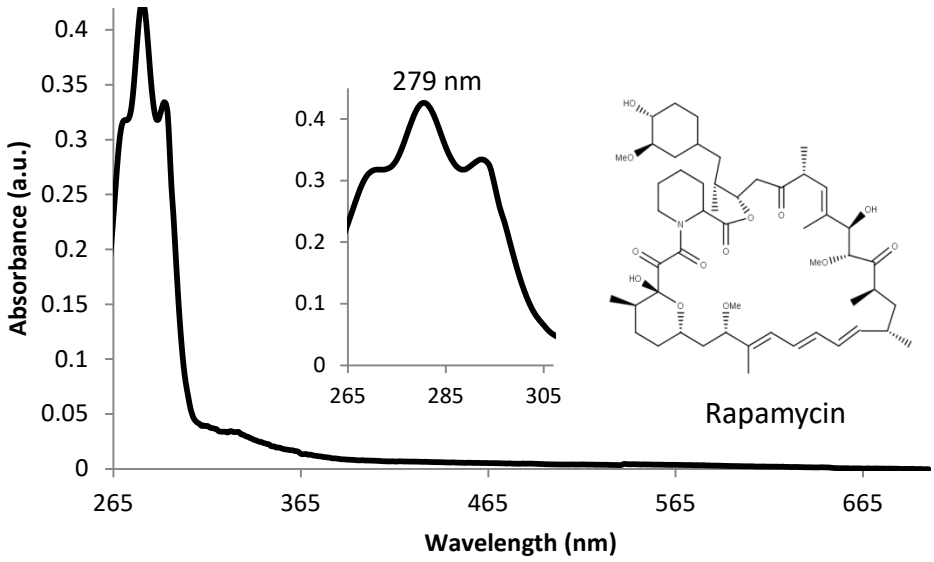
279 nm
Absorbance (a.u.)
Wavelength (nm)
Rapamycin

Figure 4.1: UV-VIS spectra of AZD2014, INK128 and rapamycin. *UV-VIS spectrum of A) AZD2014 (11 μM), B) INK128 (16 μM) and C) rapamycin (10 μM) in DMSO solvent. Solvent (DMSO) only absorbance spectrum was subtracted from raw spectra for deconvolution purposes. Data is representative of three independent experiments.*

4.2.2 Fluorescence spectroscopy analysis of AZD2014 in solution

The UV-VIS absorption data from **4.2.1** was used to determine any fluorescence emission of AZD2014 by performing emission spectra at the absorption maxima (283 nm or 393 nm). A solution of AZD2014 (7 μM) in DMSO solvent was ran using a fluorimeter (see **Chapter 2**) and an emission peak at 468 nm was obtained (**Figure 4.2A**). Using the emission peak of AZD2014, an excitation spectra using the fluorimeter was carried out on a solution of AZD2014 (7 μM) in DMSO. Two excitation peaks were determined at 284 nm and 393 nm, respectively (**Figure 4.2A**) that matched the UV-VIS data. As both the fluorescence spectra and its relative intensities are generally dependent on the molecule environment, the effects of solvation by solvents can be used to elucidate possible characteristics of the molecule in a cellular system. The fluorescence properties of AZD2014 were therefore investigated in a variety of solvents that included: DMSO, PBS and 1 mM BSA (a serum protein to mimic the cytosol and nucleosol environment of the cell) diluted in PBS. As shown in **Figure 4.2B**, the fluorescence intensity of AZD2014 was quenched in both PBS and BSA solutions (by 72%) compared to DMSO indicating that the solvent environment has significant effects on the spectral emission properties of AZD2014. The optical densities (OD) of these solutions remained similar (presented in section **4.2.3**) suggesting that the quantum yield may be changing. The excitation spectra of these solutions are given in **Appendix C.3** and show a 7 nm shift in the excitation spectrum of PBS compared to DMSO as well as a decrease in excitation intensities of 71%. Most notably, the 284 nm excitation peak of AZD2014 in 1 mM BSA disappeared showing a single 42% intensity reduced excitation peak at 393 nm (**Appendix C.3**). It is plausible that due to the

reported intrinsic fluorescence properties of BSA (Fujimori *et al.*, 1981), (Ex= ~380 and ~410 nm; Em= 450 nm), the lack of excitation may be caused by wavelength dependent attenuation.

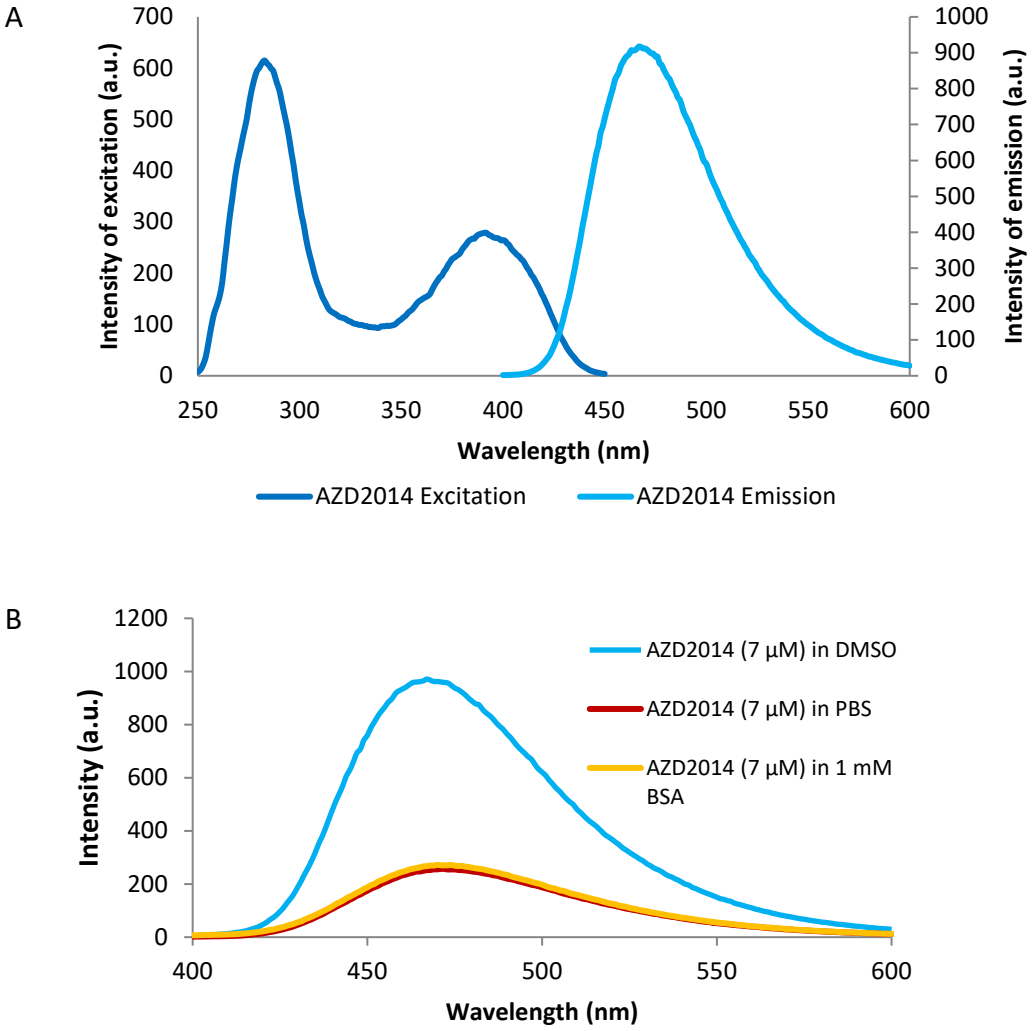

Figure 4.2: Fluorescence spectra of AZD2014 in various solvents. *A) Fluorescence spectrum of AZD2014 (7 µM) in DMSO showing excitation profile in black and emission profile in cyan. Spectra shown on two different axis and were taken at different detector settings to provide clean spectrum. B) Fluorescence spectra of AZD2014 (7 µM) in DMSO, PBS (1X) and 1 mM BSA in PBS (1X). Colour coded key of spectra solvents is shown in the top right hand corner. Data repeated minimum of three independent times.*

4.2.3 Determining the quantum yields of AZD2014 in solution

Having confirmed AZD2014 fluorescence, the strength of its fluorescence was examined. The quantum yield (ϕ_F) of a fluorescent molecule gives a measure of its

efficiency to convert absorbed photons into emitted photons and is provided as a numerical number between 0 and 1 with the latter exhibiting 100% quantum efficiency. Using coumarin-1 (ϕ_F of 0.73 in ethanol) (Jones *et al.*, 1985) and quinine sulphate (ϕ_F of 0.55 in sulphuric acid) (Heller *et al.*, 1974) as standards, the ϕ_F of AZD2014 in both DMSO and PBS was determined using the relative or comparative methods (see **Chapter 2** for details). The ϕ_F of AZD2014 in DMSO was determined as 0.47 ± 0.02 (**Figure 4.3**) at 393 nm excitation. In comparison, the ϕ_F of AZD2014 in PBS at 393 nm was determined as 0.11 ± 0.01. The 74% decrease in quantum yield observed in PBS supports the decrease in AZD2014 fluorescence emission in section **4.2.2** and indicates AZD2014 may be brighter in environments similar to DMSO than PBS. As a control, the ϕ_F of coumarin-1 was assumed to be unknown and was calculated using quinine sulphate with a value of 0.70 obtained (within 3% of the literature value, 0.73) (Jones *et al.*, 1985). In a similar fashion, a third standard was also trialled, rhodamine 6G (R6G) in ethanol (ϕ_F = 0.95) (Kubin and Fletcher, 1982). A lower ϕ_F value for R6G to that of the literature was determined most likely owing to the inner filter effect where R6G's fluorescence emission was found relatively proportional to the absorbed light, indicating that some emission may be re-absorbed, giving inaccurate fluorescence integrations (spectral overlap given in **Appendix C.4**), on this basis R6G was rejected as a suitable standard.

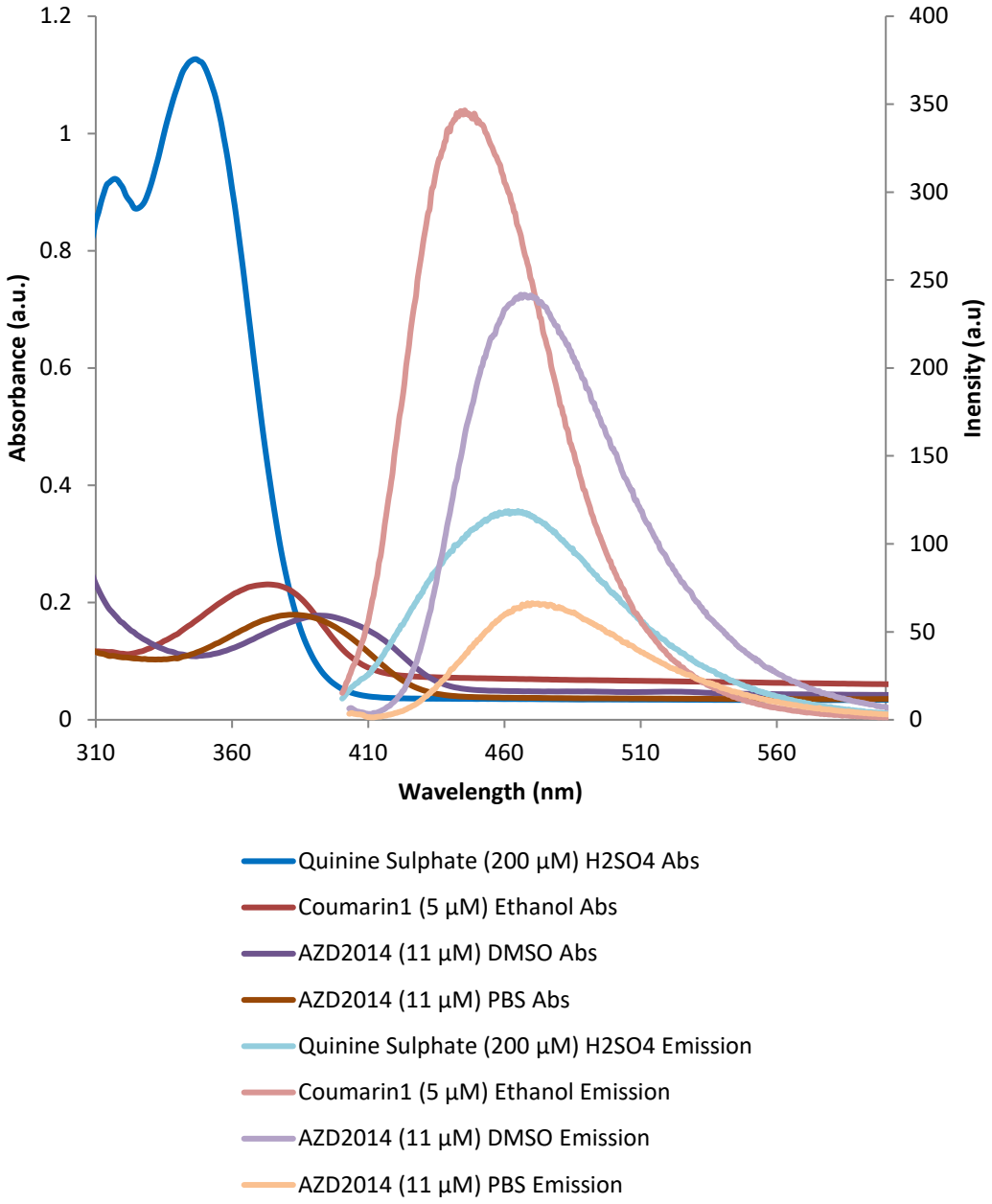

Figure 4.3: Quantum yield absorbance and fluorescence spectra of AZD2014 and standard. *UV-VIS spectra of AZD2014 in DMSO and PBS, coumarin-1 in ethanol, quinine sulphate in sulphuric acid (H_2SO_4) with fluorescence emissions of the same solutions. All settings were kept constant for each experiment. AZD2014 and standards were excited at 393 nm. Absorbance values at 393 nm and integrated fluorescent intensities were used for quantum yield calculations. Data repeated two independent times.*

4.2.4 Multiphoton excitation spectrum of AZD2014

Having confirmed the fluorescence of AZD2014 using one-photon excitation fluorimetry, the multiphoton excitation properties were next investigated by using a lambda scan to record a series of confocal images across a series of multiphoton excitation wavelengths from a drop of AZD2014 solution (7 μM) in DMSO placed on a coverslip. As shown in **Figure 4.4**, a spectrum was produced from the intensities of the confocal images. A two-photon excitation peak at 798 ± 36 nm was determined as well as a second peak below 680 nm. The second rising peak could be due to the UV absorption at 283 (x2) nm. However, laser tunability stops at 680 nm and so any peaks below 680 nm could not be defined. Based on UV-VIS results from **section 4.2.1**, a two-photon excitation at around 600 nm and 800 nm could be expected as doubling the single photon excitation (~300 nm and ~400 nm) wavelength of AZD2014 would meet the requirement of a two-photon excitation. No attempts to obtain a two-photon absorption cross section were made as this is not the current focus of this study.

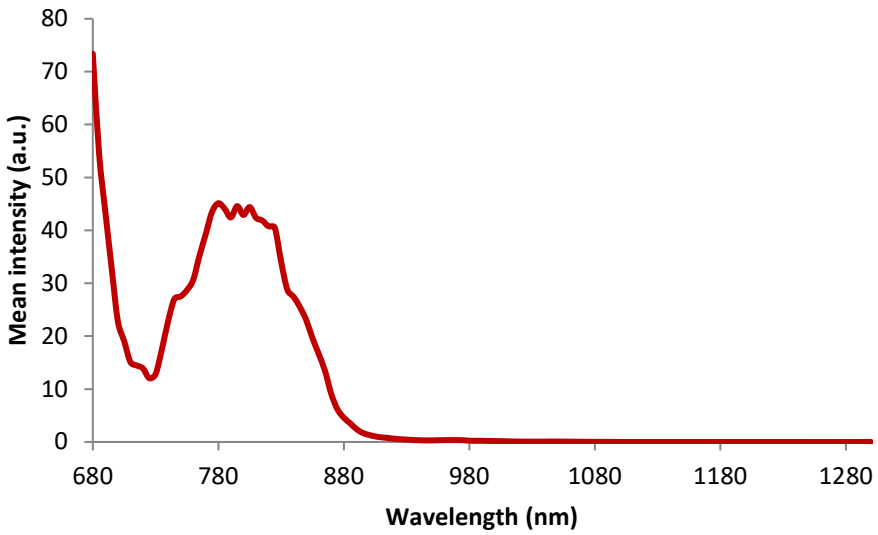

Figure 4.4: Two-photon excitation spectrum of AZD2014. *Lambda scan of 7 μM AZD2014 in DMSO. Data taken from confocal multiphoton images and intensities quantified in ImageJ version 1.58. Intensities against wavelength plotted and spectrum shown in red.*

4.2.5 AZD2014 FRET characterisation with EGFP

To shed further insight into the mechanism of action of AZD2014, attempts to use AZD2014 as a donor molecule and GFP an acceptor molecule for FRET-FLIM studies were performed as a proof-of-concept for piloting direct drug-protein interactions in living cells. First, the fluorescence absorbance of purified GFP in water was obtained which showed an overlap with the emission spectrum of AZD2014 (**Figure 4.5**). The spectral overlap percentage for FRET between AZD2014 emission and EGFP absorption was determined as 73%. After confirming that there was significant overlap for FRET, the fluorescence lifetime of a drop of AZD2014 in ethyl glycerol alone was measured as 4.0 ± 0.22 ns using 600 nm excitation, since 405 nm excitation was found unsuitable as presented in section **4.2.14**. A 1:1 ratio of AZD2014 and purified GFP was made in ethyl glycerol which gave a shortening in AZD2014 lifetime to 2.70 ± 0.24 ns, as shown in **Figure 4.5**. As a control experiment for acceptor bleed-through, no intensity (hence no lifetime) of only purified GFP in ethyl glycerol was detected at 600 nm excitation and this will become crucial for section **4.2.15** where drug-protein interactions are probed. Overall, these findings provide confirmation for using AZD2014 and GFP tagged proteins as energy transfer acceptors (FRET pairs) for studying drug-protein interactions in the cellular model, see section **4.2.15**.

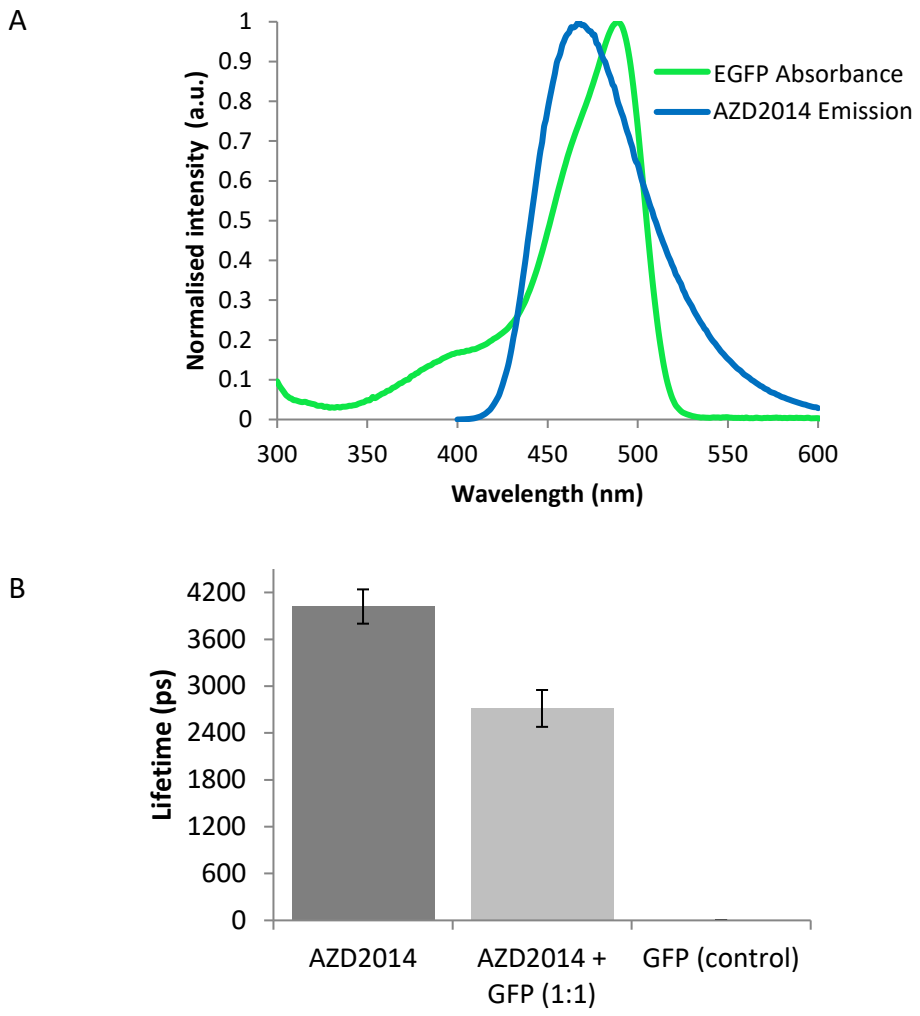

Figure 4.5: AZD2014 FRET interaction with EGFP in solution. *A) Spectral overlap between EGFP absorption and AZD2014 emission by normalisation to the maximum peaks of each spectra. B) Bar chart showing lifetimes (ps) of AZD2014, GFP and both mixed (1:1) in ethyl glycerol solutions using 600 nm multiphoton excitation. Data repeated minimum of three independent times. Error bars show standard deviation.*

4.2.6 AZD2014 TCSPC measurements in solution

To determine the excited state fluorescence lifetime of AZD2014 in different solvents (see **Chapter 2: Materials and methods**) a drop of AZD2014 placed onto a microscope coverslip was excited at 600 nm two-photon or at 405 nm one-photon excitation in DMSO, PBS and 1 mM BSA solvents**.** As shown in **Table 4.1**, the lifetime of AZD2014 was longer with a mono-exponential decay profile (6.6 ± 0.16 ns) than in PBS (2 ± 0.02 ns). The reason for any lifetime differences to that found in section **4.2.5** may be likely due to solvent effects that may enhance or decrease

AZD2014 lifetime. A similar reduced lifetime (3.3 ± 0.18 ns) was observed in 1 mM BSA although the data fitted better to a double-exponential decay model. Taken together, these results suggest that AZD2014 may be more stable in lipid environments as DMSO mimics hydrophobic environments closer to that found in a cellular system, particularly lipidic membrane structures. Calibration curves for one-photon and two-photon excitation of AZD2014 are given in **Appendix C5.**

Table 4.1: Various lifetimes and pre-exponential components of AZD2014 in solution

	τ_m (ps) (mean)	SD ±	τ_1 (ps) (mean)	SD ±	a (%)(mean)	SD ±	τ_2 (ps) (mean)	SD ±	b (%) (mean)	SD ±
AZD2014 (7 µM) in DMSO	6660	161	-	-	-	-	-	-	-	-
AZD2014 (7 µM) in PBS	2028	23	-	-	-	-	-	-	-	-
AZD2014 (7 µM) in 1mM BSA	3252	181	970	291	46	9	5158	712	54	9

4.2.7 Fluorimetry analysis of INK128

The fluorescence of INK128 in DMSO was also investigated. A 7 µM solution of INK128 in DMSO was ran in a fluorimeter for an emission scan using an excitation at 300 nm as a starting point following the UV-Vis spectrometer studies in section **4.2.1**. A broad emission peak at 400 nm was observed indicating that INK128 exhibits fluorescence properties (**Figure 4.6A**). Using this information, the emission was set at 400 nm and an excitation profile was ran and showed a peak at 308 nm **Figure 4.6A**. The fluorescence emissions of 7 µM INK128 in either DMSO or PBS was compared to provide an understanding of the environmental favourability of the molecule. As shown in **Figure 4.6B**, the fluorescence of INK128 was solvent quenched in PBS compared to DMSO, evident by a significantly reduced (by 99%) emission peak, demonstrating that this mTOR inhibitor may generally favour polar aprotic environments.

In comparison, no fluorescence excitation or emission was observed (in the region of 300- 500 nm) when 7 µM of rapamycin was ran in the fluorimeter using the detector at its highest sensitivity setting.

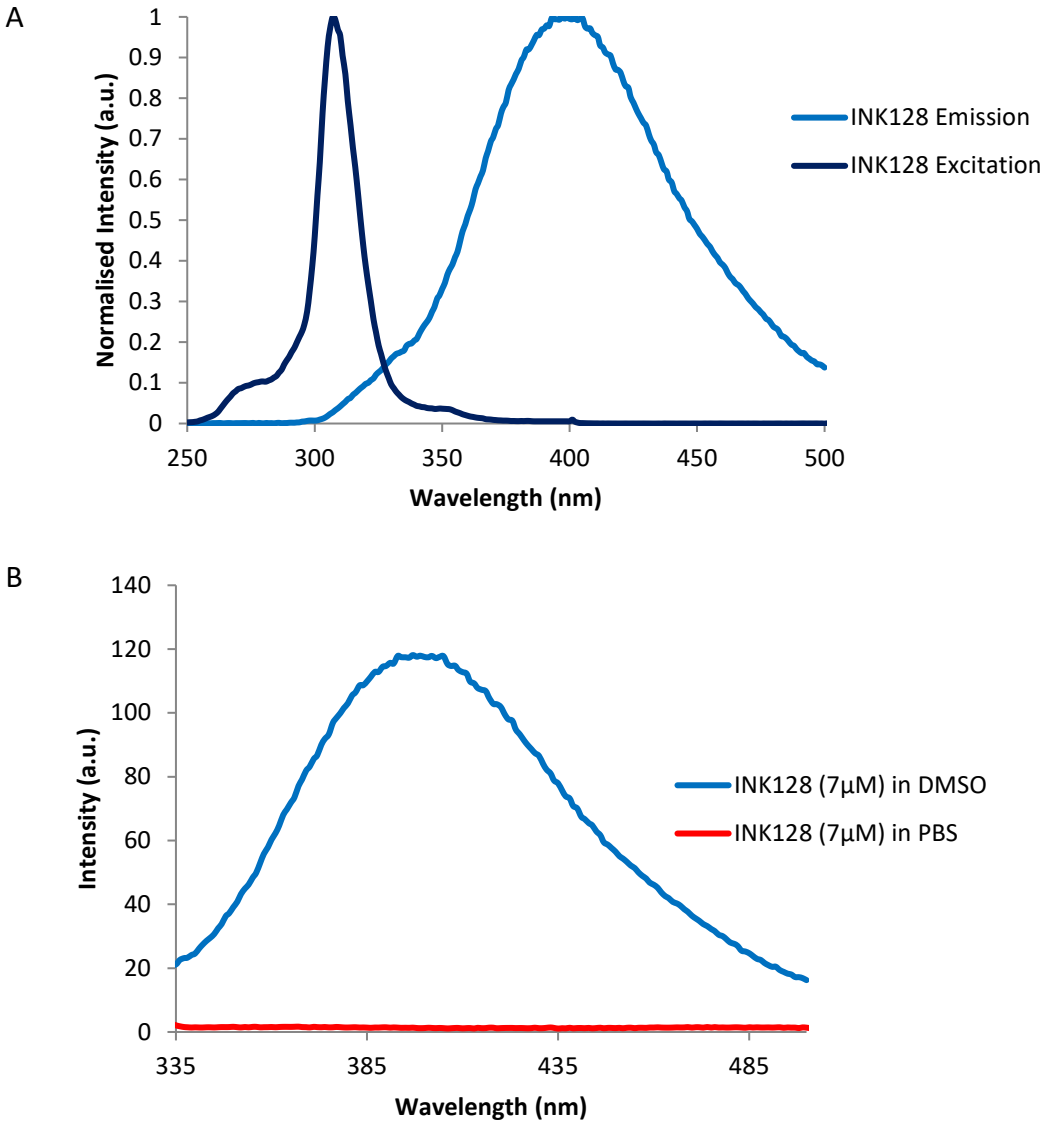

Figure 4.6: Fluorescence spectra of INK128 in various solvents. *A) Fluorescence spectrum of INK128 (7 µM) in DMSO showing excitation profile in dark blue and emission profile in lighter blue. B) Fluorescence spectra of INK128 (7 µM) in DMSO and PBS (1X). Colour coded key is shown in the top right hand corner. Repeated minimum of three independent times.*

4.2.8 Fluorescence lifetime and ϕ_F of INK128 in solution

The fluorescence lifetime of INK128 using TSCPC was examined. A concentration of 70 µM INK128 exhibited weak fluorescence and thus a higher concentration of 3.2 mM was used to acquire better meaningful statistical lifetime information. Self-quenching at this higher concentration needs to be considered but this not known to be a problem when using multiphoton excitation. The lifetime of INK128 was determined to be 4.7 ± 0.13 ns in DMSO whilst INK128 in PBS showed low counts and thus its lifetime could not be accurately determined.

Similarly to section **4.2.3**, the quantum yield of INK128 in DMSO was determined as 0.33 using quinine sulphate as a standard (spectral data shown in **Figure 4.7**) at 300 nm excitation. This value is lower than that obtained for AZD2014 (0.47) indicating that INK128 is 30% less efficient at emitting light compared to AZD2014.

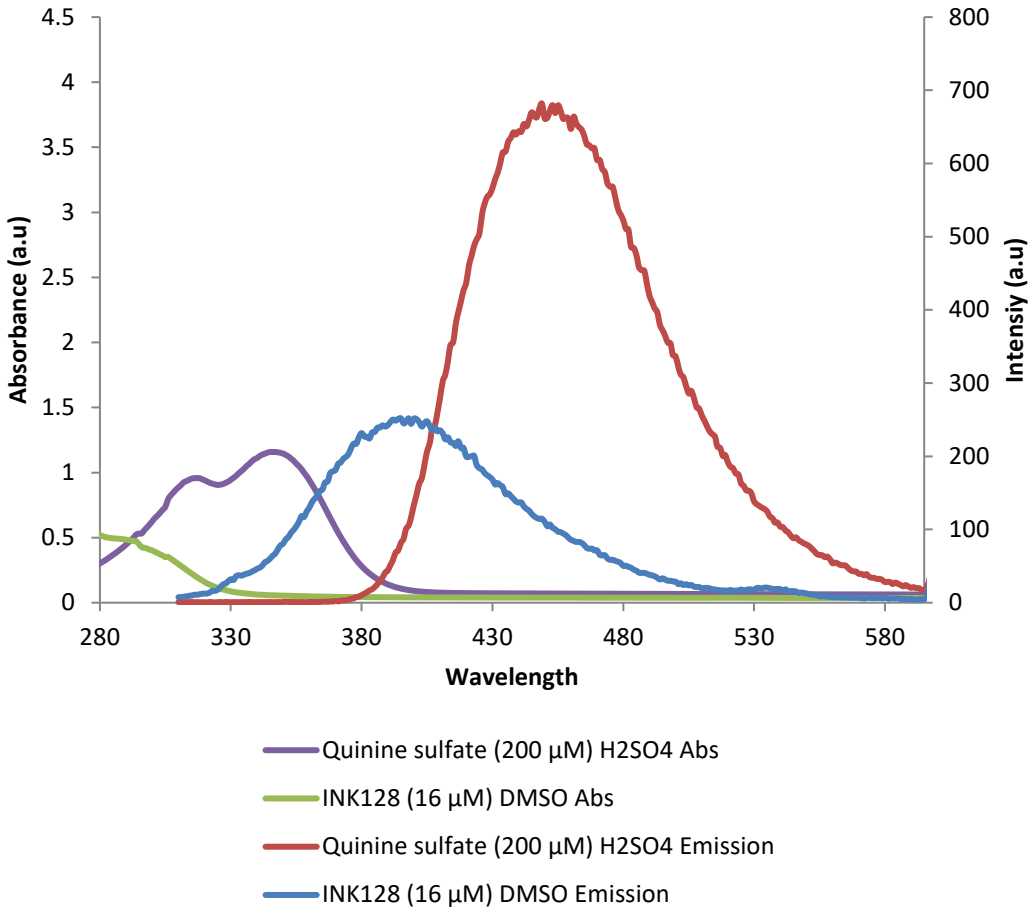

Figure 4.7: Quantum yield absorbance and fluorescence spectra of INK128 and standard. *UV-VIS spectra of INK128 in DMSO and quinine sulphate in sulphuric acid (H_2SO_4) with fluorescence emissions of the same solutions. All settings were kept constant for each experiment. INK128 and standards were excited at 300 nm. Absorbance values at 300 nm and integrated fluorescent intensities were used for quantum yield calculations.*

4.2.9 Uptake of AZD2014 in living cells

Following on from the solution studies, the uptake and imaging of AZD2014 in live mammalian cells was investigated. A solution of AZD2014 (7 μM) in complete growth media was added to adherent exponentially growing HEK293 cells and the uptake determined by acquiring confocal images over a 20 minute time period with one minute time intervals using 405 nm excitation (**Figure 4.8**). **Figure 4.8** shows that AZD2014 was taken up by cells within 1 minute of addition (k_{uptake}= 1 minute, defined by time at 1/2 the maximum intensity saturation) and plateaued at around 4 minutes. In addition, AZD2014 in HEK293 cells was imaged 15 minutes after administration using confocal microscopy and showed localisation in the nucleus, the cytosol and peri-nuclear subcellular regions of the cell (**Figure 4.8C**). Trypan blue exclusion test for cell viability was also performed in HEK293 cells in solution with varying concentrations of AZD2014. Testing for viability at the concentrations similar to that administered in the cell studies, **Figure 4.8D**, showed at least 80% cell viability with 10 μM treatment of AZD2014 at 30 minutes indicating that although concentration range used for live cell imaging may have some detrimental effect to the cell, it is however still sufficient for obtaining good quality cell data. It is worth noting the 7 μM AZD2014 is similar to the concentration using in pre-clinical studies (Pike *et al.*, 2013). It is suggested that future use of AZD2014 be carried out below 7 μM.

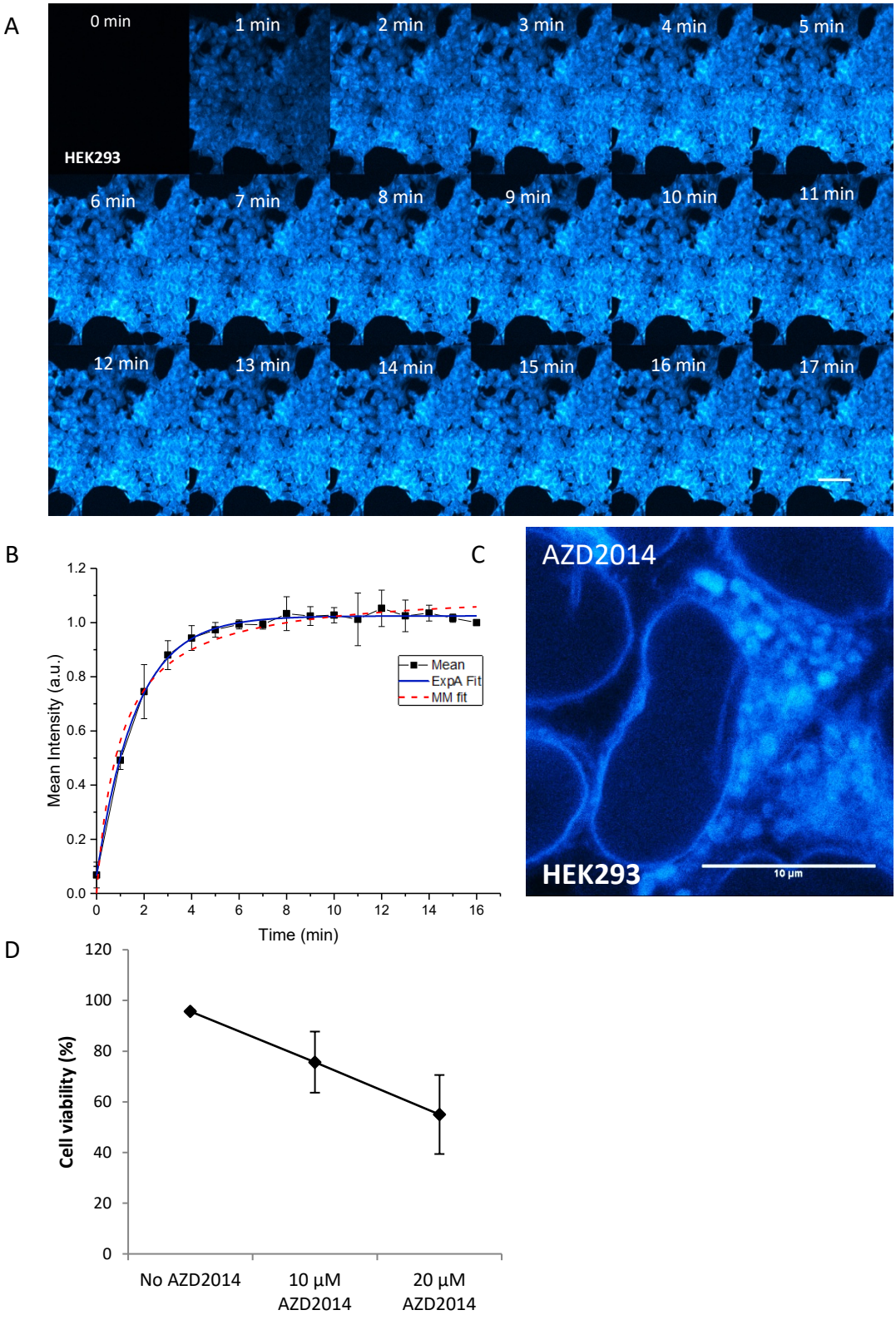

Figure 4.8: Uptake and imaging of AZD2014 in HEK293 cells. *A) Confocal images of AZD2014 (7 µM) uptake in HEK293 cells taken over 17 minutes of administration, with one minute time intervals using 405 nm excitation. Scale bar = 50 µm. B) Plot of extracted confocal intensities of AZD2014 (7 µM) over the 17 minutes with Michaelis–Menten (MM) and non-linear (ExpA) fitting. C) Airyscan confocal imaging of AZD2014 in live HEK293 cells.*

Scale bar = 10 µm. D) Trypan blue exclusion test of HEK293 cell viability with AZD2014 treatment. Repeated minimum of three independent times. Error bars show standard deviation from three experiments.

4.2.10 Imaging AZD2014 in other living mammalian cell lines

To verify that the localisation of AZD2014 observed in the HEK293 cell line was similar for other mammalian cells, experiments were repeated using CHO and MCF7 cells. **Figure 4.9A** shows treatment of CHO cells with 7 µM of AZD2014 and indicates similar localised nuclear and cytoplasmic fluorescence intensities of AZD2014 to that observed for the HEK293 cells. Moreover, similar results were observed when AZD2014 was administered to MCF7 cells (**Figure 4.9B**) with comparable results to both CHO cells and HEK293 cells. Together, these findings demonstrate specificity in localisation of AZD2014 although some differences in mammalian cells may be due to simply cell specificity in organelles.

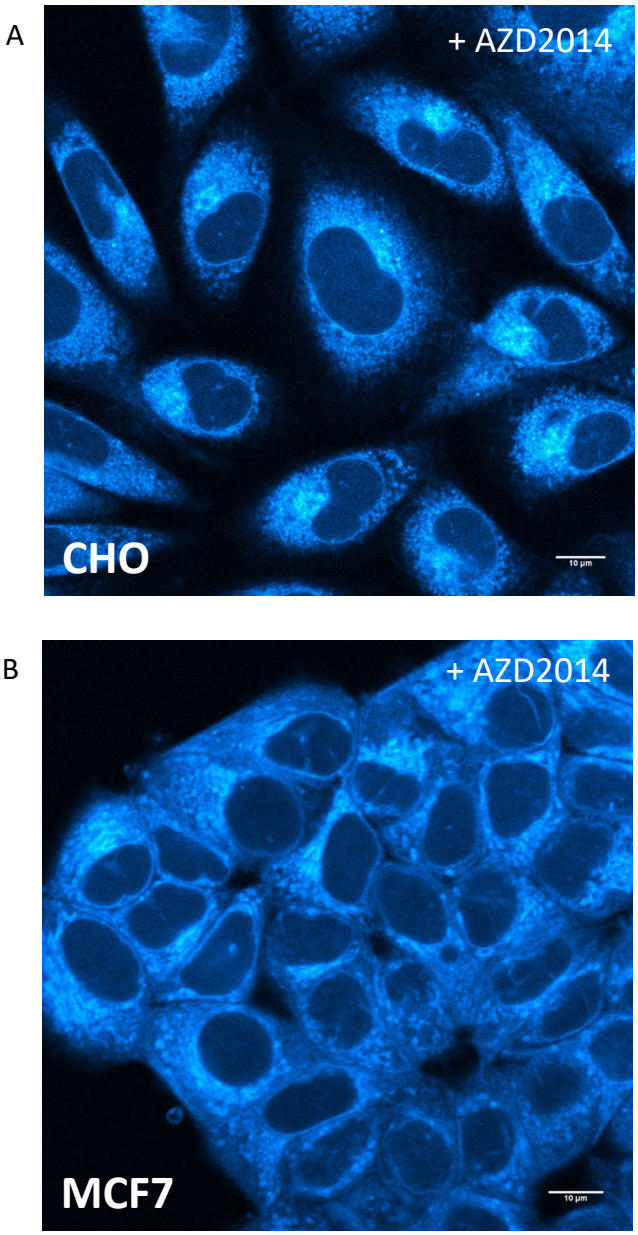

Figure 4.9: Imaging AZD2014 in CHO and MCF7 live cells. *Confocal images of AZD2014 (7 μM) in A) CHO and B) MCF7 cell lines with 405 nm excitation. Repeated minimum of three independent times. Scale bar = 10 μm*

4.2.11 Quantifying AZD2014 accumulation in living cells

Having successfully imaged the pan-mTOR inhibitor AZD2014 naturally within its physiologically live cell environment, an attempt was made to quantify the accumulated AZD2014 within both the nucleus and the cytoplasm. This was achieved by measuring the average fluorescence intensity of various concentrations of AZD2014 in media solution with 600 nm two-photon excitation under the same

settings to generate a calibration line graph, see **Figure 4.10**. Two-photon excitation was chosen over single (405 nm) excitation because of its advantage in inducing lower photodamage and so is more suitable for long time-lapse imaging. Under the same acquisition settings, the fluorescence intensity of HEK293 cells, treated with 7 μM of AZD2014 was determined 15 minutes following administration to allow the uptake to plateau. These concentration dependent intensities were then used to extrapolate concentrations from the solution calibration graph. The accumulated concentration of AZD2014 in the nucleus was calculated as 124 μM and in the cytoplasm as 213 μM whilst the average concentration in the whole cell was determined as 148 μM (**Figure 4.10**). These findings suggest that even though a small dosage (7 μM) may be administered to cells, this does not reflect the final concentration within the cell, a finding critical to pre-clinical characterisation and toxicity effects of any drug. This may also explain the small (~20%) of cell killing observed in the viability studies (**section 4.2.9**).

A

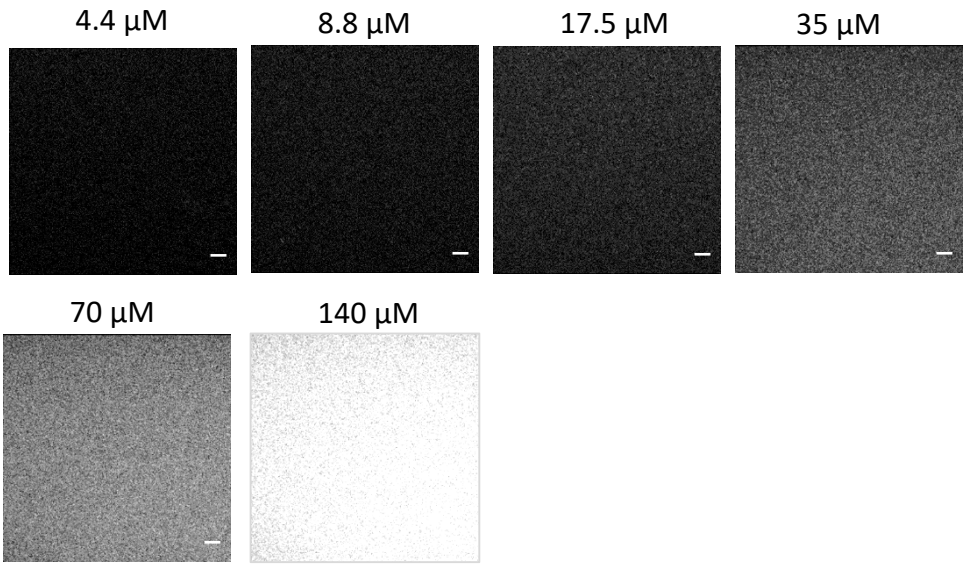

B

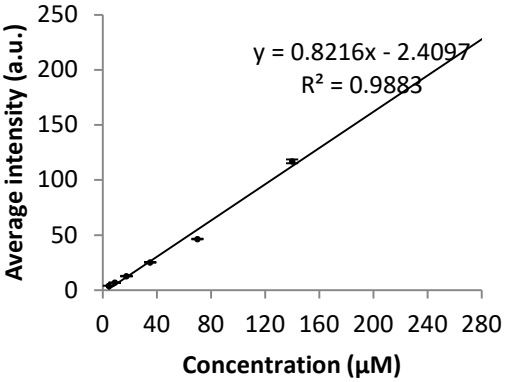

C

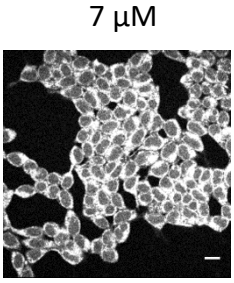

D

Sub-cellular localisation	Average AZD2014 cell intensity (a.u.)	SD (±)	Calculated concentration (µM)
Nucleus	98	5	122.6
Cytoplasm	210	19	258.5
Whole cell	125	11	155.4

Figure 4.10: Quantification of AZD2014 in live HEK293 cells. *A) Two-photon confocal images of AZD2014 in complete growth media using 600 nm excitation at 1 mW. B) Calibration line graph of increasing concentrations of AZD2014 in complete growth media*

with extracted intensities using 600 nm excitation. C) Two-photon confocal image of HEK293 cells treated with 7 μM AZD2014. D) Extrapolated nuclear, cytoplasmic and whole cell concentrations in HEK293 cells administered with 7 μM AZD2014. Repeated minimum of three independent times. Error bars show standard deviation. Scale bar = 10 μm

4.2.12 Uptake of INK128 in living cells

The localisation of INK128 in live HEK293 cells was also investigated in order to correlate any similarities between the second generation mTOR inhibitors. Initial attempts were made using one-photon excitation wavelengths, however, due to weak INK128 fluorescence, two-photon excitation was turned to for UV excitation whilst minimising any unwanted cellular background signals, a key advantage of multiphoton microscopy. Seeded HEK293 cells only were initially imaged over time with 600 nm excitation. As expected the two-photon excitation gave low levels of autofluorescence at 0.9 mW (**Figure 4.11**). It is expected that at higher laser powers, natural indole molecules such as tryptophan and derivatives will also be efficiently excited and observed below 380 nm (Guo *et al.*, 1998; Botchway *et al.*, 2008). Next, 70 μM of INK128 was added to HEK293 cells at room temperature and imaged over time with 600 nm excitation. An increase in fluorescence intensity was observed illustrating uptake and accumulation of INK128 in living cells (**Figure 4.11A**) at these detectable levels. The uptake was fitted to Michaelis–Menten kinetics, showing an uptake within 1 minute (k_{uptake}= 42 seconds) and a plateau reached within 2 minutes (**Figure 4.11B**). Multiphoton imaging at 600 nm of INK128 in live HEK293 cells showed a similar localisation to that of AZD2014, showing fluorescence in the nucleus and accumulation of fluorescence in the cytosol with similar sub-structure localisation to that observed with AZD2014 (**Figure 4.11C**). Together, these results show *in situ* detection of pan-mTOR inhibitors in the living cell environment using the two-photon microscopy approach.

A

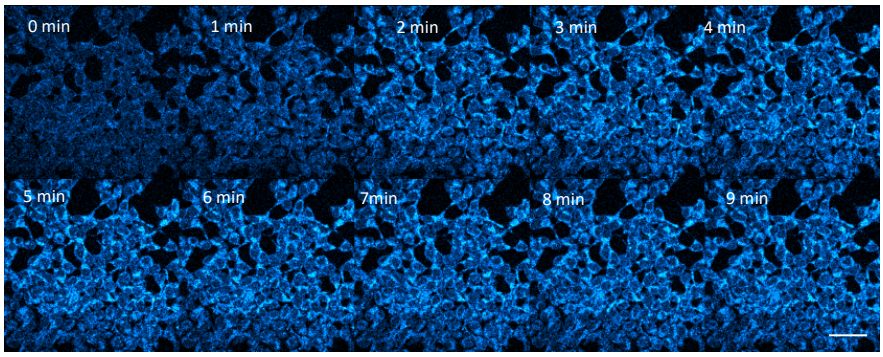

+ INK128 (70 µM)

B

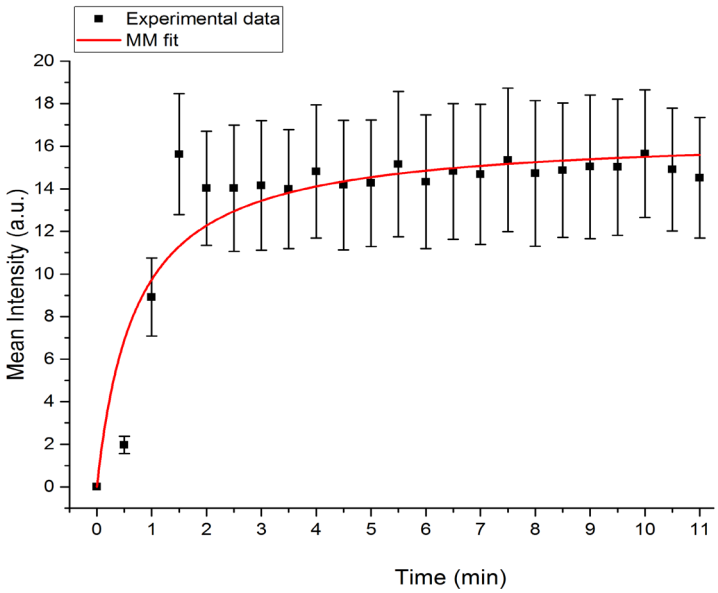

C

Intensity map

Grey

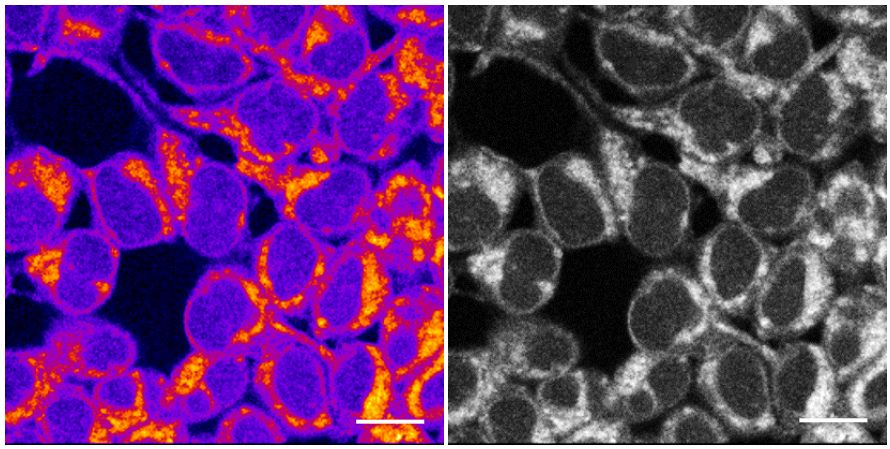

+ INK128 (70 µM)

D

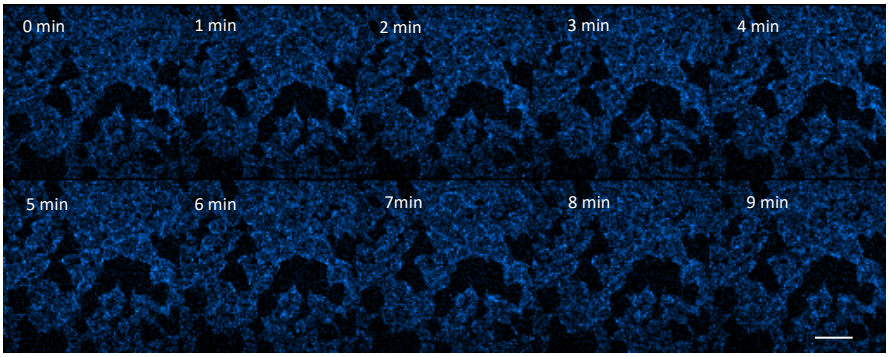

Control

Figure 4.11: Imaging the uptake of INK128 in live HEK293 cells. *A) Series of multiphoton images of HEK293 administered with INK128 (70 μM) illuminated with 600 nm over time. B) Uptake curve of INK128 (70 μM) in HEK293 cells over time by extracting average intensity from multiphoton confocal images with a Michaelis–Menten (MM) fitting. Data representative of one of three independent repeats where error bars show standard deviation. C) Two-photon confocal image of INK128 in live HEK293 cells shown both in greyscale and also in an intensity map (LUT). Scale bar = 10 μm. D) Series of multiphoton images of HEK293 without treatment illuminated with 600 nm over time. Scale bar = 50 μm. Data repeated minimum of three independent times.*

4.2.13 Uptake and imaging of AZD2014 in living HEK293 spheroids

Due to the higher concentration required to image INK128, deemed excessively high and potentially toxic to the cell, only AZD2014 was taken forward for further investigation. The next step was to characterise the uptake of AZD2014 in a spheroid tumour model mimicking the three-dimensional physiology and functions of living tissues. HEK293 spheroids were formed as described in **Chapter 2** using the low melting point agarose method. Light sheet fluorescence microscopy was chosen to study AZD2014 administration to the spheroids due to its ability to image in real-time at high speeds with extremely low levels of laser power, making it ideal for short or long-term time lapse measurements. As shown in **Figure 4.12A,** the fluorescence of AZD2014 (7 μM) was observed across all depths (z planes) in the volume of the spheroid from the surface layer cells to the core planes. The rate of uptake into the outer surface of the spheroid was faster (5-times) compared to that found in the core of the spheroid, indicating possible diffusion control through to the core (**Figure 4.12B and C**) as the intensity of the drug in the media of the spheroid remained relatively constant over time. The uptake of AZD2014 into the 3D spheroid was similar to that observed in the monolayer studies with uptake within 1 minute of administration supporting the use of the spheroid model for studying cellular signalling.

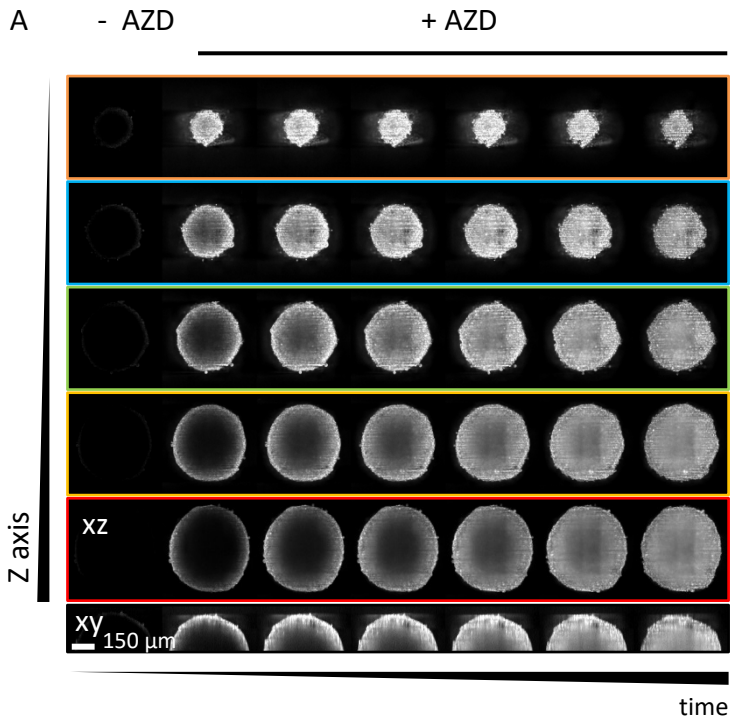
A
- AZD
+ AZD
Z axis
xz
xy
150 µm
time

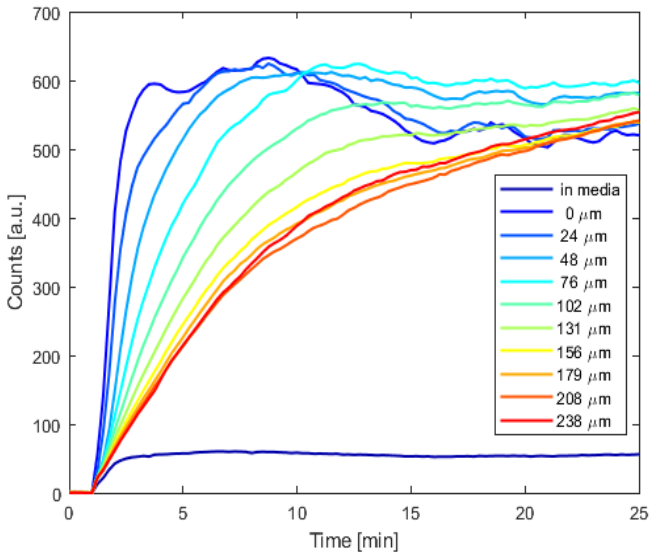
B
Counts [a.u.]
Time [min]
in media
0 µm
24 µm
48 µm
76 µm
102 µm
131 µm
156 µm
179 µm
208 µm
238 µm

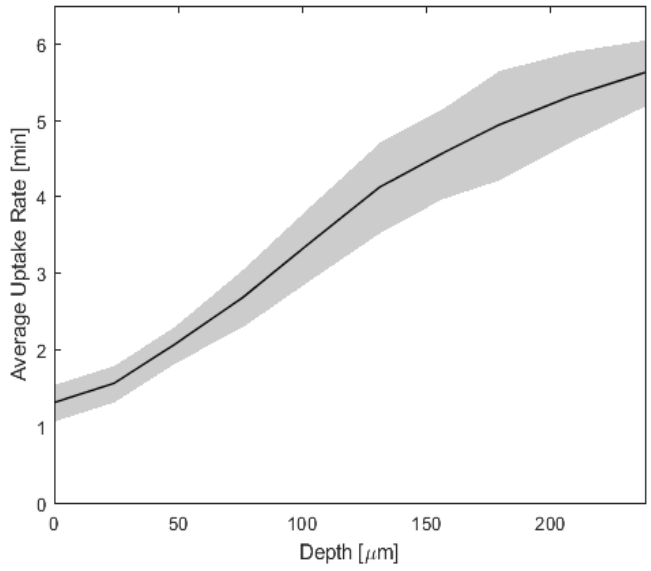
C
Average Uptake Rate [min]
Depth [µm]

Figure 4.12: Uptake of AZD2014 in multi-cellular spheroids. *A) AZD2014 (7 μM) was administrated (+) in the media and the spheroids imaged using Light sheet microscopy for 2 hours by recording stacks of 780 μm x 780 μm x 300 μm volume composed of 44 planes taken every 15 seconds. Compiled intensity projection images over time are shown with increasing depths (z planes). Images without AZD2014 treatment are also shown (-). B) The uptake of the AZD2014 fluorescence in the spheroid for the first 25 minutes was studied at different depths (z planes in μm). C) The mean rates of uptake, determined as the time at half-saturation of the fluorescence, for the various depths are shown. Scale bar = 150 μm. Repeated minimum of three independent times. (n=12).*

4.2.14 AZD2014 photo-activated disassembly and cell death of spheroids

The effect of 405 nm illumination on the HEK293 spheroids with administered 7 μM AZD2014 present in surrounding media was investigated to develop an understanding of the photochemical properties of the drug. After 30 minutes of illumination, a 2.3-times increase in volume of the spheroid was observed (**Figure 4.13**). Cellular death was immediately observed in the transmitted light channel as well as the expansion of the spheroid and accumulation of drug into the core as seen by an increase in fluorescence intensity, most likely due to disruption in cell-cell contacts that 'loosen' the spheroid. Control experiments were also ran with 405 nm illumination or 7 μM AZD2014 alone without 405 nm excitation. The results showed that although the illumination itself gave a 1.2-times increase in volume, this was insignificant compared to the combination of both drug and 405 nm excitation (**Figure 4.13**). AZD2014 administration alone without light illumination did not give any volume increase supporting a photo-activated effect of AZD2014 (**Figure 4.13**). These results implicate AZD2014 as a potential photosensitizer agent towards combined mTOR targeting and photodynamic therapy (PDT) against tumours.

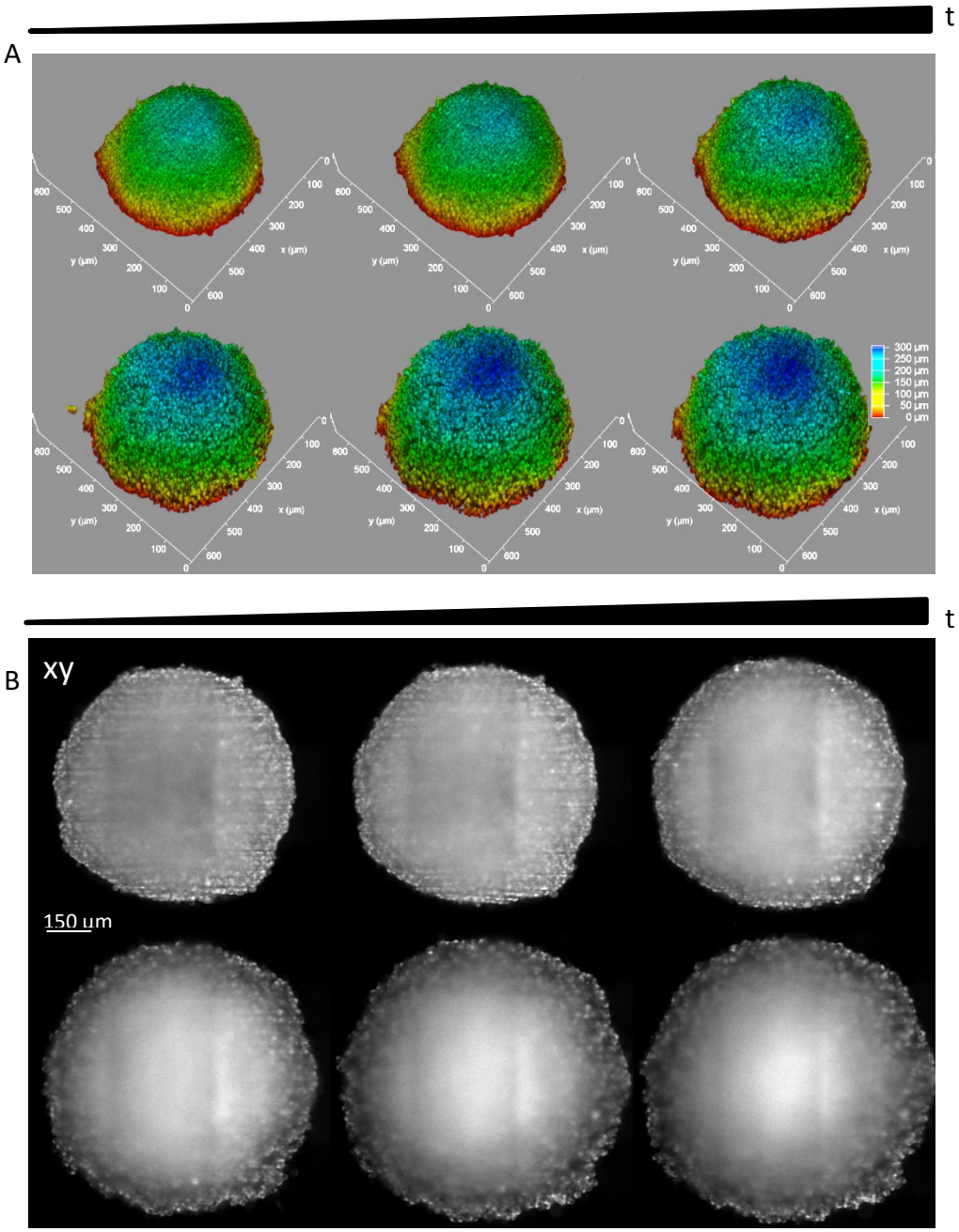
t
A
300 µm
250 µm
200 µm
150 µm
100 µm
50 µm
0 µm
t
B
xy
150 µm
C
Fold increase (a.u.)
3
2.5
2
1.5
1
0.5
0
Drug + Light
Light
Drug

Figure 4.13: AZD2014 photo-activation in multi-cellular spheroids. *A) 3D renders of HEK293 spheroid volumes with AZD2014 (7 μM) imaged over time using Lightsheet microscopy. B) Intensity projections of HEK293 spheroid volumes with AZD2014 (7 μM) over time. C) Graph showing fold increase of HEK293 spheroid volume with AZD2014 (drug) only, 405 nm (light) only and both AZD2014 and 405 nm (drug + light) treatments. Repeated minimum of three independent times. Error bars show standard deviation. All scale bars = 150 μm.*

4.2.15 Unsuitability of GFP tagged S6K1 acceptor for one-photon FRET-FLIM

The application of using AZD2014 to determine mTORC1 interactions was explored in living mammalian cells. The S6K1 protein with a GFP tag was first turned to as a pilot for this study to test the hypothesis whether AZD2014 functions by interacting with downstream mTOR targets. HEK293 expressing fluorescently tagged S6K1 (S6K1-GFPSpark) were treated with AZD2014 (7 μM). The lifetime of AZD2014 in cells was measured using a ~60 ps pulsed 405 nm excitation source and exhibited a single exponential decay with a mean lifetime of 4.60 ± 0.05 ns that is shown in **Figure 4.14**. Upon AZD2014 addition to S6K1-GFPSpark expressing cells, a change in mean lifetime from 4.60 ± 0.05 ns to 3.70 ± 0.50 ns was observed, as given in **Figure 4.14**. Although this quenching suggests that AZD2014 may be directly and physically interacting with S6K1, there may be possible fluorescence emission directly from excitation of GFP at 405 nm since certain GFPs have been known to be excited at 405 nm. To investigate such interference, S6K1-GFPSpark in cells as a control was tested. **Figure 4.15** shows that there is indeed some emission occurring with a lifetime of 0.9 ± 0.3 ns. This suggests that the measured change in AZD2014 lifetime may be due to the presence of this second fast component and fitting to a single exponential decay results in an average shortened lifetime. Similar results on decay properties using 405 nm excitation of GFP-like fluorescent proteins has been reported previously (Habuchi *et al.*, 2005). Overall this suggests that any interactions of AZD2014 with S6K1 using single photon excitation may be problematic.

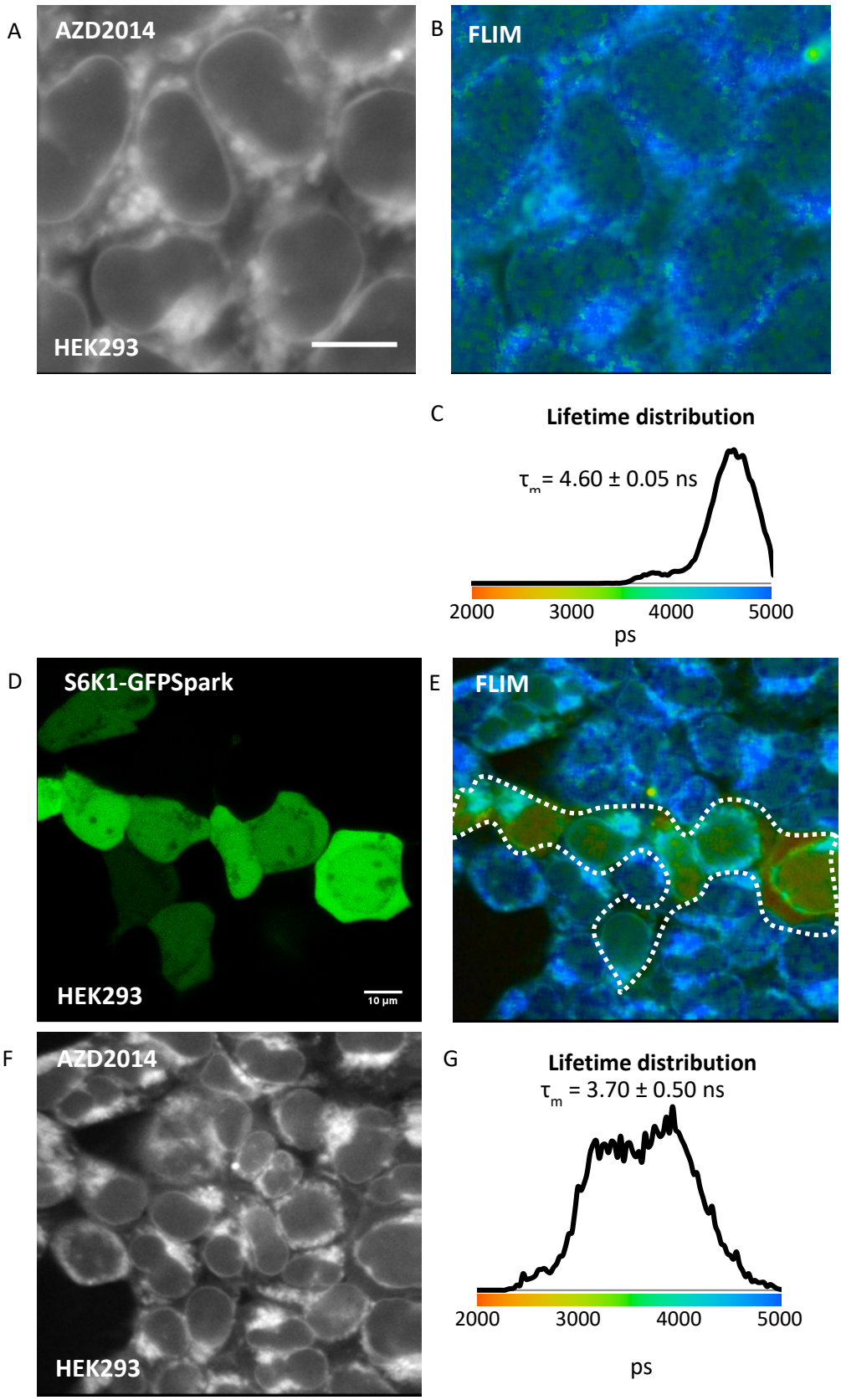

Figure 4.14: AZD2014 possible interaction with S6K1-GFPSpark in live cells. *A) Photon intensity image of AZD2014 in HEK293 cells. B) FLIM image of AZD2014 at 405 nm. C) Lifetime distributions of AZD2014 with a lifetime mean (τ_m). D) Confocal image of S6K1-GFPSpark. E) FLIM image of AZD2014 with region of interest shown in white dotted line. F)*

Intensity of AZD2014. G) Lifetime distributions of AZD2014 from selected FLIM region. Repeated minimum of three independent times. Error bars show standard deviation. Scale bar = 10 μm.

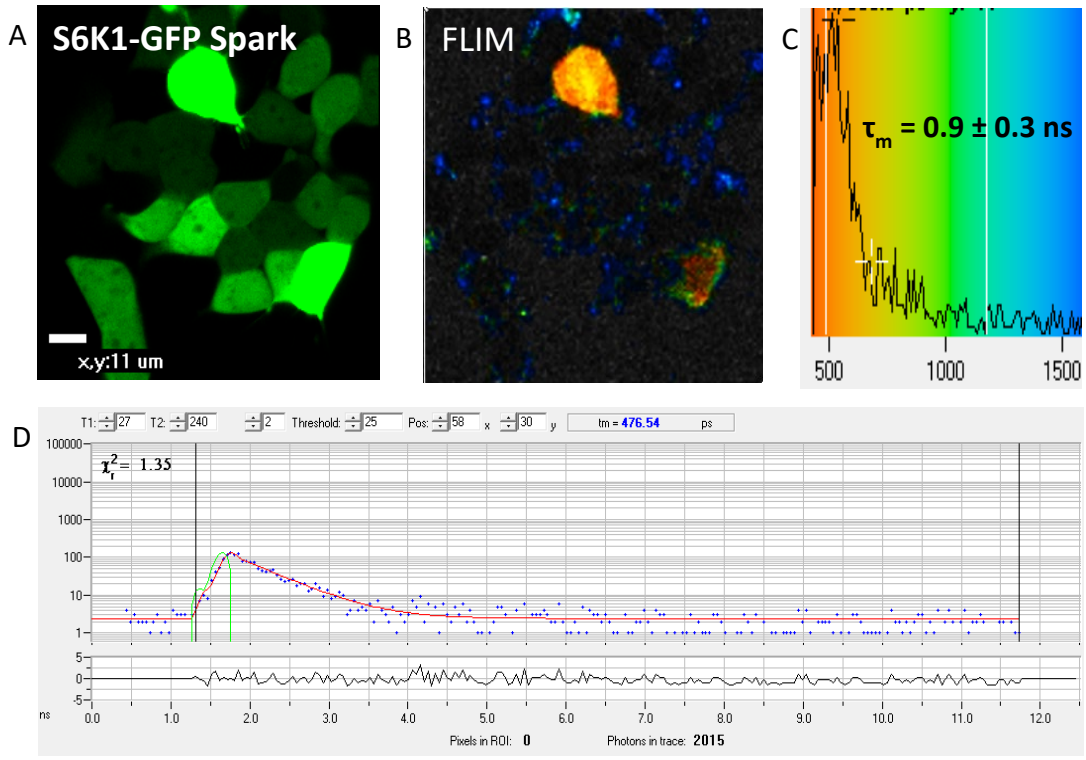

Figure 4.15: GFP acceptor spectral bleed-through with 405 nm excitation. *A) Confocal image of S6K1-GFPspark expressed in HEK293 cells at 488nm excitation. B) FLIM of S6K1-GFPSpark at 405 nm excitation. C) Lifetime distributions of S6K1-GFPSpark at 405 nm excitation. D) Fitted fluorescence decay of S6K1-GFPSpark to two components. Repeated minimum of three independent times. Error bars show standard deviation. Scale bar = 11 μm.*

4.2.16 AZD2014 interaction with EGFP-mTORC1 using multiphoton FRET-FLIM

Having resolved the problems with 405 nm single excitation (see section **4.2.5**), exciting into the 283 nm absorption peak of AZD2014 using multiphoton excitation (600 nm) was investigated for live cell drug-protein interactions using GFP tagged as acceptors. GFP alone is expected to be minimally excited in this region as found by solution studies in section **4.2.5**. Seeded adherent HEK293 cells were treated with AZD2014 (35 μM) and imaged after 15 minutes of incubation. Using FLIM, mono-exponential shorter and longer lifetimes were extracted within subcellular regions of the cell (**Figure 4.16**) with the nucleus showing a lifetime of 3.6 ± 0.42 ns

and the cytosol a lifetime of 4.6 ± 0.28 ns from one of three independent experiments. Such a large difference in lifetimes between cellular regions advocates that AZD2014 favours the cytosol which contain mTOR membrane bound organelles and support the in solution studies in section **4.2.6** where longer lifetimes of AZD2014 were seen in DMSO and shorter lifetimes were seen in PBS.

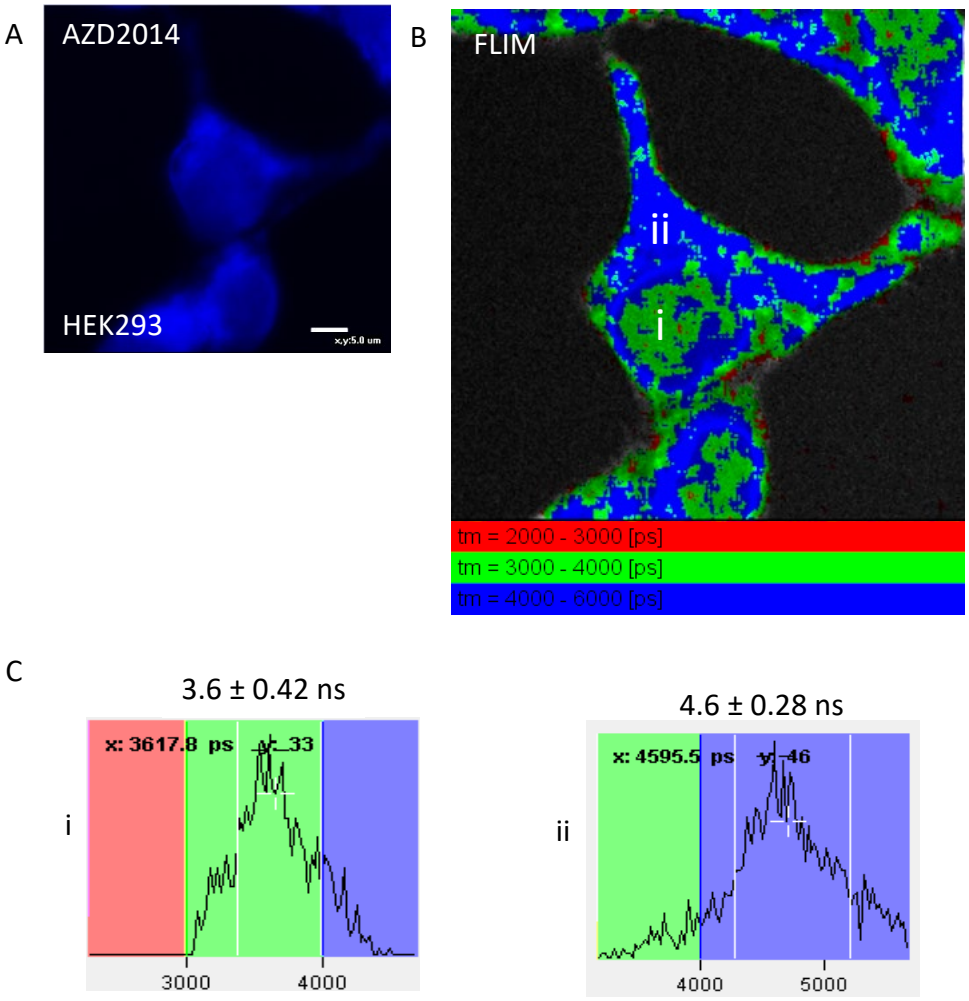

Figure 4.16: Cellular lifetimes of AZD2014 in mammalian cells. *A) Confocal image of HEK293 cells treated with AZD2014 (35 μM). Scale bar = 5 μm. B) FLIM image with 600 nm excitation. Lifetime colour key provided. Regions of interests, nucleus and cytosol shown in roman numerals, respectively (i and ii). C) Histogram distributions of region of interest lifetimes (i and ii). Experiments performed minimum of three independent times, data shown in representative of one the three experiments. Errors = standard error from the mean.*

Other organelles within the cell, as stated in section **4.2.12** can be excited directly at 600 nm due to co-factors such as NADH, thus a low laser power (0.25 or 0.5 mW)

was used with a higher concentration of AZD2014, 35 μM or 70 μM, to avoid excitation of these cellular molecules and to attain high counts for accurate lifetime statistics. No autofluorescence from HEK293 cells was observed under these conditions (results given in **Appendix C.6**). The mean lifetime of AZD2014 (donor) across a minimum of three independent experiments was determined in live HEK293 cells as 4.0 ± 0.5 ns (**Figure 4.17**). The error for these and following experiments were particularly high as the lifetime of AZD2014 varied across all experiments even using new and old stock/batch of the drug. This may suggest that the drug could be unstable and unsuitable for long term storage although storing conditions are not known to the manufacture. When AZD2014 was added to HEK293 cells expressing EGFP-S6K1 a change in average donor lifetime to 3.2 ± 0.3 ns was observed whilst changes of 3.4 ± 0.5 ns, 3.6 ± 0.4 ns and 3.6 ± 0.6 ns was determined in cells expressing EGFP-Rheb, EGFP-raptor and EGFP-mTOR, respectively (see **Figure 4.17**). These results show greater quenching of the excited state of AZD2014 beyond the 200 ps changes observed for the EGFP-mCherry interactions reported in **Chapter 3** due to greater spectral overlap; and indicate that AZD2014 is physically interacting with mTORC1 components in living cells. Quenches in lifetime between cytoplasm and nucleus could not be accurately distinguished as the counts in the nucleus were lower for precise model fitting, thus the mean lifetime (τ_m) of whole cells was integrated to provide an overall lifetime value. The change in lifetime of 800 ps observed with EGFP-S6K1 suggests that AZD2014 binds strongly with S6K1 or at an interface on mTORC1 that is closer to S6K1 and Rheb as the mean quench value with EGFP-Rheb was 600 ps. To test for any acceptor bleed-through, EGFP tagged acceptors were imaged alone under the same conditions and no significant counts were detected (such as EGFP-S6K1 alone, result given in **Appendix C.7**) indicating no other contributing factors influenced the lifetime results observed in this study.

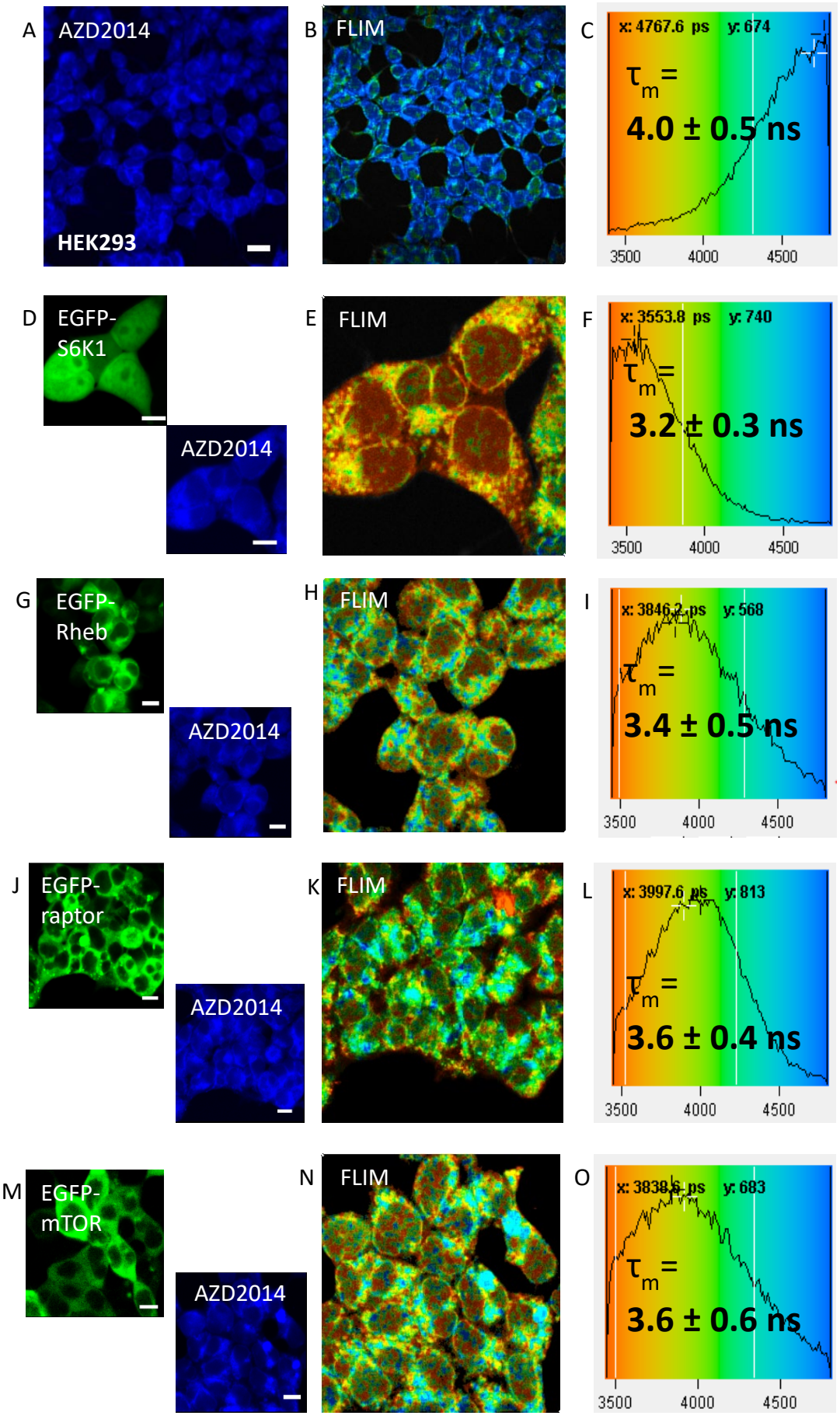
A
AZD2014
HEK293
B
FLIM
C
x: 4767.6 ps
y: 674
τm =
4.0 ± 0.5 ns
3500
4000
4500
D
EGFP-S6K1
AZD2014
E
FLIM
F
x: 3553.8 ps
y: 740
τm =
3.2 ± 0.3 ns
3500
4000
4500
G
EGFP-Rheb
AZD2014
H
FLIM
I
x: 3846.2 ps
y: 568
τm =
3.4 ± 0.5 ns
3500
4000
4500
J
EGFP-raptor
AZD2014
K
FLIM
L
x: 3997.6 ps
y: 813
τm =
3.6 ± 0.4 ns
3500
4000
4500
M
EGFP-mTOR
AZD2014
N
FLIM
O
x: 3838.8 ps
y: 683
τm =
3.6 ± 0.6 ns
3500
4000
4500

Figure 4.17: AZD2014 interactions with mTORC1 in living cells. *A) Confocal images of HEK293 cells treated with AZD2014 (70 μM). B) FLIM image of AZD2014. C) Lifetime distribution with x axis showing lifetime in picoseconds and y axis showing number of pixels. Scale bar = 20 μm. D) Confocal images of HEK293 cells expressing EGFP-S6K1 treated with AZD2014 (70 μM). E) FLIM image of AZD2014. F) Lifetime distribution. Scale bar = 10 μm. G) Confocal images of HEK293 cells expressing EGFP-Rheb treated with AZD2014 (70 μM). H) FLIM image of AZD2014. I) Lifetime distribution. J) Confocal images of HEK293 cells expressing EGFP-raptor treated with AZD2014 (70 μM). K) FLIM image of AZD2014. L) Lifetime distribution. M) Confocal images of HEK293 cells expressing EGFP-mTOR treated with AZD2014 (70 μM). N) FLIM image of AZD2014. O) Lifetime distribution. Experiments repeated minimum of three independent times. SD= standard deviation. All other scale bars = 10 μm.*

4.2.17 Co-localisation of AZD2014 with Rheb in living cells

Following the interaction studies observed in the section above, the co-localisation of AZD2014 with the Rheb mTORC1 was explored firstly due to its similar localisation and secondly because of its interaction. AZD2014 (7 μM) was administered to HEK293 cells transiently overexpressing mDsRed-Rheb. Steady-state co-localisation analysis using the Colocalization Colormap plugin for ImageJ, between AZD2014 and fluorescently labelled Rheb mapped regions of co-localisation with strong yellow-red 'hot-spot' areas indicating strong co-localisation particularly in the ER/Golgi sub-cellular regions of the cell, see **Figure 4.18**. This co-localisation analysis is more effective than other intensity dependent types of analyses which do not provide accurate pixel-pixel based correlations (Jaskolski, Mulle and Manzoni, 2005). The index of correlation (Icorr) value which represents the fraction of positively correlated pixels in the image was determined as 0.546, indicating that AZD2014 may localise to specific subcellular regions where mTORC1 localisation sits (i.e. lysosomal, ER/Golgi membranes).

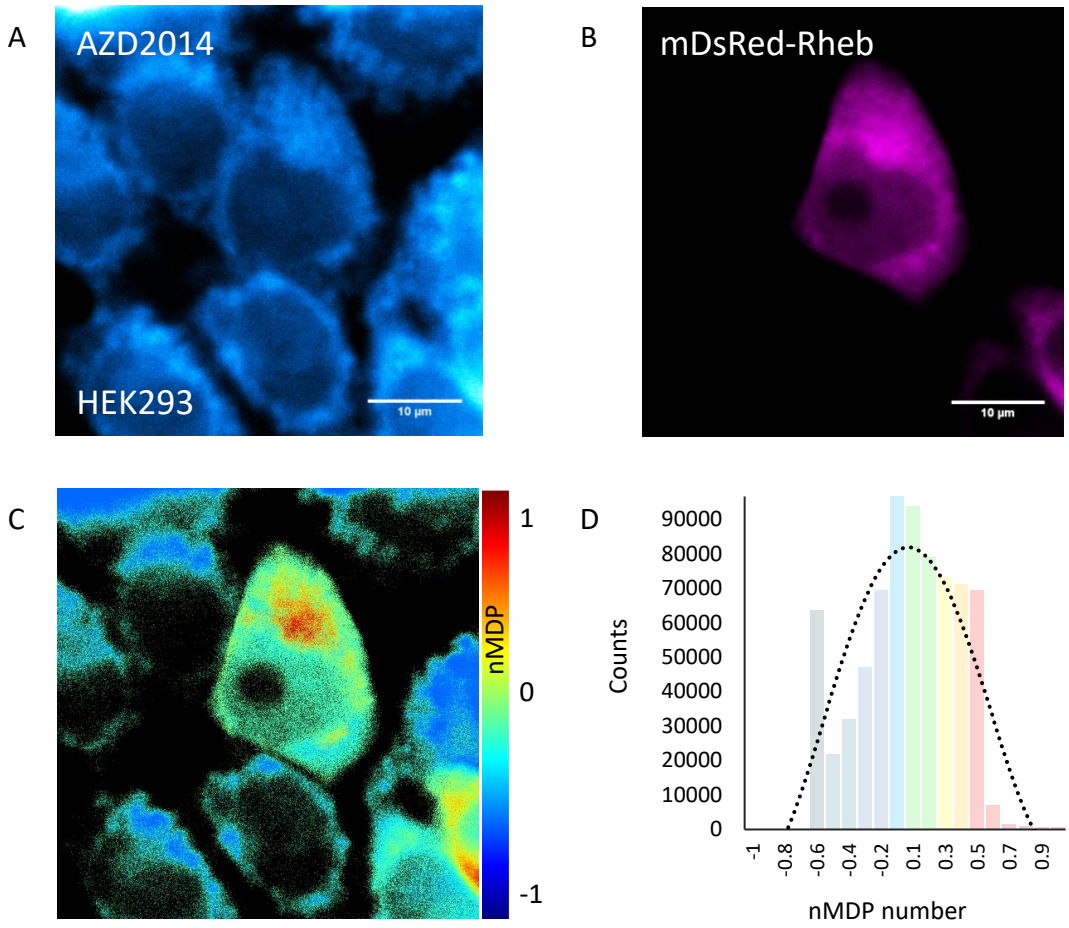

Figure 4.18: Specific AZD2014-mTORC1 subcellular targeting*. Confocal images of A) 7 µM AZD2014 with B) mDsRed-Rheb expression in HEK293 cells. Analysis performed in ImageJ version 1.48 using Colocalisation Colormap plugin.C) Colour map produced from plugin re-presenting co-localisation between AZD2014 and Rheb GTPase protein. Distribution of nMDP (normalized mean deviation product) values (ranging from -1 to 1) is visualised with a colour scale. Negative indexes are represented by cold colours (exclusion). Indexes above 0 are represented by hot colours (co-localisation). d) Respected histogram with a normal distribution (dotted) is also shown. Repeated minimum of three independent times. Scale bar = 10 µm.*

4.2.18 mTOR inhibition using AZD2014 with SensOR

To correlate the fluorescence imaging of AZD2014 observed in this chapter to its physiological significance interaction with the mTOR signalling pathway, both *in vitro* and *in vivo* methods to probe for mTOR activity were performed. Western blot analysis of HEK293 cells overexpressing EGFP-S6K1 treated with either 7 nM or 7 µM AZD2014 or no AZD2014 for 2 hours. A decrease in phospho-S6K1 activity (less intense chemiluminescent band) with 7 µM AZD2014 treatment was observed but

not with the 7 nM treatment (**Figure 4.19**). The live cell FRET biosensor (mCherry-S6K1-EGFP), SensOR, developed in **Chapter 3** to report directly on mTOR activity, was tested using this effective concentration (7 μM) of AZD2014 to validate AZD2014 function with respect to the live cell imaging results observed in this chapter. To investigate the treatment of AZD2014 in cancer models where mTOR is hyperactivated due to aberrant expressed Rheb levels (Liu *et al.*, 2018), a cyan tagged fluorescent Rheb protein (CFP-Rheb) was co-expressed with SensOR for spectrally separated three colour imaging. As a control, CFP-Rheb was co-expressed with SensOR and treated with rapamycin under identical conditions to the same experiment performed in **Chapter 3** without CFP-Rheb expression, and similar lifetime changes were obtained. Next, AZD2014 was added to HEK293 cells co-expressing SensOR and changes in the fluorescence lifetime of SensOR in the cytoplasm from 2.4 ± 0.06 ns (closed configuration of the sensor) to 2.52 ± 0.04 ns (open configuration) was observed with AZD2014 (7 μM) treatment using one-photon FRET-FLIM (**Figure 4.19**). These changes in lifetime correlate with the proposed opening of the FRET biosensor conformation in living cells which represents inhibition in mTOR activity (dephosphorylation). The individual values for the fluorescence lifetime at each pixel from this data can be presented in a polar diagram (Phasor plot) combined with the time-domain FLIM image where pixels with similar lifetimes and decay characteristics are clustered together (**Figure 4.19)**. This approach is highly efficient in identifying subtle changes in lifetime in the same field of view. Shown in **Figure 4.19C,** the population of SensOR lifetime pixels shifted towards longer lifetime (evident by position on semi-circle) after AZD2014 treatment, shown in blue pseudo-colouring. In summary, these results validate AZD2014 for fluorescent microscopy and highlight its importance for cancer associated hyperactivated mTOR mutants that are rapamycin or rapalogue insensitive.

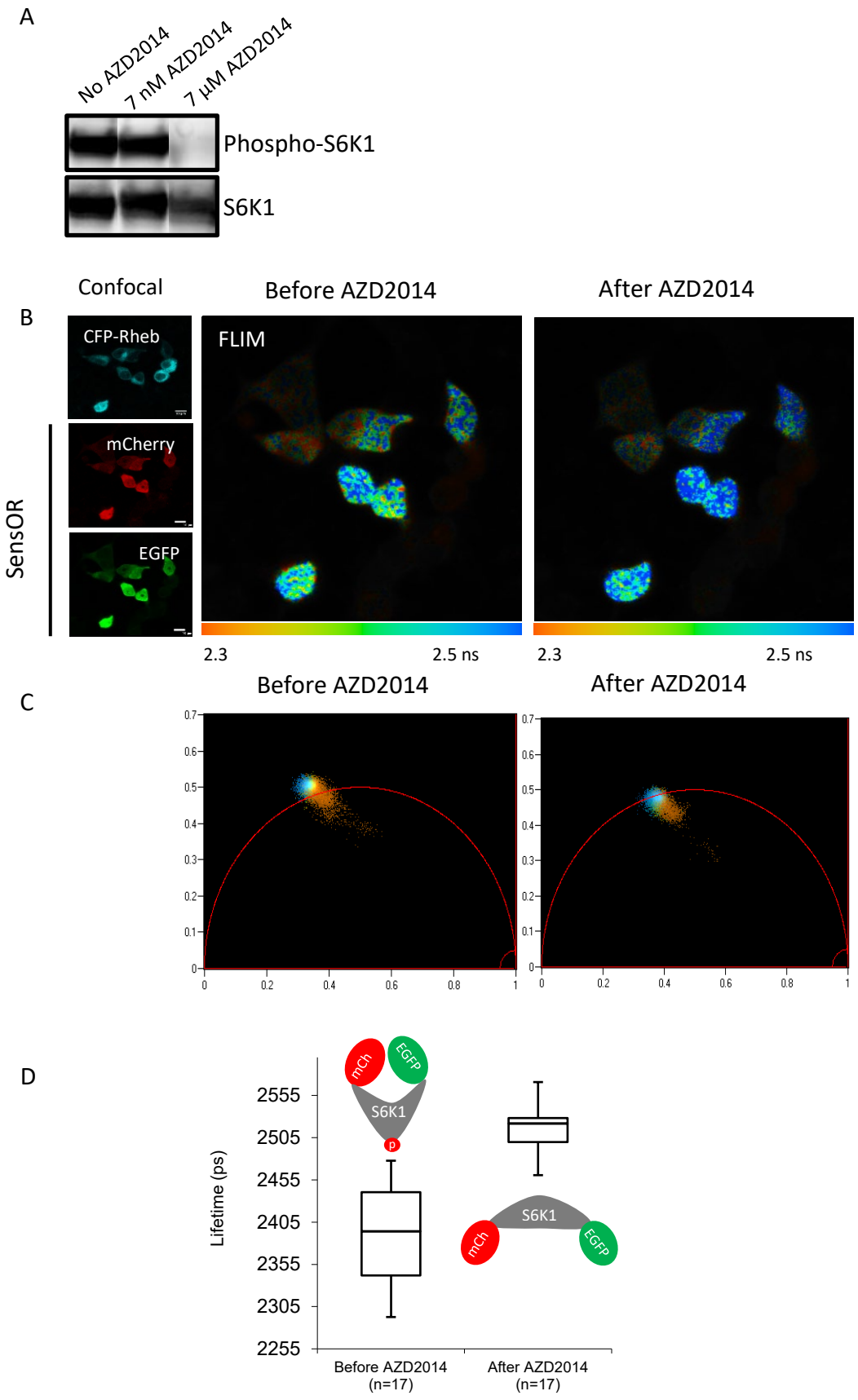

Figure 4.19: Phospho-S6K1 inhibition with AZD2014 in cells. *A) Western blot showing phospho-S6K1 and total S6K1 levels with and without AZD2014 treatment. Concentrations*

are shown. B) Confocal images showing mCherry-S6K1-EGFP (SensOR) co-expressed with CFP-Rheb and FLIM images of SensOR before and after AZD2014 (7 μM) treatment. Scale bar = 10 μm. C) Phasor plots of FLIM image pixels before and after AZD2014 treatment with phasor coordinates; x-axis =g and y-axis = s. Data was calibrated with fluorescein at pH 9 (4 ns, monoexponetial). Single-lifetime species are on the semicircle, complex species are inside the semicircle and excited-state products are outside the semicircle. D) Box plot of SensOR cytoplasmic lifetimes before and after AZD2014 treatment. Number of pixels analysed = 17. Data taken from three repeats.

4.3 Discussion

Identifying where drugs localise within cancer cells and living tissues is imperative to both understanding the mechanism of pharmaceutical drugs and their effectiveness in binding to drug targets on a sub-cellular level (Stumpf, 2005; Rutkowska *et al.*, 2016) as well as to optimise their effect. Although most common ways to study drug localisation involve making fluorescent analogues of the drug (Miller, Fricker and Drewe, 1997; Kozany *et al.*, 2009), fixing/ablating samples as found in forms of mass spectroscopy imaging (Ait-Belkacem *et al.*, 2012; Vismeh *et al.*, 2012), stimulated Raman scattering microscopy has been mostly replied upon to directly image drug localisation in living cells (Tipping *et al.*, 2016). However, the use of natural fluorescence as a tool for live cell drug imaging is largely overlooked. In this chapter, the fluorescence properties of two pan-mTOR inhibitors have been characterised AZD2014 and INK128. The main mTOR inhibitor, rapamycin, did not show useful fluorescence for live cell imaging. During the preparation of this thesis, it was also reported that AZD2014 was naturally fluorescent and emitted in the 483/32 nm region (Conway *et al.*, 2018). The fluorimeter studies from this chapter support these findings and have shown that AZD2014 is strongly fluorescent (emission peak at 468 nm) with absorption peaks at both 284 nm and 393 nm using one-photon excitation and one of the two-photon excitation peaks characterised at 795 nm. AZD2014 can also be used as fluorophore as its molar extinction coefficients (ε) have been determined as 36,790 M^{-1} cm^{-1} (284 nm) and 1,166 M^{-1} cm^{-1} (393 nm) with a very good quantum yield (QY) of 0.47 in DMSO. Since the

brightness of a fluorophore is related to the product of its molar extinction coefficient and its quantum yield, the brightness of AZD2014 can be calculated as 17,291 $M^{-1}cm^{-1}$ and 548 $M^{-1}cm^{-1}$ depending on the excitation wavelength. In comparison, the QY of EGFP is 0.6 and its ε is 55,000 $M^{-1}cm^{-1}$ giving it a brightness of 33,000 $M^{-1}cm^{-1}$ (Kaishima *et al.*, 2016). Therefore, AZD2014 can be used as a suitable fluorescent marker for studying mTOR inhibitor localisation and uptake within cancer cells. The fluorescence of AZD2014 may be attributed to its highly delocalised conjugated cyclic aromatic and purine ring structure which appears to be a feature of most fluorescent chromophores.

However, although UV-Vis spectroscopy showed that rapamycin may be excited using wavelengths below 300 nm, no fluorescence was observed in this programme of work, indicating very low QY. This would support previous studies that have needed to conjugate rapamycin to external fluorophores such as nitrobenzoxadiazole (NBD) for imaging in killifish renal proximal tubules (Miller, Fricker and Drewe, 1997) as well as for *in-vitro* spectroscopy for studying binding of fluorescein-coupled rapamycin analogues to FKBP family proteins (Kozany *et al.*, 2009). The addition of fluorophores to macrolide structures such as rapamycin and rapamycin analogues is unfavourable as the addition of a dye to a compound could hinder uptake, solubility, and also function (Snipstad *et al.*, 2017). Furthermore, as rapamycin has been shown to have variable and inconsistent results in targeting both mTORC1 and mTORC2 (Mukhopadhyay *et al.*, 2016), studying second generation mTOR inhibitors provides a more reliable route for studying mTOR function.

This chapter reports that INK128, another pan-mTOR inhibitor, also exhibits fluorescence properties with an excitation at 308 nm and an emission at 400 nm which is expected as the molecule shares similarity with the nicotinamide moiety of nicotinamide adenine dinucleotide (NADH) known to be excited at 340 nm (Blacker

et al., 2014) as well as DNA purines such as adenosine and guanine (excitation between 240-300 nm) (Kuimova *et al.*, 2006). The ε of INK128 has been determined to be 16,215 M^{-1} cm^{-1} at 293 nm whist its QY in DMSO is 0.33. The brightness of INK128 is therefore 5,350 M^{-1} cm^{-1}. This indicates that at these excitation wavelengths, AZD2014 is 69% brighter than INK128. A summary of the ε and QYs for AZD2014 and INK128 are given in **Table 4.2**.

Table 4.2: Wavelengths, molar extinction coefficients and quantum yields of AZD2014 and INK128

	Wavelength (nm)	**ε ($M^{-1}cm^{-1}$)**	**QY_F (ϕ)**
AZD2014 (DMSO)	284	36,790	0.47 ± 0.02
	393	1,166	
AZD2014 (PBS)	-	-	0.11 ± 0.01
INK128 (DMSO)	293	16,215	0.33
EGFP	488	55,000	0.60

The solution lifetime and spectroscopy studies of AZD2014 and INK128 showed longer lifetime and higher fluorescence yields in DMSO compared to PBS, supporting the notion that these molecules favour lipophilic rich environments such as the ER/Golgi/ peri-nuclear membranes observed in the live cell imaging. Similarly, cell work also shows longer lifetimes in the cytoplasm (subcellular organic structures) and shorter lifetimes in the nucleus (polar environments) (Asaad, Otter and Engberts, 2004). Another interesting result obtained from the experiments reported in this chapter was the extrapolation of the accumulated concentration of AZD2014 within the live cell which was shown to be 30-times higher than the concentration administered. In comparison to human clinical AZD2014 dosages that

are given at 25-100 mg (Basu *et al.*, 2015; Powles *et al.*, 2016) and pre-clinical doses at 7.5 and 15 mg/kg given to mice (Guichard *et al.*, 2015), accumulation of clinically administered AZD2014 at 30x greater concentrations inside human cells could explain undesirable side effects such as fatigue (78%) and nausea (51%) (Basu *et al.*, 2015). Currently, administered doses for INK128 range between 2-7 mg and patients have also exhibited adverse effects such as fatigue (10%) thrombocytopenia (15%) and neutropenia (5%) (Ghobrial *et al.*, 2016). This accumulation effect could be vital for phase III clinical trials where repeated doses or dose intervals on larger populations of test patients could lead to unwanted clinical consequences (Brocks and Mehvar, 2010).

The novelty of this work shows the ability to directly image mTOR inhibitors in living cells using both single photon and multiphoton microscopy. The uptake of both AZD2014 and INK128 in real-time has been established in monolayer HEK293 cells and found to be taken up within one minute with a maximum saturation reached within 10-15 minutes of administration. These findings are in line with previous work that observed a similar rate of uptake using multiphoton excitation to monitor and measure the anti-cancer drug combretastatin uptake in mammalian cells (CHO) (Bisby *et al.*, 2012). Furthermore, in this chapter, similar uptake rate of AZD2014 was found in the outer surface of multi-cellular HEK293 spheroid models with slower rates of uptake observed in the core z planes, using Light sheet microscopy. These findings are similar to experiments measuring drug uptake of combretastatin (E-CA4) in C8161 spheroids using confocal microscopy (Scherer *et al.*, 2015). Understanding mTOR inhibitor uptake in a model close to real tumours is imperative towards the understanding of mTOR activity in the tumour environment. Other studies have shown that spheroids exhibit altered mTOR signalling with a ~50% reduction in mTOR activity compared to 2D monolayers (Riedl *et al.*, 2016). Using immunofluorescence staining to probe for mTOR activity of downstream substrate

phosphorylation, the recent study has shown a fluorescence intensity gradient, starting from the outer layers to the inner layers of fixed spheroids (Riedl *et al.*, 2016). This highlights the significance for mTOR inhibitors to be designed to diffuse beyond the outer layers of tumours. However, it is worth noting that this gradient staining showing lack of labelling in the core layers of the spheroid could be an artefact from antibodies not being able to permeate through the spheroid layers (Riedl *et al.*, 2016).

Intriguingly, the treatment of spheroids with AZD2014 followed by 405 nm excitation in this programme of work, led to the possible discovery of a photo-activated effect where the spheroid volume increased by 2.3-times as measured by light sheet microscopy. Light sheet microscopy provides superior imaging over conventional imaging methods due to its ability to rapidly image live cell events in 3D over long time periods without inducing significant photo-toxicity owing to low laser power illumination (Candeo *et al.*, 2017). The light-induced activation of AZD2014 resulted in cells undergoing cell death (apoptosis), a mechanism known to be specific to photodynamic therapy (PDT) (Agostinis *et al.*, 2011). Although the involvement of reactive oxygen species (ROS) is not always essential in inducing apoptosis (Scherer *et al.*, 2016) (Type IV mechanism), their relevance to AZD2014 has not been yet identified in the literature. A direct effect, currently unknown, would involve the drug itself reacting with some primary component of the cell to cause cell death.

This work found similar localisations of both AZD2014 and INK128 to sub-cellular membrane regions (particularly the ER, Golgi and perinuclear) similar to that observed with fluorescently labelled Rheb (Yadav *et al.*, 2013; Hao *et al.*, 2018) across HEK293, CHO and MCF7 cells. The strong co-localisation between AZD2014 and mDsRed-Rheb established in this chapter supports the notion that AZD2014 may inherently target mTORC1 sub-structures and thus the question is raised whether mTOR drugs function by targeting proteins upstream of mTOR such

as Rheb which functions to activate the mTOR kinase (Long *et al.*, 2007). Both AZD2014 and INK128 were also present in the nucleus, where mTOR localisation is reported (Yadav *et al.*, 2013) as well as mTOR functionality (Giguère, 2018) and thus pan-mTOR inhibitors may automatically target mTOR in the cell.

The mechanism of AZD2014, in relation to the mTORC1 pathway has been investigated in this chapter by advancing the applications of FRET-FLIM technology. First, the biological effect of AZD2014 treatment in HEK293 cells was found to inhibit mTOR activity by monitoring S6K1 phosphorylation through Western blot analysis and also by utilising the live cell FRET SensOR (developed in **Chapter 3**) with Rheb overexpression. The SensOR studies used in this chapter demonstrates the effectiveness in using AZD2014 against hyperactivated mTOR cancers that are rapamycin or rapalogue insensitive (Xie, Wang and Proud, 2016; Xu *et al.*, 2016). The phasor plot approach demonstrated here requires no model fitting and therefore benefits from displaying raw FLIM data which can be used to discriminate clusters or lifetime changes. Furthermore, in support of the dual-selectivity of AZD2014 against both mTOR complexes, live cell mTORC2 inhibition has been detected using a Eevee-Akt-mT2 FRET sensor to explore changes in mTORC2 activity with AZD2014 treatment in KPC cells (Conway *et al.*, 2018).

The lifetime of AZD2014 alone in HEK293 cells in this chapter was determined to be 4.0 ± 0.5 ns whilst others have reported its lifetime to be 5.4 ± 0.03 ns in KPC cells (Conway *et al.*, 2018). Such differences in observed lifetimes may be due to the purity of AZD2014 used or from cell lines differences. Furthermore, the τ of AZD2014 in this chapter was obtained at 600 or 405 nm excitation whilst the recent study has used 760 nm (Conway *et al.*, 2018). The stability of the drug is yet unknown and this may be reliant on the correct storage conditions and time-usage of the drug, although storage at -20ºC and use of the drug for more than 2 months may not be suitable as found in this study. Nevertheless, direct interactions between

AZD2014 and the mTORC1 proteins have been determined in living cells by using AZD2014 as a donor and EGFP tagged proteins as an acceptor, yielding changes in lifetime greater than the 200 ps found in **Chapter 3** between S6K1 and raptor. The spectral overlap between AZD2014 and EGFP has been determined to be more than 70% making this type of FRET acceptors-donor pairs most suited to observing large dynamic range quenching which is similar to modern-day FP FRET pairs (Mastop *et al.*, 2017). The FRET changes determined here show selectivity towards certain mTORC1 proteins as evident by greater changes in lifetime, in particular for S6K1 and Rheb. A summary of these energy transfer (FRET) efficiencies are shown in **Table 4.3**. These findings are not surprising, as AZD2014 has been shown to have selectivity against some proteins such as those from the PIKK family as well as the Wnk2 kinase protein at similar concentrations (10 μM) used in this chapter (Pike *et al.*, 2013; Guichard *et al.*, 2015).

Table 4.3: FRET Efficiencies of AZD2014 interactions with GFP mTORC1 proteins. *FRET efficiency (E) obtained from AZD2014 alone lifetime (τ_D) and AZD2014 lifetime with an acceptor (τ_{DA}) using $E=1-(\tau_{DA}/\tau_D) \times 100$*

Donor +/- acceptor	FRET efficiency (%)
AZD2014 only	-
AZD2014 + EGFP-S6K1	18.70
AZD2014 + EGFP-Rheb	15.80
AZD2014 + EGFP-raptor	10.73
AZD2014 + EGFP-mTOR	10.60

The interaction between S6K1 and AZD2014 could support a working model for an indirect involvement of AZD2014 for PDT treatment where directly inhibiting S6K1 phosphorylation has shown to induce apoptosis (Song *et al.*, 2014). It is also worth noting that there are large deviations in the measured lifetime of AZD2014 and the average lifetime taken across independent experiments may skew the overall magnitude of change in each interaction.

4.4 Conclusions

In conclusion, mTOR inhibitors such as AZD2014 and INK128 display fluorescent properties that can be used as markers for determining cellular uptake and localisation in living cells using advanced imaging microscopy. It has been observed that the inhibitors localise to sub-cellular lipid-rich endomembrane regions within the cell known to be associated with the tethering of mTORC1. AZD2014 has a longer lifetime and higher quantum yield in DMSO than in PBS. AZD2014 is 69% brighter than INK128. Both AZD2014 and INK128 are taken up into 2D monolayer mammalian cells within one minute of addition whilst AZD2014 accumulated at a 30-times higher concentration. AZD2014 uptake rate into 3D cell spheroids was similar to that in monolayer cells. Upon light photo-activation, AZD2014 causes expansion in the diameter of living spheroids leading to cell death. AZD2014 interacts with the mTORC1 subunit proteins on the complex. Strong interactions between S6K1 and Rheb proteins were found in particular. SensOR was found to be responsive even in cells overexpressing Rheb. The use of this FRET-FLIM method paves the way for future technological development to study the effects of AZD2014 direct binding to the mTORC1 complex for both medical and pharmaceutical research.

5.0 mTORC1 large-scale expression and purification

5.1 Brief introduction

The key objective of structural biology is to provide a detailed atomic map of biological macromolecules (Murata and Wolf, 2018). However, a key hurdle before obtaining a structure by X-ray crystallography or cryo-Electron Microscopy (cryo-EM) is to successfully express large quantities of pure and stable (*i.e.* not misfolded or degraded) protein. The requirement for this stability prior to structural determination becomes more challenging when dealing with large protein complexes. The direction of the work taken in the previous results chapters is one which supports S6K1 directly complexed onto mTORC1 aided by raptor interaction. As no such structure of the complex has been published to date, this aspect of the work aimed to purify raptor and S6K1 together for a future structural analysis. Structural information could ultimately aid the development of novel strategies to prevent S6K1 recruitment and hence phosphorylation. This chapter also sought to purify the novel FRET biosensor (SensOR) developed in **Chapter 3** capable of determining S6K1 phosphorylation (i.e. mTOR activity) that was used for preliminary *in vitro* spectroscopy studies; these results are presented in **Chapter 3**.

The main hypothesis of this chapter is:

- The stability of S6K1 bound onto mTORC1 heavily depends on its interaction with raptor and thus subsquent mTOR phosphorylation is aided by subtle S6K1 conformational changes related to the phosphorylated state of S6K1

5.2 Results

5.2.1 PCR screen validation of mCherry-S6K1-EGFP-STREP (SensOR)

To purify the mCherry-S6K1-EGFP (SensOR) protein for *in vitro* characterisation, a new plasmid construct was prepared containing a STREP purification tag for large scale insect cell expression. As described in **Chapter 2**, the combined mCherry-S6K1 gene product was infused with separately isolated EGFP and cloned into the pOPINEneo-3C-2STREPStop vector. Individually isolated PCR products were used to avoid any primer mismatching. A PCR screen using agarose gel electrophoresis was performed to determine success of cloning using a T7F (forward) and a NeoRev2 (reverse) primer. A single band corresponding to 3871 bp upon UV illumination was detected matching to the DNA base pair lengths of mCherry, S6K1 and EGFP combined (see **Figure 5.1**). Further validation of the construct was provided by Sanger sequencing.

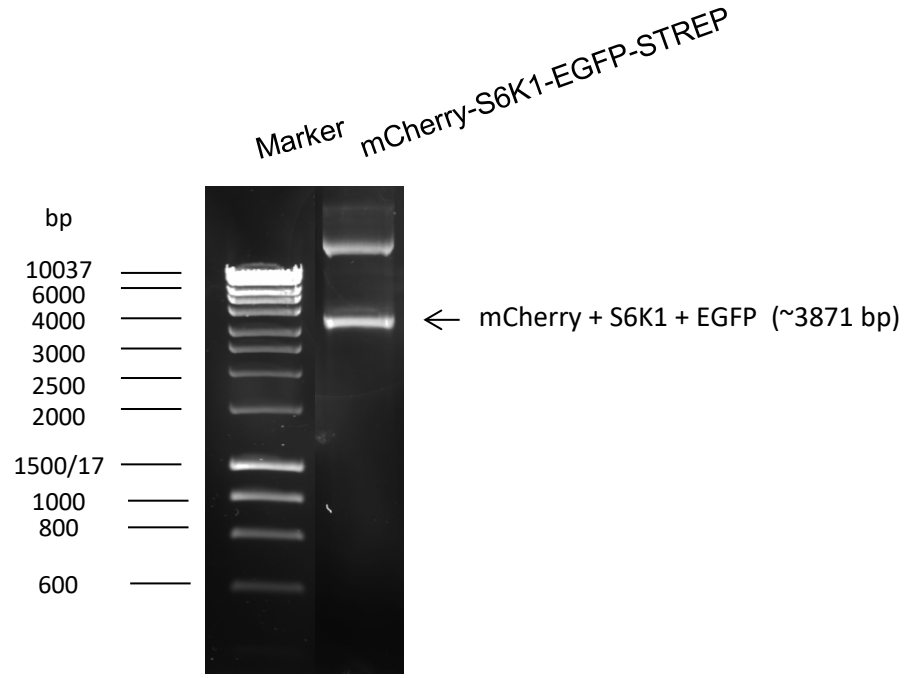

Figure 5.1: Reverse PCR screen of SensOR-STREP construct. *Analysis of PCR products separated by agarose gel electrophoresis. Marker is shown on the left (bp) with insert product on the right with bands corresponding to mCherry-S6K1 and EGFP combined in the pOPINEneo-3C-2STREPStop vector.*

5.2.2 Expression and pilot purification of mCherry-S6K1-EGFP-STREP (SensOR)

Having confirmed the integrity of the cloned STREP tagged mCherry-S6K1-EGFP biosensor, the plasmid was combined with a bacmid and transfected in Sf9 insect cells. Upon confirmation of expression by wide-field fluorescence imaging in both green and red channels, virus generation from P0 was taken to P1 and to P2 stages. However, following expression and pilot purification, major degradation products were observed using a fluorescence gel imaging system as evident by multiple EGFP and mCherry bands at incorrect molecular weight sizes and detection of a weak red intensity signal, given in **Appendix D.1**. Attempts were made to prevent degradation by optimisation of expression conditions; harvesting samples at different time points and infecting cells with different dilutions of virus. However, this was unsuccesful. The observed degradation may have been related to the protease activity of the bacmid. A bacmid deficient of proteases has shown less protein degradation and corresponding improvement in expression (Park, Abe and Kato, 2008).

Therefore, a recombinant bacmid that was deficient in proteases (see **Chapter 2** for details) was produced and co-transfected with the SensOR-STREP construct in Sf9 insect cells and amplified to P2 virus generation, as described above. As shown in **Figure 5.2**, wide-field fluorescence imaging confirmed high expression of the SensOR construct in both P0 and P1 stages with high levels of fluorescence in both green and red channels. The transfection efficiency was determined to be between 70-80%. Western blot analysis verification using various concentrations of P1 infected virus cells at 48-hour or 72-hour time points showed single high molecular weight (MW) bands corrosponding to the combined MWs of mCherry, S6K1 and

GFP (~130 kDa) indicating that intact full length SensOR was expressed a high levels (**Figure 5.3**).

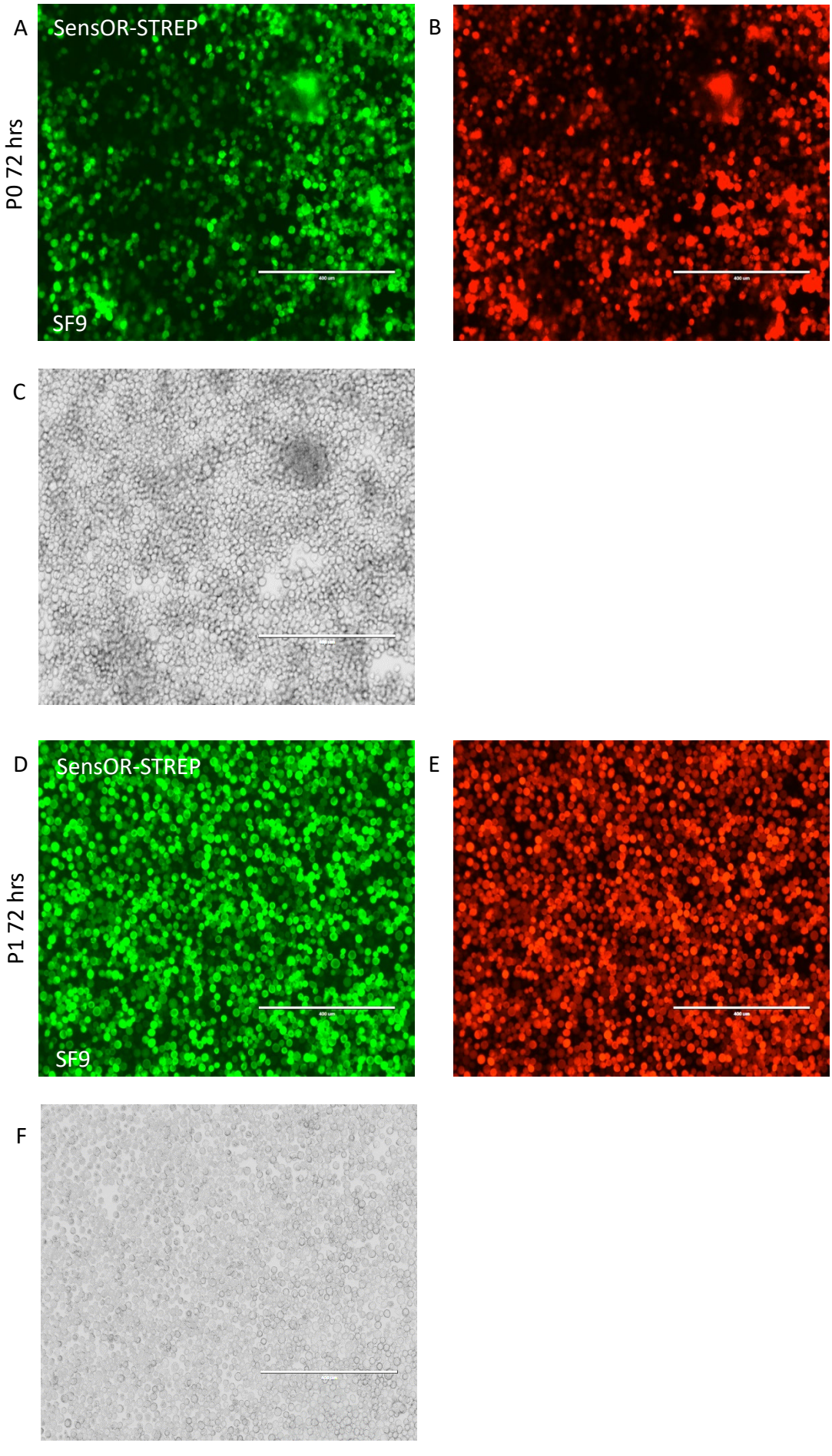
A
SensOR-STREP
P0 72 hrs
SF9
B
C
D
SensOR-STREP
P1 72 hrs
SF9
E
F

Figure 5.2: Expression of SensOR-STREP in insect cells. *Wide-field fluorescence images showing A) GFP of SensOR B) mCherry of SensOR and C) transmitted light of P0 virus after 72 hours expression in Sf9 cells. Fluorescence images showing D) GFP of SensOR E) mCherry of SensOR and F) transmitted light of P1 virus after 72 hours expression in Sf9 cells. All scale bars = 400 µm. High expression was observed at each stage P0-P1.*

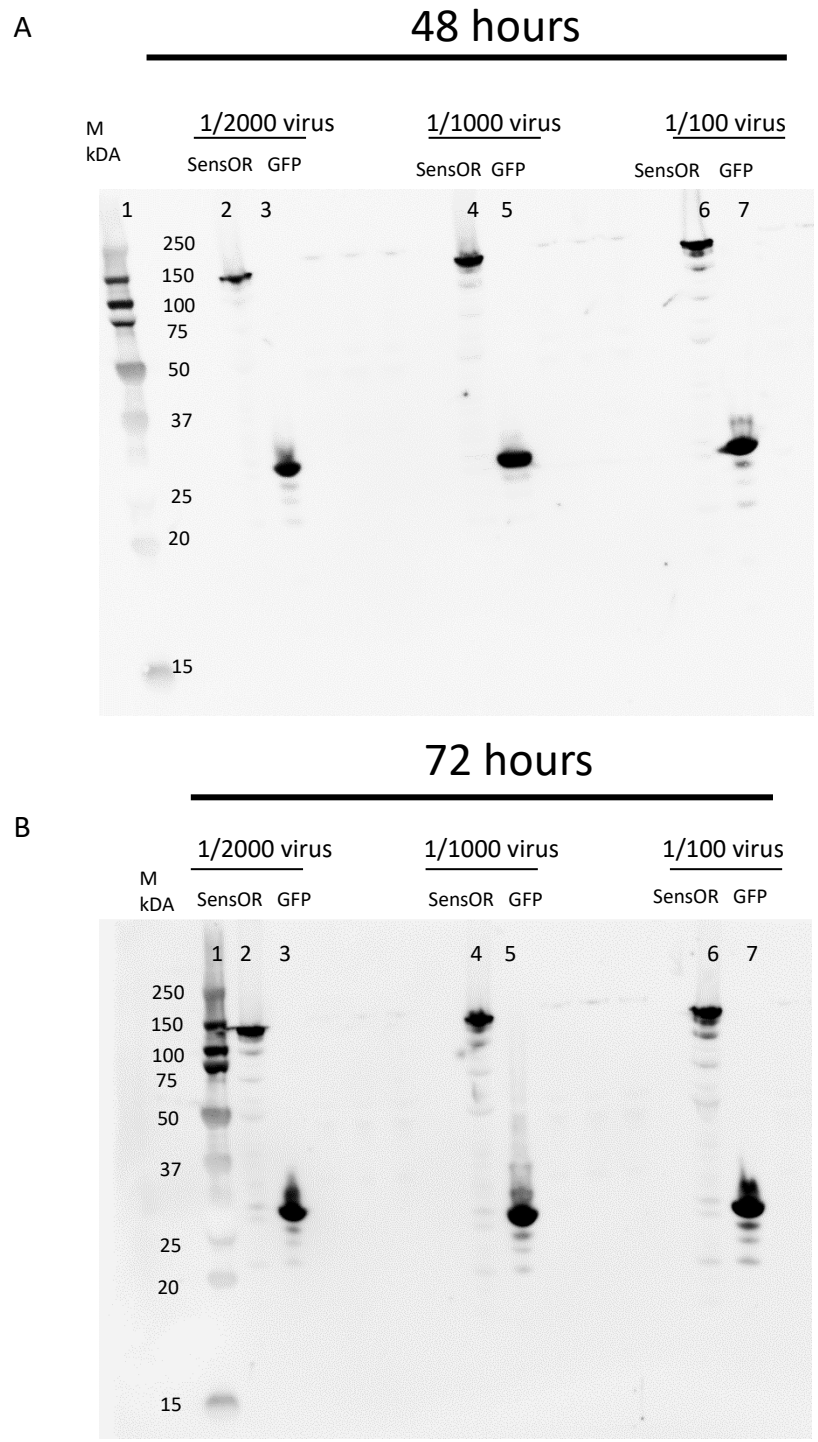

Figure 5.3: Western blot validation of SensOR expression. *A) Western blot loaded with various P1 virus concentrations expressing SensOR (lanes 2,4,6) and GFP control (lanes 3,5,7) at 48 hours. B) Western blot loaded with various P1 virus concentrations expressing SensOR (lanes 2,4,6) and GFP control (lanes 3,5,7) at 72 hours. Moleculer weight markers are shown on the left of blots. Blots labelled with anti-STREP antibody.*

5.2.3 Purification of mCherry-S6K1-EGFP-STREP (SensOR)

After validating the expression of mCherry-S6K1-STREP in Sf9 cells, a 2.5 litre scale up using P2 virus (1/1000) was performed and infected cells harvested into 6 aliquots (~400 ml) after 72 hours of infection. One of the 6 pellets was lysed as described in **Chapter 2** and purified using a StrepTrap column on a ÄKTA Xpress system followed by gel filtration chromatography (SEC) to separate the SensOR protein on the basis of its size (by a set of standard proteins, per manufacturer's protocol). As shown in **Figure 5.4**, a monodisperse peak indicating a monomer form of the protein was detected. SDS PAGE gel electrophoresis of eluted sample fractions confirmed a single band at a 130 kDa as determined by in-gel fluorescence and by gel coomassie stain, demonstrating that the protein was monomeric and of high purity (**Figure 5.4**). The protein was also subjected to QC analysis 24 hours after purification and both in-gel fluorescence and gel coomassie stain confirmed protein stability, with no aggregation or degradation detected. A faint band was occasionally observed in highly concentrated samples and this may be related to a post-modification of S6K1 which may have changed the apparent electrophoresis mobility of the protein. Although, human S6K1 is not known to be glycosylated, goat S6K1 has been reported to undergo a glycosylation post-modification (Manlin *et al.*, 2013). A final high yield concentration of 3.65 mg/ml SensOR protein was obtained.

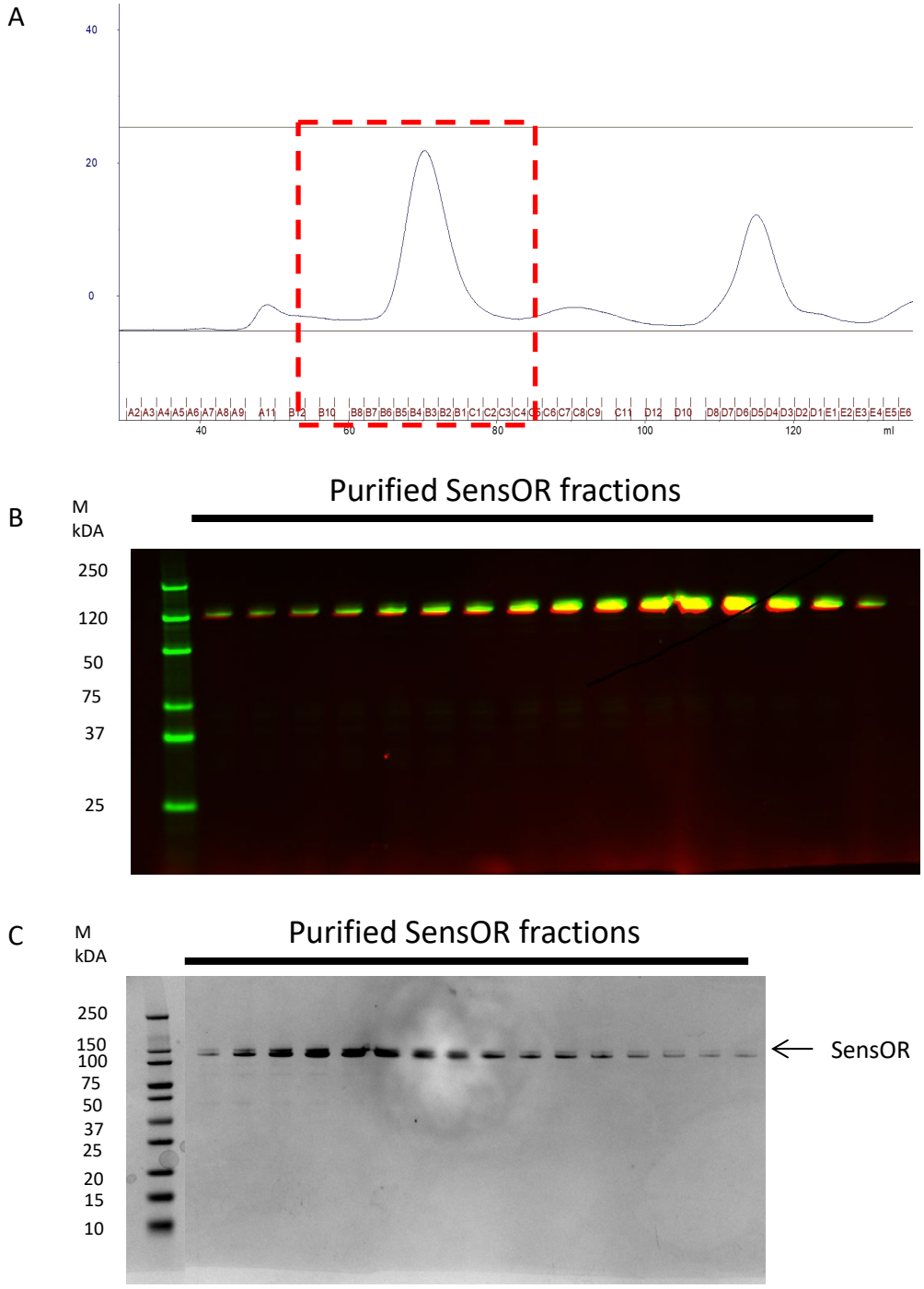

Figure 5.4: Large scale purification of SensOR. *A) Chromatogram obtained for mCherry-S6K1-EGFP-STREP after purification using the ÄKTA Xpress protein purification system. (x axis = volume; y axis = absorbance at 280 nm). The blue peak represents the eluted proteins and the red dashed box represents fraction used for SDS PAGE confirmation. Other peaks may represent small aggregation of protein or free fluorescent protein. Gel electrophoresis of purified SensOR fractions from the ÄKTA Xpress system showing B) in-gel fluorescence overlay of both GFP and RFP channels and C) gel coomassie staining. Molecular weight markers are also shown.*

5.2.4 Generation of mTORC1 virus for structural studies

The mTORC1 constructs for insect cell expression were designed and made by GenScript®, see **Chapter 2** for details. These constructs were co-transfected into Sf21 cells with bacmid for baculovirus expression and P0, P1 and P2 viruses were successfully generated. As these constructs do not have a fluorescence tag to determine expression, a change in both mean cell size and cell viability was used as a measure to validate protein expression (Janakiraman *et al.*, 2006). As shown in **Table 5.1**, an increase in mean cell size from 11.9 µm in non-infected cells to 14-16 µm was observed in all P2 post-72 hour generated virus infected cells. In addition, the cells also showed a decline in viability compared to non-infected cells which is another indication of successful virus infection in insect cells. Non-infected Sf21 cells are expected to double every 24 hours and a decrease in doubling time in infected cells, as given in **Table 5.1**, can be used as a final marker for successful infection.

Table 5.1: mTORC1 P2 virus generation results in SF21 cells. *(n=1)*

Construct	Protein(s)	Live cell count (10^6)	Cell viability (100%)	Cell size (μm)
Non-infected	N/A	9.1	99	11.9
EV5831	raptor-His	1.7	88	14
EV5832_EV5831	S6K1-FLAG + raptor-His	3.3	94	14.5
EV5830_EV5831	FLAG-S6K1 + raptor-His	2.7	94	14.5
EV5834_EV5831	ΔS6K1-FLAG + raptor-His	2.2	93	14.4
EV5833_EV5828	myc-ΔmTOR + mLST8	2.4	89	14.7
EV5827_EV5828	myc-mTOR + mLST8	5.1	96	15.3
EV5832_ EV5827_ EV5828	S6K1-FLAG + myc-mTOR + mLST8	4.5	98	16.2
EV5831_EV5832_EV5827_EV5828	raptor-His + S6K1-FLAG + myc-mTOR + mLST8	2.0	94	14.7

5.2.5 Small scale scouting expression of mTORC1 proteins in insect cells

To find the best conditions for protein expression, different time-points and multiplicity of infection (MOI) were investigated. Using the Baculovirus Infected

Insect Cells (BICCs) described above, Sf21 cells were infected using 0.2, 1 or 5 MOI and harvested at 24 hours or 72 hours post-infection and these results are shown in **Table 5.2** and **Table 5.3**. An increase in cell size and decrease in viability indicated that cells were successfully infected. To validate the expression and levels of protein production from these cells, lysates were prepared and subjected to Western blot analysis using antibodies. As shown in **Figures 5.5** and **Figure 5.6**, the S6K1 and truncated S6K1 with raptor constructs appeared to express highest post 72 hours of infection, evident by an increase in intensity of the protein bands compared to 48 hours of infection. S6K1 with mTOR and mLST8, and S6K1 with mTOR, raptor and mLST8 also showed S6K1 expression (bands at 75 kDa), see **Figure 5.7**. Expression with an MOI of 5 yielded highest protein production. It was also observed that both full length and truncated S6K1 (38 kDa) were soluble as shown by the levels of protein in the soluble fractions correlating to the total fractions. A faint band at 76 kDA for truncated S6K1 was observed which may represent the MW of the protein in its dimer form. On the other hand, raptor did not co-express well for any of the constructs as anti-His antibody labelling did not detect any bands at 150 kDa (representating that of raptor) although faint bands were faintly visible, shown in **Figure 5.6**, suggesting that either the raptor protein is expressed at very low levels, failed to fold correctly or the His tag attached to the raptor protein is masked, resulting in poor labelling efficiency with the anti-His antibody. For the construct containing S6K1 with raptor, mTOR and mLST8, a raptor specific antibody was used which showed bands at ~150 kDa indicating that raptor levels are poorly expressed and a more sensitive antibody is required to validate its expression (**Figure 5.7**).

The expression of full length mTOR and truncated mTOR were also tested under different MOI conditions. Infection post 72 hours was only investigated as expression with the constructs above yielded low levels of protein. **Figure 5.8** shows that full length mTOR failed to express correctly as evident by the lack of bands at

its correct molecular weight size of 289 kDa as well as intense degradation bands (~15 kDa) detected by the anti-myc antibody. However, the truncated mTOR construct (1376-2549 amino acid residues) expressed well with an expected band size of ~150 kDa. Moreover, when comparing total fractions to soluble fractions, no bands for truncated mTOR were observed in the soluble lanes (**Figure 5.8**), indicating that the protein must be in the insoluble fraction of the cell lysate (i.e. associated with membrane bound organelles and structures). It is highly likely that the truncated form of mTOR lacks the correct localisation sequences and therefore may not localise properly.

Reasons for degradation and poor raptor expression in insect cells may be due to the absence of human chaperones within the insect cell system required to correctly fold such large proteins and this is discussed in section **5.3**. These findings are investigated further in the next sub-chapter where S6K1-raptor constructs were subjected to manual purification from a larger infected culture volume.

Table 5.2: Scouting expression results post-48 hours infection. *Live cell count (C), cell viability (V) and cell size (S) are given. (n=1).*

48 hours		MOI 0.2			MOI 1			MOI 5		
Construct	**Protein (s)**	**C (10^6)**	**V (100%)**	**S (µm)**	**C (10^6)**	**V (100%)**	**S (µm)**	**C (10^6)**	**V (100%)**	**S (µm)**
Untransfected	N/A	2.4	97	12.6	-	-	-	-	-	-
EV5831	raptor-His	1.2	97	15.9	1.3	98	16.9	1.2	91	15.8
EV5832_EV5831	S6K1-FLAG + raptor-His	2.2	93	16	1.1	96	15.6	0.93	90	15.3
EV5830_EV5831	FLAG-S6K1 + raptor-His	1.5	95	16.5	1.1	96	16.1	0.82	85	14.5
EV5834_EV5831	ΔS6K1-FLAG + raptor-His	1.2	96	14.9	1.4	94	15.7	8.1	97	15.5
EV5833_EV5828	myc-ΔmTOR + mLST8	1.9	96	14.9	0.74	95	14.3	0.72	90	12.6

Table 5.3: Scouting expression results post-72 hours infection. *Live cell count (C), cell viability (V) and cell size (S) are given. (n=1).*

72 hours		MOI 0.2			MOI 1			MOI 5		
Construct	**Protein (s)**	**C (10^6)**	**V (100 %)**	**S (µm)**	**C (10^6)**	**V (100%)**	**S (µm)**	**C (10^6)**	**V (100 %)**	**S (µm)**
Untransfected	N/A	9.8	99	12.8	-	-	-	-	-	-
EV5831	raptor-His	1.9	96	15.9	1.9	92	16.2	1.4	83	16.6
EV5832_EV5831	S6K1-FLAG + raptor-His	1.5	93	15.9	0.87	89	16.0	1.6	92	16.6
EV5830_EV5831	FLAG-S6K1 + raptor-His	1.0	92	15.5	1.2	93	15.1	0.85	86	15.6
EV5834_EV5831	ΔS6K1-FLAG + raptor-His	1.5	94	16.0	1.2	93	15.0	1.5	96	14.9
EV5833_EV5828	myc-ΔmTOR + mLST8	1.5	88	14.6	0.9	83	13.1	1.6	81	13.1
EV5827_EV5828	myc-mTOR + mLST8	5.4	95	15.7	2.4	94	16.6	7.8	96	17.2
EV5832_ EV5827_ EV5828	S6K1-FLAG + myc-mTOR + mLST8	2.2	90	16.6	0.7	72	16.7	0.8	74	15.6
EV5831_EV5832_EV5827_EV5828	raptor-His + S6K1-FLAG + myc-mTOR + mLST8	2.7	95	15.2	2.5	96	16.0	1.7	95	15.5

A

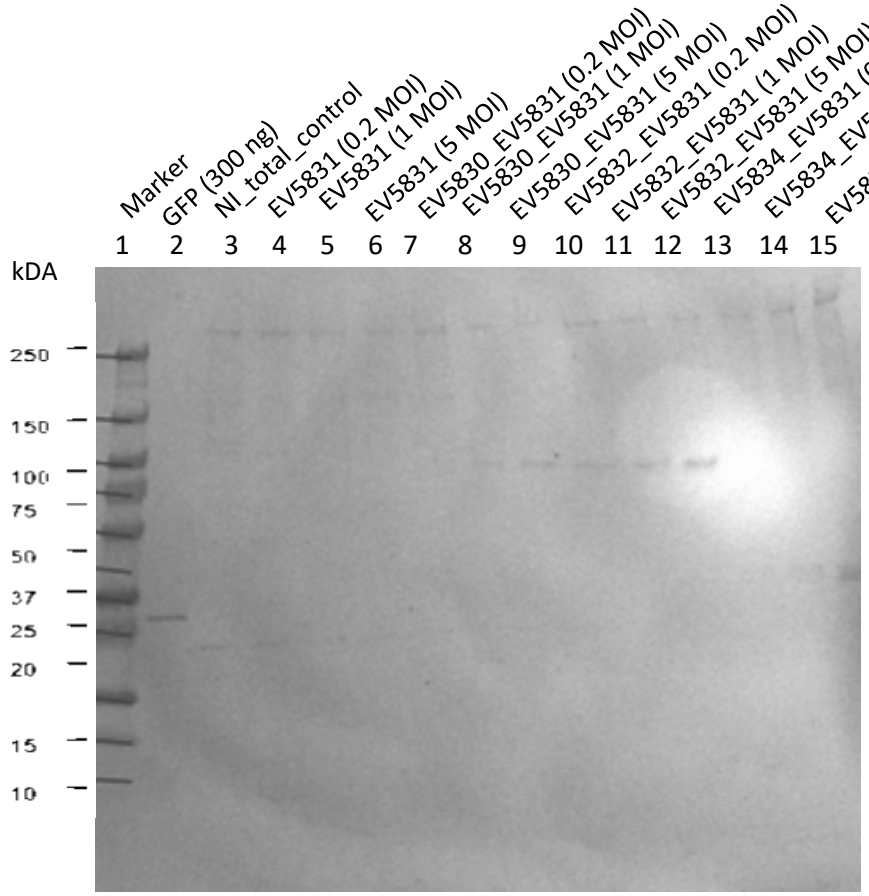
Marker
GFP (300 ng)
NI_total_control
EV5831 (0.2 MOI)
EV5831 (1 MOI)
EV5831 (5 MOI)
EV5830_EV5831 (0.2 MOI)
EV5830_EV5831 (1 MOI)
EV5830_EV5831 (5 MOI)
EV5832_EV5831 (0.2 MOI)
EV5832_EV5831 (1 MOI)
EV5832_EV5831 (5 MOI)
EV5834_EV5831 (0.2 MOI)
EV5834_EV5831 (1 MOI)
EV5834_EV5831 (5 MOI)
1 2 3 4 5 6 7 8 9 10 11 12 13 14 15
kDA
250
150
100
75
50
37
25
20
15
10

B

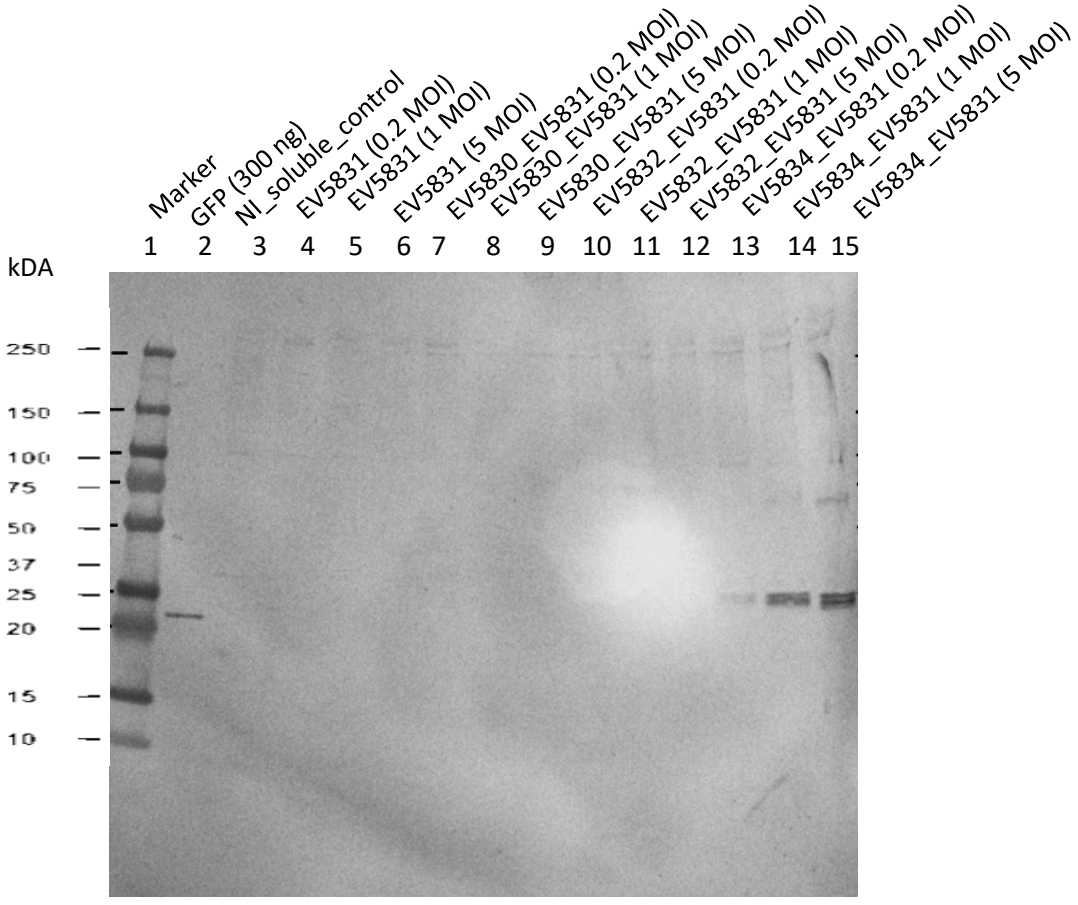
Marker
GFP (300 ng)
NI_soluble_control
EV5831 (0.2 MOI)
EV5831 (1 MOI)
EV5831 (5 MOI)
EV5830_EV5831 (0.2 MOI)
EV5830_EV5831 (1 MOI)
EV5830_EV5831 (5 MOI)
EV5832_EV5831 (0.2 MOI)
EV5832_EV5831 (1 MOI)
EV5832_EV5831 (5 MOI)
EV5834_EV5831 (0.2 MOI)
EV5834_EV5831 (1 MOI)
EV5834_EV5831 (5 MOI)
1 2 3 4 5 6 7 8 9 10 11 12 13 14 15
kDA
250
150
100
75
50
37
25
20
15
10

Figure 5.5: Scouting expression results for post 48 hours infection of S6K1-raptor constructs. *Western blot analysis using both anti-His and anti-FLAG antibodies at the same time for A) total lysate samples B) soluble fraction lysate samples. Molecular weights shown on the left with marker. GFP control contains His tag. Non-infected (NI) total and soluble control samples also shown.*

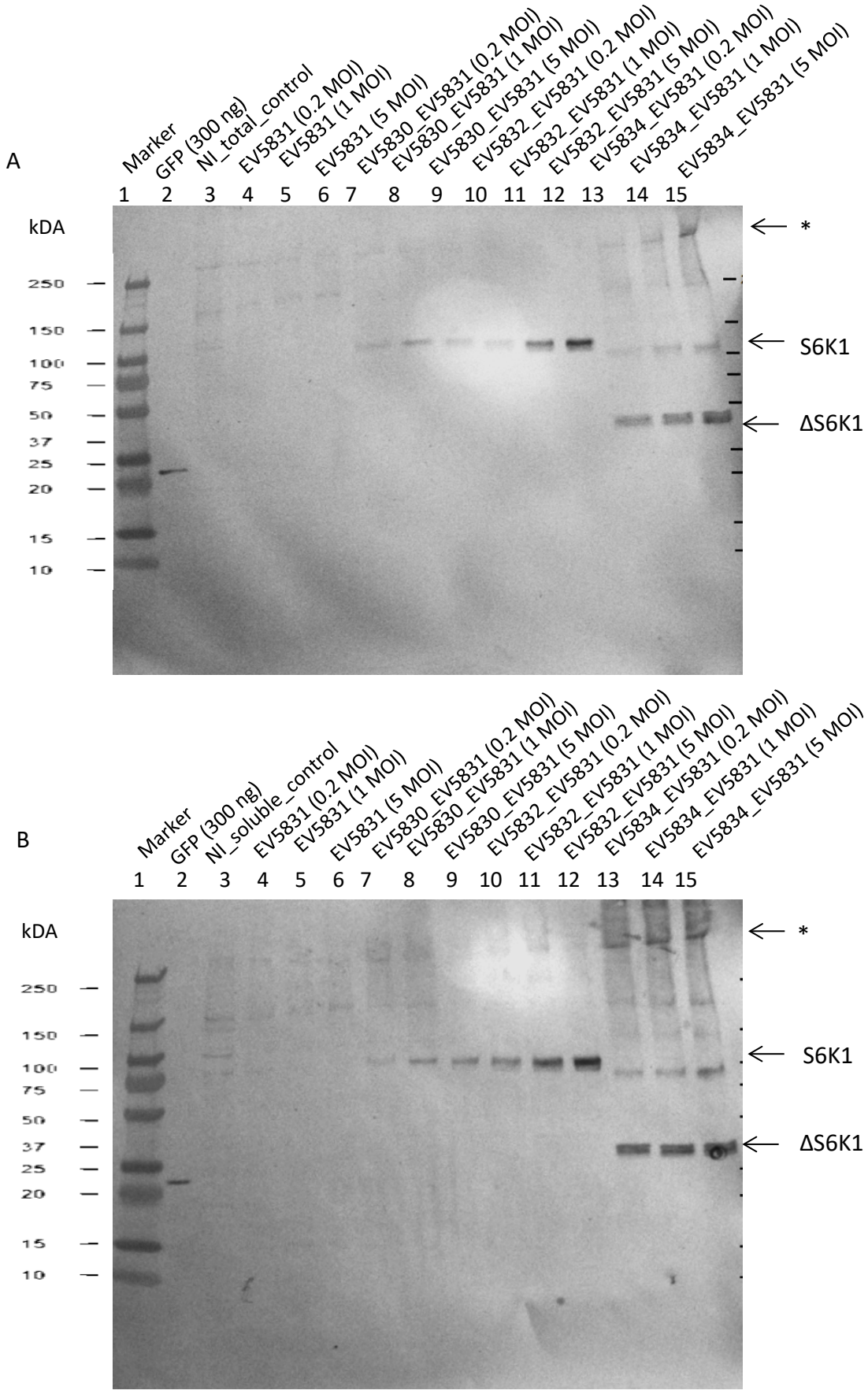

Figure 5.6: Scouting expression results for post 72 hours infection of S6K1-raptor constructs. *Western blot analysis using both anti-His and anti-FLAG antibodies at the same time for A) total lysate samples B) soluble fraction lysate samples. Molecular weights shown*

on the left with marker. GFP control contains FLAG tag. Non-infected (NI) total (T) and soluble (S) control samples also shown; (*) may represent high MW mTORC1 complex.

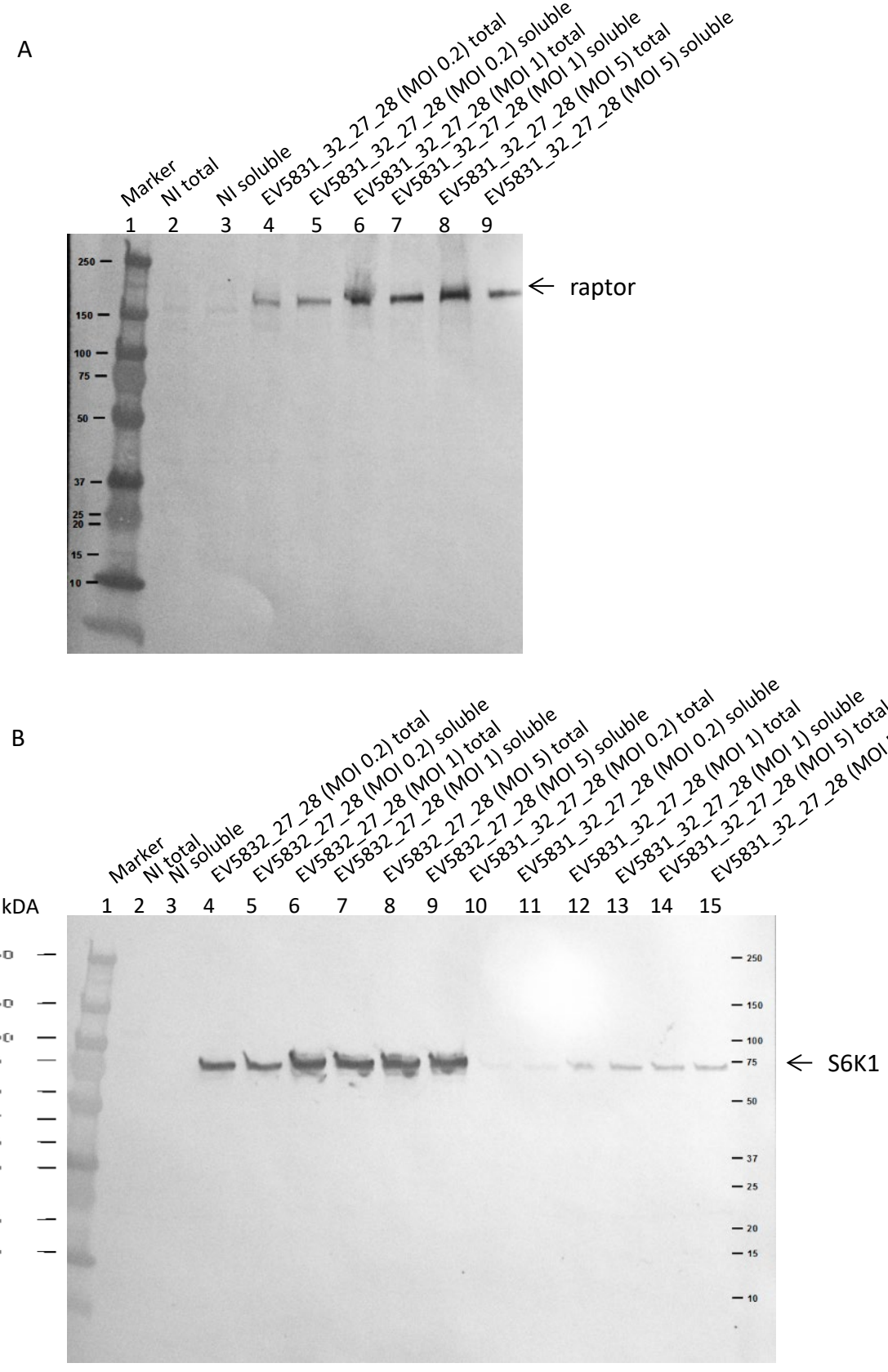

Figure 5.7: Scouting expression results for post 72 hours infection of S6K1-mTOR-mLST8 and S6K1-raptor-mTOR-mLST8 constructs. *Western blot analysis of total and soluble lysates using A) anti-raptor antibodies and B) anti-FLAG antibodies. Non-infected (NI) total and soluble control samples also shown.*

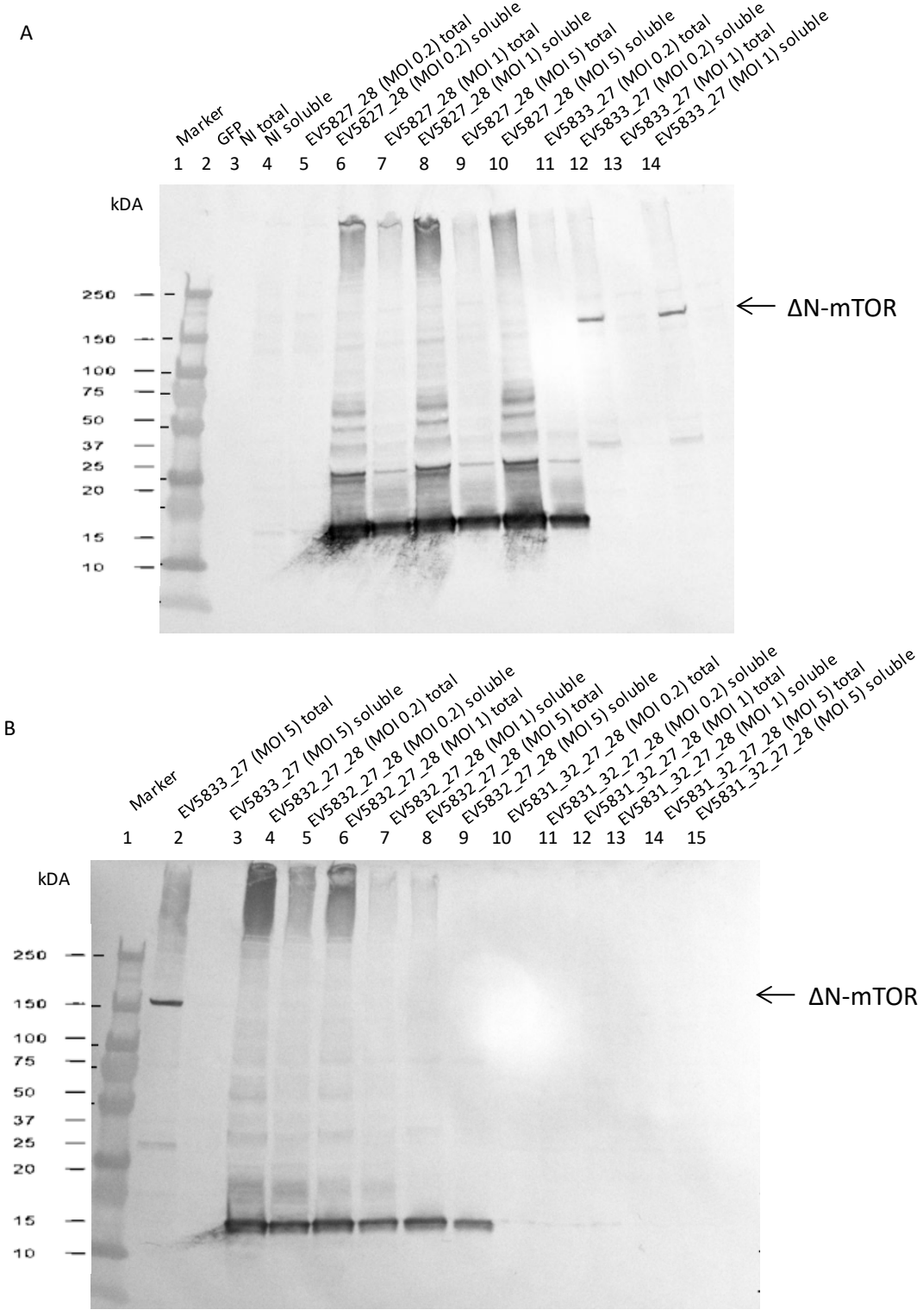

Figure 5.8: Scouting expression results for post 72 hours infection of mTOR-mLST8, S6K1-mTOR-mLST8 and S6K1-raptor-mTOR-mLST8 constructs. *A) and B) Western blot analysis of total and soluble lysates using anti-myc antibodies. Non-infected (NI) total and soluble control samples also shown.*

5.2.6 Small scale purification of S6K1-raptor constructs

Having established that raptor may be expressed at extremely low levels in insect cells, a larger volume from 3 ml to 45 ml of insect cells was infected with an MOI of 5 and harvested after 72 hours (determined to be the optimised expression conditions; see sub-chapter above). Cell pellets were lysed and subjected to manual batch-bind purification using Ni-NTA resin. Protein levels as total, soluble and eluted fractions for all S6K1-raptor and mutated S6K1-raptor constructs were evaluated by Western blot analysis as shown in **Figure 5.9**. Strong bands at 150 kDa were observed for full length raptor using anti-raptor antibodies as well as fainter bands higher than 250 kDa (possible undenatured mTORC1 dimer). Strong bands at 75 kDa for full length S6K1 and at 38 kDa for the truncated S6K1 sequence using anti-FLAG antibodies were detected. Both S6K1 and raptor bands were observed in the elution lanes (**Figure 5.9**) indicating that both proteins were bound together, supporting the FRET-FLIM data in **Chapter 3**. Interestingly, truncated S6K1 and raptor was also found in the elution fractions suggesting that this construct does interact with raptor. This may be a consequence due to the TOS motif that was artificially added before the truncated S6K1 sequence that allowed this construct to bind to raptor. This result further validates the S6K1 TOS motif in substrate recruitment carried out using imaging in **Chapter 3**. Non-specific bands were observed in the elution fractions (**Figure 5.9**), these may have arisen from the lack of optimisation of the purification protocol used. Modifications to the salt, incubation time and imidazole concentrations could yield cleaner product elution.

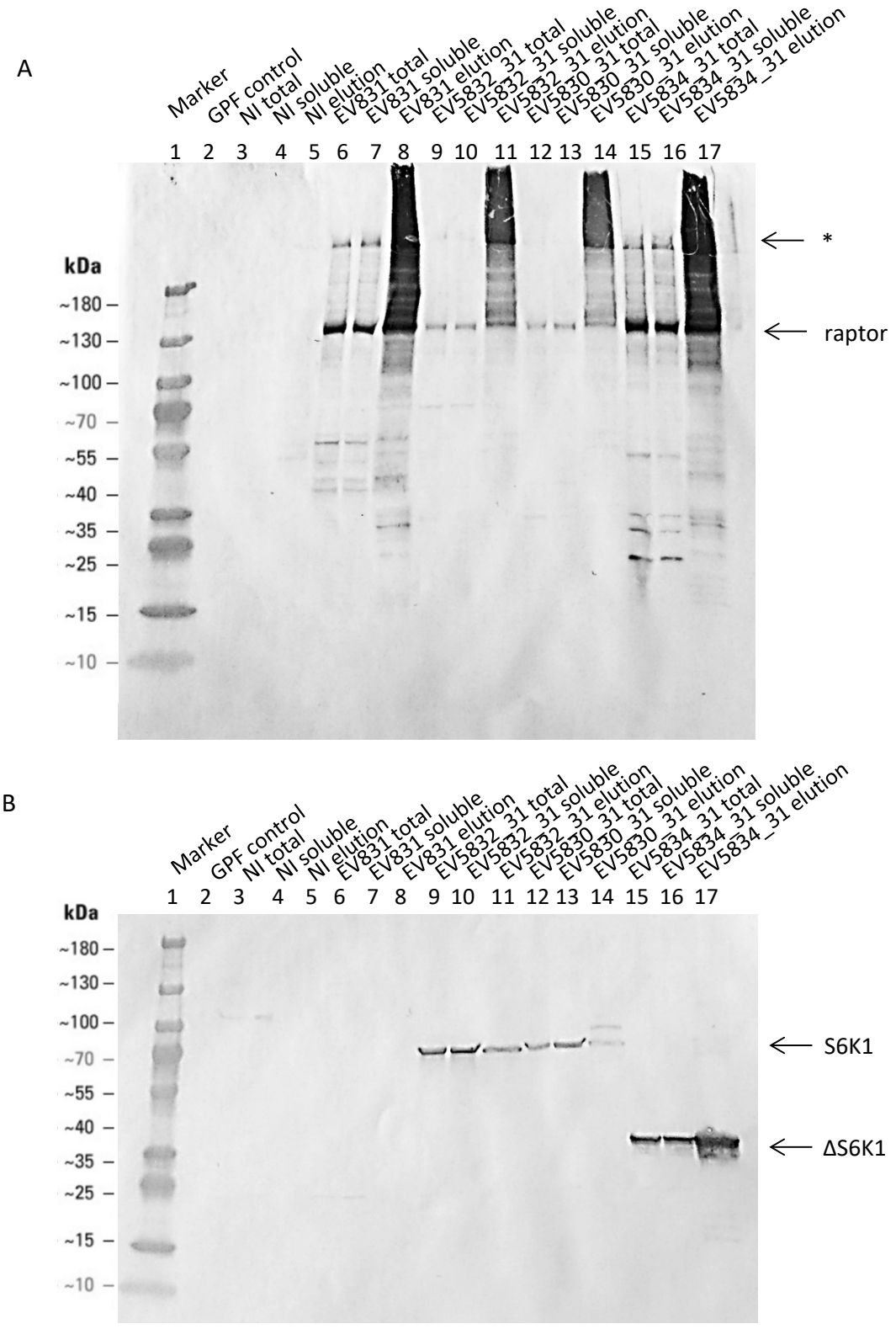

Figure 5.9: Expression and batch-binding purification of S6K1-raptor constructs. *Western blot analysis of total lysate, soluble lysate and eluted sample using A) anti-raptor antibodies and B) anti-FLAG antibodies. Non-infected (NI) total and soluble control samples also shown. (*) may represent high MW mTORC1 complex.*

5.2.7 Large scale pilot expression and purification of S6K1-raptor

Upon confirmation that S6K1 and raptor are complexed together in insect cells from small scale purification results, a larger scale purification with a 5 litre culture was attempted. Two 2.5 litre flasks were infected with S6K1-raptor P2 BIICs and monitored after 48 hours and 53 hours (**Table 5.4**) for cell viability. Cells were harvested after 53 hours as the cell viability decreased to 90%. An average increase from 12.3 ± 0.4 µm to 15.2 ± 0.4 µm taken from both flasks was observed at the 53-hour time-point indicating successful infection of the S6K1-FLAG + raptor-His construct.

Table 5.4: Large scale S6K1-raptor infection results in SF21 cells*. (n=1).*

Time point	Flask number	Construct	Volume	Live cell count	Cell viability	Cell size
0	1	EV5831_32	2.5 litre	1.5×10^6	98%	12.6 µm
0	2	EV5831_32	2.5 litre	1.2×10^6	98%	12 µm
48 hours	1	EV5831_32	2.5 litre	1.7×10^6	92%	14.0 µm
48 hours	2	EV5831_32	2.5 litre	2×10^6	93%	14.3 µm
53 hours	1	EV5831_32	2.5 litre	1.2×10^6	94%	14.8 µm
53 hours	2	EV5831_32	2.5 litre	1.4×10^6	90%	15.5 µm

A cell pellet of 29.3 g was obtained following harvesting and was then lysed as described in **Chapter 2**. Soluble lysate was loaded onto an ÄKTA purifier for immobilized metal affinity chromatography (IMAC) using a nickel resin column (HisTrap), designed to bind to raptor with S6K1 bound (ÄKTA results given in **Appendix D.3**). Following overnight purification, eluted protein fractions were subjected to SDS-PAGE gel separation and Western blot analysis for verifying success of purification. Although the coomassie SDS-PAGE staining showed multiple non-specific protein contaminant bands (see **Appendix D.4**), Western blot analysis (**Figure 5.10**) using anti-His antibodies detected low levels of the raptor

protein at 150 kDa. Intense bands at around 100 kDa were also observed, these bands were probabably due to natural histidine expressing proteins within insect cells that may have bound to the Ni resin column.

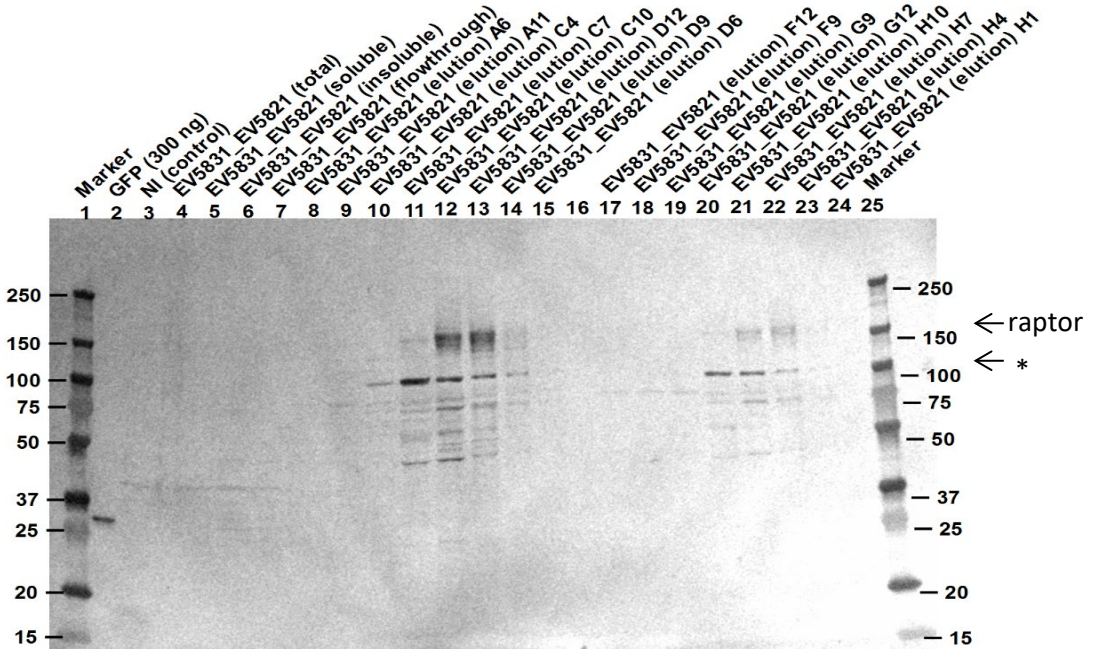

Figure 5.10: Purification of S6K1-raptor construct. *Western blot analysis of total lysate, soluble lysate and eluted sample fractions using anti-His antibodies. Non-infected (NI) and GFP-His control samples also shown. (*) Bands may be contaminants.*

Following the IMAC purification, the eluted protein in the fractions were concentrated and then subjected to size-exclusion chromatography (SEC) in an attempt to separate the raptor-S6K1 complex from the other contaminants that are likely to be natural insect cell histidine containing proteins. SEC results (**Figure 5.11**) showed a broad peak of absorbance (i.e. concentration), indicating multiple species of high molecular weights (>200 kDA). Following overnight purification, fractions were eluted and analysed by SDS-PAGE with coomassie staining (**Figure 5.11**). The staining again showed multiple bands in the elution products indicating presence of non-specific proteins/ contaminants. Distinct and clear bands at 150 kDa, ascribed to the MW of raptor, were not observed indicating that there has been loss of protein from IMAC to the SEC purification.

Further attempts were carried out to yield purer S6K1-raptor protein complex. Eluted samples from the SEC were loaded onto the automated Phynexus purification system with Ni affinity resin PhyNexus PhyTips and eluted in smaller volumes to remove the non-specific contaminants and concentrate the S6K1-raptor complex. The analysis of the coomassie stain of the eluted samples showed cleaner bands with some non-specific contaminants. Intense bands at 150 kDa (raptor) and at 75 kDa (S6K1) were observed (given in **Appendix D.5**). The concentration of raptor calculated as an average from all three eluted fractions was determined to be 931 ng (~1 mg of protein) using the known concentration of purified GFP loaded as a standard. As a cross-check given in **Figure 5.12**, Western blot analysis of these purified fractions showed bands for raptor as well as bands for S6K1. However due to the poor purity and poor yield of the raptor protein, no further work in insect cells was carried out.

A

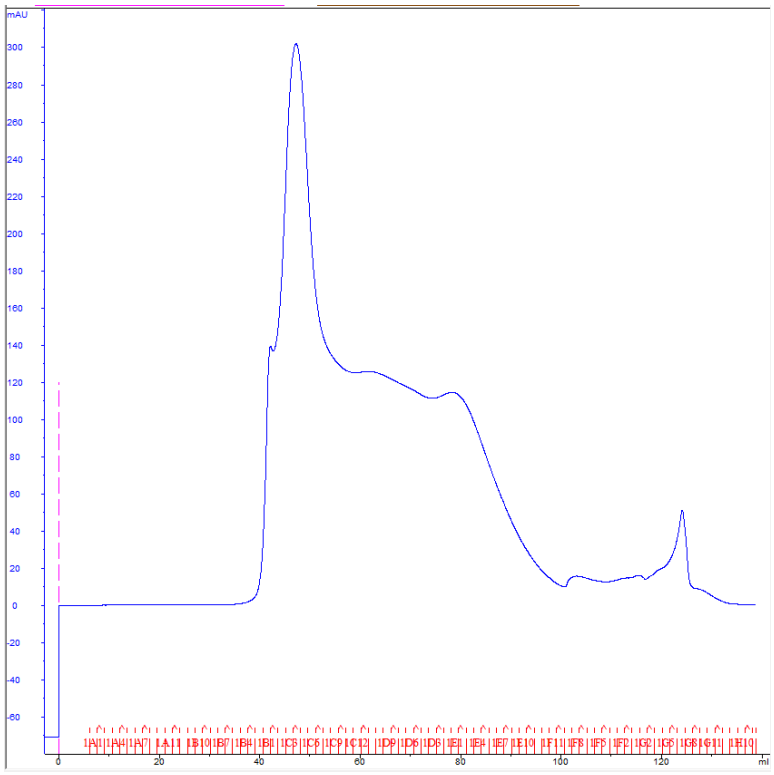
mAU
300
280
260
240
220
200
180
160
140
120
100
80
60
40
20
0
-20
-40
-60
0
20
40
60
80
100
120
ml

B

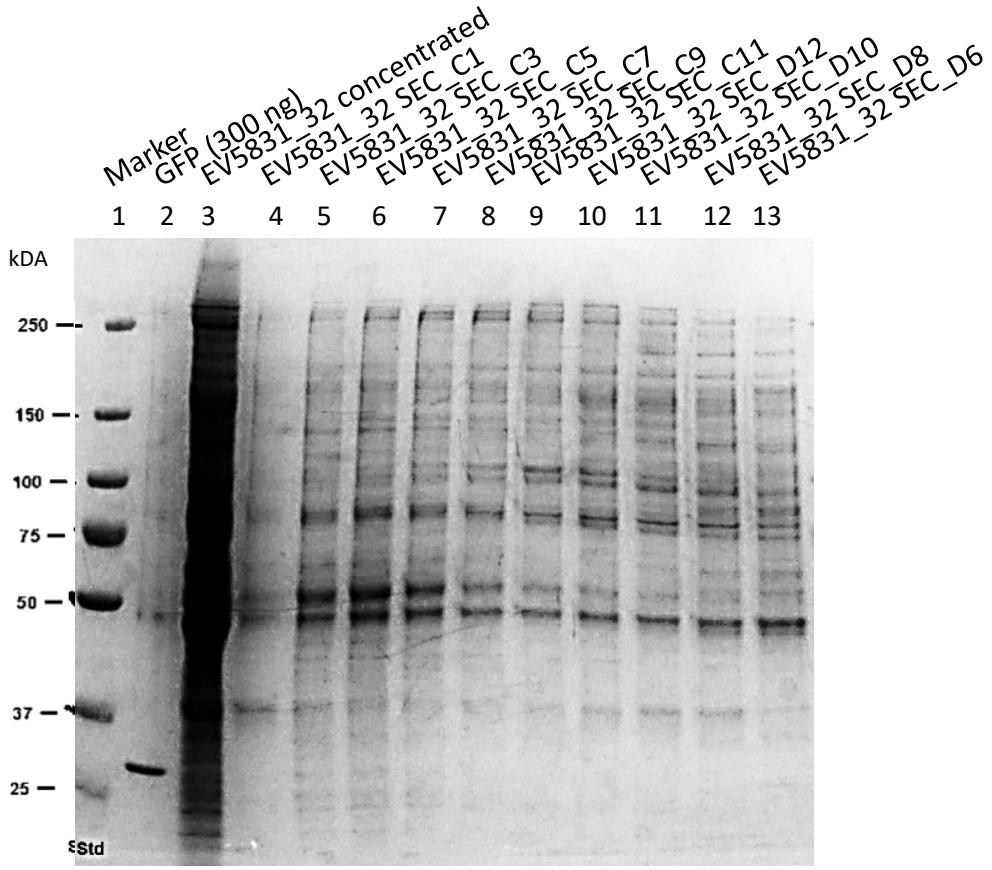
Marker
GFP (300 ng)
EV5831_32 concentrated
EV5831_32 SEC_C1
EV5831_32 SEC_C3
EV5831_32 SEC_C5
EV5831_32 SEC_C7
EV5831_32 SEC_C9
EV5831_32 SEC_C11
EV5831_32 SEC_D12
EV5831_32 SEC_D10
EV5831_32 SEC_D8
EV5831_32 SEC_D6
1 2 3 4 5 6 7 8 9 10 11 12 13
kDA
250
150
100
75
50
37
25
Std

Figure 5.11: SEC purification of S6K1-raptor construct. *A) Chromatogram obtained for S6K1-FLAG + raptor-His after SEC using the ÄKTA protein purification system. The blue peak represents the eluted protein fractions (x axis = volume; y axis= absorbance at 280 nm). B) Coomassie stain of SEC elution fractions. GFP control and markers shown.*

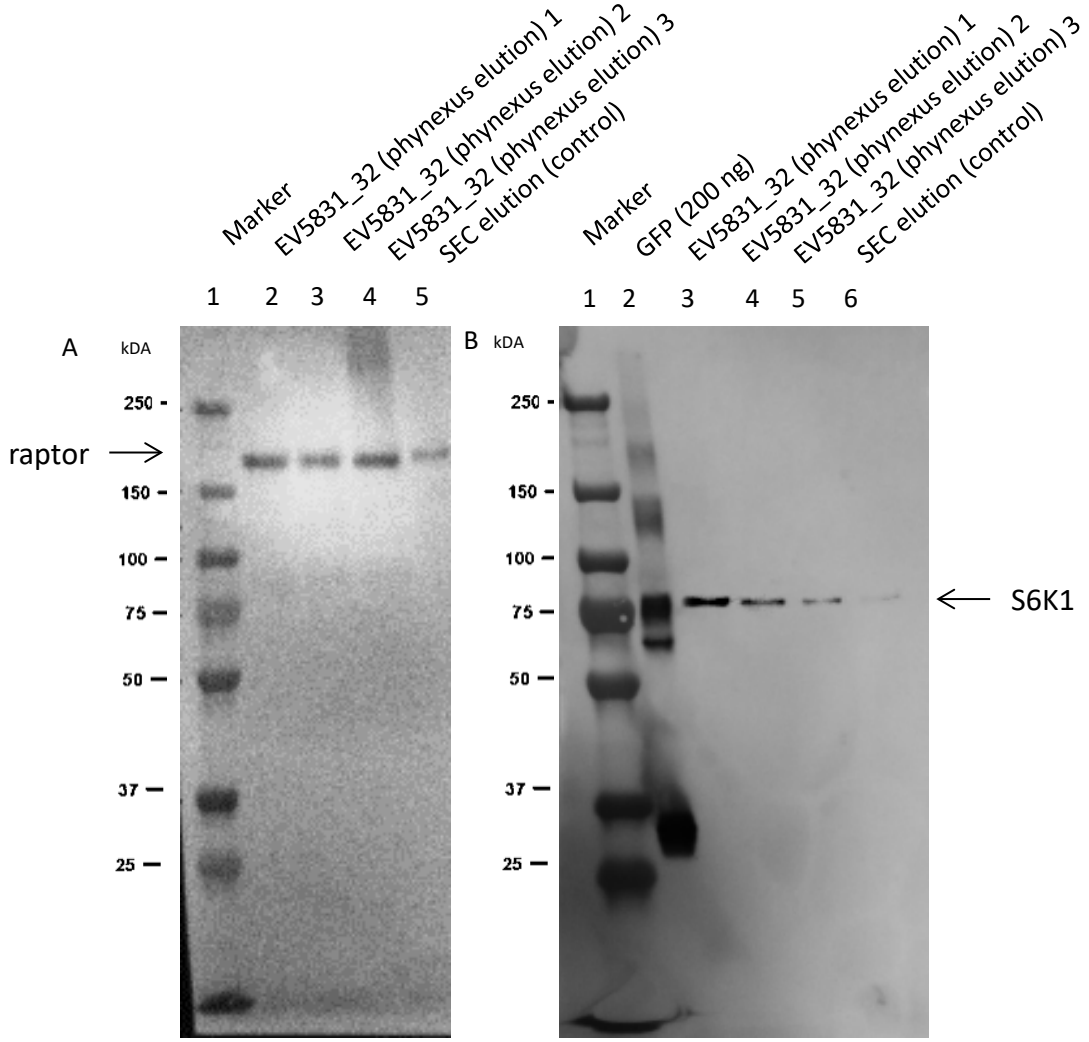

Figure 5.12: Phynexus purification of S6K1-raptor construct. *A) Western blot of eluted fractions using anti-raptor antibody. B) Western blot of eluted fractions using anti-FLAG antibody. GFP control and markers shown. GFP-FLAG control also shown (containing other impurities).*

5.3 Discussion

The baculovirus expression system has been used throughout this chapter to produce mTORC1 subunit proteins. Firstly, the results demonstrate that that SensOR, a live cell FRET sensor for determining mTOR activity (**see Chapter 3**), can be produced in large quantities (~3.7 mg) from Sf9 insect cells. This tandem construct with the full length S6K1 at its heart and a STREP tag purification epitope attached, highlights the flexibility of insect cells in producing full length mammalian kinase proteins (Li *et al.*, 2011). It is intriguing to discover that there is to date, currently no full length structure of the S6K1 kinase protein despite many published X-ray crystallography structures deposited in the RCSB PDB Protein Data bank showing truncated forms of the protein using both *E.coli* and baculovirus-infected insect cell expression systems (summarised in **Table 5.5**) (Wang *et al.*, 2013; Niwa *et al.*, 2014; Qin *et al.*, 2015). Crystallisation trials of full length S6K1 may have been attempted but have failed to produce significantly useful good quality diffraction data (resolution) due to possible highly disordered regions within the protein sequence, as predicted using bioinformatics tools (given in **Appendix D.6**). However, by having the addition of fluorescent proteins to the S6K1 structure, future crystal studies of SensOR could provide a novel full length S6K1 structure locked into one its phosphorylated states and thus provide a direct link between S6K1 structural change and mTOR phosphorylation. Secondly, the use of the STREP tag in this section of the results chapter also validates the superiority of the epitope tag for purification, supporting the findings that STREP tag does not interfere with protein folding (Kimple, Brill and Pasker, 2018) and enables a one-step purification with minimal contaminants due to the high affinity between the STREP peptide and StrepTactin resin in the purification column (Maertens *et al.*, 2015; Schmidt and Skerra, 2015). Natural biotinylated proteins or free biotin found internally in mammalian cells could bind to StrepTactin resin leading to unspecific binding,

however these proteins are less abundant in insect cells as described in the manufacturer's protocol, and thus allow for elution of ultrapure protein.

Table 5.5: Summary of S6K1 expression systems for X-ray crystallography work

PDB code:	Resolution	Length (amino acids)	Vector/ tags	Complex or alone	Expression system
4RLO/ 4RLP	2.53 Å	Truncated S6K1 constructs (84–384, 1–421, 1–421 T412E)	Cloned into pFASTbac HTB vector	Alone	Baculovirus-infected insect cells
3WF4/5/6/7/8/9	2.04 Å	Truncated S6K1 (75–399)	Cloned into pDEST 10 vector	Alone	Baculovirus-infected insect cells
4C33	1.7 Å	Truncated S6K1 (residues 1-421)	HIS/ GST	With PKA	*Escherichia coli*
4L3J	2.1 Å	Truncated kinase domain (residues 52–379) and the kinase domain plus the hydrophobic motif (residues 52–394)	pFastHTB vector	Alone	Baculovirus-infected insect cells
3A62	2.35 Å	Truncated - 75–399 of human p70S6K1	pVL1392 (Pharmingen) with HIS tag	Alone	Baculovirus-infected insect cells

The results obtained in this chapter also show that the expression of other larger mTORC1 proteins, namely mTOR and raptor in SF21 insect cells using the baculovirus system was highly inefficient for large quantities (milligrams) of pure protein essential for structural studies. The findings that raptor expressed at poor levels and that the mTOR protein was degraded, are in support of eukaryotic membrane proteins expression work that that found membrane proteins misfolded

and inactive in baculovirus-infected insect cells whilst the same proteins extracted from mammalian cells were found to be folded and active (Thomas and Tate, 2014). Moreover, the insect cell lacks the human chaperone machinery required to fold eukaryotic proteins. Other studies have co-expressed various human chaperones (e.g. Hsp70) with relevant co-factors to increase the solubility and expression of a target protein by up to 7-fold using the insect cell system (Tate, Whiteley and Betenbaugh, 1999; Yokoyama *et al.*, 2000). Thus, trials using various human chaperones with raptor and mTOR in insects may improve protein production in insect cells. The poor and misfolded expression of raptor and mTOR using the Sf21 insect cell expression system observed in this work differ to previous work that has expressed large quantities of the raptor-mTOR-mLST8 complex together in SFf21 insect cells (Aylett *et al.*, 2016). In comparison, similar culture reagents and lysis buffer were used with the exceptions that the insect cells in the present study were cultured in the presence of 2.5 μM rapamycin and that the mTORC1 complex was purified via FLAG tag. In addition, the mTORC2 complex (mTOR-mLST8-Rictor-SIN1-Protor-1) has also been recently purified from Sf21 insect cells via FLAG tag. Interestingly, low yields of the mTORC2 complex was found, within the nmol range from a 10 litre expression (Stuttfeld *et al.*, 2018), indicating that mTOR components may struggle to express and come together in the insect cell system. In addition, the mTOR protein was found to be unstable after purification and was stabalised by fixation (Stuttfeld *et al.*, 2018). Purification through the FLAG tag epitope (Gerace and Moazed, 2015) is often preferred over His tag purification as both insect and mammalian cells contain high levels of endogenous histidine containing proteins which tend to bind to the nickel resin (Kimple, Brill and Pasker, 2018) and this was evident in the results of this chapter as several non-specific protein contaminant bands were observed.

Another alternative strategy to express the mTORC1 complex containing raptor, has relied on mammalian cell expression (Yang *et al.*, 2013, 2016, 2017). The expression of mTORC2 containing proteins to form mTORC2 has also been performed in mammalian HEK293 cells using the maltose-binding protein (MBP) epitope tag for purification (Chen *et al.*, 2018). The mammalian expression system is advantageous for eukaryotic proteins as post-modifications required for protein functionality are maintained (Khan, 2013). However, although production time-scale is shorter compared to that of the insect cell expression, differences in lead time of 2-3 weeks, milligrams-to-grams of pure transfection quality DNA plasmid is required compared to nanogram quantities used in baculovirus insect cell infection. A summary of the expression systems and their respected structures of mTORC1 available on the RCSB PDB Protein Data bank is given in **Table 5.6**.

Table 5.6: Summary of mTORC1 expression systems for Cryo-EM work

PDB code:	Resolution	Length (amino acids)	Vector/ tags	Complex or alone	Expression system
6BCX	3.0 Å Cryo-EM	Full	pcDNA3.1(+) vector. FLAG tag. pFastBac1 with GST.	Complex/ raptor alone (not human)	HEK293-F cell line that was stably transfected. Insect cell for raptor (*at*)
5H64	4.4 Å Cryo-EM	Full	FLAG and Myc tagged mTORC1 subunits, separate vectors	Complex	HEK293F cells in suspension culture. Anti-Flag affinity resin, followed by ion exchange and gel filtration
5FLC	5.9 Å X-ray combined with Cryo-EM to give reconstruction	Full	A fusion vector containing mTORC1 (pAB2G-mTOR, pIDK-His10-myc-flag-Raptor, pIDC-mLST8)	Complex and raptor alone (also not human)	"MultiBac" system in Insects cells. Expression with rapamycin addition; stabilisation by glutaraldehyde gradient fixation
4JSV	3.5 Å X-ray crystallagraphy	Truncated (1376–2549) mTOR with mLST8	FLAG tagged mTOR and mLST8	Complex	HEK293-F cell line that was stably transfected

Similarities between the overall 3D structures of mTORC1 and mTORC2 have been identified (Yang *et al.*, 2018) with a tighter conformation of the complex found in mTORC2, shown to sterically hinder the binding of the rapamycin-FKBP12 complex (Karuppasamy *et al.*, 2017; Chen *et al.*, 2018). These structural differences explain the mechanism behind why mTORC2 is not sensitive to rapamycin treatment. However, the possible role of raptor in bringing the mTORC1 components together is still not fully examined. On one hand, it has been indicated that raptor indirectly mediates the dimerisation of mTOR (Jain *et al.*, 2014; Aylett *et al.*, 2016), whilst in

TORC1 (yeast) it has been shown that raptor binding directly facilitates the formation of the TOR dimer (Baretić *et al.*, 2016). Other studies in yeast have genetically engineered chimeric TORC1 and TORC2 proteins each containing elements of the other TOR protein, that still function and stably associate with its respected TOR subunit proteins (Hill *et al.*, 2018). These results redefine the structural basis of TOR by proposing a new model where complex specificity is regulated. In a similar line of direction, the downstream target for TORC1 activity (RPS6) involved in protein synthesis, has been found to be phosphorylated by both TORC1 and TORC2 in yeast (Yerlikaya *et al.*, 2016). Previously, it has been found that the Ypk3 kinase protein shares similar homology to S6K1 and directly phosphorylates RPS6 in a TORC1-dependent fashion (Gonzalez *et al.*, 2015). Thus, questions are raised if Ypk3/ S6K1 are targets for TORC2/mTORC2 mediated phosphorylation and can associate with the TORC2/mTORC2 complexes.

Having discussed the pitfalls in the approaches used in this work, the significance of obtaining a structure of S6K1 and raptor complexed together or S6K1 bound onto mTORC1 must not be overlooked. Acquiring such structural information is seen as critical to the generation of novel mTORC1 treatments where targeting S6K1 recruitment can provide selectivity against mTORC1 disease states as targeting both mTOR complexes with current pan-mTOR inhibitors can result in undesirable side effects such as hyperglycaemia and hyperinsulinemia (Ong *et al.*, 2016). Such a strategy is currently being proposed for selectively inhibiting mTORC2 by targeting mTORC2 substrate recruitment to avoid inhibition of vital biological processes such as protein synthesis regulated by mTORC1 (Yang *et al.*, 2018).

5.4 Conclusions

The expression of full length S6K1 with and without the addition of fluorescent protein tags has been attempted in insect cells using the baculovirus expression system. The FRET bio-sensor (SensOR) was successfully produced and purified in large quantities. Some S6K1-raptor complex was produced with an estimated quantity of less than 1 mg, but this low yield combined with other protein impurities is not suitable for X-ray crystallography or cryo-EM. The expression of raptor and mTOR in insect cells resulted in poor quantities and misfolding of protein; a different expression system such as the mammalian expression system with alternatve purification tags or supplementing insect cell media with rapamycin could provide larger yields of pure mTORC1 protein for future work.

6.0 Overall summary and future work

6.1 Overall summary

This body of research has focused on four main areas. They are (1) identifying the localisation and interaction of S6K1 protein in relation to the mTORC1 pathway, (2) the phosphorylation of S6K1 in live cells, (3) identifying the localisation and interaction of the AZD2014 drug with other mTORC1 components, and (4) large scale production of the S6K1-mTORC1 complex at high quantities for future structural studies.

This work has shown the S6K1 protein localises equally in both the cytoplasm (~52%) and the nucleus (~48%) of living mammalian cells (HEK293, HeLa and U20S) using GFP technology and advanced light microscopy. This subcellular localisation observed in this research project was found to be similar to that reported in plants (Mahfouz, 2006) whilst cell fractionation studies have also suggested both nuclear and cytoplasmic localisations for S6K1 (Rosner and Hengstschläger, 2011). However, fixed cell studies have shown only cytoplasmic localisation (Lun *et al.*, 2017) and this may be due to cell fixative induced influences (Schnell *et al.*, 2012). The results from this project agree with previously published studies involving cell fractionation, and have the added advantage of being performed in living cells under *in vivo* conditions that closely resemble the physiological environment.

Tagging S6K1 and other mTOR proteins with fluorescent labelling technology (acceptor and donor combinations) has provided new real-time evidence of the interactions of the S6K1 protein with mTORC1 in living cells. The evidence for this interaction is obtained from FRET-FLIM results and pull-down assays. Both techniques indicate that S6K1 is physically bound to raptor (with ~200 ps change in donor lifetime following FLIM studies) and supports previous published work (Nojima

et al., 2003; Mahfouz, 2006) and indicate S6K1 within binding proximity to mTOR (~100 ps change in donor lifetime). Although previous pull-down interaction studies indicate an interaction between S6K1 and mTOR (Ali and Sabatini, 2005), the outcome of the work from this project shows that this interaction may be bridged by raptor, a tertiary component. This advances current knowledge which postulates that S6K1 is separate to the rest of the mTOR complex (Saxton and Sabatini, 2017). The docking of S6K1 onto mTORC1 is highest for raptor (in order of binding efficiency of raptor with mTOR and with Rheb) supports the 'scaffold' function of the raptor protein in recognising and recruiting mTORC1 substrates (Nojima *et al.*, 2003).

The overexpression of both S6K1 and raptor together is identified to cause translocation of S6K1 (**Chapter 3**) out of the nucleus into the cytoplasm, correlating with increased levels of raptor co-expression in the cytoplasm. The translocation process has been shown to be mediated by the TOS motif of S6K1 and not triggered by mTOR mediated phosphorylation. A similar translocation event was also observed with 4EBP1, which moves out of the nucleus when co-expressed with the raptor protein. Using three-colour live cell imaging the main mTORC1 substrates with TOS motifs (S6K1, 4EBP1 and PRAS40) have been shown to compete for raptor binding, resulting in a 2x decrease in S6K1 recruitment as measured by confocal imaging when 4EBP1 or PRAS40 are expressed. These findings go beyond other studies that observed similar results *in vitro* (Nojima *et al.*, 2003; Schalm *et al.*, 2003; Wang *et al.*, 2007; Dennis, Kimball and Jefferson, 2013) by providing novel dynamic insights into mTORC1 behaviour in the live cell. Thus, if raptor functions to recognise and recruit mTOR substrates onto mTORC1, the translocation of these downstream target proteins could be used as a visual marker for recruitment. Although raptor may be involved in the primary stages of substrate recruitment onto the complex, a secondary recruitment mechanism involving a full

functioning mTOR found from mutations studies in **Chapter 3** appears to exist. This supports recent structural studies that found a fragment of the S6K1 bound to mTOR (Yang *et al.*, 2017). Looking to the future, new fourth generation inhibitors could be designed and made to block S6K1 recruitment onto mTORC1 to provide selective mTOR inhibition.

The protein overexpression system has been proven throughout this project to be a key tool in using living cells as metaphorical 'test tubes' for studying cellular signalling events. However, the possibility that protein overexpression introduces artefacts or that excess protein levels mask endogenous protein behaviours must be considered. It has been reported in imaging studies that the transient overexpression of GFP tagged mTORC1 proteins, particularly raptor and mTOR, do not localise to lysosomes upon amino acid starvation, whilst endogenously tagged raptor and mTOR have been found to do so (Manifava *et al.*, 2016). With regard to the work performed in this thesis, the overexpression system offers an advantage for identifying intracellular mechanisms due to perturbations caused by high levels of protein expression (in excess of endogenous) such as S6K1 recruitment and translocation.

Co-localisation and FRET-FLIM results from this project showed that S6K1 poorly co-localises with the Rheb protein, particularly in the ER/Golgi sub-localised regions of the cell despite a 128% increase in S6K1 phosphorylation with Rheb co-expression. The work in this thesis also shows that S6K1 does not physically interact with Rheb, as shown by a lack of change in donor lifetime from the FRET-FLIM studies. Despite a lack of interaction, the mechanism of S6K1 phosphorylation by Rheb induction, in the context of the living cell, remains unknown. Moreover, rapamycin studies indicated that rapamycin inhibition of S6K1 was dependent on Rheb. Whilst some studies have shown rapamycin alone to effectively inhibit S6K1 phosphorylation, others have obtained varied results for different cell lines and

concentration effects (Choo and Blenis, 2009; Mukhopadhyay *et al.*, 2016) and this may explain any discrepancies observed with rapamycin not effectively functioning alone.

The use of cell fixation with immunofluorescence labelling was shown to be unreliable for determining the localisation of cytosolic proteins and in particularly phosphorylated S6K1 in cells. Both paraformaldehyde and methanol fixation caused artefacts marked by loss of soluble GFP tagged S6K1 protein from either the cytoplasm (by 37%) or nucleus (by 19%). Cell fixation also caused leakage of GFP tagged protein into the nucleolus of cells as well as masking epitopes of S6K1 for efficient phospho-S6K1 labelling. Sensitivity and specificity of antibodies against the S6K1 target protein also resulted in the generation of artefacts such as non-specific binding and poor labelling determined by immunofluorescence studies. Taken together, these findings cast doubt on other indirect methods of studying phospho-S6K1 that greatly rely on cell fractionation studies (Rosner, Schipany and Hengstschläger, 2012) and immunofluorescence labelling of fixed cells (Kim *et al.*, 2013).

Using the concept developed for FRET sensors (Lindenburg and Merkx, 2014), where the protein is closed upon phosphorylation and reopened upon dephosphorylation, EGFP was tagged to the C-terminus of S6K1 with mCherry on the N-terminus. The biologically relevant environment of S6K1 phosphorylation has been examined using a novel live cell FRET biosensor (named SensOR) that successfully reports on mTOR activity in living cells. The functionality of SensOR has been validated by western blot analysis which shows a 6-times increase in RPS6 (downstream S6K1 target) phosphorylation. SensOR relies on FRET-FLIM technology to identify structural changes in S6K1 upon phosphorylation. Folded SensOR in the cytoplasm (lifetime of ~2.3 ns) has been shown to be directly responsive to serum starvation and rapamycin treatment. Real-time imaging showed

unfolding of SensOR resulting in longer lifetimes (~2.5 ns) in live cells. AZD2014 addition to cells expressing SensOR also showed a conformational change to longer lifetimes as evidenced by an increase of 120 ps in the natural lifetime of the FRET biosensor. These changes in lifetime are similar to a study using EGFP-aurora kinase A-mCherry as a FRET bio-sensor which reported a 130 ps lifetime change (Bertolin *et al.*, 2016) for aurora kinase activity. Such lifetime differences seen between rapamycin and AZD2014 may be due to AZD2014 additionally binding to S6K1, (discussed further later) and locking S6K1 into a more rigid conformation. It is worth emphasising that lifetime alone cannot be used to report changes in single GFP-tagged mTORC1 proteins, whereas the dual FP tagged SensOR construct can. Activation of SensOR with amino acids (e.g. leucine and arginine) re-folds the SensOR protein indicating it is regulated by mTOR mediated phosphorylation. Purified SensOR *in vitro* showed temperature dependent kinetic unfolding at lower temperatures and re-folding at higher temperatures, in support of preliminary SensOR temperature dependent *in vivo* studies. The direct relationship between observed changes in the lifetime of SensOR with conformational change was confirmed with the addition of ATP to purified SensOR, which showed responsiveness (change in lifetime to 2.3 ns) during the activation (phosphorylation) of S6K1. The lower lifetime observed in the cytoplasm can be taken as the site of phosphorylation and supports previous work where other mTORC1 proteins, namely mTOR, raptor, and Rheb, are found to assemble to the same cytoplasmic localisation site (Yadav *et al.*, 2013). In comparison to current alternative mTOR related FRET bio-sensors, only SensOR is capable of localising to both the nucleus and cytoplasm whilst at the same time directly reporting on mTOR mediated phosphorylation that is rapamycin sensitive (Komatsu *et al.*, 2011; Zhou *et al.*, 2015).

Pan-mTOR inhibitors such as AZD2014 and INK128 display natural fluorescence properties which can be exploited using light microscopy. AZD2014 has been shown to be highly fluorescent molecule (quantum yield of 0.47 in DMSO, reducing to 0.11 in PBS) with a dual-absorbance at 284 nm (ε=36,790 $M^{-1}cm^{-1}$ in DMSO) and 393 nm (ε=1,166 $M^{-1}cm^{-1}$ in DMSO), and fluorescence peak emission at 460 nm. Both single (λ_{ex}=405 nm) and two-photon excitation (λ_{ex}=600 nm) microscopy were used to investigate AZD2014. Longer AZD2014 lifetimes and emissions are observed in polar aprotic solvents such as DMSO compared to protic solvents like PBS. This correlates with preferred localisation of AZD2014 in lipid rich cytosolic substructures such as ER/perinuclear membranes and the Golgi apparatus, known for mTOR localisation (Betz and Hall, 2013). AZD2014 is taken-up rapidly by mammalian cells within one minute of administration, and accumulates at a concentration 30 times greater than the administered dose (7 μM). Human clinical doses have been trialled at 25-100 mg (Basu *et al.*, 2015; Powles *et al.*, 2016) and pre-clinical doses in mice are as high as 7.5-15 mg/kg (Guichard *et al.*, 2015). Considering the range of these doses, the drug's property for heightened accumulation could explain undesirable side effects reported in trials such as fatigue (78%) and nausea (51%) (Basu *et al.*, 2015).

Using multi-cellular spheroids to represent tumour environment, AZD2014 is taken up at similar rates (≥1 minute) in the outer spheroid compared to monolayer cell culture with the inner core of the spheroid showing a slower uptake rate (≥5 minutes). These uptakes support similar findings of the uptake of E- combretastatins in spheroids (Scherer *et al.*, 2015). Furthermore, the combination of 405 nm illumination and AZD2014 treatment resulted in cell death of cells, leading to doubling of spheroid diameter. This photo-activated effect makes AZD2014 a possible candidate for future Photodynamic Therapy (PDT) studies (Bisby *et al.*, 2012), although the precise mechanism of cell death has not been determined.

AZD2014 was established to co-localise strongly with fluorescently tagged Rheb in living cells, which is known to tether mTORC1 to lysosomes, ER, and Golgi substructures (Yadav *et al.*, 2013; Hao *et al.*, 2018). Therefore, one of the ways AZD2014 may function to inhibit mTOR is by automatically localising to mTORC1 subcellular sites. Two-photon excitation of AZD2014 using 600 nm excitation is better suited for determining interactions between AZD2014 and EGFP-mTORC1 using FRET-FLIM. The lifetime of AZD2014 varies (± 0.5 ns), in similar range of that reported recently (Conway *et al.*, 2018), indicating AZD2014 may be photochemically unstable and this would support the spheroid studies. AZD2014 interacts with all mTORC1 subunit proteins although it interacts more strongly with S6K1 (~800 ps change in lifetime) and Rheb (~600 ps change in lifetime). These findings open up newer avenues to combat mTOR disease states such as cancer by directly targeting S6K1 or Rheb (Qin *et al.*, 2015; Mahoney *et al.*, 2018).

Spectroscopic studies on INK128 found this pan-mTOR inhibitor to be less fluorescent (Abs = 293 nm, E_m = 400 nm) than AZD2014 as evident by (quantum yield of 0.33 and molecular coefficient of 16,215 $M^{-1}cm^{-1}$ in DMSO) but shows similar favourability to solvent environments such as DMSO. INK128 can be taken up into cells within 42 seconds and has comparable sub-cellular localisation to that of AZD2014 in living mammalian cells (i.e. cytosolic/ peri-nuclear localised). Taken together, second generation mTOR inhibitors may have common localisation properties.

Generation of large quantities of human mTORC1 complexes in this project have been attempted as a means to provide sufficient material for structural determination of S6K1 bound to mTORC1. Using an insect cell expression system, ~1 mg of raptor-S6K1 protein was produced which although high in concentration, other protein impurities made it insufficient to continue on with for structural studies. The level produced improves upon lower quantities of mTOR complex produced

previously in insect cells (Stuttfeld *et al.*, 2018). However, the mammalian cell seems to be the most popular choice of expression system for generating large quantities of mTORC1 (Yang *et al.*, 2013, 2016, 2017) and the findings here support such a protocol. Human full length and truncated S6K1 have been found to express in high amounts in baculovirus-infected insect cells whilst full length human mTOR and raptor express very poorly or are degraded. This may be due to the lack of the human chaperone system in insect cells that is required to fold eukaryotic proteins (Yokoyama *et al.*, 2000). The use of the His-tag epitope has been found unsuitable for the purification of S6K1-raptor complexes as natural histidine containing proteins non-specifically interact with the purification column, yielding impurities. On the other hand, insect cell expression system combined with the STREP tag purification epitope can produce large quantities of pure SensOR protein with single step purification. On the whole, the expression and purification results shows the dependability of the STREP purification epitope for protein purification and brings attention to its implementation for future protein purification work (Kimple, Brill and Pasker, 2018).

6.2 Future work

This research has applied overexpression of proteins to investigate the interactions of S6K1 in live cells. Although, this ‘test tube’ approach has worked well, endogenous levels of protein expression need to be further examined. Future work entailing the use of CRISPR/Cas9 to tag endogenous mTORC1 proteins with GFP could be used to achieve this goal and further assayed to determine endogenous mTORC1 protein-protein interactions with FRET-FLIM imaging (Lackner *et al.*, 2015; Ratz *et al.*, 2015; Manifava *et al.*, 2016; Khan *et al.*, 2017). Although it has been suggested that S6K1 functions through the mTORC1 pathway, S6K1 has been reported to phosphorylate the mTORC2 pathway (Treins *et al.*, 2010). The interaction between S6K1 and the rictor protein using FRET-FLIM technology could

be investigated in future studies. The implication of S6K1 within the mTORC2 pathway and its synergy across both mTOR complexes would help identify the architectural and structural functions of the mTOR protein. A hybrid mTOR complex consisting of both mTORC1 and mTORC2 subunit proteins and complexes without mTORC1 and mTORC2 subunits have been identified (Jain *et al.*, 2014; Gough, 2016), proposing that the differentiation and specificity of either mTORC1 or mTORC2 from a single complex origin could exist. The first steps towards achieving this goal would entail determining the live cell localisation of fluorescently tagged rictor with respect to S6K1. The rictor protein tagged with GFP on the N-terminus has been published and shows localisation predominately in the cytoplasm whilst some localisation in the nucleus can also be seen (Tao *et al.*, 2015). It would be interesting to determine interaction, if any, between S6K1 and rictor as well as whether S6K1 is capable of translocating with rictor co-expression (Ali and Sabatini, 2005). The mSin1 protein in mTORC2 has been reported to act as a scaffold, similar to raptor's role in mTORC1, to maintain firstly the stability of mTORC2 and secondly to recruit mTORC2 substrates such as AKT, PKCα and SGK1 (Karuppasamy *et al.*, 2017; Tatebe *et al.*, 2017). A better understanding of the recruitment of mTOR substrates could be aided by determining the live cell co-localisations and interactions of the mTORC2 substrates with mTORC2 subunit proteins such as mSin1, rictor, mTOR and Protor1/2 using the combination of GFP and FRET-FLIM technology. The interplay between the recruitment mechanisms of mTORC1 and mTORC2 could be critical in providing novel treatments against mTOR disease states as well as combatting cancers that have developed resistance against current clinical drugs that target only the mTORC1 pathway.

The S6K2 homologue protein of S6K1 is also a direct substrate of mTOR mediated phosphorylation (Park *et al.*, 2002). The localisation and role of S6K2 and its interaction with mTORC1 have to date not been thoroughly investigated. The only

published live cell image of the S6K2 protein is in a plant cell, indicating a predominantly nuclear localisation (Mahfouz, 2006). The sub-cellular localisation of S6K2 in living mammalian cells is yet unknown. Overexpressed S6K2 has been labelled using immunofluorescence techniques and has shown strong staining mostly in the nucleus with some staining in the cytoplasm. Investigating whether S6K2 interacts with the mTORC1 subunit proteins provide a possible inhibition target for the mTOR complex. This may lead to newer strategies to target mTORC1 by exploiting other Ribosomal S6 kinase (RSK) targets.

Determining multiple protein interactions in a cell simultaneously is imperative to defining exact mechanisms of intricate protein cascade events in cellular signalling pathways. The application of dual-channel FRET-FLIM or three-colour FRET with multiple donor-acceptor combinations (Grant *et al.*, 2008; Sun *et al.*, 2010; Scott and Hoppe, 2015; Laviv *et al.*, 2016; Bunt and Wouters, 2017) could provide sub-nanosecond time resolution in detecting multiple mTORC1 or mTORC2 protein subunit interactions and any connection between them. The ability to probe multiple interactions could verify formations of downstream substrate proteins onto mTOR complexes as well as concisely determining their subcellular localisation and exact positions of binding.

In addition, improvements in the FRET-FLIM methodology could be made by implementing more stable and brighter FP proteins. For example, the recently developed mScarlet, has been reported to have a quantum yield of 0.7 (Bindels *et al.*, 2016) whilst the quantum yield of mCherry is 0.22. Such acceptors with EGFP donor tagged proteins could provide better FRET efficiency as equal amounts of donor: acceptor levels can be determined more efficiently during FRET-FLIM measurements. The lifetime of mTurqouise2 (donor) when directly interacting with the mNeonGreen (acceptor) protein has been shown to result in a lifetime change of almost 2 ns (Mastop *et al.*, 2017). Thus, using newer donor-acceptor FP pairs could

be more suitable for studying direct interactions between S6K1 and mTOR. Any long distance interactions (>10 nm) between S6K1 and mTOR could also be investigated using Fluorophore Localisation Imaging with Photobleaching (FLImP), which is capable of defining interactions from around 10 nm up to 100 nm (Needham *et al.*, 2016).

The enhanced resolution offered by super-resolution microscopy techniques such as stimulated emission depletion (STED) and structured illumination microscopy (SIM) techniques have furthered the understanding of cellular signalling mechanisms (D'Abrantes *et al.*, 2018). Currently, there is a lack of super-resolution imaging studying the mTOR pathway. Such work could provide novel insights into mTORC1 sub-cellular localisation. In addition, the combination of these super-resolution techniques (i.e. STED or SIM) with FRET-FLIM technology (Lenz *et al.*, 2011; Görlitz *et al.*, 2017) could further map mTORC1 spatial interactions and dynamics that have been otherwise undetected using conventional diffraction limited microscopy.

Implementation of the donor-acceptor FP pair improvements described above could also be applied to the live cell SensOR construct for directly reporting on mTORC1 activity. Future work may involve developing a high-throughput FRET-FLIM screening method (Margineanu *et al.*, 2016) where mammalian cells expressing mTurq2-S6K1-EGFP or mTurq2-S6K1-mNeonGreen in a 96-well plate are screened against a selection of pre-clinical and clinical mTOR inhibitors. Any changes in lifetime could be used as a marker for determining the efficiency of the drugs in targeting mTOR mediated phosphorylation. The instrumental operation in a clinical context could help provide better treatments whilst as well as the development of new designs for the next generation mTOR inhibitors.

Research into establishing the photosensitising properties of AZD2014 as well as its mechanism could enhance the potency of the anti-cancer drug in clinical trials. Such work would be aided by better understanding the photostability and photophysical characteristics of the drug. Other pan-mTOR inhibitors such as AZD8055 and OSI-027 (Xie, Wang and Proud, 2016), based upon their chemical structure, may display fluorescent properties. Similar studies to that performed with AZD2014 on these second generation inhibitors would help identify common localisation properties and binding mechanism amongst these types of inhibitors. These studies could also be extended to investigating the mechanism and localisation of third generation mTOR inhibitors such as RapaLink where the second generation mTOR moiety in its chemical structure could be utilised as a fluorophore marker (Fan *et al.*, 2017).

Although many dimeric raptor-mTOR based cryoEM structures, resolved at good resolution (4.4 - 5.9 Å) are available, the structure of mTORC1 substrates such as S6K1 or 4EBP1 bound onto the complex is still unknown. Identifying how S6K1 binds mTORC1 at the atomistic level can be expected to lead to improving the ability to design novel inhibitor candidates that are able to disrupt the recruitment mechanism (i.e. fourth generation mTOR inhibitors). Generating large and stable quantities of mTORC1 protein complex may be helped by using human chaperone proteins in the baculovirus-infected insect cell system for assisting the folding of mTOR and raptor proteins (Yokoyama *et al.*, 2000). Other mTORC1 expression attempts could be trialled in the mammalian cell system using Expi293 or ExpiCHO Expression Systems. In addition, the use of other epitope purification tags, particularly the STREP or FLAG tag, could be developed for a one-step purification, to give clean and purer S6K1-mTORC1 complexes (Gerace and Moazed, 2015; Schmidt and Skerra, 2015). Since no full length S6K1 crystal structure is available, X-ray crystallisation or cryoEM trials of the purified SensOR generated from the programme of this work, may provide a structure of S6K1 locked into one of its

phosphorylated states. Identifying the structural basis/conformational workings of S6K1 with respect to mTOR phosphorylation is seen as imperative to preventing and controlling hyperactive mTOR mutations in cancer patients.

References

Agostinis, P. *et al.* (2011) 'Photodynamic therapy of cancer: an update', *CA: a cancer journal for clinicians*, 61(4), pp. 250–281. doi: 10.3322/caac.20114.

Ait-Belkacem, R. *et al.* (2012) 'Mass spectrometry imaging is moving toward drug protein co-localization', *Trends in Biotechnology*, 30(9), pp. 466–474. doi: 10.1016/j.tibtech.2012.05.006.

Ali, S. M. and Sabatini, D. M. (2005) 'Structure of S6 kinase 1 determines whether raptor-mTOR or rictor-mTOR phosphorylates its hydrophobic motif site', *Journal of Biological Chemistry*, 280(20), pp. 19445–19448. doi: 10.1074/jbc.C500125200.

Amaral, C. L. *et al.* (2016) 'S6Ks isoforms contribute to viability, migration, docetaxel resistance and tumor formation of prostate cancer cells', *BMC Cancer*, 16(602), pp. 1–9. doi: 10.1186/s12885-016-2629-y.

Anjum, R. and Blenis, J. (2008) 'The RSK family of kinases: emerging roles in cellular signalling', *Nature Reviews Molecular Cell Biology*, 9(10), pp. 747-758.

Arif, A. *et al.* (2017) 'EPRS is a critical mTORC1-S6K1 effector that influences adiposity in mice', *Nature*, 542(7641), pp. 357–361. doi: 10.1038/nature21380.

Asaad, N., Otter, M. J. Den and Engberts, J. B. F. N. (2004) 'Aqueous solutions that model the cytosol: studies on polarity , chemical reactivity and enzyme kinetics', *Organic & Biomolecular Chemistry*, 2(9), pp. 1404–1412.

Aylett, C. H. S. *et al.* (2016) 'Architecture of human mTOR complex 1', *Science*, 351(6268), pp. 48–52. doi: 10.1126/science.aaa3870.

Bachmann, R. A. *et al.* (2006) 'A Nuclear Transport Signal in Mammalian Target of Rapamycin Is Critical for Its Cytoplasmic Signaling to S6 Kinase 1', *JBC*, 281(11), pp. 7357–7363. doi: 10.1074/jbc.M512218200.

Bajar, B. T. *et al.* (2016) 'A guide to fluorescent protein FRET pairs', *Sensors (Switzerland)*, 16(9), pp. 1–24. doi: 10.3390/s16091488.

Banaszynski, L. A., Liu, C. W. and Wandless, T. J. (2005) 'Characterization of the FKBP-rapamycin-FRB ternary complex', *Journal of the American Chemical Society*, 127(13), pp. 4715–4721. doi: 10.1021/ja043277y.

Baretić, D. *et al.* (2016) 'Tor forms a dimer through an N-terminal helical solenoid with a complex topology', *Nature Communications*, 7, p. 11016. doi: 10.1038/ncomms11016.

Basu, B. *et al.* (2015) 'First-in-human pharmacokinetic and pharmacodynamic study of the dual m-TORC 1/2 inhibitor AZD2014', *Clinical Cancer Research*, 21(15), pp. 3412–3419. doi: 10.1158/1078-0432.CCR-14-2422.

Becker, W., Bergmann, A., *et al.* (2004) 'Advanced time-correlated single photon counting techniques for spectroscopy and imaging in biomedical systems', *Proceedings of SPIE - The International Society for Optical Engineering*, 5340, pp. 104–112. doi: 10.1117/12.529143.

Becker, W., Bergmann, A., *et al.* (2004) 'Fluorescence Lifetime Imaging by Time-Correlated Single-Photon Counting', *Microscopy Research and Technique*, 63(1), pp. 58–66. doi: 10.1002/jemt.10421.

Becker, W. (2012) 'Fluorescence lifetime imaging - techniques and applications', *Journal of Microscopy*, 247(2), pp. 119–136. doi: 10.1111/j.1365-2818.2012.03618.x.

Beecher, D. (2015) 'Nicolás Monardes, John Frampton and the Medical Wonders of the New World', in *Nicolás Monardes, John Frampton and the Medical Wonders of the New World*. Aveiro: UA Editora - Universidade de Aveiro, pp. 141–160. doi: http://dx.doi.org/10.14195/978-989-26-0941-6_6.

Ben-Hur, V. *et al.* (2013) 'S6K1 Alternative Splicing Modulates Its Oncogenic Activity and Regulates mTORC1', *Cell Reports*. The Authors, 3(1), pp. 103–115. doi: 10.1016/j.celrep.2012.11.020.

Berney, C. and Danuser, G. (2003) 'FRET or no FRET: A quantitative comparison', *Biophysical Journal*, 84(6), pp. 3992–4010. doi: 10.1016/S0006-3495(03)75126-1.

Berrow, N. S. *et al.* (2007) 'A versatile ligation-independent cloning method suitable for high-throughput expression screening applications.', *Nucleic Acids Research*, 35(6), p. e45. doi: 10.1093/nar/gkm047.

Bertolin, G. *et al.* (2016) 'A FRET biosensor reveals spatiotemporal activation and functions of aurora kinase A in living cells', *Nature Communications*, 7(12674), pp. 1–16. doi: 10.1038/ncomms12674.

Betz, C. and Hall, M. N. (2013) 'Where is mTOR and what is it doing there?', *Journal of Cell Biology*, 203(4), pp. 563–574. doi: 10.1083/jcb.201306041.

Beugnet, A., Wang, X. and Proud, C. G. (2003) 'Target of Rapamycin (TOR)-signaling and RAIP Motifs Play Distinct Roles in the Mammalian TOR-dependent Phosphorylation of Initiation Factor 4E-binding Protein', *Journal of Biological Chemistry*, 278(42), pp. 40717–40722. doi: 10.1074/jbc.M308573200.

Bevis, B. J. and Glick, B. S. (2002) 'Rapidly maturing variants of the Discosoma red fluorescent protein (DsRed)', *Nature Biotechnology*, 20(1), pp. 83–87. doi: 10.1038/nbt0102-83.

Bindels, D. S. *et al.* (2014) 'Optimisation of fluorescent proteins', in *Fluorescence Spectroscopy and Microscopy: Methods and Protocols, Methods in Molecular Biology*, 1076, pp. 371–417. doi: 10.1007/978-1-62703-649-8.

Bindels, D. S. *et al.* (2017) 'mScarlet : a bright monomeric red fluorescent protein for cellular imaging', *Nature Methods*, 14, pp. 53–56. doi: 10.1038/nmeth.4074.

Bird, L. E. *et al.* (2015) 'Green Fluorescent Protein-based Expression Screening of Membrane Proteins in Escherichia coli', *Journal of Visualized Experiments*, e52357(95), pp. 1–7. doi: 10.3791/52357.

Bisby, R. H. *et al.* (2012) 'Fluorescence lifetime imaging of E-combretastatin uptake and distribution in live mammalian cells.', *European Journal of Cancer*, 48(12), pp. 1896–1903. doi: 10.1016/j.ejca.2011.11.025.

Blacker, T. S. *et al.* (2014) 'Separating NADH and NADPH fluorescence in live cells and tissues using FLIM', *Nature Communications*, 5, p. 3936.

Botchway, S. W. *et al.* (2008) 'Real-time cellular uptake of serotonin using fluorescence lifetime imaging with two-photon excitation.', *Microscopy Research and Technique*, 71(4), pp. 267–273. doi: 10.1002/jemt.20548.

Brocks, D. R. and Mehvar, R. (2010) 'Rate and extent of drug accumulation after multiple dosing revisited.', *Clinical Pharmacokinetics*, 49(7), pp. 421–438. doi: 10.2165/11531190-000000000-00000.

Brown, E. J. *et al.* (1994) 'A mammalian protein targeted by G1-arresting rapamycin-receptor complex', *Nature*, 369(6483), pp. 756–758. doi: 10.1038/369756a0.

Brown, E. J. *et al.* (1995) 'Control of p70 S6 kinase by kinase activity of FRAP in vivo.', *Nature*, 377(6548), pp. 441–446. doi: 10.1038/377441a0.

Brown, M. C. *et al.* (2017) 'MNK Controls mTORC1 : Substrate Association through Regulation of TELO2 Binding with mTORC1, *Cell Reports*, 18(6), pp. 1444–1457. doi: 10.1016/j.celrep.2017.01.023.

Buerger, C., DeVries, B. and Stambolic, V. (2006) 'Localization of Rheb to the endomembrane is critical for its signaling function', *Biochemical and Biophysical Research Communications*, 344(3), pp. 869–880. doi: 10.1016/j.bbrc.2006.03.220.

Bunt, G. and Wouters, F. S. (2017) 'FRET from single to multiplexed signaling events', *Biophys Rev*. Biophysical Reviews, 9, pp. 119–129. doi: 10.1007/s12551-017-0252-z.

Burris, H. A. *et al.* (2017) 'TAK-228 (formerly MLN0128), an investigational dual TORC1/2 inhibitor plus paclitaxel, with/without trastuzumab, in patients with advanced solid malignancies', *Cancer Chemotherapy and Pharmacology*, 80(2), pp. 261–273. doi: 10.1007/s00280-017-3343-4.

Caccamo, A. *et al.* (2015) 'Reducing Ribosomal Protein S6 Kinase 1 Expression Improves Spatial Memory and Synaptic Plasticity in a Mouse Model of Alzheimer's Disease', *Journal of Neuroscience*, 35(41), pp. 14042–14056. doi: 10.1523/JNEUROSCI.2781-15.2015.

Calton, M. A. and Vollrath, D. (2016) 'The mTOR kinase inhibitor INK128 blunts migration of cultured retinal pigment epithelial cells', in *Advances in Experimental Medicine and Biology*, 854, pp. 709-715 doi: 10.1007/978-3-319-17121-0_94.

Candeo, A. *et al.* (2017) 'Light Sheet Fluorescence Microscopy Quantifies Calcium Oscillations in Root Hairs of Arabidopsis thaliana.', *Plant & Cell Physiology*, 58(7), pp. 1161–1172. doi: 10.1093/pcp/pcx045.

Chalfie, M. *et al.* (1994) 'Green fluorescent protein as a marker for gene expression', *Science*, 263(5148), pp. 802–805. doi: 10.1126/science.8303295.

Chambers, A. C. *et al.* (2018) 'Overview of the Baculovirus Expression System', in *Current Protocols in Protein Science*, p. 5.4.1-5.4.6. doi: 10.1002/cpps.47.

Chantranupong, L. *et al.* (2016) 'The CASTOR proteins are arginine sensors for the mTORC1 pathway', *Cell*, 165(1), pp. 153–164. doi: 10.1016/j.cell.2016.02.035.The.

Chen, X. *et al.* (2018) 'Cryo-EM structure of human mTOR complex 2.', *Cell Research*, 28(5), pp. 518–528. doi: 10.1038/s41422-018-0029-3.

Chiu, M. I., Katz, H. and Berlin, V. (1994) 'RAPT1, a mammalian homolog of yeast Tor, interacts with the FKBP12/rapamycin complex.', *Proceedings of the National Academy of Sciences*, 91(26), pp. 12574–12578. doi: 10.1073/pnas.91.26.12574.

Choi, J. *et al.* (1996) 'Structure of the FKBP12-Rapamycin complex Interactign with the Binding Domain of Human FRAP', *Science*, 273(5272), pp. 239–242.

Choi, K. M., McMahon, L. P. and Lawrence, J. C. (2003) 'Two motifs in the translational repressor PHAS-I required for efficient phosphorylation by mammalian target of rapamycin and for recognition by raptor', *Journal of Biological Chemistry*, 278(22), pp. 19667–19673. doi: 10.1074/jbc.M301142200.

Choo, A. Y. *et al.* (2008) 'Rapamycin differentially inhibits S6Ks and 4E-BP1 to mediate cell-type-specific repression of mRNA translation', *Proceedings of the National Academy of Sciences*, 105(45), pp. 17414–17419. doi: 10.1073/pnas.0809136105.

Choo, A. Y. and Blenis, J. (2009) 'Not all substrates are treated equally Implications for mTOR, rapamycin-resistance and cancer therapy', *Cell Cycle*, 8(4), pp. 567–572. doi: 10.4161/cc.8.4.7659.

Coffer, P. J. and Woodgett, J. R. (1994) 'Differential Subcellular Localization of Two Isoforms of p70 S6 Protein Kinase', *Biochemical and Biophysical Research Communications*, 198(2), pp. 780–786. doi: https://doi.org/10.1006/bbrc.1994.1112.

Coffman, K. *et al.* (2014) 'Characterization of the raptor/4E-BP1 interaction by chemical cross-linking coupled with mass spectrometry analysis', *Journal of Biological Chemistry*, 289(8), pp. 4723–4734. doi: 10.1074/jbc.M113.482067.

Conway, J. R. W. *et al.* (2018) 'Intravital Imaging to Monitor Therapeutic Response in Moving Hypoxic Regions Resistant to PI3K Pathway Targeting in Pancreatic Cancer.', *Cell reports*. United States, 23(11), pp. 3312–3326. doi: 10.1016/j.celrep.2018.05.038.

Costantini, L. M. *et al.* (2015) 'A palette of fluorescent proteins optimized for diverse cellular environments.', *Nature communications*, 6(7670), pp. 1-13. doi: 10.1038/ncomms8670.

Cranfill, P. J. *et al.* (2016) 'Quantitative assessment of fluorescent proteins', *Nature Methods*, 13(7), pp. 557–562. doi: 10.1038/nmeth.3891.

Crino, P. B. (2016) 'The mTOR signalling cascade: Paving new roads to cure neurological disease', *Nature Reviews Neurology*. Nature Publishing Group, 12(7), pp. 379–392. doi: 10.1038/nrneurol.2016.81.

D'Abrantes, S. *et al.* (2018) 'Super-Resolution Nanoscopy Imaging Applied to DNA Double-Strand Breaks.', *Radiation research*, 189(1), pp. 19–31. doi: 10.1667/RR14594.1.

Dann, S. G., Selvaraj, A. and Thomas, G. (2007) 'mTOR Complex1-S6K1 signaling: at the crossroads of obesity, diabetes and cancer', *Trends in Molecular Medicine*, 13(6), pp. 252–259. doi: 10.1016/j.molmed.2007.04.002.

Dean, K. M. and Palmer, A. E. (2014) 'Advances in fluorescence labeling strategies for dynamic cellular imaging', *Nature chemical biology*, 10(7), pp. 512–523. doi: 10.1038/nchembio.1556.Advances.

Demeautis, C. *et al.* (2017) 'Multiplexing PKA and ERK1&2 kinases FRET biosensors in living cells using single excitation wavelength dual colour FLIM', *Scientific Reports*. The Author(s), 7, p. 41026. doi: 10.1038/srep41026.

Dennis, M. D., Kimball, S. R. and Jefferson, L. S. (2013) 'Mechanistic target of rapamycin complex 1 (mTORC1)-mediated phosphorylation is governed by competition between substrates for interaction with raptor', *Journal of Biological Chemistry*, 288(1), pp. 10–19. doi: 10.1074/jbc.M112.402461.

Djouder, N. *et al.* (2007) 'S6K1-Mediated Disassembly of Mitochondrial URI/PP1γ Complexes Activates a Negative Feedback Program that Counters S6K1 Survival Signaling', *Molecular Cell*, 28(1), pp. 28–40. doi: 10.1016/j.molcel.2007.08.010.

Dumont, F. J. and Su, Q. (1995) 'Mechanism of action of the immunosuppressant rapamycin', *Life Sciences*, 58(5), pp. 373–395. doi: 10.1016/0024-3205(95)02233-3.

Dyachok, J. *et al.* (2016) 'Amino Acids Regulate mTORC1 by an Obligate Two-Step Mechanism, The *Journal of Biological Chemistry*, 291(43), pp. 22414-22426. doi: 10.1074/jbc.M116.732511.

Ellinger, P. and Hirt, A. (1929) 'Mikroskopische Beobachtungen an lebenden Organen mit Demonstrationen (Intravitalmikroskopie)', *Archiv Experimentelle Pathologie und Pharmakologie*, 147(63), pp. 1–3. doi: 10.1007/BF01946036.

Erickson, M. G., Moon, D. L. and Yue, D. T. (2003) 'DsRed as a potential FRET partner with CFP and GFP.', *Biophysical journal*, 85(1), pp. 599–611. doi: 10.1016/S0006-3495(03)74504-4.

Faes, S., Demartines, N. and Dormond, O. (2017) 'Resistance to mTORC1 Inhibitors in Cancer Therapy: From Kinase Mutations to Intratumoral Heterogeneity of Kinase Activity', *Oxidative Medicine and Cellular Longevity*, 1726078, pp. 1–10. doi: 10.1155/2017/1726078.

Fan, Q. W. *et al.* (2017) 'A Kinase Inhibitor Targeted to mTORC1 Drives Regression in Glioblastoma', *Cancer Cell*, 31(3), pp. 424–435. doi: 10.1016/j.ccell.2017.01.014.

Fenton, T. R. and Gout, I. T. (2011) 'Functions and regulation of the 70 kDa ribosomal S6 kinases', *International Journal of Biochemistry and Cell Biology*, 43(1), pp. 47–59. doi: 10.1016/j.biocel.2010.09.018.

Flannery, P. C. *et al.* (2018) 'Preclinical analysis of MTOR complex 1/2 inhibition in diffuse intrinsic pontine glioma', *Oncology Reports*, 39(2), pp. 455–464. doi: 10.3892/or.2017.6122.

Fritz, J. V *et al.* (2008) 'Direct Vpr-Vpr interaction in cells monitored by two photon fluorescence correlation spectroscopy and fluorescence lifetime imaging.', *Retrovirology*, 5(1), p. 87. doi: 10.1186/1742-4690-5-87.

Fujimori, E. *et al.* (1981) 'Blue fluorescence and crosslinking of photooxidized proteins', *FEBS Letters*, 135(2), pp. 2–5.

Garami, A. *et al.* (2003) 'Insulin activation of Rheb, a mediator of mTOR/S6K/4E-BP signaling, is inhibited by TSC1 and 2', *Molecular Cell*, 11(6), pp. 1457–1466. doi: 10.1016/S1097-2765(03)00220-X.

Ge, Y., Yoon, M. S. and Chen, J. (2011) 'Raptor and rheb negatively regulate skeletal myogenesis through suppression of insulin receptor substrate 1 (IRS1)', *Journal of Biological Chemistry*, 286(41), pp. 35675–35682. doi: 10.1074/jbc.M111.262881.

Gerace, E. and Moazed, D. (2015) 'Affinity Pull-Down of Proteins Using Anti-FLAG M2 Agarose Beads', *Methods in Enzymology*, 559, pp. 99–110. doi: 10.1016/bs.mie.2014.11.010.

Gerritsen, H. C. *et al.* (2002) 'Fluorescence lifetime imaging in scanning microscopes: Acquisition speed, photon economy and lifetime resolution', *Journal of Microscopy*, 206(3), pp. 218–224. doi: 10.1046/j.1365-2818.2002.01031.x.

Ghobrial, I. M. *et al.* (2016) 'TAK-228 (formerly MLN0128), an investigational oral dual TORC1/2 inhibitor: A phase I dose escalation study in patients with relapsed or refractory multiple myeloma, non-Hodgkin lymphoma, or Waldenström's macroglobulinemia', *American Journal of Hematology*. Wiley-Blackwell, 91(4), pp. 400–405. doi: 10.1002/ajh.24300.

Ghodke, H. *et al.* (2016) 'Single-Molecule Specific Mislocalization of Red Fluorescent Proteins in Live Escherichia coli', *Biophysical Journal*, 111(1), pp. 25–27. doi: https://doi.org/10.1016/j.bpj.2016.05.047.

Giguère, V. (2018) 'Canonical signaling and nuclear activity of mTOR—a teamwork effort to regulate metabolism and cell growth', *The FEBS Journal*, 285(9), pp. 1572–1588. doi: 10.1111/febs.14384.

Goedhart, J. *et al.* (2012) 'Structure-guided evolution of cyan fluorescent proteins towards a quantum yield of 93%', *Nature Communications*, 3(751), pp. 1–9. doi: 10.1038/ncomms1738.

Gökmen-Polar, Y. *et al.* (2012) 'Investigational drug MLN0128, a novel TORC1/2 inhibitor, demonstrates potent oral antitumor activity in human breast cancer xenograft models', *Breast Cancer Research and Treatment*, 136(3), pp. 673–682. doi: 10.1007/s10549-012-2298-8.

Gonzalez, A. *et al.* (2015) 'TORC1 promotes phosphorylation of ribosomal protein S6 via the AGC kinase Ypk3 in Saccharomyces cerevisiae.', *PloS one*, 10(3), p. e0120250. doi: 10.1371/journal.pone.0120250.

Görlitz, F. *et al.* (2017) 'Mapping Molecular Function to Biological Nanostructure: Combining Structured Illumination Microscopy with Fluorescence Lifetime Imaging (SIM + FLIM)', *Photonics* . doi: 10.3390/photonics4030040.

Gough, N. R. (2016) 'Another mTOR complex?', *Science Signaling*, 9(436), p. ec160.

Grant, D. M. *et al.* (2008) 'Multiplexed FRET to Image Multiple Signaling Events in Live Cells', *Biophysical Journal*. The Biophysical Society, 95(10), pp. L69–L71. doi: 10.1529/biophysj.108.139204.

Guichard, S. M. *et al.* (2015) 'AZD2014, an Inhibitor of mTORC1 and mTORC2, Is Highly Effective in ER+ Breast Cancer When Administered Using Intermittent or Continuous Schedules', *Molecular Cancer Therapeutics*, 14(11), pp. 2508–2518. doi: 10.1158/1535-7163.MCT-15-0365.

Guo, M., Xu, Y. and Gruebele, M. (2012) 'Temperature dependence of protein folding kinetics in living cells', *Proceedings of the National Academy of Sciences of the United States of America*. National Academy of Sciences, 109(44), pp. 17863–17867. doi: 10.1073/pnas.1201797109.

Guo, Y. *et al.* (1998) 'Noninvasive two-photon-excitation imaging of tryptophan distribution in highly scattering biological tissues', *Optics Communications*, 154(5), pp. 383–389. doi: https://doi.org/10.1016/S0030-4018(98)00207-7.

Guo, Y. and Kwiatkowski, D. J. (2013) 'Equivalent Benefit of Rapamycin and a Potent mTOR ATP-Competitive Inhibitor, MLN0128 (INK128), in a Mouse Model of Tuberous Sclerosis', *Molecular Cancer Research*, 11(5), pp. 467–473. doi: 10.1158/1541-7786.MCR-12-0605.

Habuchi, S. *et al.* (2005) 'Reversible single-molecule photoswitching in the GFP-like fluorescent protein Dronpa', *Proceedings of the National Academy of Sciences of the United States of America*, 102(27), pp. 9511-9516.

Hanker, A. B. *et al.* (2010) 'Differential Requirement of CAAX-mediated Posttranslational Processing for Rheb Localization and Signaling', *Oncogene*, 29(3), pp. 380–391. doi: 10.1038/onc.2009.336.Differential.

Hao, F. *et al.* (2018) 'Rheb localized on the Golgi membrane activates lysosome-localized mTORC1 at the Golgi-lysosome contact site', *Journal of Cell Science*, 131(3). doi: 10.1242/jcs.208017.

Hara, K. *et al.* (2002) 'Raptor, a binding partner of target of rapamycin (TOR), mediates TOR action', *Cell*, 110(2), pp. 177–189. doi: 10.1016/S0092-8674(02)00833-4.

Harada, M. *et al.* (2015) 'The novel combination of dual mTOR inhibitor AZD2014 and pan-PIM inhibitor AZD1208 inhibits growth in acute myeloid leukemia via HSF pathway suppression', *Oncotarget*, 6(35), pp. 37930–37947. doi: 10.18632/oncotarget.6122.

Heitman, J., Movva, N. R. and Hall, M. N. (1991) 'Targets for cell cycle arrest by the immunosuppressant rapamycin in yeast', *Science*, 253(5022), pp. 905–909. doi: 10.1126/science.1715094.

Heller, C. A. *et al.* (1974) 'Fluorescence Spectra and Quantum Yields : Quinine , Uranine , 9,10-Diphenylanthracene, and 9,10-Bis(phenylethynyl)anthracenes', *Journal of Chemical and Engineering Data*, 19(3), pp. 214–219. doi: 10.1021/je60062a002.

Hill, A. *et al.* (2018) 'Redesigning TOR Kinase to Explore the Structural Basis for TORC1 and TORC2 Assembly', *Biomolecules*. MDPI, 8(2), p. 36. doi: 10.3390/biom8020036.

Hitchman, R. B. *et al.* (2011) 'Optimizing the baculovirus expression vector system', *Methods*, 55(1) doi: 10.1016/j.ymeth.2011.06.011.

Hochreiter, B., Garcia, A. P. and Schmid, J. A. (2015) 'Fluorescent proteins as genetically encoded FRET biosensors in life sciences', *Sensors (Switzerland)*, 15(10), pp. 26281–26314. doi: 10.3390/s151026281.

Holz, M. K. *et al.* (2005) 'mTOR and S6K1 mediate assembly of the translation preinitiation complex through dynamic protein interchange and ordered phosphorylation events', *Cell*, 123(4), pp. 569–580. doi: 10.1016/j.cell.2005.10.024.

Hsieh, A. C. *et al.* (2012) 'The translational landscape of mTOR signalling steers cancer initiation and metastasis', *Nature*, 485, pp.55-61. doi: 10.1038/nature10912.

Huang, L. *et al.* (2014) 'Potential Pitfalls and Solutions for Use of Fluorescent Fusion Proteins to Study the Lysosome', *PLoS ONE*. Edited by H. Yang. Public Library of Science, 9(2), p. e88893. doi: 10.1371/journal.pone.0088893.

Huber, L. A., Pfaller, K. and Vietor, I. (2003) 'Implications for Subcellular Fractionation in Proteomics', *Circulation Research*, (92), pp. 962–969. doi: 10.1161/01.RES.0000071748.48338.25.

Ingels, A. *et al.* (2013) '158 Pre-Clinical Trial of a New Dual Mtor Inhibitor : INK128 for Renal Cell Carcinoma', *The Journal of Urology*, 189(4), p. e65. doi: 10.1016/j.juro.2013.02.1538.

Inoki, K. *et al.* (2003) 'Rheb GTpase is a direct target of TSC2 GAP activity and regulates mTOR signaling', *Genes and Development*, 17(15), pp. 1829–1834. doi: 10.1101/gad.1110003.

Ishikawa-Ankerhold, H. C., Ankerhold, R. and Drummen, G. P. C. (2012) 'Advanced fluorescence microscopy techniques-FRAP, FLIP, FLAP, FRET and FLIM', *Molecules*, pp. 4047–4132. doi: 10.3390/molecules17044047.

Ismail, S. A. *et al.* (2011) 'Arl2-GTP and Arl3-GTP regulate a GDI-like transport system for farnesylated cargo', *Nature Chemical Biology*, 7(12), pp. 942–949. doi: 10.1038/nchembio.686.

Jain, A. *et al.* (2014) 'Stoichiometry and assembly of mTOR complexes revealed by single-molecule pulldown', *Proceedings of the National Academy of Sciences*, 111(50), pp. 17833–17838. doi: 10.1073/pnas.1419425111.

Janakiraman, V. *et al.* (2006) 'A rapid method for estimation of baculovirus titer based on viable cell size', *Journal of Virological Methods*, 132(1), pp. 48–58. doi: https://doi.org/10.1016/j.jviromet.2005.08.021.

Janes, M. R. *et al.* (2013) 'Efficacy of the investigational mTOR kinase inhibitor MLN0128/INK128 in models of B-cell acute lymphoblastic leukemia', *Leukemia*, 27(3), pp. 586–594. doi: 10.1038/leu.2012.276.

Jaskolski, F., Mulle, C. and Manzoni, O. (2005) 'An automated method to quantify and visualize colocalized fluorescent signals', *Journal of Neuroscience Methods*, 146(1), pp. 42-49. doi: 10.1016/j.jneumeth.2005.01.012.

Jensen, E. C. (2012) 'Types of Imaging, Part 2: An Overview of Fluorescence Microscopy', *The Anatomical Record*, 295(10), pp. 1621–1627. doi: 10.1002/ar.22548.

Jones, G. *et al.* (1985) 'Solvent effects on emission yield and lifetime for coumarin laser dyes. Requirements for a rotatory decay mechanism', *The Journal of Physical Chemistry*, 89(2), pp. 294–300. doi: 10.1021/j100248a024.

Jonkman, J. and Brown, C. M. (2015) 'Any way you slice it—A comparison of confocal microscopy techniques', *Journal of Biomolecular Techniques*, 26(2), pp. 54–65. doi: 10.7171/jbt.15-2602-003.

Kaishima, M. *et al.* (2016) 'Expression of varied GFPs in Saccharomyces cerevisiae: codon optimization yields stronger than expected expression and fluorescence intensity', *Scientific Reports*, 6(35932), pp. 1–15.

Karuppasamy, M. *et al.* (2017) 'Cryo-EM structure of Saccharomyces cerevisiae target of rapamycin complex 2', *Nature Communications*, 8(1), p. 1729. doi: 10.1038/s41467-017-01862-0.

Keshwani, M. M. *et al.* (2011) 'Hydrophobic motif phosphorylation is not required for activation loop phosphorylation of p70 ribosomal protein S6 kinase 1 (S6K1)', *Journal of Biological Chemistry*, 286(26), pp. 23552–23558. doi: 10.1074/jbc.M111.258004.

Khan, A. O. *et al.* (2017) 'CRISPR-Cas9 Mediated Labelling Allows for Single Molecule Imaging and Resolution', *Scientific Reports*, 7(1), p. 8450. doi: 10.1038/s41598-017-08493-x.

Khan, K. H. (2013) 'Gene Expression in Mammalian Cells and its Applications', *Advanced Pharmaceutical Bulletin*. Tabriz University of Medical Sciences, 3(2), pp. 257–263. doi: 10.5681/apb.2013.042.

Kim, D. *et al.* (2009) 'Regulation and localization of ribosomal protein S6 kinase 1 isoforms', *Growth Factors*, 27(1), pp. 12–21. doi: 10.1080/08977190802556986.

Kim, D. H. *et al.* (2002) 'mTOR interacts with raptor to form a nutrient-sensitive complex that signals to the cell growth machinery', *Cell*, 110(2), pp. 163–175. doi: 10.1016/S0092-8674(02)00808-5.

Kim, J. *et al.* (2012) 'Quantification of protein interaction in living cells by two-photon spectral imaging with fluorescent protein fluorescence resonance energy transfer pair devoid of acceptor bleed-through', *Cytometry Part A*, 81(2), pp. 112–119. doi: 10.1002/cyto.a.21150.

Kim, J. *et al.* (2013) 'Arginine, Leucine, and Glutamine Stimulate Proliferation of Porcine Trophectoderm Cells Through the MTOR-RPS6K-RPS6-EIF4EBP1 Signal Transduction Pathway1', *Biology of Reproduction*, 88(5), p. 113. doi: 10.1095/biolreprod.112.105080.

Kim, J. E. and Chen, J. (2000) 'Cytoplasmic – nuclear shuttling of FKBP12-rapamycin-associated protein is involved in rapamycin-sensitive signaling and translation initiation', *PNAS*, 97(26), pp. 14340–14345.

Kim, S. J. and Kahn, C. R. (1997) 'Insulin stimulates p70 S6 kinase in the nucleus of cells.', *Biochemical and biophysical research communications*, 234(3), pp. 681–685. doi: 10.1006/bbrc.1997.6699.

Kim, S. Y. *et al.* (2014) 'S6K1 Negatively Regulates TAK1 Activity in the Toll-Like Receptor Signaling Pathway', *Molecular and Cellular Biology*, 34(3), pp. 510–521. doi: 10.1128/MCB.01225-13.

Kimple, M. E., Brill, A. L. and Pasker, R. L. (2018) 'Overview of Affinity Tags for Protein Purification', *Current Protocols in Protein Science*, 73(1), p. 9.9.1-9.9.23. doi: 10.1002/0471140864.ps0909s73.

Kimura, S. and Wilson, T. (1991) 'Confocal scanning optical microscope using single-mode fiber for signal detection', *Appl. Opt.* OSA, 30(16), pp. 2143–2150. doi: 10.1364/AO.30.002143.

Koltin, Y. *et al.* (1991) 'Rapamycin sensitivity in Saccharomyces cerevisiae is mediated by a peptidyl-prolyl cis-trans isomerase related to human FK506-binding protein', *Molecular and cellular biology*. United States, 11(3), pp. 1718–1723.

Komatsu, N. *et al.* (2011) 'Development of an optimized backbone of FRET biosensors for kinases and GTPases', *Molecular Biology of the Cell*, 22(23), pp. 4647–4656. doi: 10.1091/mbc.E11-01-0072.

Komatsu, N. *et al.* (2018) 'A platform of BRET-FRET hybrid biosensors for optogenetics , chemical screening , and in vivo imaging', *Scientific Reports*. Springer US, 8(8984), pp. 1–14. doi: 10.1038/s41598-018-27174-x.

Korobchevskaya, K. *et al.* (2017) 'Exploring the Potential of Airyscan Microscopy for Live Cell Imaging', *Photonics*, 4(41), pp. 1–19. doi: 10.3390/photonics4030041.

Kozany, C. *et al.* (2009) 'Fluorescent probes to characterise FK506-binding proteins.', *Chembiochem : a European Journal of Chemical Biology*, 10(8), pp. 1402–1410. doi: 10.1002/cbic.200800806.

Kremers, G.-J. *et al.* (2009) 'Photoconversion in orange and red fluorescent proteins', *Nature Methods*, 6(5), pp. 355–358. doi: 10.1038/nmeth.1319.

Kriechbaumer, V. *et al.* (2015) 'Reticulomics: Protein-protein interaction studies with two plasmodesmata-localized reticulon family proteins identify binding partners enriched at plasmodesmata, endoplasmic reticulum, and the plasma membrane', *Plant Physiology*, 169(November), pp. 1933–1945. doi: 10.1104/pp.15.01153.

Kriechbaumer, V., Botchway W, S. and Hawes, C. (2016) 'Localization and interactions between Arabidopsis auxin biosynthetic enzymes in the TAA/YUC-dependent pathway', *Journal of Experimental Botany*, 67(12), pp. 4195–4207.

Kubin, R. F. and Fletcher, A. N. (1982) 'Fluorescence quantum yields of some rhodamine dyes', *Journal of Luminescence*, 27(4), pp. 455–462. doi: https://doi.org/10.1016/0022-2313(82)90045-X.

Kuimova, M. K. *et al.* (2006) 'Monitoring the direct and indirect damage of DNA bases and polynucleotides by using time-resolved infrared spectroscopy', *Proceedings of the National Academy of Sciences*, 103(7), pp. 2150–2153.

Lackner, D. H. *et al.* (2015) 'A generic strategy for CRISPR-Cas9-mediated gene tagging', *Nature Communications*, 6(10237), pp. 1–7.

Lakowicz, J. R. (2006) *Principles of Fluorescence Spectroscopy, Springer, 3rd edition, 2006.* doi: 10.1007/978-0-387-46312-4.

Laplante, M. *et al.* (2009) 'mTOR signaling at a glance.', *Journal of Cell Science*, 122(Pt 20), pp. 3589–3594. doi: 10.1242/jcs.051011.

Laplante, M. and Sabatini, D. M. (2012) 'mTOR signaling in growth control and disease', *Cell*, 149(2), pp. 274–293. doi: 10.1016/j.cell.2012.03.017.

Laptenok, S. P. *et al.* (2010) 'Global analysis of Förster resonance energy transfer in live cells measured by fluorescence lifetime imaging microscopy exploiting the rise time of acceptor fluorescence', *Physical Chemistry Chemical Physics*, 12(27), p. 7593. doi: 10.1039/b919700a.

Laviv, T. *et al.* (2016) 'Simultaneous dual-color fluorescence lifetime imaging with novel red-shifted fluorescent proteins.', *Nature methods*. United States, 13(12), pp. 989–992. doi: 10.1038/nmeth.4046.

Lawrence, R. E. *et al.* (2018) 'A nutrient-induced affinity switch controls mTORC1 activation by its Rag GTPase–Ragulator lysosomal scaffold', *Nature Cell Biology*. doi: 10.1038/s41556-018-0148-6.

Lee, J. *et al.* (2016) 'S6K1 Phosphorylation of H2B Mediates EZH2 Trimethylation of H3 : A Determinant of Early Short Article S6K1 Phosphorylation of H2B Mediates EZH2 Trimethylation of H3 : A Determinant of Early Adipogenesis', *Molecular Cell*. Elsevier Inc., 62(3), pp. 443–452. doi: 10.1016/j.molcel.2016.03.011.

Lee, V. H. Y. *et al.* (2008) 'Analysis of the regulatory motifs in eukaryotic initiation factor 4E-binding protein 1', *FEBS Journal*, 275(9), pp. 2185–2199. doi: 10.1111/j.1742-4658.2008.06372.x.

Lenz, M. *et al.* (2011) 'A STED-FLIM microscope applied to imaging the Natural Killer cell immune synapse', *Progress in Biomedical Optics and Imaging - Proceedings of SPIE*, 7903. doi: 10.1117/12.875018.

Li, C. *et al.* (2015) 'The preclinical evaluation of the dual mTORC1/2 inhibitor INK-128 as a potential anti-colorectal cancer agent', *Cancer Biology & Therapy*, 16(1), pp. 34–42. doi: 10.4161/15384047.2014.972274.

Li, X. *et al.* (2018) 'Efficacy of PI3K / AKT / mTOR pathway inhibitors for the treatment of advanced solid cancers : A literature-based meta-analysis of 46 randomised control trials', *PLOS ONE*, 13(2), pp. 1–18.

Li, Y. *et al.* (2007) 'Bnip3 mediates the hypoxia-induced inhibition on mammalian target of rapamycin by interacting with Rheb', *Journal of Biological Chemistry*, 282(49), pp. 35803–35813. doi: 10.1074/jbc.M705231200.

Li, Y. *et al.* (2011) 'Highly efficient purification of protein complexes from mammalian cells using a novel streptavidin-binding peptide and hexahistidine tandem tag system: Application to Bruton's tyrosine kinase', *Protein Science*, 20(1), pp. 140–149. doi: 10.1002/pro.546.

Liao, H. *et al.* (2015) 'Dramatic antitumor effects of the dual mTORC1 and mTORC2 inhibitor AZD2014 in hepatocellular carcinoma', *American Journal of Cancer Research*, 5(1), pp. 125–139.

Lichtman, J. W. and Conchello, J.-A. (2005) 'Fluorescence microscopy', *Nature Methods*, 2, pp. 910-919.

Lindenburg, L. and Merkx, M. (2014) 'Engineering genetically encoded FRET sensors', *Sensors (Switzerland)*, 14(7), pp. 11691–11713. doi: 10.3390/s140711691.

Liu, F. *et al.* (2018) 'Overexpression of RHEB is associated with metastasis and poor prognosis in hepatocellular carcinoma', *Oncology Letters*, 15(3), pp. 3838–3845. doi: 10.3892/ol.2018.7759.

Liu, X. and Zheng, X. F. S. (2007) 'Endoplasmic reticulum and Golgi localization sequences for mammalian target of rapamycin.', *Molecular Biology of the Cell*, 18(3), pp. 1073–82. doi: 10.1091/mbc.E06-05-0406.

Llères, D., Swift, S. and Lamond, A. I. (2007) *Detecting protein-protein interactions in vivo with FRET using multiphoton fluorescence lifetime imaging microscopy (FLIM)*, *Current Protocols in Cytometry*. doi: 10.1002/0471142956.cy1210s42.

Long, X., Ortiz-Vega, S., *et al.* (2005) 'Rheb binding to mammalian target of rapamycin (mTOR) is regulated by amino acid sufficiency', *Journal of Biological Chemistry*, 280(25), pp. 23433–23436. doi: 10.1074/jbc.C500169200.

Long, X., Lin, Y., *et al.* (2005) 'Rheb binds and regulates the mTOR kinase', *Current Biology*, 15(8), pp. 702–713. doi: 10.1016/j.cub.2005.02.053.

Long, X. *et al.* (2007) 'The Rheb switch 2 segment is critical for signaling to target of rapamycin complex 1', *Journal of Biological Chemistry*, 282(25), pp. 18542–18551. doi: 10.1074/jbc.M610736200.

Lowder, M. *et al.* (2000) 'Effect of Starvation and the Viable-but-Nonculturable State on Green Fluorescent Protein (GFP) Fluorescence in GFP-Tagged Pseudomonas fluorescens A506', *Applied and Environmental Microbiology*, 66(8), pp. 3160–3165.

Lun, X. K. *et al.* (2017) 'Influence of node abundance on signaling network state and dynamics analyzed by mass cytometry', *Nature Biotechnology*, 35(2), pp. 164–172. doi: 10.1038/nbt.3770.

Maertens, B. *et al.* (2015) 'Strep-Tagged Protein Purification.', *Methods in enzymology*. United States, 559, pp. 53–69. doi: 10.1016/bs.mie.2014.11.008.

Magnuson, B., Ekim, B. and Fingar, D. C. (2012) 'Regulation and function of ribosomal protein S6 kinase (S6K) within mTOR signalling networks', *Biochemical Journal*, 441(1), pp. 1–21. doi: 10.1042/BJ20110892.

Mahfouz, M. M. (2006) 'Arabidopsis TARGET OF RAPAMYCIN Interacts with RAPTOR, Which Regulates the Activity of S6 Kinase in Response to Osmotic Stress Signals', *the Plant Cell Online*, 18(2), pp. 477–490. doi: 10.1105/tpc.105.035931.

Mahoney, S. J. *et al.* (2018) 'A small molecule inhibitor of Rheb selectively targets mTORC1 signaling', *Nature Communications*, 9(1), p. 548. doi: 10.1038/s41467-018-03035-z.

Maiman, T. H. (1960) 'Stimulated optical radiation in Ruby', *Nature*, 187(4736), pp. 493–494. doi: 10.1038/187493a0.

Manifava, M. *et al.* (2016) 'Dynamics of mTORC1 activation in response to amino acids', pp. 1–21. doi: 10.7554/eLife.19960.

Manlin, W. *et al.* (2013) 'Molecular Characterization and Expression Analysis of S6K1 in Cashmere Goats (Capra hircus)', *Asian-Australasian Journal of Animal Sciences*, 26(8), pp. 1057–1064. doi: 10.5713/ajas.2012.12710.

Marabita, M. *et al.* (2016) 'S6K1 Is Required for Increasing Skeletal Muscle Force during Hypertrophy', *Cell Reports*, 17(2), pp. 501–513. doi: 10.1016/j.celrep.2016.09.020.

Marchant, J. S. *et al.* (2001) 'Multiphoton-evoked color change of DsRed as an optical highlighter for cellular and subcellular labeling.', *Nature biotechnology*, 19(7), pp. 645–649. doi: 10.1038/90249.

Marcu, L., French, P. M. W. and Elson, D. S. (2014) 'Fluorescence lifetime spectroscopy and imaging : principles and applications in biomedical diagnostics', *Journal of biomedical optics*, 19(10), p. 109901.

Margineanu, A. *et al.* (2016) 'Screening for protein-protein interactions using Förster resonance energy transfer (FRET) and fluorescence lifetime imaging microscopy (FLIM)', *Scientific Reports*, 6, p. 28186.

Martin, K. J. *et al.* (2018) 'Accepting from the best donor; analysis of long-lifetime donor fluorescent protein pairings to optimise dynamic FLIM-based FRET experiments', *PLoS ONE*, 13(1), pp. 1–25. doi: 10.1371/journal.pone.0183585.

Martin, R. *et al.* (2016) 'Caspase-mediated cleavage of raptor participates in the inactivation of mTORC1 during cell death', *Cell Death Discovery*, 2(16024), pp. 1-11. doi: 10.1038/cddiscovery.2016.24.

Martin, T. D. *et al.* (2014) 'Ral and Rheb GTPase Activating Proteins Integrate mTOR and GTPase Signaling in Aging, Autophagy, and Tumor Cell Invasion', *Molecular Cell*, 53(2), pp. 209–220. doi: 10.1016/j.molcel.2013.12.004.

Masters, B. and So, P. (2001) 'Confocal microscopy and multi-photon excitation microscopy of human skin in vivo', *Optics Express*, 8(1), pp. 2–10. doi: 10.1364/OE.8.000002.

Mastop, M. *et al.* (2017) 'Characterization of a spectrally diverse set of fluorescent proteins as FRET acceptors for mTurquoise2', *Scientific Reports*, 7(1), p. 11999. doi: 10.1038/s41598-017-12212-x.

Meyer-Almes, F.-J. (2017) 'Fluorescence Lifetime based Bioassays', *Methods and Applications in Fluorescence*. IOP Publishing, 5, pp. 1–31. doi: 10.1088/2050-6120/aa7c7a.

Miller, D. S., Fricker, G. and Drewe, J. (1997) 'p -Glycoprotein-Mediated Transport of a Fluorescent Rapamycin Derivative in Renal Proximal Tubule 1', *The Journal of Pharmacology and Experimental Therapeutics*, 282(1), pp. 440–444.

Minsky, M. (1988) 'Memoir on inventing the confocal scanning microscope', *Scanning*, 10(4), pp. 128–138. doi: 10.1002/sca.4950100403.

Mori, C. *et al.* (2013) 'Over-expression of ATR causes autophagic cell death', *Genes to Cells*, 18(4), pp. 278–287. doi: 10.1111/gtc.12034.

Mukhopadhyay, S. *et al.* (2016) 'The Enigma of Rapamycin Dosage', *Molecular Cancer Therapeutics*, 15(3), pp. 347–353. doi: 10.1158/1535-7163.MCT-15-0720.

Murakoshi, H. *et al.* (2015) 'A dark green fluorescent protein as an acceptor for measurement of Förster resonance energy transfer', *Scientific Reports*, 5, p. 15334. doi: 10.1038/srep15334.

Murata, K. and Wolf, M. (2018) 'Cryo-electron microscopy for structural analysis of dynamic biological macromolecules', *Biochimica et Biophysica Acta - General Subjects*. Elsevier, 1862(2), pp. 324–334. doi: 10.1016/j.bbagen.2017.07.020.

Needham, S. R. *et al.* (2016) 'EGFR oligomerization organizes kinase-active dimers into competent signalling platforms', *Nature Communications*, 7(13307), pp. 1-14.

Nettleship, J. E. *et al.* (2010) 'Recent advances in the production of proteins in insect and mammalian cells for structural biology', *Journal of Structural Biology*, 172(1), pp. 55–65. doi: 10.1016/j.jsb.2010.02.006.

Nienhaus, K. and U Nienhaus, G. (2014) 'Fluorescent proteins for live-cell imaging with super-resolution', *Chemical Society Reviews*, 43(4), pp. 1088–1106. doi: 10.1039/c3cs60171d.

Nifosı, R. and Yi, L. (2007) 'Origin of the Anomalous Two-Photon Absorption in Fluorescent Protein DsRed', *The Journal of Physical Chemistry B*, 111(3), pp. 505–507.

Niwa, H. *et al.* (2014) 'Crystal structures of the S6K1 kinase domain in complexes with inhibitors', *Journal of structural and functional genomics*, 15(3), pp. 153–164. doi: 10.1007/s10969-014-9188-8.

Nojima, H. *et al.* (2003) 'The mammalian target of rapamycin (mTOR) partner, raptor, binds the mTOR substrates p70 S6 kinase and 4E-BP1 through their TOR signaling (TOS) motif', *Journal of Biological Chemistry*, 278(18), pp. 15461–15464. doi: 10.1074/jbc.C200665200.

O'Connor, D. V and Phillips, D. (1984) 'Time-Correlated Single Photon Counting, Time-Correlated Single Photon Counting', *Acedemic Press.* doi: http://dx.doi.org/10.1016/B978-0-12-524140-3.50001-0.

Ong, P. S. *et al.* (2016) 'Judicious Toggling of mTOR Activity to Combat Insulin Resistance and Cancer: Current Evidence and Perspectives', *Frontiers in Pharmacology*, 7, pp. 1-27. doi: 10.3389/fphar.2016.00395.

Oshiro, N. *et al.* (2004) 'Dissociation of raptor from mTOR is a mechanism of rapamycin-induced inhibition of mTOR function', *Genes to Cells*, 9(4), pp. 359–366. doi: 10.1111/j.1356-9597.2004.00727.x.

Oshiro, N. *et al.* (2007) 'The proline-rich Akt substrate of 40 kDa (PRAS40) is a physiological substrate of mammalian target of rapamycin complex 1', *Journal of Biological Chemistry*, 282(28), pp. 20329–20339. doi: 10.1074/jbc.M702636200.

Osz-Papai, J. *et al.* (2015) 'Insect cells-baculovirus system for the production of difficult to express proteins.', in *Methods in Molecular Biology*, pp. 181–205. doi: 10.1007/978-1-4939-2205-5_10.

Pardo, O. E. and Seckl, M. J. (2013) 'S6K2: The Neglected S6 Kinase Family Member.', *Frontiers in Oncology*, 3(191), pp. 1-11. doi: 10.3389/fonc.2013.00191.

Park, E. Y., Abe, T. and Kato, T. (2008) 'Improved expression of fusion protein using a cysteine- protease- and chitinase-deficient Bombyx mori (silkworm) multiple nucleopolyhedrovirus bacmid in silkworm larvae.', *Biotechnology and Applied Biochemistry*, 49(Pt 2), pp. 135–140. doi: 10.1042/BA20070098.

Park, I.-H. *et al.* (2002) 'Regulation of ribosomal S6 kinase 2 by mammalian target of rapamycin.', *The Journal of Biological Chemistry*, 277(35), pp. 31423–31429. doi: 10.1074/jbc.M204080200.

Parmigiani, A. *et al.* (2014) 'Sestrins inhibit mTORC1 kinase activation through the GATOR complex.', *Cell reports*, 9(4), pp. 1281–1291. doi: 10.1016/j.celrep.2014.10.019.

Pedersen, M., Carmosino, M. and Forbush, B. (2008) 'Intramolecular and intermolecular fluorescence resonance energy transfer in fluorescent protein-tagged Na-K-Cl cotransporter (NKCC1): sensitivity to regulatory conformational change and cell volume.', *The Journal of Biological Chemistry*, 283(5), pp. 2663–2674. doi: 10.1074/jbc.M708194200.

Periasamy, A. *et al.* (1996) 'Time-resolved fluorescence lifetime imaging microscopy using a picosecond pulsed tunable dye laser system', *Review of Scientific Instruments*, 67(10), pp. 3722–3731. doi: 10.1063/1.1147139.

Peter, M. *et al.* (2005) 'Multiphoton-FLIM quantification of the EGFP-mRFP1 FRET pair for localization of membrane receptor-kinase interactions', *Biophysical Journal*. Elsevier, 88(2), pp. 1224–1237. doi: 10.1529/biophysj.104.050153.

Pike, K. G. *et al.* (2013) 'Optimization of potent and selective dual mTORC1 and mTORC2 inhibitors: The discovery of AZD8055 and AZD2014', *Bioorganic and Medicinal Chemistry Letters*, 23(5), pp. 1212–1216. doi: 10.1016/j.bmcl.2013.01.019.

Piston, D. W. and Kremers, G. J. (2007) 'Fluorescent protein FRET: the good, the bad and the ugly', *Trends in Biochemical Sciences*, 32(9), pp. 407–414. doi: 10.1016/j.tibs.2007.08.003.

Planck, M. (1900) 'On the Theory of the Energy Distribution Law of the Normal Spectrum', *Verhandlungen der Deutschen Physikalischen Gesellschaft*, 2(237), pp. 1–8.

Ploem, J. S. (1967) 'The use of a vertical illuminator with interchangeable dichroic mirrors for fluorescence microscopy with incident light', *Z. Wiss. Mikrosk.* Germany, 68(3), pp. 129–142.

Powles, T. *et al.* (2016) 'Platinum Priority – Renal Disease A Randomised Phase 2 Study of AZD2014 Versus Everolimus in Patients with VEGF-Refractory Metastatic Clear Cell Renal Cancer', *European Urology*, 69(3), pp. 450–456. doi: 10.1016/j.eururo.2015.08.035.

Prelich, G. (2012) 'Gene Overexpression: Uses, Mechanisms, and Interpretation', *Genetics*, 190(3), pp. 841–854. doi: 10.1534/genetics.111.136911.

Prendergast, F. G. and Manni, K. G. (1978) 'Chemical and Physical Properties of Aequorin and the Green Fluorescent Protein Isolated from Aequorea forskilea', *Biochemistry*, 17(17), pp. 3448–3453. doi: Doi 10.1021/Bi00610a004.

Qian, S. B. *et al.* (2010) 'mTORC1 links protein quality and quantity control by sensing chaperone availability', *Journal of Biological Chemistry*, 285(35), pp. 27385–27395. doi: 10.1074/jbc.M110.120295.

Qin, J. *et al.* (2015) 'Development of organometallic S6K1 inhibitors', *Journal of Medicinal Chemistry*, 58(1), pp. 305–314. doi: 10.1021/jm5011868.

Rahman, A. and Haugh, J. M. (2017) 'Kinetic modeling and analysis of the Akt/mechanistic target of rapamycin complex 1 (mTORC1) signaling axis reveals cooperative, feedforward regulation', *Journal of Biological Chemistry*, 292(7), pp. 2866–2872. doi: 10.1074/jbc.M116.761205.

Ratz, M. *et al.* (2015) 'CRISPR/Cas9-mediated endogenous protein tagging for RESOLFT super-resolution microscopy of living human cells.', *Scientific reports*, 5, p. 9592. doi: 10.1038/srep09592.

Reinhard, C. *et al.* (1994) 'Nuclear localization of p85s6k: functional requirement for entry into S phase.', *The EMBO journal*, 13(7), pp. 1557–65.

Rekas, A. *et al.* (2002) 'Crystal structure of venus, a yellow fluorescent protein with improved maturation and reduced environmental sensitivity', *Journal of Biological Chemistry*, 277(52), pp. 50573–50578. doi: 10.1074/jbc.M209524200.

Rhoads, J. M. *et al.* (2008) 'Arginine stimulates cdx2-transformed intestinal epithelial cell migration via a mechanism requiring both nitric oxide and phosphorylation of p70 S6 kinase.', *The Journal of nutrition*, 138(9), pp. 1652–1657. doi: 138/9/1652 [pii].

Richter, K. N. *et al.* (2017) 'Glyoxal as an alternative fixative to formaldehyde in immunostaining and super-resolution microscopy', *EMBO Journal*, 37(1), pp. 139–159. doi: 10.15252/embj.201695709.

Riedl, A. *et al.* (2016) 'Comparison of cancer cells in 2D vs 3D culture reveals differences in AKT – mTOR – S6K signaling and drug responses', *Journal of Cell Science*, 130(1), pp. 203–218. doi: 10.1242/jcs.188102.

Robinson, L. C. and Marchant, J. S. (2005) 'Improved "optical highlighter" probes derived from discosoma red fluorescent protein', *Biophysical Journal*, 88(2), pp. 1444–1457. doi: 10.1529/biophysj.104.045617.

Rodriguez, E. A. *et al.* (2017) 'The Growing and Glowing Toolbox of Fluorescent and Photoactive Proteins', *Trends in Biochemical Sciences*, 42(2), pp. 111–129. doi: 10.1016/j.tibs.2016.09.010.

Rodrik-Outmezguine, V. S. *et al.* (2016) 'Overcoming mTOR resistance mutations with a new-generation mTOR inhibitor', *Nature*, 534(7606), pp. 272–276. doi: 10.1038/nature17963.

Rohrmann, G. F. (2013) 'Chapter 12 : The AcMNPV genome : Gene content , conservation , and function', *Baculovirus Molecular Biology*, 113. 3rd Edition.

Rong, L. *et al.* (2008) 'Control of eIF4E cellular localization by eIF4E-binding proteins, 4E-BPs', *RNA*, 14(7), pp. 1318–1327. doi: 10.1261/rna.950608.

Rose, A. S. and Hildebrand, P. W. (2015) 'NGL Viewer: A web application for molecular visualization', *Nucleic Acids Research*, 43(W1), pp. W576–W579. doi: 10.1093/nar/gkv402.

Rosner, M. and Hengstschläger, M. (2011) 'Nucleocytoplasmic localization of p70 S6K1, but not of its isoforms p85 and p31, is regulated by TSC2/mTOR', *Oncogene*, 30(44), pp. 4509–4522. doi: 10.1038/onc.2011.165.

Rosner, M., Schipany, K. and Hengstschläger, M. (2012) 'P70 S6K1 nuclear localization depends on its mTOR-mediated phosphorylation at T389, but not on its kinase activity towards S6', *Amino Acids*, 42(6), pp. 2251–2256. doi: 10.1007/s00726-011-0965-4.

Roux, P. P. *et al.* (2007) 'RAS/ERK signaling promotes site-specific ribosomal protein S6 phosphorylation via RSK and stimulates cap-dependent translation', *Journal of Biological Chemistry*, 282(19), pp. 14056–14064. doi: 10.1074/jbc.M700906200.

Rutkowska, A. *et al.* (2016) 'A Modular Probe Strategy for Drug Localization, Target Identification and Target Occupancy Measurement on Single Cell Level', *ACS Chemical Biology*. American Chemical Society, 11(9), pp. 2541–2550. doi: 10.1021/acschembio.6b00346.

Sabatini, D. M. *et al.* (1994) 'RAFT1: A mammalian protein that binds to FKBP12 in a rapamycin-dependent fashion and is homologous to yeast TORs', *Cell*, 78(1), pp. 35–43. doi: 10.1016/0092-8674(94)90570-3.

Sabers, C. J. *et al.* (1995) 'Isolation of a protein target of the FKBP12-rapamycin complex in mammalian cells', *Journal of Biological Chemistry*, 270(2), pp. 815–822. doi: 10.1074/jbc.270.2.815.

Salomon, I., Janssen, H. and Neefjes, J. (2010) 'Mechanical forces used for cell fractionation can create hybrid membrane vesicles', *International Journal of Biological Sciences*, 6(7), pp. 649–654. doi: 10.7150/ijbs.6.649.

Sancak, Y. *et al.* (2007) 'PRAS40 Is an Insulin-Regulated Inhibitor of the mTORC1 Protein Kinase', *Molecular Cell*, 25(6), pp. 903–915. doi: 10.1016/j.molcel.2007.03.003.

Sancak, Y. *et al.* (2008) 'The rag GTPases bind raptor and mediate amino acid signaling to mTORC1', *Science*, 320(5882), pp. 1496–1501. doi: 10.1126/science.1157535.

Sato, T. *et al.* (2009) 'Specific activation of mTORC1 by Rheb G-protein in vitro involves enhanced recruitment of its substrate protein', *Journal of Biological Chemistry*, 284(19), pp. 12783–12791. doi: 10.1074/jbc.M809207200.

Sauer, M., Hofkens, J. and Enderlein, J. (2011) 'Basic Principles of Fluorescence Spectroscopy', in *Handbook of Fluorescence Spectroscopy and Imaging*. Wiley-Blackwell, pp. 1–30. doi: 10.1002/9783527633500.ch1.

Saxton, R. A. and Sabatini, D. M. (2017) 'mTOR Signaling in Growth, Metabolism, and Disease', *Cell*, 8(168), pp. 960–976. doi: 10.1016/j.cell.2017.02.004.

Say, Y. and Hooper, N. M. (2007) 'Contamination of nuclear fractions with plasma membrane lipid rafts', *Proteomics*, 7, pp. 1059–1064. doi: 10.1002/pmic.200600849.

Schalm, S. S. *et al.* (2003) 'TOS Motif-Mediated Raptor Binding Regulates 4E-BP1 Multisite Phosphorylation and Function', *Current Biology*, 13(10), pp. 797–806. doi: 10.1016/S.

Schalm, S. S. and Blenis, J. (2002) 'Identification of a conserved motif required for mTOR signaling', *Current Biology*, 12(8), pp. 632–639. doi: 10.1016/S0960-9822(02)00762-5.

Schalm, S. S., Tee, A. R. and Blenis, J. (2005) 'Characterization of a conserved C-terminal motif (RSPRR) in ribosomal protein S6 kinase 1 required for its mammalian target of rapamycin-dependent regulation', *Journal of Biological Chemistry*, 280(12), pp. 11101–11106. doi: 10.1074/jbc.M413995200.

Scherer, K. M. *et al.* (2015) 'Three-dimensional imaging and uptake of the anticancer drug combretastatin in cell spheroids and photoisomerization in gels with multiphoton excitation.', *Journal of Biomedical Optics*, 20(7), p. 78003. doi: 10.1117/1.JBO.20.7.078003.

Scherer, K. M. *et al.* (2016) 'New Approaches to Photodynamic Therapy from Types I , II and III to Type IV Using One or More Photons', *Anticancer Agents Med Chem*, 17(2), pp. 171–189.

Schmidt, T. and Skerra, A. (2015) 'The Strep-tag System for One-Step Affinity Purification of Proteins from Mammalian Cell Culture', *Methods in Molecular Biology*, 128, pp. 83-95. doi: 10.1007/978-1-4939-2447-9_8.

Schnell, U. *et al.* (2012) 'Immunolabeling artifacts and the need for live-cell imaging', *Nature Methods*, 9(2), pp. 152–158. doi: 10.1038/nmeth.1855.

Schoberer, J. and Botchway, S. W. (2014) 'Investigating Protein–Protein Interactions in the Plant Endomembrane System Using Multiphoton-Induced FRET-FLIM', *Methods Mol Biol*, 1209, pp. 81–95.

Scott, B. L. and Hoppe, A. D. (2015) 'Optimizing fluorescent protein trios for 3-Way FRET imaging of protein interactions in living cells', *Scientific reports*, 5, p. 10270. doi: 10.1038/srep10270.

Scully, A. D. *et al.* (1996) 'Development of a laser-based fluorescence microscope with subnanosecond time resolution', *Journal of fluorescence*, 6(2), pp. 119–125. doi: 10.1007/BF00732051.

Sekar, R. B. and Periasamy, A. (2003) 'Fluorescence resonance energy transfer (FRET) microscopy imaging of live cell protein localizations', *Journal of Cell Biology*, 160(5), pp. 629–633. doi: 10.1083/jcb.200210140.

Selman, C. *et al.* (2009) 'Ribosomal protein S6 kinase 1 signaling regulates mammalian life span', *Science*, 326(5949), pp. 140–144. doi: 10.1126/science.1177221.

Selvin, P. R. (2000) 'The renaissance of fluorescence resonance energy transfer', *Nature Structural Biology*, 7(9), pp. 730–734. doi: 10.1038/78948.

Sfakianos, A. P. *et al.* (2018) 'The mTOR-S6 kinase pathway promotes stress granule assembly', *Cell Death and Differentiation*, pp. 1–15. doi: 10.1038/s41418-018-0076-9.

Shaner, N. C., Steinbach, P. A. and Tsien, R. Y. (2005) 'A guide to choosing fluorescent proteins', *Nat Methods*, 2(12), pp. 905–9.

Shemiakina, I. I. *et al.* (2012) 'A monomeric red fluorescent protein with low cytotoxicity', *Nature Communications*, 3(1204), pp. 1-7.

Sheppard, C. J. R. and Choudhury, A. (1977) 'Image Formation in the Scanning Microscope', *Optica Acta: International Journal of Optics*, 24(10), pp. 1051–1073. doi: 10.1080/713819421.

Shimomura, O., Johnson, F. H. and Saiga, Y. (1962) 'Extraction, purification and properties of aequorin, a bioluminescent', *Journal of cellular and comparative physiology*, 59(3), pp. 223–239. doi: 10.1002/jcp.1030590302.

Shin, J. H. *et al.* (2013) 'TAK1 regulates autophagic cell death by suppressing the phosphorylation of p70 S6 kinase 1', *Scientific Reports*, 3, p. 1561. doi: 10.1038/srep01561.

Singh, A. and Gopinathan, K. P. (1998) 'Confocal microscopy: A powerful technique for biological research', *Current Science*, 74(10), pp. 841–851.

Skorokhod, O. M., Khoruzhenko, A. I. and Filonenko, V. V (2013) 'Adaptor protein TDRD7 is co-localized with ribosomal protein S6 kinases S6K1 and S6K2 in cell lines of different tissue origin', *Biopolymers and Cell*, 29(6), pp. 468–472. doi: 10.7124/bc.00083B.

Snipstad, S. *et al.* (2017) 'Labeling nanoparticles: Dye leakage and altered cellular uptake.', *Cytometry Part A*, 91(8), pp. 760–766. doi: 10.1002/cyto.a.22853.

So, P. T. C. *et al.* (2000) 'Two-Photon Excitation Fluorescence Microscopy', *Annual Review of Biomedical Engineering*, 2(1), pp. 399–429. doi: 10.1146/annurev.bioeng.2.1.399.

Song, X. *et al.* (2014) 'Rapamycin-enhanced mitomycin C-induced apoptotic death is mediated through the S6K1–Bad–Bak pathway in peritoneal carcinomatosis', *Cell Death & Disease*, 5, p. e1281.

Sparks, C. A. and Guertin, D. A. (2010) 'Targeting mTOR: Prospects for mTOR complex 2 inhibitors in cancer therapy', *Oncogene*, 29(26), pp. 3733–3744. doi: 10.1038/onc.2010.139.

Specht, E. A., Braselmann, E. and Palmer, A. E. (2017) 'A Critical and Comparative Review of Fluorescent Tools for Live-Cell Imaging', *Annual Review of Physiology*, 79(1), pp. 93–117. doi: 10.1146/annurev-physiol-022516-034055.

Stocker, H. *et al.* (2003) 'Rheb is an essential regulator of S6K in controlling cell growth in Drosophila', *Nature Cell Biology*, 5(6), pp. 559–565. doi: 10.1038/ncb995.

Stokes, G. G. (1852) 'On the Change of Refrangibility of Light', *Philosophical Transactions of the Royal Society of London*, 142(0), pp. 463–562. doi: 10.1098/rstl.1852.0022.

Straub, M. *et al.* (2000) 'Live cell imaging by multifocal multiphoton microscopy', *European Journal of Cell Biology*, 79(10), pp. 726–734. doi: 10.1078/0171-9335-00105.

Stubbs, C. D. *et al.* (2005) 'The use of time-resolved fluorescence imaging in the study of protein kinase C localisation in cells', *BMC Cell Biology*, 6(1), p. 22. doi: 10.1186/1471-2121-6-22.

Stumpf, W. E. (2005) 'Drug localization and targeting with receptor microscopic autoradiography.', *Journal of pharmacological and toxicological methods*, 51(1), pp. 25–40. doi: 10.1016/j.vascn.2004.09.001.

Stuttfeld, E. *et al.* (2018) 'Architecture of the human mTORC2 core complex', *eLife*, 7, pp. 1–12. doi: 10.7554/eLife.33101.

Subach, F. V and Verkhusha, V. V (2012) 'Chromophore Transformations in Red Fluorescent Proteins', *Chemical Reviews*, 112(7), pp. 4308–4327. doi: 10.1021/cr2001965.

Suhling, K. *et al.* (2015) 'Fluorescence lifetime imaging (FLIM): Basic concepts and some recent developments', *Medical Photonics*, 27, pp. 3-40. doi: 10.1016/j.medpho.2014.12.001.

Sulaimanov, N. *et al.* (2017) 'Understanding the mTOR signaling pathway via mathematical modeling', *Wiley Interdisciplinary Reviews: Systems Biology and Medicine*, 9(4), pp. 1-18. doi: 10.1002/wsbm.1379.

Sun, Y. *et al.* (2010) 'Three-color spectral FRET microscopy localizes three interacting proteins in living cells', *Biophysical Journal*. Biophysical Society, 99(4), pp. 1274–1283. doi: 10.1016/j.bpj.2010.06.004.

Sun, Y., Day, R. N. and Periasamy, A. (2011) 'Investigating protein-protein interactions in living cells using fluorescence lifetime imaging microscopy', *Nat Protoc*, 6(9), pp. 1324–1340. doi: 10.1038/nprot.2011.364.Investigating.

Sunami, T. *et al.* (2010) 'Structural basis of human p70 ribosomal S6 kinase-1 regulation by activation loop phosphorylation', *Journal of Biological Chemistry*, 285(7), pp. 4587–4594. doi: 10.1074/jbc.M109.040667.

Suzuki, K. *et al.* (2010) 'REAP: A two minute cell fractionation method', *BMC Research Notes*, 3(1), p. 294. doi: 10.1186/1756-0500-3-294.

Tabernero, J. *et al.* (2012) 'A phase I, open label, dose escalation study of oral mammalian target of rapamycin inhibitor INK128 administered by intermittent dosing regimens in patients with advanced malignancies', *Cancer Research*, 72(8).

Taipale, M. (2018) 'Two protein / protein interaction assays in one go', *Molecular sytems biology*, 14(e8485), pp. 1–3. doi: 10.15252/msb.20188485.

Takahashi, K. *et al.* (2005) 'Differential membrane localization of ERas and Rheb, two Ras-related proteins involved in the phosphatidylinositol 3-kinase/mTOR pathway', *Journal of Biological Chemistry*, 280(38), pp. 32768–32774. doi: 10.1074/jbc.M506280200.

Tao, R. *et al.* (2015) 'Sestrin 3 protein enhances hepatic insulin sensitivity by direct activation of the mTORC2-Akt signaling.', *Diabetes*, 64(4), pp. 1211–1223. doi: 10.2337/db14-0539.

Tate, C. G., Whiteley, E. and Betenbaugh, M. J. (1999) 'Molecular Chaperones Stimulate the Functional Expression of the Cocaine-sensitive Serotonin Transporter', *Journal of Biological Chemistry* , 274(25), pp. 17551–17558. doi: 10.1074/jbc.274.25.17551 .

Tatebe, H. *et al.* (2017) 'Substrate specificity of TOR complex 2 is determined by a ubiquitin-fold domain of the Sin1 subunit', The journal of *eLife*, e19594. doi: 10.7554/eLife.19594.

Tauer, U. (2002) 'Advantages and risks of multiphoton microscopy in physiology', *Experimental Physiology*, 87(6), pp. 709–714. doi: 10.1113/eph8702464.

Tavares, M. R. *et al.* (2015) 'The S6K protein family in health and disease', *Life Sciences*, 131, pp. 1–10. doi: 10.1016/j.lfs.2015.03.001.

Thomas, J. A. and Tate, C. G. (2014) 'Quality Control in Eukaryotic Membrane Protein Overproduction', *Journal of Molecular Biology*. 426(24), pp. 4139–4154. doi: 10.1016/j.jmb.2014.10.012.

Tipping, W. J. *et al.* (2016) 'Stimulated Raman scattering microscopy: an emerging tool for drug discovery', *Chem. Soc. Rev,* 45, pp. 2075-2089. doi: 10.1039/C5CS00693G.

Treins, C. *et al.* (2010) 'Rictor is a novel target of p70 S6 kinase-1', *Oncogene*, 29(7), pp. 1003–1016. doi: 10.1038/onc.2009.401.

Ustione, A. and Piston, D. W. (2011) 'A simple introduction to multiphoton microscopy', *Journal of Microscopy*, 243(3), pp. 221–226. doi: 10.1111/j.1365-2818.2011.03532.x.

Verveer, P. J. and Hanley, Q. S. (2009) 'Chapter 2 Frequency domain FLIM theory, instrumentation, and data analysis', in *Fret and Flim Techniques*. Laboratory Techniques in Biochemistry and Molecular Biology, pp. 59–94. doi: https://doi.org/10.1016/S0075-7535(08)00002-8.

Vismeh, R. *et al.* (2012) 'Localization and Quantification of Drugs in Animal Tissues by Use of Desorption Electrospray Ionization Mass Spectrometry Imaging', *Analytical Chemistry*. American Chemical Society, 84(12), pp. 5439–5445. doi: 10.1021/ac3011654.

Wallrabe, H. and Periasamy, A. (2005) 'Imaging protein molecules using FRET and FLIM microscopy', *Current Opinion in Biotechnology*, 16(1), pp. 19–27. doi: 10.1016/j.copbio.2004.12.002.

Wang, J. *et al.* (2013) 'Crystal structures of S6K1 provide insights into the regulation mechanism of S6K1 by the hydrophobic motif', *Biochemical Journal*, 454(1), pp. 39–47. doi: 10.1042/BJ20121863.

Wang, L. *et al.* (2007) 'PRAS40 regulates mTORC1 kinase activity by functioning as a direct inhibitor of substrate binding', *Journal of Biological Chemistry*, 282(27), pp. 20036–20044. doi: 10.1074/jbc.M702376200.

Wang, L., Rhodes, C. J. and Lawrence, J. C. (2006) 'Activation of mammalian target of rapamycin (mTOR) by insulin is associated with stimulation of 4EBP1 binding to dimeric mTOR complex 1', *Journal of Biological Chemistry*, 281(34), pp. 24293–24303. doi: 10.1074/jbc.M603566200.

Weinberg, M. A. (2016) 'RES-529: A PI3K/AKT/mTOR pathway inhibitor that dissociates the mTORC1 and mTORC2 complexes', *Anti-Cancer Drugs*, 27(6), pp. 475–487. doi: 10.1097/CAD.0000000000000354.

Herschel W, J. F. (1845) 'On a Case of Superficial Colour Presented by a Homogeneous Liquid Internally Colourless', *Royal Society of London*, 135(1), pp. 143–145. doi: 10.1098/rspl.1843.0039.

Williams, Y. *et al.* (2008) 'Comparison of three cell fixation methods for high content analysis assays utilizing quantum dots.', *Journal of microscopy*, 232(1), pp. 91–98. doi: 10.1111/j.1365-2818.2008.02083.x.

Wilson, T. and Sheppard, C. (1984) *Theory and Practice of Scanning Optical Microscopy*. Academic Press.

Wolfson, R. L. *et al.* (2017) 'KICSTOR recruits GATOR1 to the lysosome and is necessary for nutrients to regulate mTORC1', *Nature*, 543(7645), pp. 438-442. doi: 10.1038/nature21423.

Xie, J., Wang, X. and Proud, C. G. (2016) 'mTOR inhibitors in cancer therapy', *F1000Research*, 5(2078), pp. 1–11. doi: 10.12688/f1000research.9207.1.

Xu, J. *et al.* (2016) 'Mechanistically distinct cancer-associated mTOR activation clusters predict sensitivity to rapamycin', *The Journal of Clinical Investigation*, 126(9), pp. 3527–3539. doi: 10.1172/JCI86120DS1.

Yadav, R. B. *et al.* (2013) 'mTOR direct interactions with Rheb-GTPase and raptor: Sub-cellular localization using fluorescence lifetime imaging', *BMC Cell Biology*. BMC Cell Biology, 14(1), p. 3. doi: 10.1186/1471-2121-14-3.

Yang, H. *et al.* (2013) 'MTOR kinase structure, mechanism and regulation', *Nature*, 497(7448), pp. 217–223. doi: 10.1038/nature12122.

Yang, H. *et al.* (2016) '4.4 Å Resolution Cryo-EM structure of human mTOR Complex 1', *Protein and Cell*, 7(12), pp. 878–887. doi: 10.1007/s13238-016-0346-6.

Yang, H. *et al.* (2017) 'Mechanisms of mTORC1 activation by RHEB and inhibition by PRAS40', *Nature*, 552(7685), pp. 368–373. doi: 10.1038/nature25023.

Yang, H. *et al.* (2018) 'The structure of mTOR complexes at a glance', *Precision Cancer Medicine*, 1(7), pp. 1–8. doi: 10.21037/pcm.2018.07.02.

Yao, Y., Jones, E. and Inoki, K. (2017) 'Lysosomal Regulation of mTORC1 by Amino Acids in Mammalian Cells', *Biomolecules*, 7(3), p. 51. doi: 10.3390/biom7030051.

Yerlikaya, S. *et al.* (2016) 'TORC1 and TORC2 work together to regulate ribosomal protein S6 phosphorylation in Saccharomyces cerevisiae.', *Molecular biology of the cell*, 27(2), pp. 397–409. doi: 10.1091/mbc.E15-08-0594.

Yi, S. A., Han, J. and Han, J. (2016) 'Epigenetic role of nuclear S6K1 in early adipogenesis', *BMB Rep*, 49(8), pp. 401–402. doi: 10.1016/j.molcel.2016.03.011.and.

Yip, C. K. *et al.* (2010) 'Structure of the Human mTOR Complex I and Its Implications for Rapamycin Inhibition', *Molecular Cell*, 38(5), pp. 768–774. doi: 10.1016/j.molcel.2010.05.017.

Yokoyama, N. *et al.* (2000) 'Co-expression of human chaperone Hsp70 and Hsdj or Hsp40 co-factor increases solubility of overexpressed target proteins in insect cells.', *Biochimica et biophysica acta*, 1493(1–2), pp. 119–124.

Yonehara, R. *et al.* (2017) 'Structural basis for the assembly of the Ragulator-Rag GTPase complex', *Nature Communications*, 8(1), p. 1625. doi: 10.1038/s41467-017-01762-3.

Yonezawa, K. *et al.* (2004) 'Raptor, a binding partner of target of rapamycin', *Biochemical and Biophysical Research Communications*, 313(2), pp. 437–441. doi: 10.1016/j.bbrc.2003.07.018.

Zeng, Z. *et al.* (2016) 'MLN0128, a novel mTOR kinase inhibitor, disrupts survival signaling and triggers apoptosis in AML and AML stem/ progenitor cells', *Oncotarget*, 7(34), pp. 55083–55097. doi: 10.18632/oncotarget.10397.

Zhang, X. *et al.* (2002) 'Predominant Nuclear Localization of Mammalian Target of Rapamycin in Normal and Malignant Cells in Culture', *The Journal of Biological Chemistry*, 277(31), pp. 28127–28134. doi: 10.1074/jbc.M202625200.

Zhang, G., Gurtu, V. and Kain, S. R. (1996) 'An enhanced green fluorescent protein allows sensitive detection of gene transfer in mammalian cells', *Biochemical and Biophysical Research Communications*, 227(3), pp. 707–711. doi: 10.1006/bbrc.1996.1573.

Zhang, J. *et al.* (2018) 'The p85 isoform of the kinase S6K1 functions as a secreted oncoprotein to facilitate cell migration and tumor growth', *Science Signaling*, 11(523). doi: 10.1126/scisignal.aao1052.

Zheng, B. *et al.* (2015) 'Pre-clinical evaluation of AZD2014, a novel mTORC1/2 dual inhibitor, against renal cell carcinoma', *Cancer Letters*, 357(2), pp. 468–475. doi: 10.1016/j.canlet.2014.11.012.

Zheng, Y. and Jiang, Y. (2015) 'mTOR Inhibitors at a Glance.', *Molecular and cellular pharmacology*, 7(2), pp. 15–20. doi: 10.1016/j.coviro.2015.09.001.Human.

Zhou, X. *et al.* (2009) 'Rheb controls misfolded protein metabolism by inhibiting aggresome formation and autophagy.', *Proceedings of the National Academy of Sciences of the United States of America*, 106(22), pp. 8923–8928. doi: 10.1073/pnas.0903621106.

Zhou, X. *et al.* (2015) 'Dynamic Visualization of mTORC1 Activity in Living Cells', *Cell Reports*. The Authors, 10(10), pp. 1767–1777. doi: 10.1016/j.celrep.2015.02.031.

Zipfel, W. R. *et al.* (2003) 'Live tissue intrinsic emission microscopy using multiphoton-excited native fluorescence and second harmonic generation', *Proceedings of the National Academy of Sciences*, 100(12), pp. 7075–7080. doi: 10.1073/pnas.0832308100.

Zoncu, R. *et al.* (2011) 'mTORC1 senses lysosomal amino acids through an inside-out mechanism that requires the vacuolar H(+)-ATPase.', *Science,* 334(6056), pp. 678–683. doi: 10.1126/science.1207056.

Appendices

Appendix A

A.1 NucleoSpin® Gel and PCR Clean-up Kit contents

	50 preps
Binding buffer NTI	40 ml
Wash buffer NT3 (concentrate)	25 ml
Elution buffer NE*	13 ml
NucleoSpin® Gel and PCR Clean-up columns	50
Collection tubes (2 ml)	50

* = 5 mM Tris/HCl, pH 8.5

A.2 Quick-Fusion cloning kit contents

	40 reactions
Fusion enzyme	40 µl
5x Fusion buffer	80 µl
Linearized control vector- 2.7 kb	5 µl
Control DNA fragment – 500 bp	5 µl

A.3 Protocol for LB Agar

25 g of LB, plus 20 g of Bactoagar (BD) was prepared in 1 litre of water (Milli-Q) and autoclaved in an autoclave (Rodwell) (15 minutes per cycle at 121ºC with ~8 cycles).

A.4 Protocol for LB

25g of LB (Melford) was prepared in 1 litre of water (Milli-Q) and autoclaved as described above.

A.5 Protocol for LB glycerol

70 ml of LB was mixed with 30 ml of sterile glycerol (Sigma-Aldrich). Glycerol was autoclaved prior to use.

A.6 QIAprep Spin Miniprep kit contents

	50 reactions
QIAprep 2.0 Spin columns	50
Buffer P1	20 ml
Buffer P2	20 ml
Buffer N3	30 ml
Buffer PB	30 ml
Buffer PE (concentrate)	2 x 6 ml
Buffer EB	15 ml
LyseBlue	20 µl
Loading dye	110 µl
RNase A	2 mg
Collection tubes (2 ml)	50

A.7 pOPIN primers

The pOPIN Forward primer is based on the T7 forward priming sequence and is present in most pOPIN vectors. The sequence is shown below:

pOPIN Forward primer	GAC CGA AAT TAA GAC TCA CTA TAG GG
pOPIN NeoRev2 primer	GGA ATG CTC GTC AAG AAG ACA

A.8 QIAGEN Plasmid Plus Maxi kit contents

	25 reactions
QIAGEN Plasmid Plus Spin columns	25
QIAfilter Midi Cartridges	25
Caps for QIAfilter	25
Tube Extenders (20 ml)	25
Collection Tubes (2 ml)	25
Buffer P1	110 ml
Buffer P2	110 ml
Buffer S3	2 x 70 ml
Buffer ETR	25 ml
Buffer BB	70 ml
Buffer PE (concentrate)	6 ml
Buffer EB	15 ml
RNase A	11 mg
LyseBlue	110 µl

A.9 QuikChange Multi Site-Directed Mutagenesis Kit

	30 reactions
QuikChange Multi enzyme blend (2.5 U/µl)	80 U
10 x QuikChange Multi reaction buffer	200 µl
QuikSolution	500 µl
dNTP Mix	30 µl
Dpn 1 restriction enzyme (10 U/µl)	300 U
QuikChange Multi control template (50 ng/ µl)	5 µl
QuikChange Multi control primer mix (100 ng/ µl of each of three primers)	5 µl
XL10-Gold ultracompetent cells	10 x 135 µl
XL10-Gold β-mercaptoethanol mix	2 x 50 µl
pUC18 control plasmid (0.1 ng/µl in TE buffer)	10 µl

A.10 pOPIN vectors

A.10.1 pOPINN-EGFP

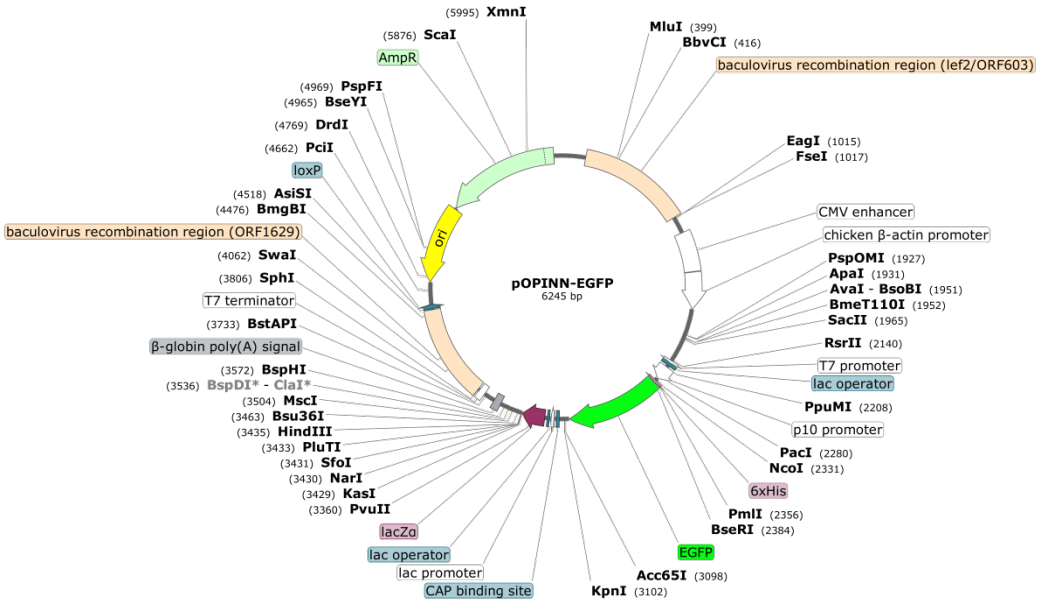

A.10.2 pOPINE-3C-mCherry

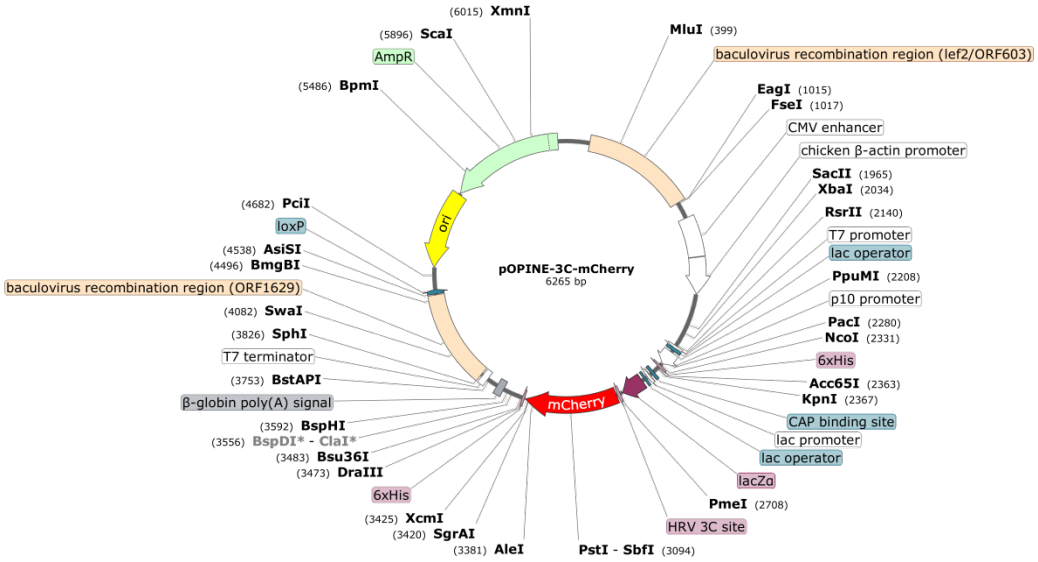

A.10.3 pOPINE-3C-mTurq2

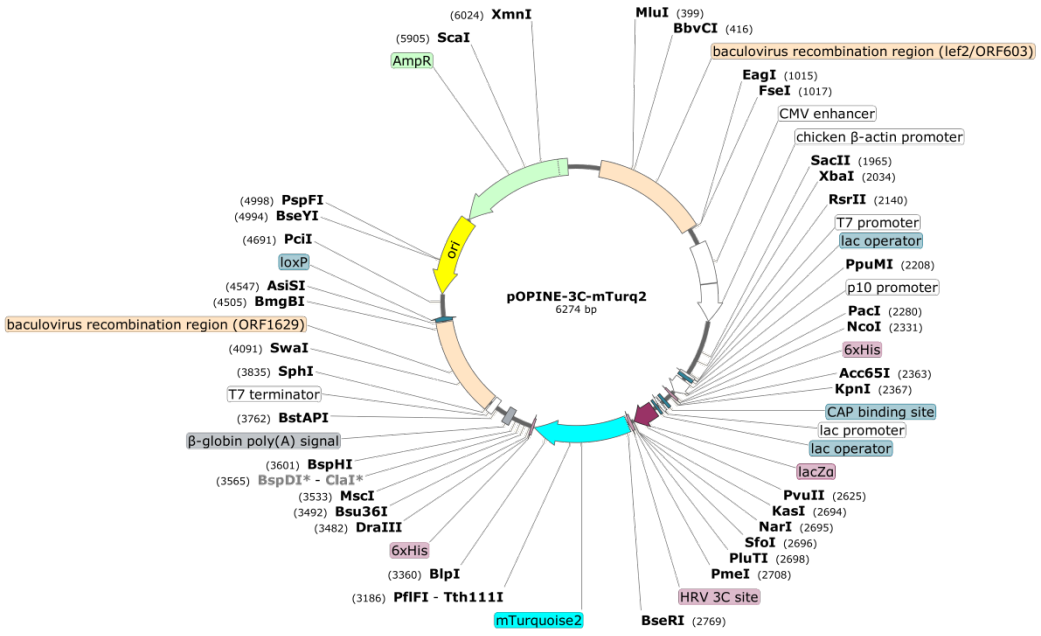

A.10.4 pOPINE-3C-EGFP

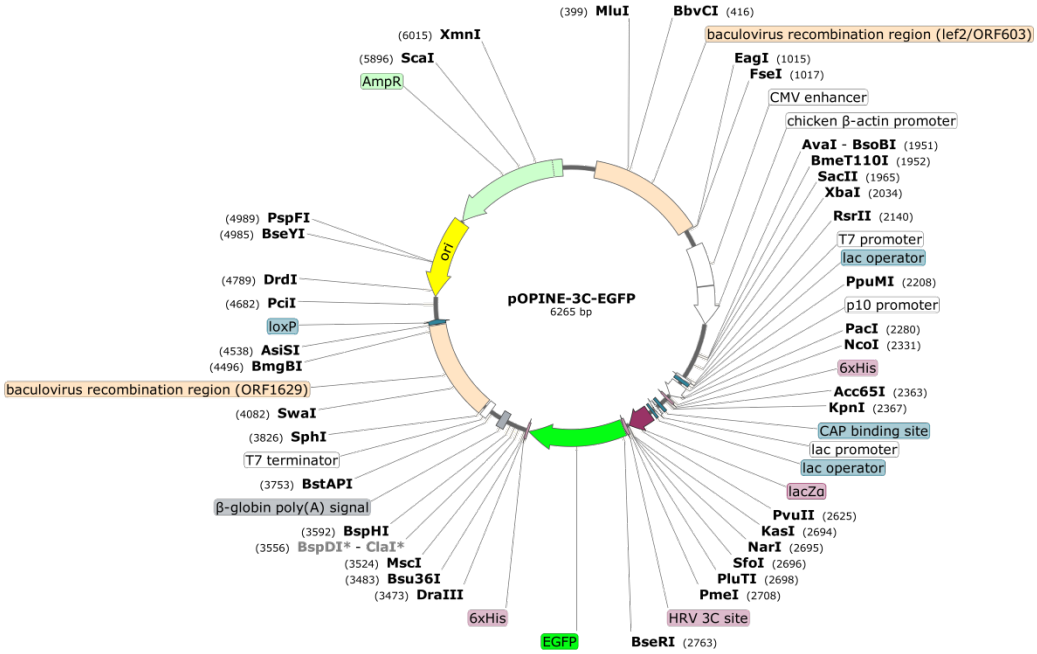

A.10.5 pOPINE-3C-YFP

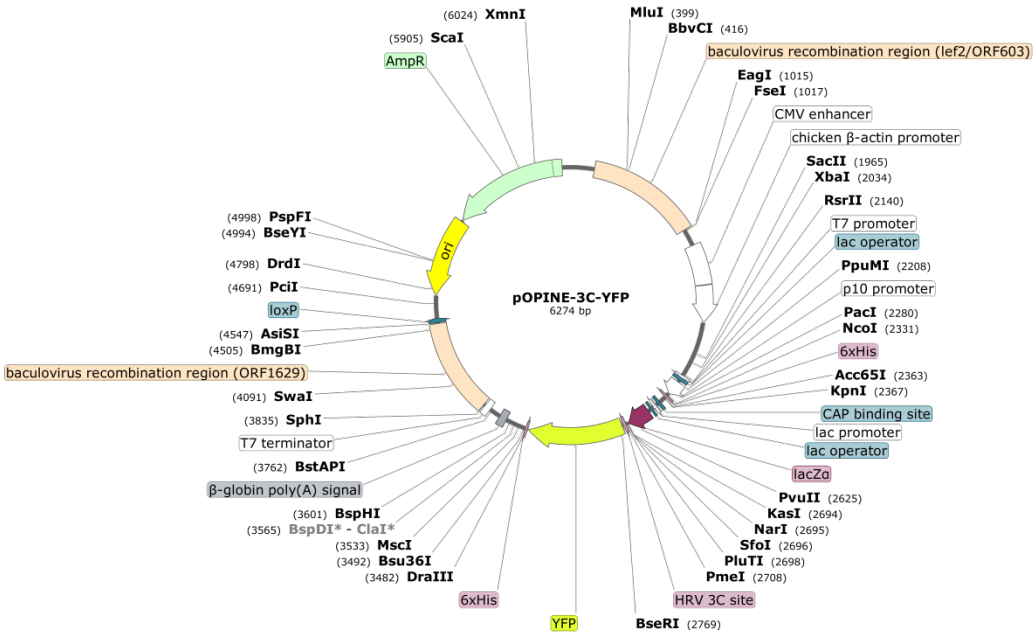

A.10.6 pOPINEneo-3C-2STREP

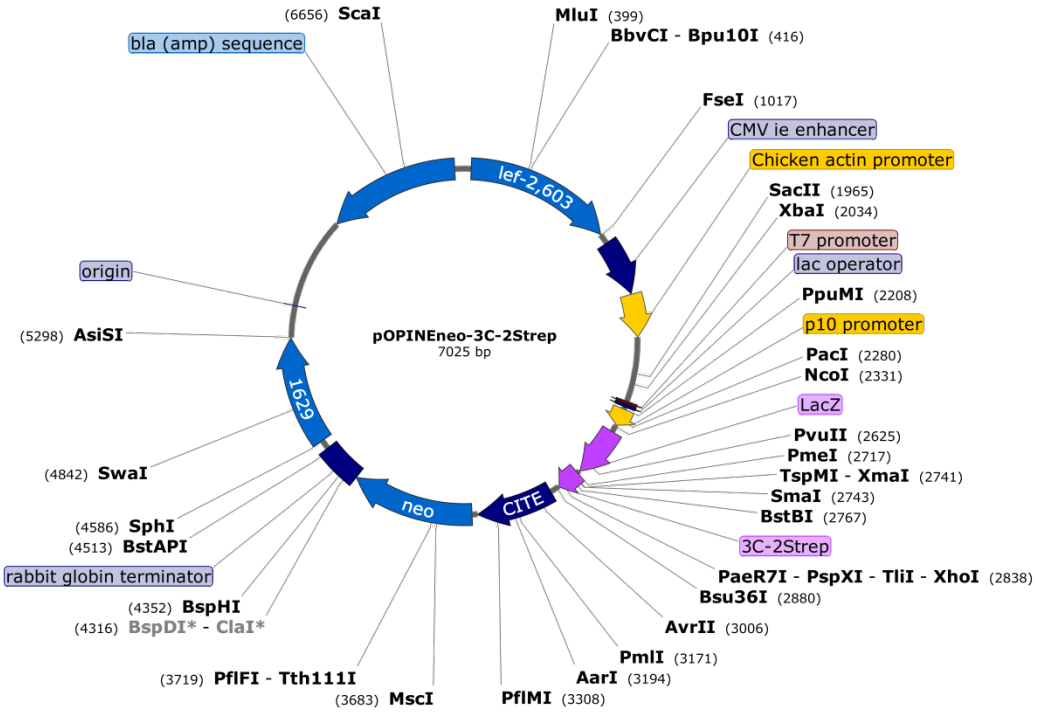

A.10.7 pBAC4x-1

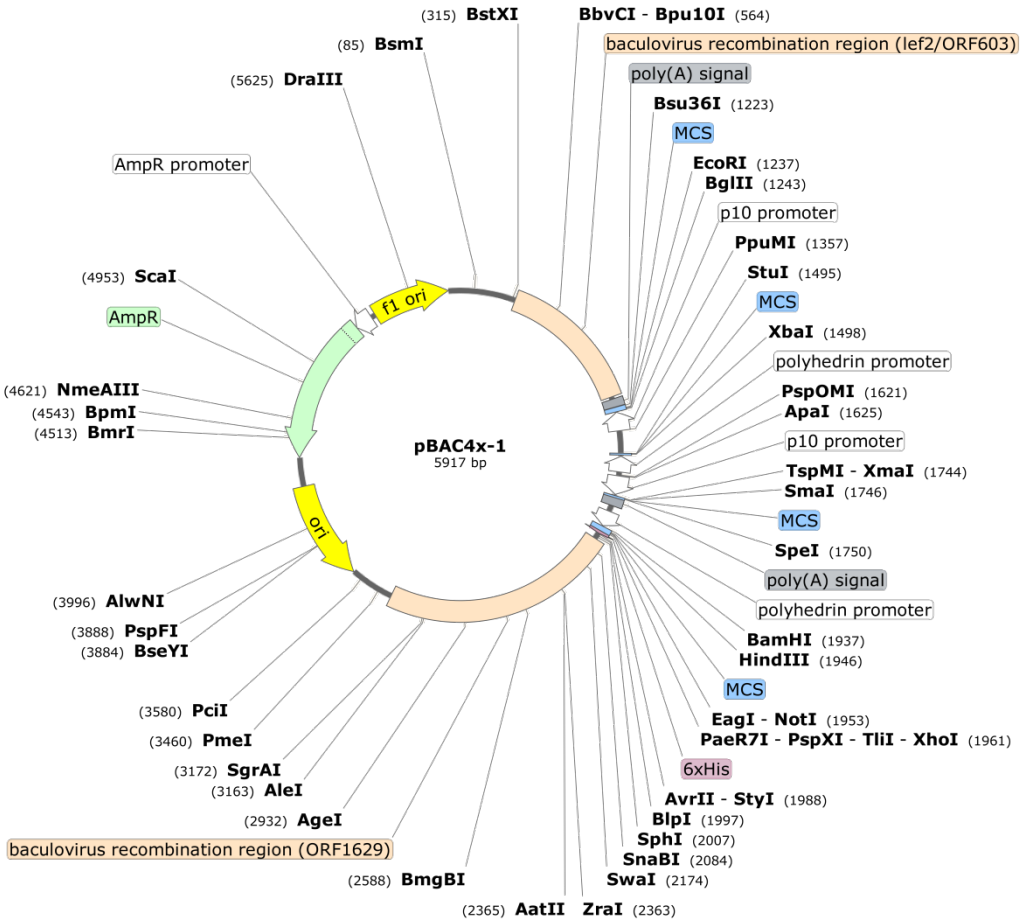

A.11 mLST8 sequence

Optimized Sequence(Optimized Sequence Length:993, GC%:57.89)

CCCGGG
ATGAACACCTCTCCTGGTACTGTGGGCTCAGACCCCGTCATCCTGGCTACCGCTGGTTACGACCACACTGTGCGC
TTCTGGCAGGCTCACTCTGGAATCTGCACCCGTACTGTCCAGCACCAGGACAGCCAGGTGAACGCTCTGGAGGTC
ACTCCTGACCGCTCTATGATCGCTGCCGCTGGATACCAGCACATCCGTATGTACGACCTGAACTCTAACAACCCT
AACCCCATCATCTCATACGACGGTGTGAACAAGAACATCGCCTCAGTCGGATTCCACGAGGACGGAAGGTGGATG
TACACCGGTGGCGAAGACTGCACTGCTAGAATCTGGGACCTGCGCTCCCGTAACCTGCAGTGCCAGAGGATCTTC
CAGGTGAACGCCCCAATCAACTGCGTCTGCCTGCACCCTAACCAAGCTGAGCTGATCGTGGGCGACCAGTCCGGA
GCTATCCACATCTGGGACCTGAAGACTGACCACAACGAACAGCTGATCCCAGAGCCTGAAGTCTCCATCACCAGC
GCCCACATCGACCCCGACGCTTCCTACATGGCCGCTGTGAACAGCACTGGCAACTGCTACGTCTGGAACCTGACC
GGAGGTATCGGAGACGAGGTGACCCAGCTGATCCCCAAGACTAAGATCCCAGCCCACACCCGTTACGCTCTGCAG
TGCAGATTCTCTCCCGACTCAACCCTGCTGGCCACTTGCAGCGCTGACCAGACTTGCAAGATTTGGCGCACCTCC
AACTTCAGCCTGATGACCGAGCTGTCTATCAAGTCAGGAAACCCAGGTGAATCCAGCCGTGGTTGGATGTGGGGC
TGCGCTTTCTCCGGCGACAGCCAGTACATCGTGACTGCCTCTTCAGACAACCTGGCTAGGCTGTGGTGCGTCGAG
ACCGGAGAAATCAAGAGAGAATACGGCGGACACCAGAAGGCCGTGGTCTGCCTGGCTTTCAACGACTCTGTCCTG
GGT
TGAACTAGT

A.12 TBST (1X)

For 1 litre of working solution, 100 ml of TBS stock (10X) was diluted in 899 ml of water (Milli Q) and stirred with a magnetic stirrer for 15 minutes. 1 ml of Tween-20 (Sigma-Aldrich) was added and left to stir for 15 minutes.

To make 10X TBS - 500 mM Tris was made from Trizma base (Sigma-Aldrich) with 1.5 M NaCl in 1 litre of water (Milli Q) and stirred with a magnetic stirrer for 15 minutes. The pH of the solution was adjusted to pH 7.4.

Appendix B

B.1. Western blot analysis of endogenous and overexpressed pS6K1

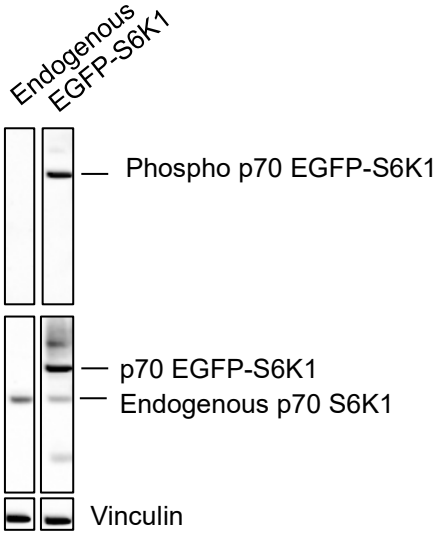

B.2. Co-localisation of S6K1 with Rheb in live cell

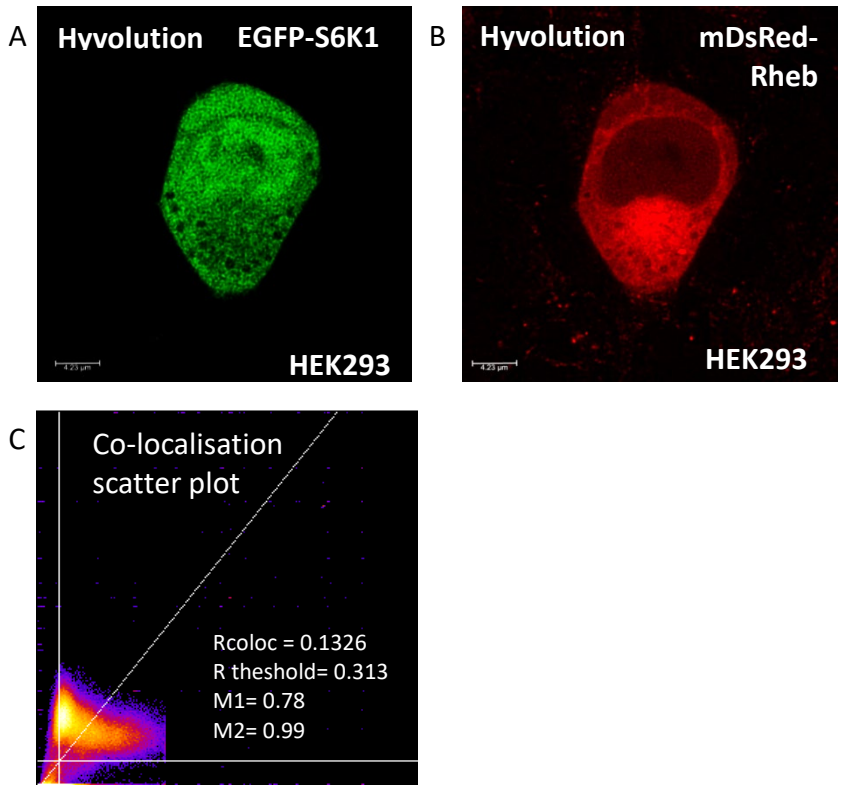

Deconvolved confocal images of A) EGFP-S6K1 with B) mDsRed-Rheb co-expression in live HEK293 cells. C) Co-localisation scatter plot of EGFP-S6K1 and mDsRed-Rheb generated in ImageJ using Co-localisation tool which calculates the thresholds for the co-localisation analysis, the Pearson's correlation (R_{colo}) and Manders coefficients (M1, M2). R_{colo} value close to 1 indicates 100% co-localisation. Scale bar = 10 µm in all images.

B.3 Full length blots for mTORC1 pull-down

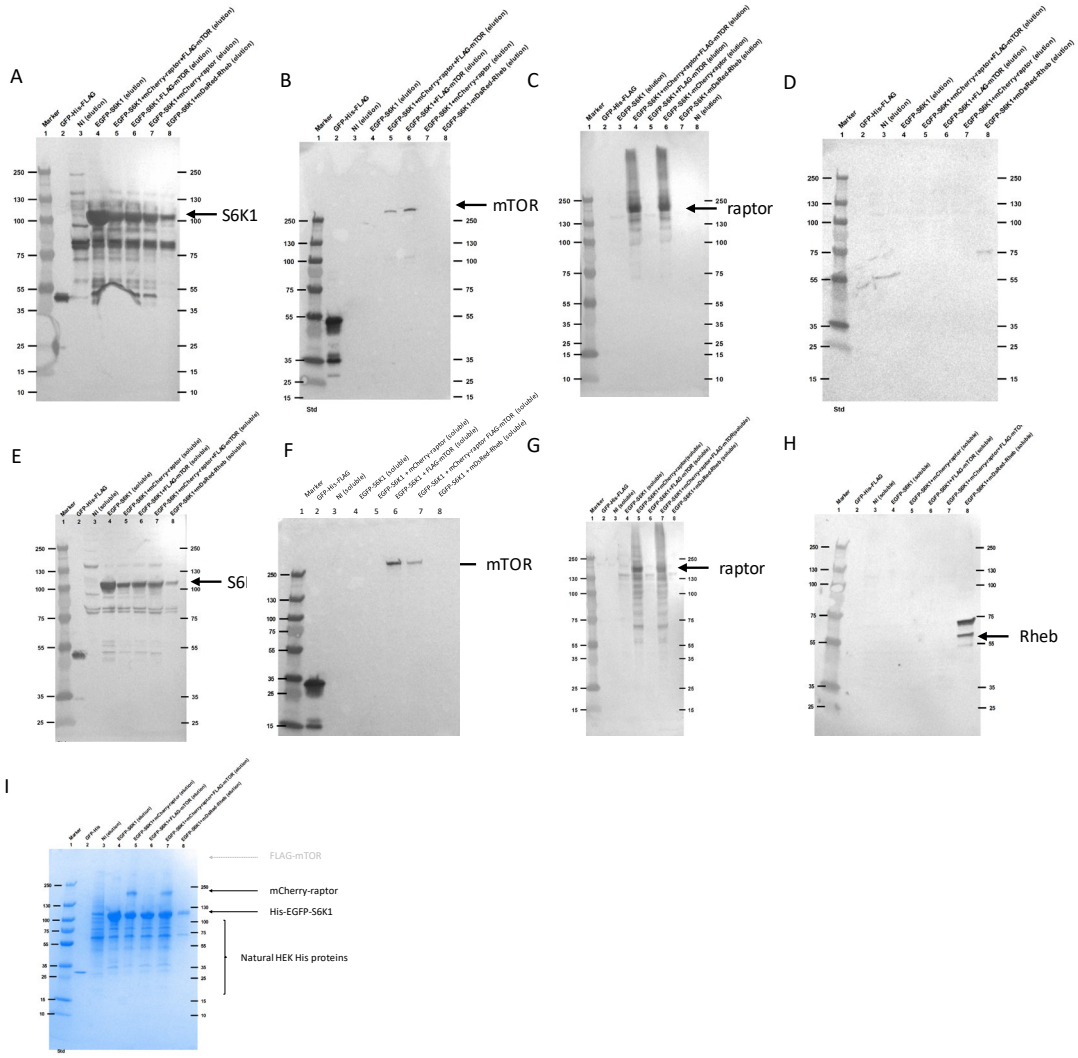

Full lengths gels for Figure 3.15. Western blot of eluted mTORC1 complexes shown for **A** S6K1 using anti-His antibodies. **B** mTOR using anti-FLAG antibodies. **C** raptor using anti-raptor antibodies. **D** Rheb using anti-Rheb antibodies. Western blots of soluble mTORC1 lystates for **E** S6K1 using anti-His. **F** mTOR using anti-FLAG. **G** raptor using anti-raptor. **H** Rheb using anti-Rheb antibodies. **I** Comassie of mTORC1 eluted fractions. Marker, GFP and no transfection (NI) controls are also shown on blots.

B.4 Lifetime comparison of EGFP in live vs fixed HEK293 cells

EGFP only live cells media

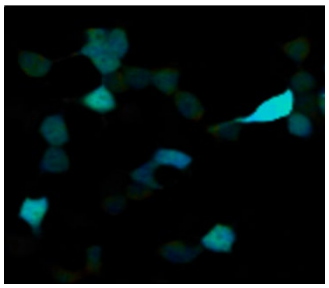

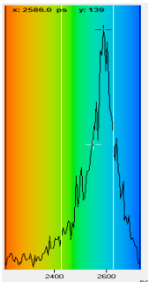

τ_m= 2.6 ns

EGFP only live cells PBS (1X)

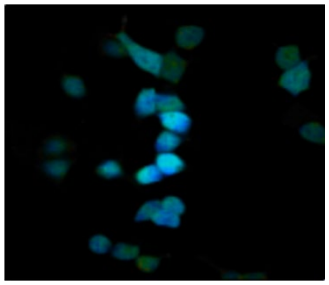

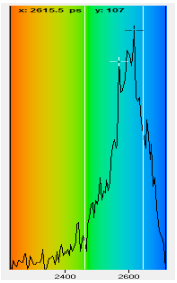

τ_m= 2.6 ns

EGFP only fixed cells PBS

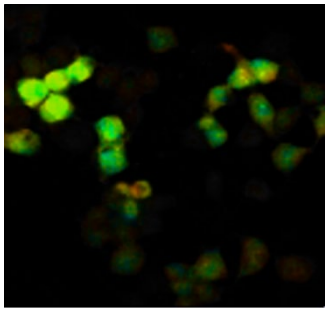

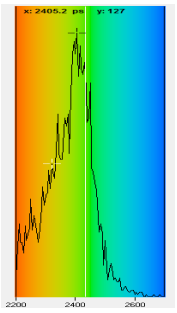

τ_m= 2.4 ns

B.5 High Rheb expression does not lead to correlated phospho-S6K1 levels

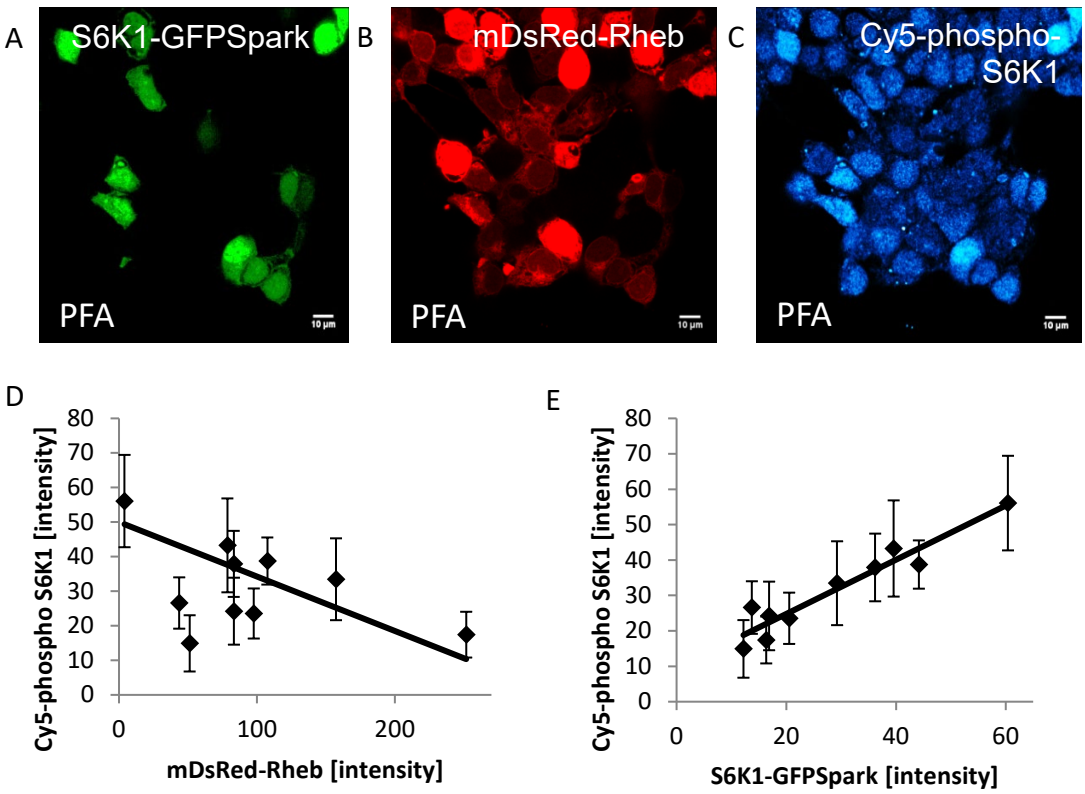

Confocal images of HEK293 cells fixed in PFA, A) S6K1-GFPSpark co-expressed with B) mDsRed-Rheb with C) anti-phopho-S6K1 and Cy5 labelling. D) Graph to show mean intensities of equal regions of interests per cell of mDsRed-Rheb levels plotted against phospho-S6K1 labelled with Cy5. E) Graph to show mean intensities of equal regions of interests per cell of S6K1-GFPSpark levels plotted against phospho-S6K1 labelled with Cy5. Data representative of one of three reproducible independent experiments where the errors shown are standard deviations in intensities of regions of interests (ROIs) encompassing both the nucleus and cytoplasm of each cell. Scale bar = 10 µm in all images.

B.6 Differences in endogenous phospho-S6K1 localisation with various antibodies

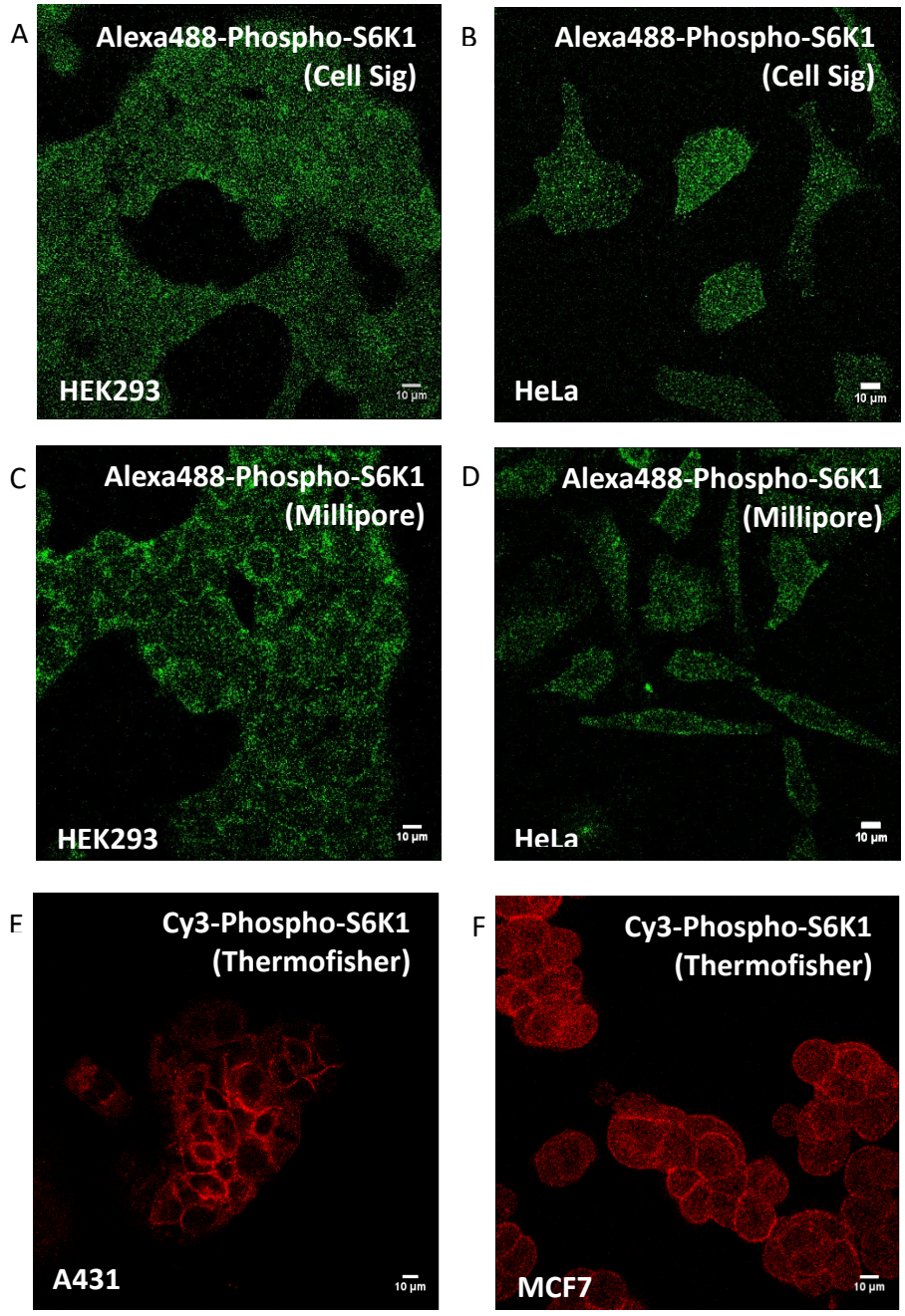

Confocal images of anti-phospho-S6K1 (Cell Signalling) and Alexa 488 labelling in A) HEK293 cells and B) HeLa cells, anti-phospho-S6K1 (Millipore) and Alexa488 labelling in C) HEK293 cells and D) Hela cells, anti-phospho-S6K1 (Thermofisher) and Cy3 labelling in E) A431 cells and F) MCF7 cells. All cells fixed in PFA. Scale bar = 10 µm in all images.

B.7 Immunofluorescence secondary antibody controls

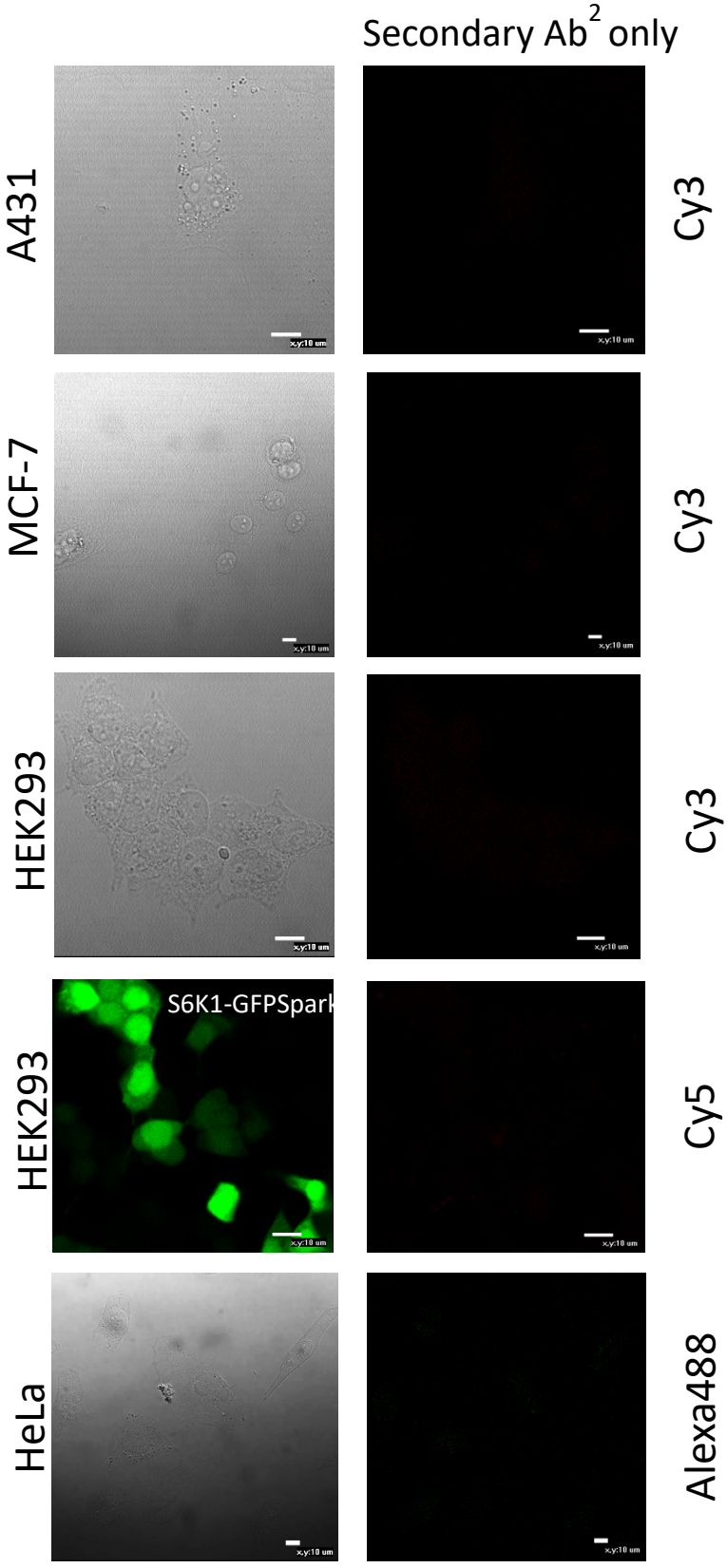

B.8 Endogenous phospho-S6K1 may be mostly nuclear and induced by Rheb overexpression

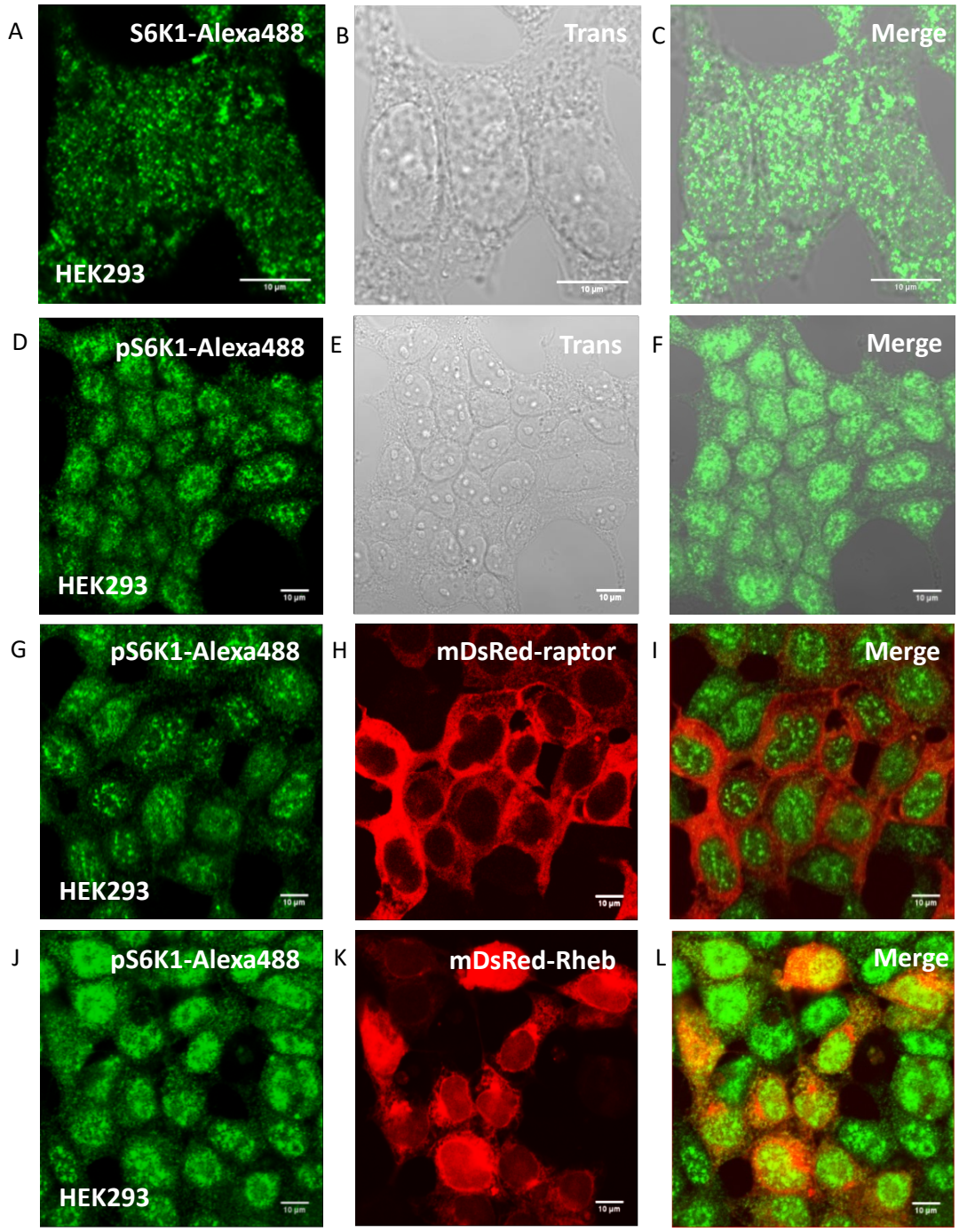

A) confocal image of fixed HEK293 cells labelled with phospho-S6K1 and Alexa 488 antibodies. B) trans white light image. C) merged image. D) fixed HEK293 cells labelled with anti-phospho S6K1 and Alexa 488 antibodies. E) trans white light image. F) merged image. G) mDsRed-raptor expressing fixed cells labelled with anti-phospho S6K1 and Alexa 488 antibodies. H) mDsRed-raptor expression. I) merged image. J) mDsRed-Rheb expressing

fixed cells labelled with anti-phospho S6K1 and Alexa 488 antibodies. K) mDsRed-Rheb expression. L) merged image. Scale bar = 10 µm in all images.

B.9 Quantifying endogenous phospho-S6K1 with overexpressed Rheb

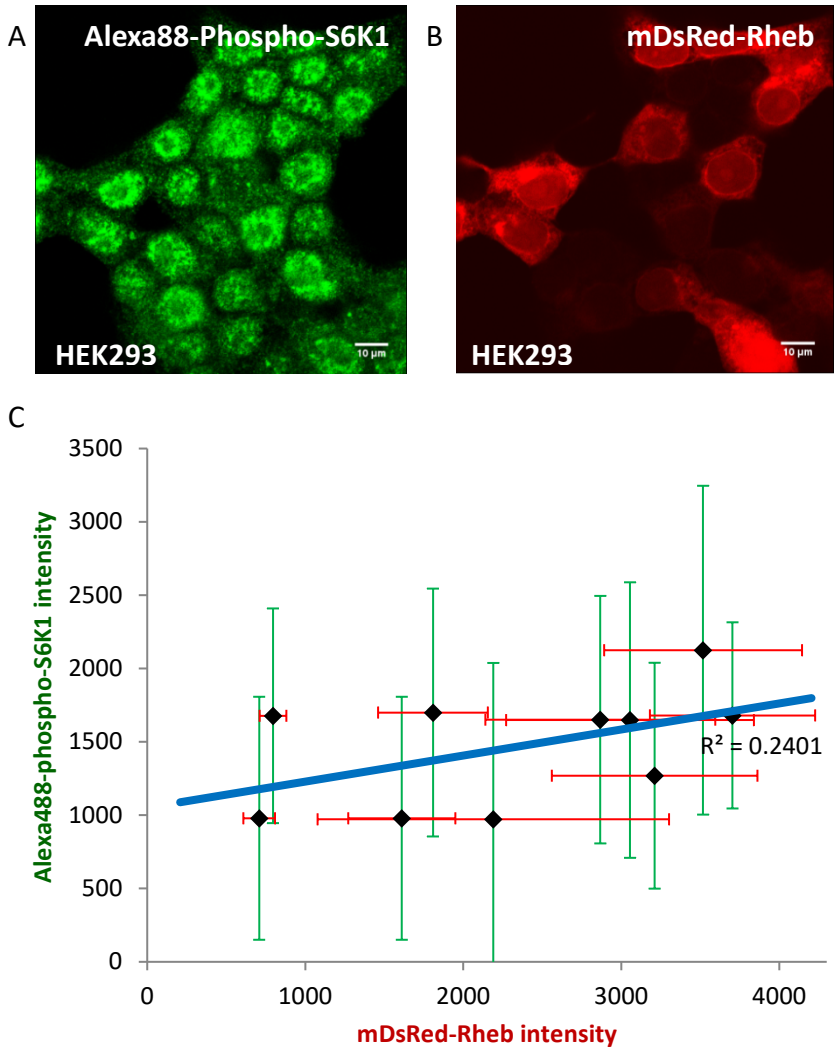

Confocal images of PFA fixed HEK293 cells labelled for A) phospho-S6K1 and Alexa488 staining with B) mDsRed-Rheb co-expression. C) graph showing phospho-S6K1 intensities per cell plotted against respective Rheb intensities. Data representative of one of three reproducible independent experiments where the errors shown are standard deviations in intensities of regions of interests (ROIs) encompassing both the nucleus and cytoplasm of each cell in both x and y as intensity levels vary in ROIs . Scale bar = 10 µm in all images.

B.10 EGFP-mTOR FRET-FLIM interaction with mCherry-raptor

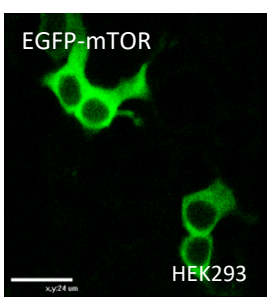

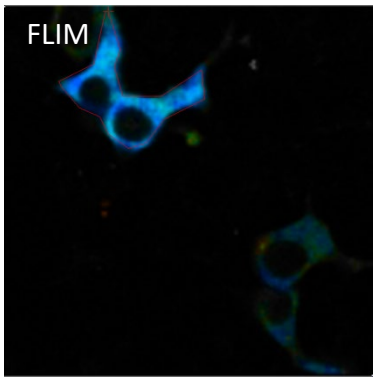

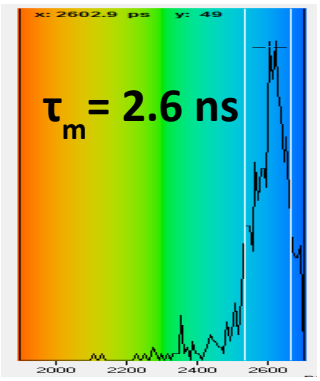

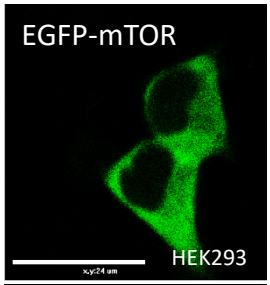

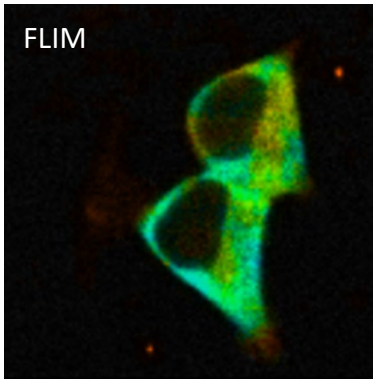

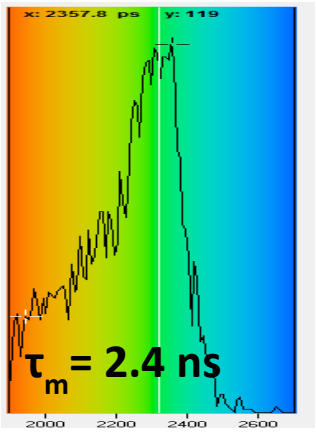

Appendix C

C.1 UV-VIS spectrum of DMSO only

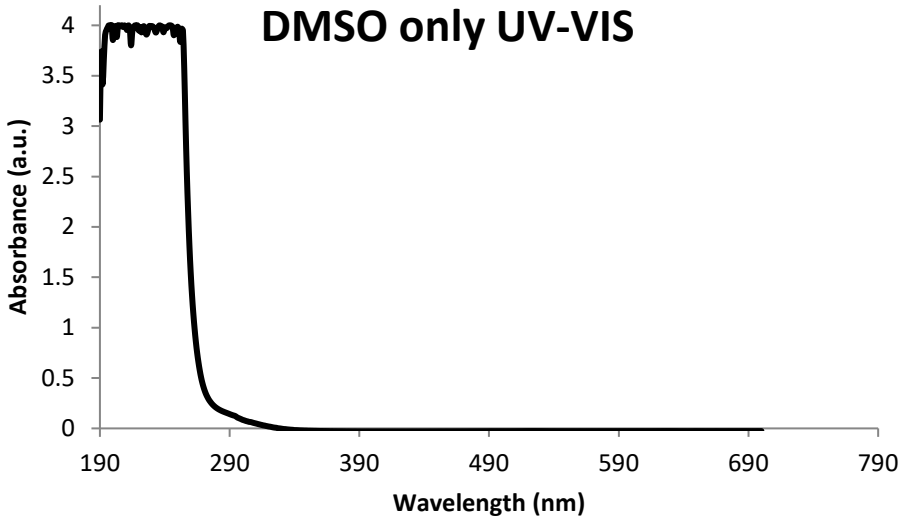

C.2 Molar extinction coefficients (ε) of AZD2014, INK128 and rapamycin

A

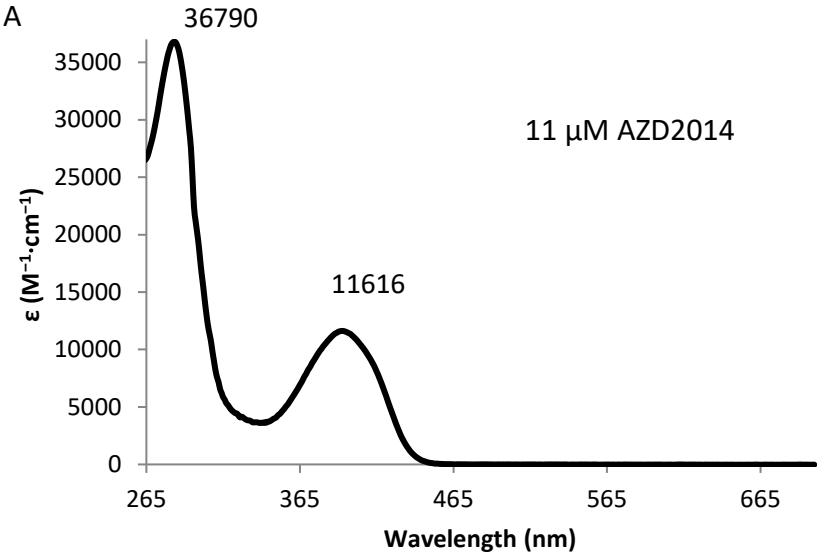

B

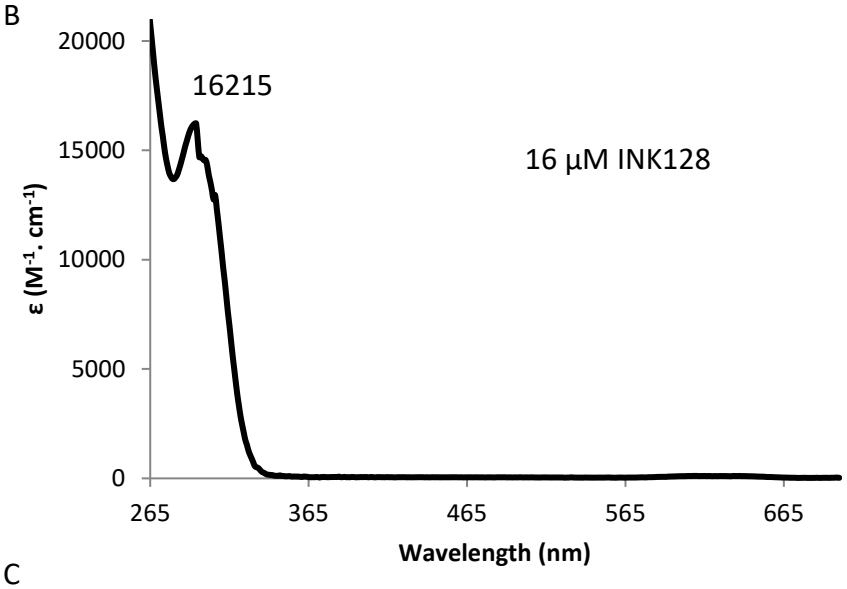

C

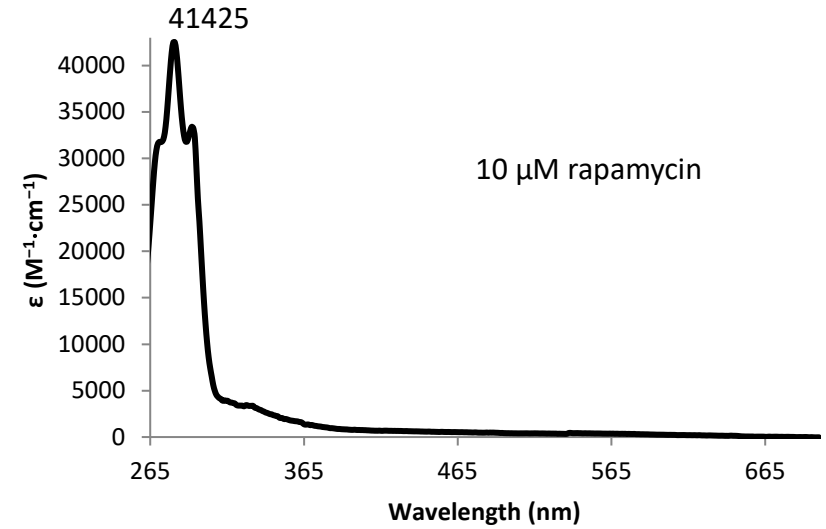

C.3 Excitation spectra of AZD2014 in various solvents

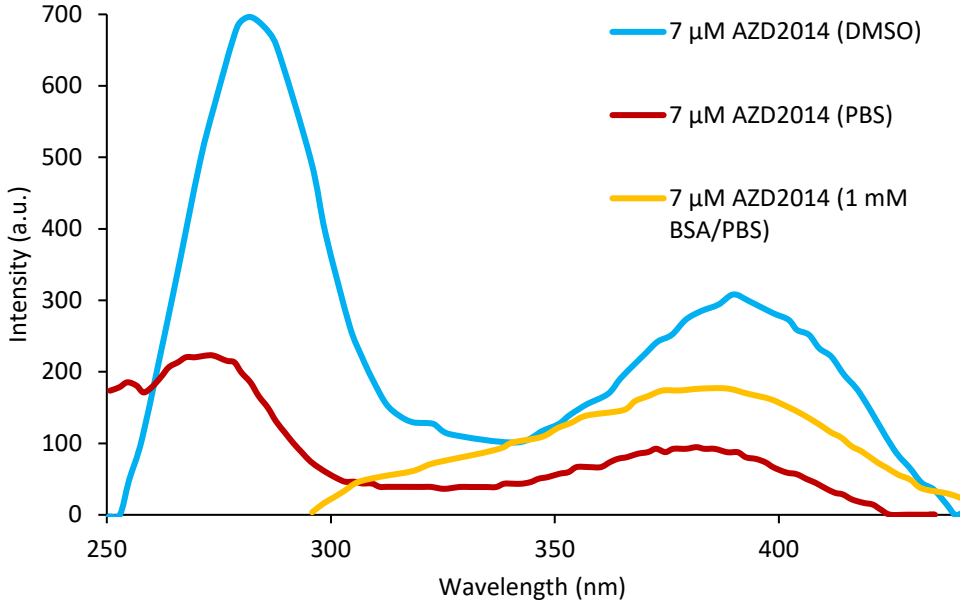

C.4 AZD2014 two-photon excitation and single photon calibration

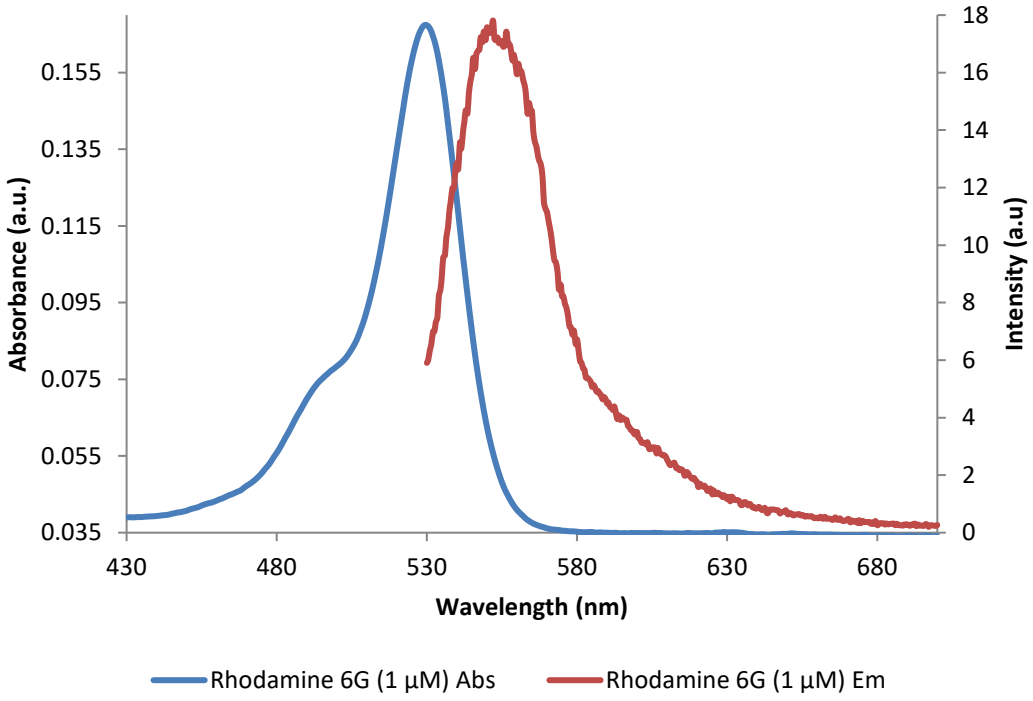

C.5 AZD2014 two-photon excitation and single photon calibration

A

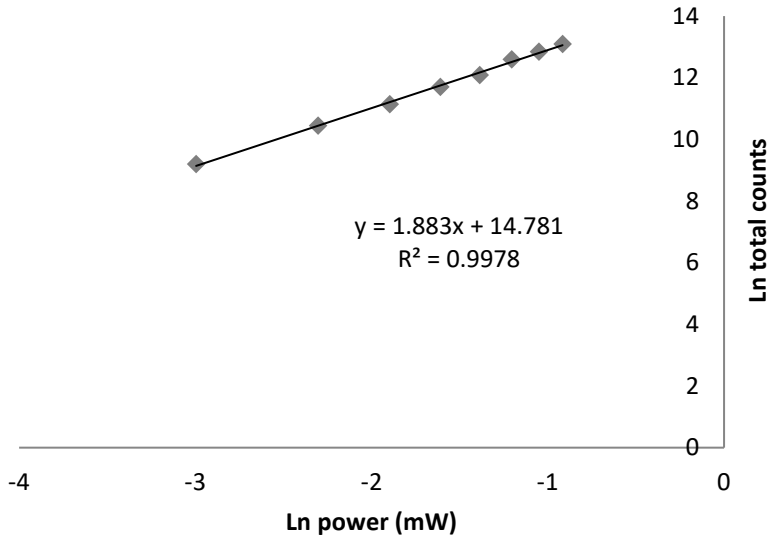

B

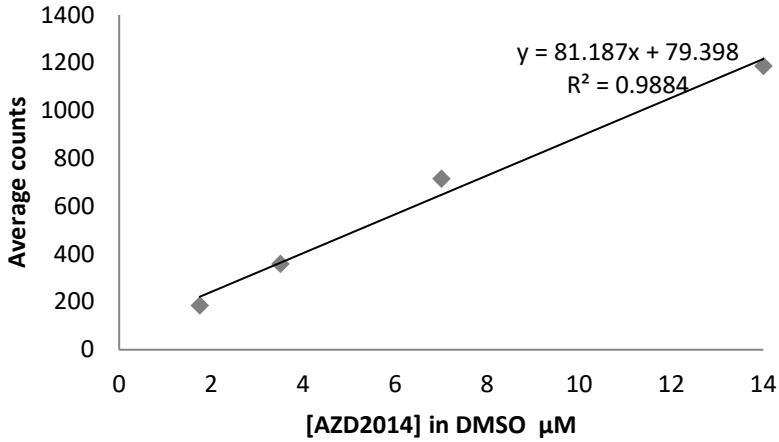

A) Log-log plot 600 nm excitation of AZD2014 in DMSO with increasing laser power. The value of the slope gives the power of a power relationship which in this case is 2 because of two-photon excitation. B) Counts against increasing [AZD2014] in DMSO using 405 nm pulsed excitation.

C.6 Multiphoton (600 nm) FLIM of HEK293 only at 0.5 mW

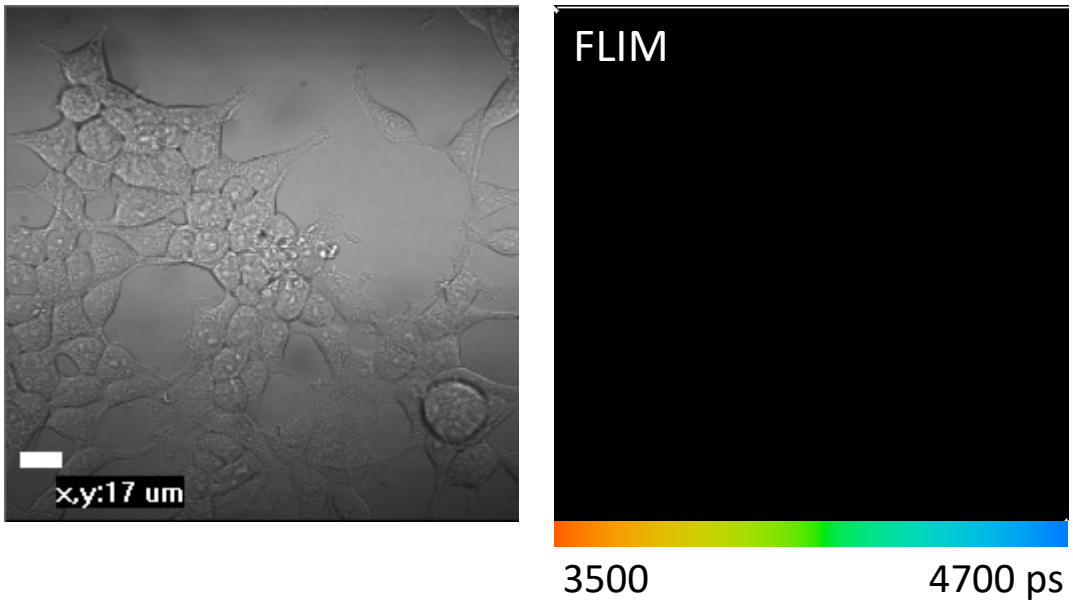

Image on left shows transmission of cells. Image on right shows a FLIM of the same cells. Emission band with filter, 460/60 with 600 nm excitation and 0.5 mW combined should give minimal excitation and emission of tryptophan

C.7 Multiphoton (600 nm) FLIM of EGFP-S6K1 only at 0.5 mW

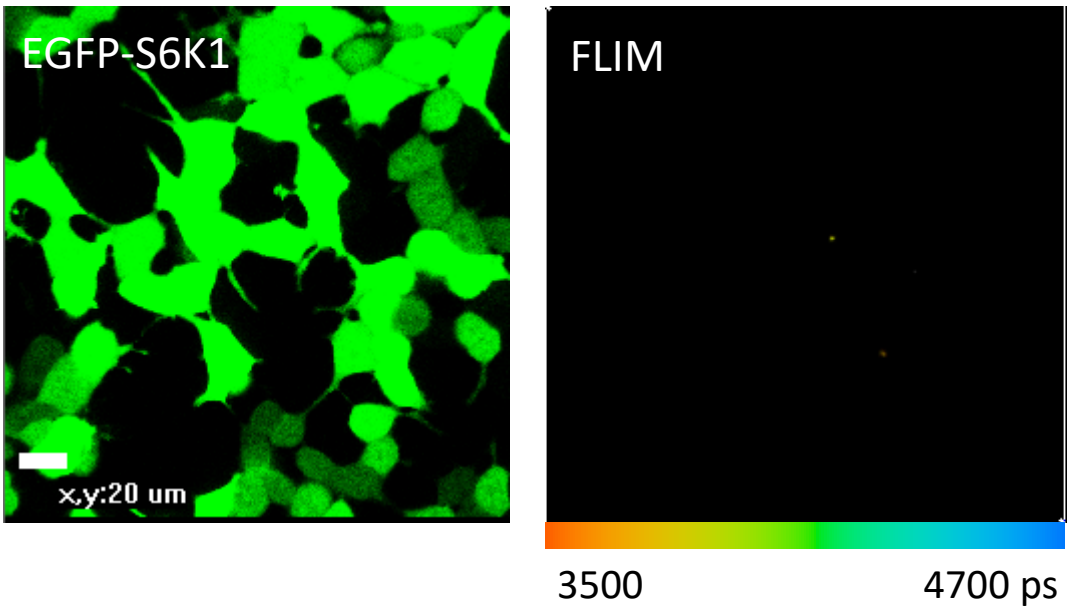

Image on left shows confocal of cells expressing EGFP-S6K1. Image on right shows a FLIM of the same cells. Emission band with filter, 460/60 with 600 nm excitation and 0.5 mW combined should give minimal excitation and emission of EGFP

Appendix D

D.1 Pilot expression and purification of SensOR

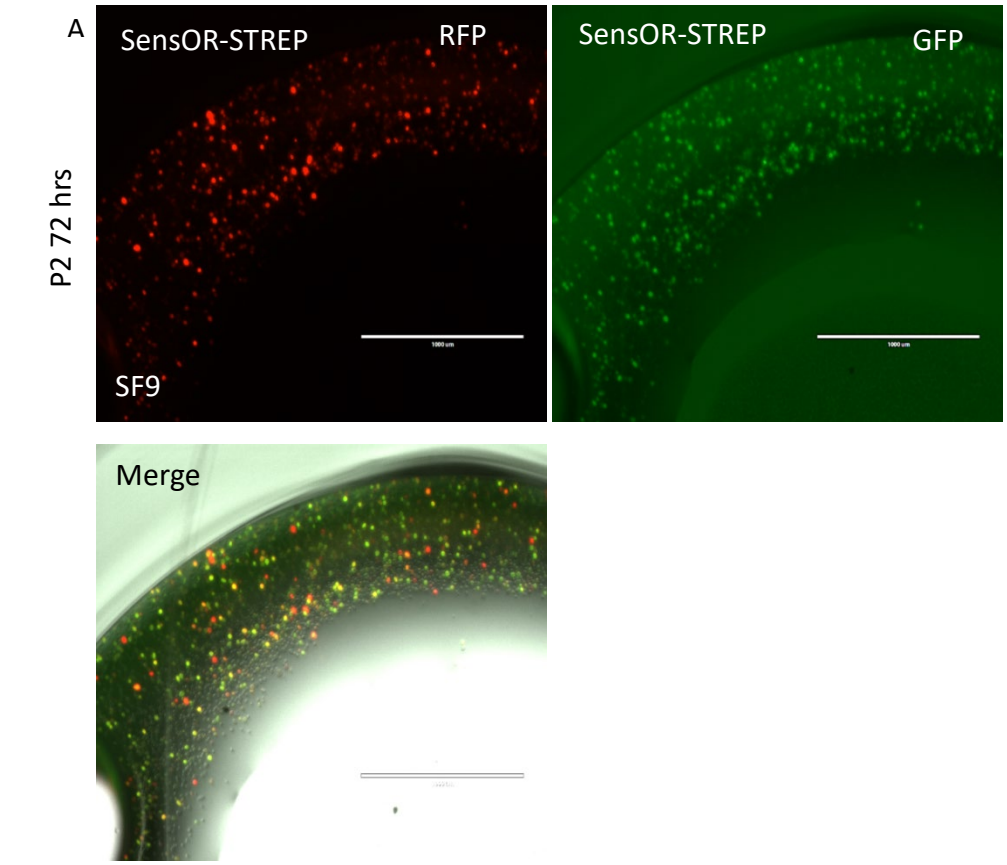

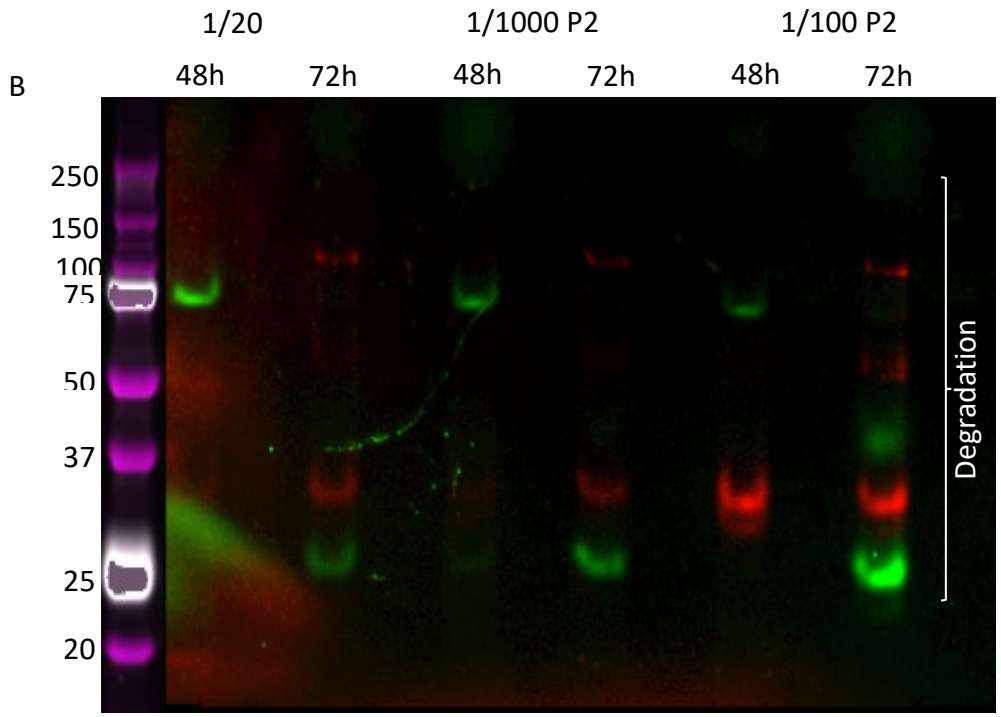

D.2 QC expression and purification of raptor and S6K1 constructs

A

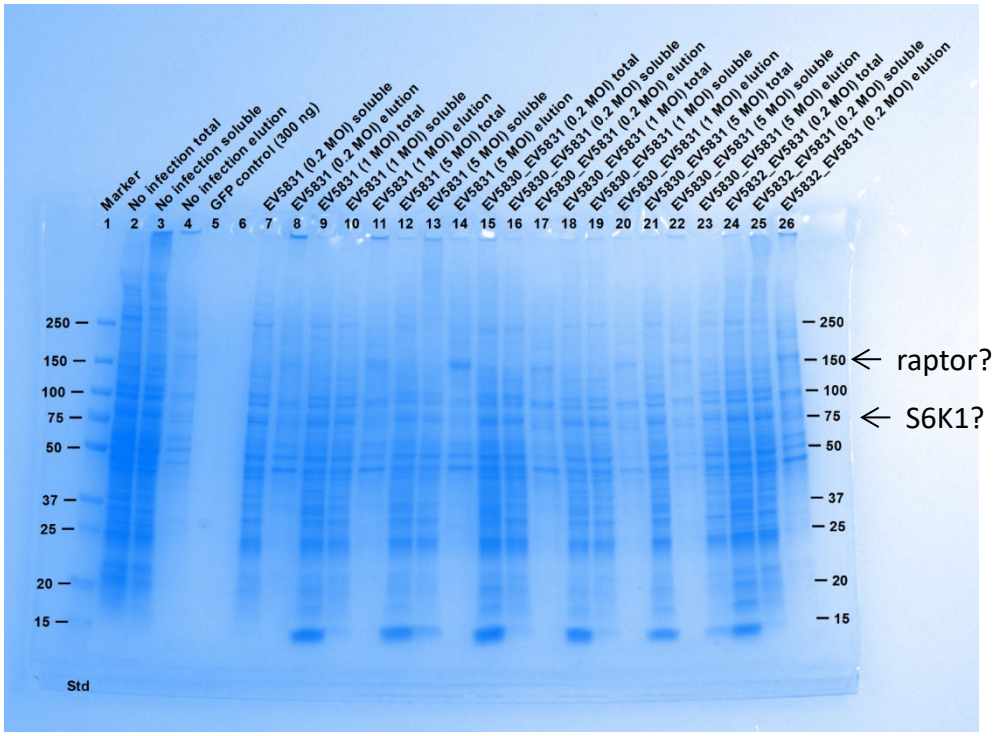

B

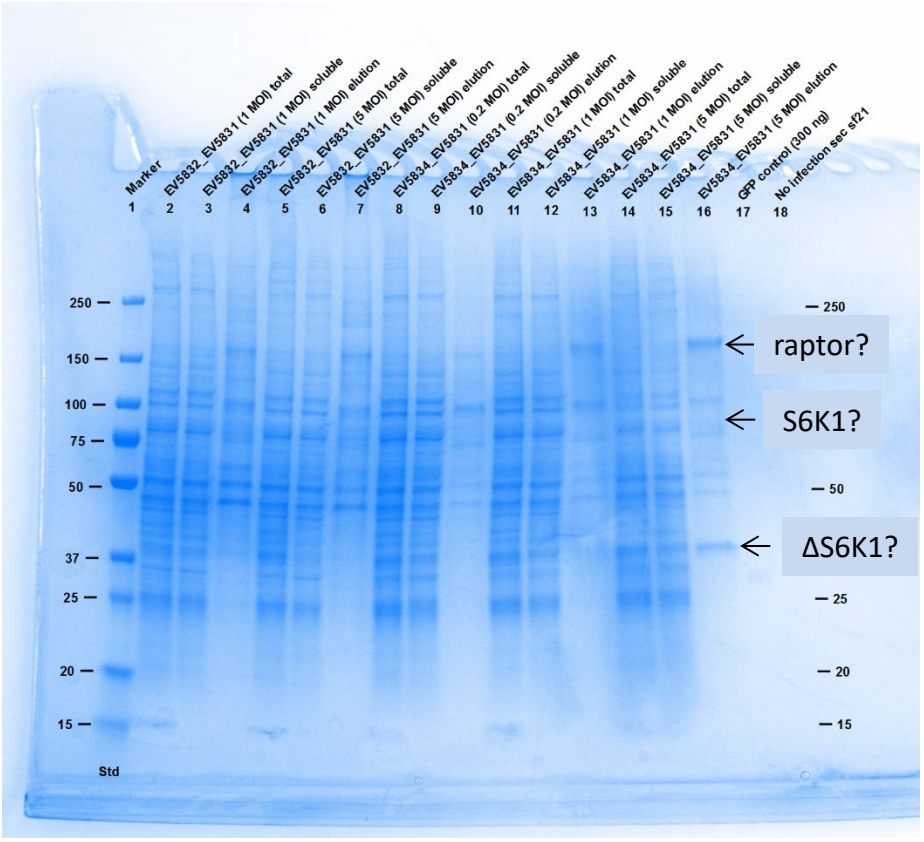

D.3 Chromatagram obtained for S6K1-FLAG + raptor-His after purification using the ÄKTA protein purification system.

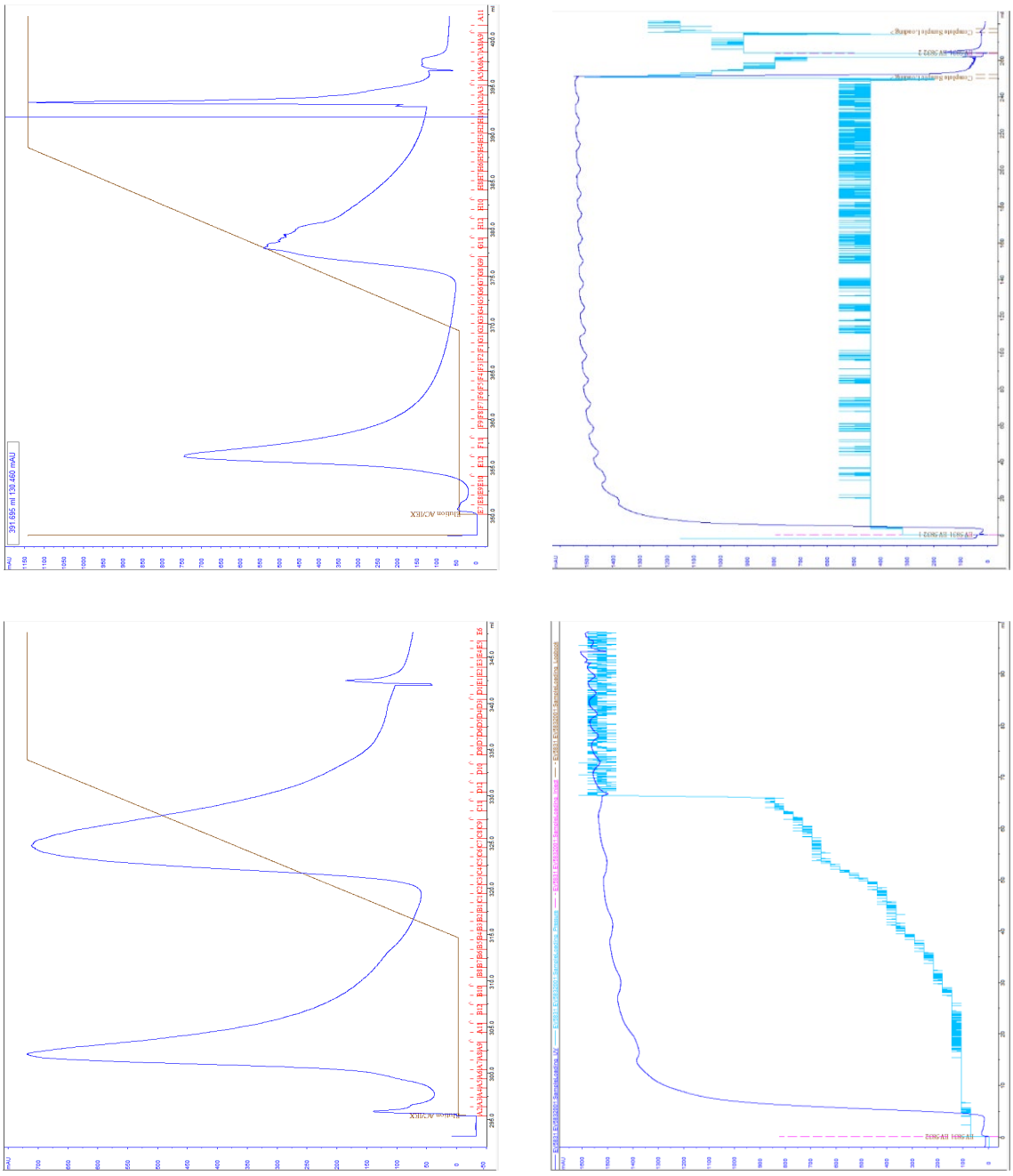

A B

The blue peak represents the eluted protein fractions. B) Curved obtained for pressure loading (cyan curve) and protein UV absorbance (dark blue) using the ÄKTA protein purification system

D.4 Coomassie of large scale iMAC of raptor and S6K1

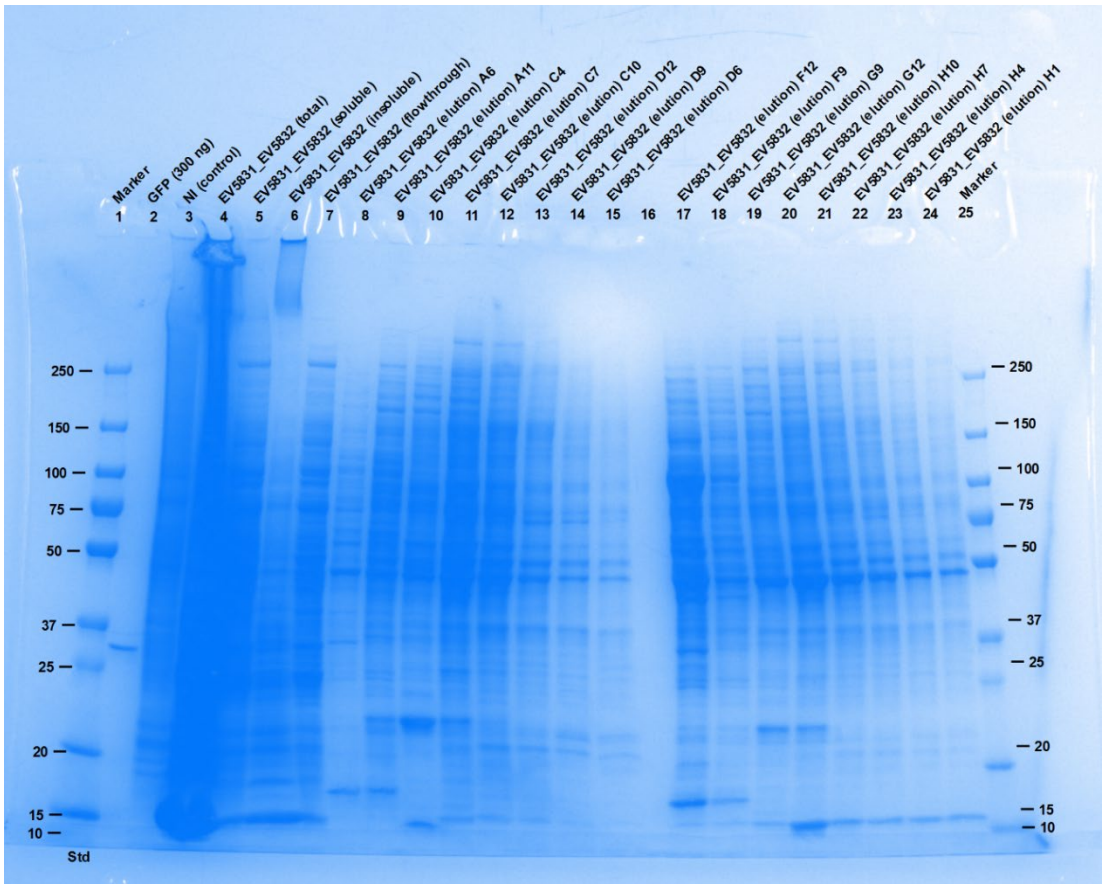

D.5 Coomassie Phynexus run raptor and S6K1 elutions

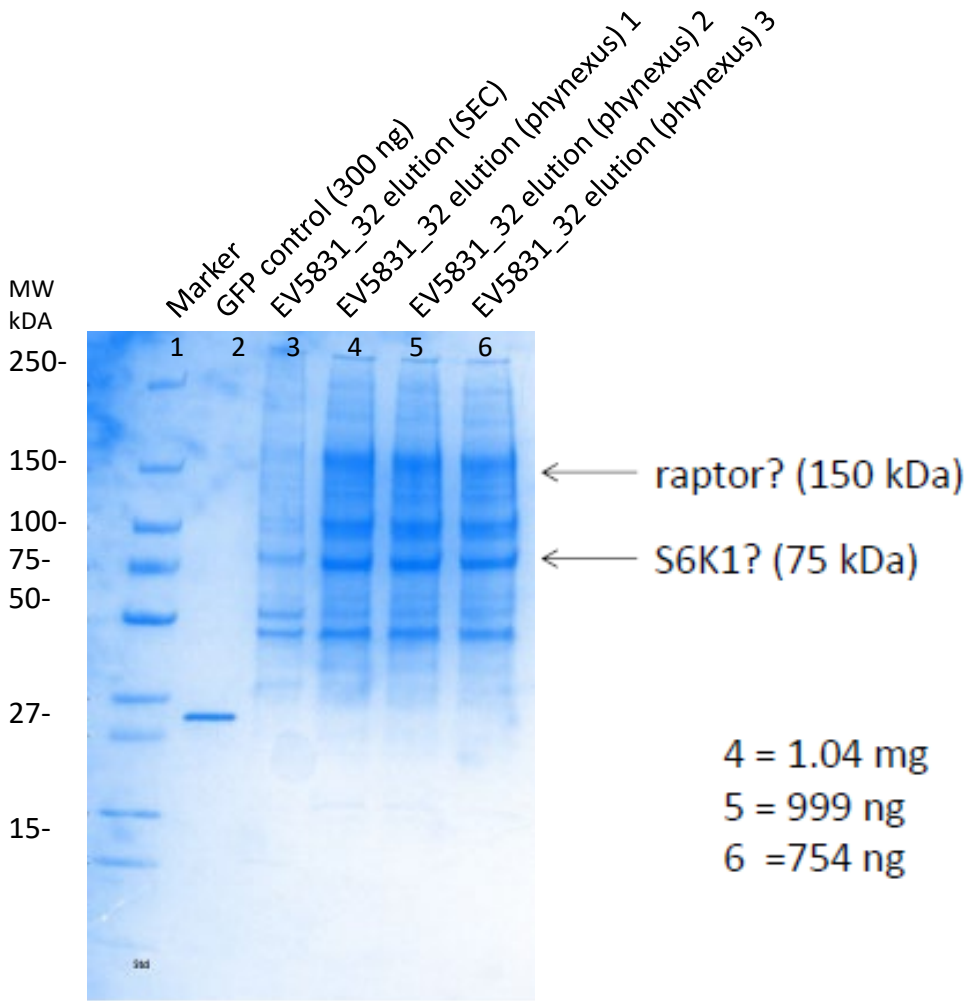

D.6 Sequence Annotated by Structure (SAS) of S6K1